Spectroscopie des processus photoélectriques dans les structures et dispositifs III-N

Marco Piccardo

NNT : 2016SACLX056

THESE DE DOCTORAT
DE
L'UNIVERSITE PARIS-SACLAY
PREPAREE A
L'ECOLE POLYTECHNIQUE

ECOLE DOCTORALE N° 573

Interfaces : approches interdisciplinaires/fondements, applications et innovations

Spécialité de doctorat : Physique

Par

M. Marco Piccardo

Spectroscopy of photoelectric processes in III-N structures and devices

Thèse présentée et soutenue à Palaiseau, le 23 septembre 2016 :

Composition du Jury :

M. Jean-Michel GERARD, Professeur	CEA-INAC	Président
M. Jean-Yves DUBOZ, Directeur de Recherche	CNRS-CRHEA	Rapporteur
M. Nicolas GRANDJEAN, Professeur	EPFL (Suisse)	Rapporteur
M. Luca PERFETTI, Professeur	Ecole Polytechnique-LSI	Examinateur
M. Jacques PERETTI, Directeur de Recherche	Ecole Polytechnique-PMC	Directeur de thèse
M. Lucio MARTINELLI, Ingénieur de Recherche	Ecole Polytechnique-PMC	Co-directeur de thèse
M. Claude WEISBUCH, Professeur	Ecole Polytechnique/UCSB	Co-directeur de thèse
M. James S. SPECK, Professeur	UCSB (Etats Unis)	Invité

To my father,

For daydreaming, from time to time, about me

"The end of one journey is simply the start of another. […] You have to start the journey anew. Always."

- *José Saramago, Journey to Portugal*

ACKNOWLEDGEMENTS

First of all I would like to thank my advisors: Prof. Claude Weisbuch, Dr. Jacques Peretti and Dr. Lucio Martinelli.

Claude is the dream of any ambitious young scholar. He is a coach, a wide-ranging master. I would like to call him my Socrates: he bombarded me with questions – good questions – during my PhD, and in this way he helped me shaping my scientific thinking. Sometimes, even if he is not around me, I can hear him in my mind asking me questions. He has not only accompanied me in this journey through science but he has also always been ready to help me in my personal life, as a friend.

Jacques gave me a large freedom to work in research. And freedom has an immeasurable value in science. When he intervened, he helped me adding profound value at the same time to my work and myself. To my work, thanks to his expertise and his perceptive vision of physics, and to myself, enhancing my career path and shaping my future.

Lucio, as everybody knows at the PMC laboratory, is magical. He is everywhere! Whenever I needed him, he appeared. And whatever the problem was, he helped me solving it. I have never seen him without a smile. He has also been a fundamental moral support for the success of my PhD.

During these years I have collaborated and discussed with several researchers at the PMC laboratory. I would like to thank in particular the following ones. Prof. Marcel Filoche, who supervised all the work in my thesis related to the localization landscape theory of disorder in semiconductors. As a theoretician, he has been an important reference for me during these years and with him I have enjoyed blackboards nicely filled with equations. I would also like to thank Dr. Fouad Maroun and Dr. Yves Lassailly, who never hesitated to give me some of their time, for discussing and working together to some experiment: Fouad, in the atomic-force microscopy measurements, and Yves, in the scanning tunneling microscopy measurements.

At the PMC laboratory I have experienced a wonderful atmosphere, thanks to all the people who animate this laboratory: the researchers, PhD students, post-docs and interns, technicians, and technical and administrative teams. I have always felt like among

friends in the coffee room of the laboratory. Thanks in particular to all the students for their solidarity and optimism, and for all the good time spent together, skiing, running, playing poker, and so on.

During these years, I have spent seven months of research welcomed in the laboratories of Prof. James Speck and Prof. Shuji Nakamura at the University of California, Santa Barbara. I would like to thank in particular Jim for having transmitted me a sense of competition and excitement that is in resonance with my feelings in research. We had a wonderful discussion a couple of years ago in a restaurant about life and research that I will never forget. Thanks also to all the graduate students who provided me with the primary source for experiments, i.e. samples, in particular: Justin Iveland, Nathan Young, Leah Kuritzy, Daniel Myers, Abdullah Alhassan and Burhan Saifaddin.

The simulation studies presented in this thesis related to the localization landscape theory of disorder in semiconductors were carried out in strict collaboration with the group of Prof. Yuh-Renn Wu at the National Taiwan University. I would like to thank Yuh-Renn and his team, in particular Dr. Chi-Kang Li, for the frequent and fruitful discussions we had and for their kind availability at any moment.

I would also like to thank Dr. Luca Perfetti, who warmly welcomed me in his laboratory at the synchrotron Soleil and who allowed me to carry out experiments autonomously on his “Ferrary” of ultra-high vacuum, a great angle-resolved photoemission spectroscopy setup.

Finally let me get to the loved ones. Thanks to all my longtime friends with whom, despite the long distance, I still share glories and despairs.

It is not sufficient to thank my family. In Japan they say that, since our birth we have a debt with our family, due to its love and sacrifices, which we will never be able to pay back. Thanks to my mother, my father and my sister for having given me wings to fly.

And to conclude, my love, because “Omnia vincit amor”. Thanks to my girlfriend, who simply completes me and allows me to be a three-dimensional man. Obrigado.

ABSTRACT

Nitride light-emitting diodes (LEDs) have triggered a real revolution in lighting. Rapid technological progress has led to very high efficiencies with recent records exceeding 300 lm/W in the case of white LEDs. But in spite of these exceptional performances, recognized by the Nobel Prize in Physics in 2014, the intrinsic properties of nitride alloys and the physics of these devices are still not well understood. Carrier dynamics and nonlinear phenomena play a fundamental role on LED performance under high injected current, but electrical measurements can hardly give access to transport processes occurring over a range of energy states larger than k_BT without resorting to models and simulations. Besides, there is growing evidence that alloy disorder plays a major role in the electrical and optical properties of nitride materials. However, modelling the disorder-induced localization effects is a practically unrealizable task in the framework of nowadays existing methods and, in fact, device design tools accounting for these effects still lack. In the course of my thesis work, novel experimental and theoretical approaches to tackle the study of the microscopic mechanisms governing the electronic properties of nitride semiconductors have been developed.

The emission of electrons from nitride compounds and devices activated to negative electron affinity was studied under optical excitation and under electrical injection of carriers. This approach gives access to the whole conduction band by low energy electron spectroscopy techniques, thereby allowing selective identification of processes involved in the excitation and transport of electrons. Near band gap photoemission spectroscopy was performed to study the conduction band structure of GaN. These measurements provided, in particular, the first direct determination of the energy position of the side valleys of the band conduction. During this study, "anomalous" photoemission processes were also evidenced. In addition, electron emission from LED under electrical injection of carriers was studied. The origin of the various structures observed in the electroemission spectra is discussed and, in particular, the contribution of anomalous photoemission processes is evaluated.

A recent theory of localization in disordered systems is applied to nitride materials and optoelectronic devices. This method allows for the first time the determination of the localization landscape induced by alloy disorder without solving the Schrödinger equation associated with the disordered system, which leads to a strong reduction of the computation time. The modelling is developed to completely describe a device in operating condition. Experimentally, the problem of disorder-induced localization is approached by photocurrent spectroscopy measurements in LEDs and solar cells whose active regions contain InGaN quantum wells. A clear signature of alloy disorder is observed in the form of an exponential absorption tail (Urbach tail) for below-gap excitation. This allows defining a characteristic energy of the disorder which is found to be in excellent agreement with the predictions given by the novel localization theory. The application of this theory to the modelling of full 3D LED structures with compositional fluctuations allows computing self-consistently device characteristics including quantum effects.

RESUME DE THESE

Les diodes électroluminescentes en nitrures (LED) ont déclenché une véritable révolution dans l'éclairage. Les progrès technologiques rapides ont conduit à des rendements très élevés, avec des records récents dépassant 300 lm/W pour les LED blanches. Mais en dépit de ces performances exceptionnelles, récompensées par le Prix Nobel de Physique en 2014, les propriétés intrinsèques des alliages de nitrures et la physique de ces dispositifs sont encore mal connues. La dynamique des porteurs et les phénomènes non linéaires jouent un rôle fondamental sur les performances des LED à fort courant injecté, mais les mesures électriques ne peuvent donner accès aux processus de transport dans une gamme d'énergie supérieure à k_BT sans recourir à des modèles et simulations. En outre, il est de plus en plus évident que le désordre d'alliage a un impact fort sur les propriétés électriques et optiques des nitrures. Cependant, la modélisation des effets de localisation induite par le désordre est une tâche pratiquement irréalisable avec les méthodes existantes et les outils de conception de dispositifs qui prennent en compte ces effets manquent encore. Au cours de cette thèse, de nouvelles approches expérimentales et théoriques pour aborder l'étude des mécanismes microscopiques régissant les propriétés électroniques des nitrures semi-conducteurs ont été développées.

L'émission d'électrons à partir de composés et dispositifs en nitrures activés en affinité négative a été étudiée, sous excitation optique et sous injection électrique de porteurs. Cette approche donne accès à l'ensemble de la bande de conduction par les techniques de spectroscopie électronique à très basse énergie, permettant ainsi une identification sélective des processus qui interviennent dans l'excitation et le transport des électrons. Les mesures de spectroscopie de photoémission sur le GaN de type p ont permis d'étudier la structure de la bande de conduction de ce composé et, en particulier, de réaliser la première mesure directe de la position en énergie des vallées latérales de la bande de conduction. Au cours de cette étude, des processus « anomaux » de photo-émission ont aussi été mis en évidence. Par ailleurs, l'émission d'électrons à partir de LED sous injection électrique de porteurs a été étudiée. L'origine des différentes structures observées dans les spectres d'électroémission est discutée et, en particulier, la contribution des processus anomaux de photoémission est évaluée.

Une théorie récente de la localisation dans les systèmes désordonnés est appliquée aux matériaux de nitrure et aux dispositifs optoélectroniques. Cette méthode permet pour la première fois la détermination du paysage de localisation induit par un désordre d'alliage sans résoudre l'équation de Schrödinger associée au système désordonné, ce qui conduit à une forte réduction du temps de calcul. La modélisation est développée pour décrire complètement un dispositif en état de fonctionnement. Expérimentalement, le problème de localisation induite par un désordre est approché par des mesures de spectroscopie de photocourants dans des LED et des cellules solaires dont les régions actives contiennent des puits quantiques InGaN. Une signature claire d'un désordre d'alliage est observée sous la forme d'une queue d'absorption exponentielle (queue d'Urbach) pour l'excitation sous l'écart. Ceci permet de définir une énergie caractéristique du désordre qui s'avère être en excellent accord avec les prédictions données par la nouvelle théorie de la localisation. L'application de cette théorie à la modélisation de structures LED 3D complètes avec des fluctuations de composition permet de calculer des caractéristiques de dispositif auto-cohérentes, y compris les effets quantiques.

CONTENTS

LIST OF ACRONYMS

2DEG	Two-dimensional electron gas
APT	Atom probe tomography
ARPES	Angle-resolved photoemission spectroscopy
BBR	Band-bending region
CB	Conduction band
CBM	Conduction band minimum
CDS	Cylindrical deflection selectors
CFL	Compact fluorescent lamp
CoO	Cost of ownership
DEDC	Derivative of energy distribution curve
DH	Double heterostructure
DOS	Density of states
EBL	Electron blocking layer
EDC	Energy distribution curve
EE	Electro-emission
EL	Electro-luminescence
EQE	External quantum efficiency
FKE	Franz-Keldysh effect
HEE	High-energy extrapolation
HEMT	High-electron mobility transistors
HET	High-energy threshold
IQE	Internal quantum efficiency
ITO	Indium tin oxide
LED	Light-emitting diode
MBE	Molecular beam epitaxy
MOCVD	Metal-organic chemical vapor deposition
MQW	Multiple quantum well
NDR	Negative differential resistance
NEA	Negative electron affinity
PE	Photoemission
PES	Photoemission spectroscopy
PL	Photoluminescence
PR	Photoresist
QCSE	Quantum-confined Stark effect
QW	Quantum well
QY	Quantum yield
SPV	Surface photovoltage
SQW	Single quantum well
TD	Threading dislocations
UHV	Ultra-high vacuum
UID	Unintentionally doped
VCSEL	Vertical cavity surface-emitting laser

INTRODUCTION

English version

This thesis work deals with the study of the electronic properties of nitride semiconductor structures and devices by an original approach based on electron emission spectroscopy and photocurrent spectroscopy techniques. This work was carried out in close collaboration with, on the one hand, the University of California in Santa Barbara (UCSB), for the experimental aspects and, on the other hand, with the Group of Physics of Irregular Systems of the PMC laboratory at the Ecole Polytechnique and the National Taiwan University (NTU), for the theoretical aspects.

The nitride industry has been developing over the last twenty years with the invention of the InGaN/GaN light-emitting diodes (LEDs) which was awarded the Nobel Prize in Physics in 2014. One of the reasons for this recognition is related to the expected impact of nitride devices in terms of energy saving. Lamps based on GaN LEDs are indeed very promising light sources for low-energy lighting. In addition, nitride compounds should allow the development of smaller, faster, more efficient and more reliable power devices than their silicon counterparts, which are voltage and frequency limited. These devices should also provide a significant reduction of losses in the transformation and distribution of electricity. However, their performances are far from the intrinsic limits that should allow achieving the targeted objectives in terms of energy efficiency.

Many different problems are encountered in nitride materials and devices which are discussed in Chapter 1 of this manuscript. Two of them are particularly critical and lead to a paradoxical situation where the GaN industry is expanding but the design of devices still relies on empirical approaches. The first problem is that the basic properties

of nitrides (band structure parameters, carrier dynamics…) are still poorly known. The second one is that the devices incorporate heterostructures based on ternary alloys which exhibit a strong compositional disorder. But the effect of composition disorder on the properties and performance of devices is not clearly identified and is usually not taken into account. The objective of my work was to identify, by direct spectroscopic methods, the mechanisms that govern photoelectric processes and the dynamics of electrons in III-N semiconductors. Two problems were more specifically addressed: the transport of hot electrons under high injection and the role of alloy disorder in optoelectronic InGaN/GaN devices.

Chapter 2 reports on the study of the emission of electrons from nitride heterostructures and LEDs activated to negative electronic affinity. The LED devices consist of a GaN p-n junction containing quantum wells of InGaN in the depletion zone. On the surface of the p-type GaN layer is deposited a cesium atomic layer which makes it possible to reach the situation of apparent negative electron affinity where the vacuum level lies below the minimum of the conduction band in the bulk crystal. In this condition, when carriers are injected electrically into the junction, the electrons which escape the active region can be emitted in vacuum. It is then possible to measure the spectrum of the emitted electrons which exhibits structures characteristic of the electronic process that compete with the radiative recombination of the carriers. This very unique approach made it possible to demonstrate the appearance of a contribution of hot electrons, dominant at high injection and correlated with the decrease in the efficiency of the emission of light. This contribution was attributed to the emission of hot electrons, generated by Auger recombination in the quantum wells, and subsequently transferred to the upper valleys of the conduction band from where they were emitted. I thus performed complementary experiments based on low-energy photoemission spectroscopy to determine the parameters of the GaN conduction band. These experiments provided a direct confirmation of the existence of a lateral valley about 1 eV above the minimum of the conduction band. This value is however much lower than those predicted by *ab initio* calculations of the GaN electronic structure but is in agreement with the contribution of hot electrons observed in the electro-emission experiments. The determination of the position of the first lateral valley of the conduction band is crucial for understanding the transport of hot electrons which is, in fact, quite generally governed by multi-valley processes. Furthermore, I have extended the study of the photoelectric processes towards low excitation energies and to different

samples and structures. A surprising variety of data was collected. For instance, at optical excitation energy smaller than the bandgap, a contribution of "super-energetic" electrons to the emitted current is observed for continuous wave excitation. In pulsed mode, a super-energetic contribution can also be generated for photon energies both lower and higher than the bandgap. These measurements show that the photoelectric processes in nitride semiconductors are complex and still partially understood, in particular for high excitation power density, including for photon energies smaller than the GaN band gap but corresponding to the light emitted by the LEDs. Thus, the study carried out in the present work shows that the photoelectric processes excited by the device's internal electroluminescence are also likely to generate contributions of hot electrons. The origin of these contributions is not yet identified. The difficulties involved in the spectroscopic measurements of electronic transport (electro-emission, below bandgap photoemission, electrostatic force microscopy) on nitrides are analyzed. In all cases, the main problem is the variety of data with excitation conditions and samples. As a consequence, the identification of the origin of the phenomena observed is uncertain and several interpretations are possible.

Chapter 3 addresses the problem of disorder-induced localization effects in optoelectronic devices incorporating InGaN quantum wells. This study includes both an experimental and a theoretical part. From an experimental point of view, the approach I developed consists in measuring the photocurrent variation in InGaN/GaN solar cells as a function of the excitation energy. In these devices, the photocarrier extraction efficiency being very close to unity, the measurement of the photocurrent provides direct access to the absorption of the quantum wells. For an excitation energy smaller than the band gap in the quantum wells, the measurements show an absorption tail, called Urbach tail, which is related to the localization of the electronic states by the compositional disorder of the alloy. The dependence of the Urbach tail on the voltage applied to the junction shows a shift towards high energy (blue shift) compatible with piezoelectric field compensation in the wells. A theoretical description of the absorption in ternary alloy quantum wells has been achieved. This description is based on a localization approach in disordered systems that allows for the first time to straightforwardly determine the localization landscape without solving the associated Schrödinger equation, which greatly reduces the computation time. In this treatment, the fluctuations of the alloy composition are those measured by atomic probe tomography. For the different studied structures, corresponding to quantum well alloy composition

varying from 0 to 30%, the Urbach tail simulations are in excellent agreement with the photocurrent spectroscopy measurements. Then, the modeling is developed to completely describe a device in operating condition. The application of this theory to the 3D modeling of LED structures exhibiting composition fluctuations allows a self-consistent calculation of the device characteristics which includes quantum effects.

Finally, the manuscript is complemented by a list of References and an Appendix section which provides supplementary information on various side issues addressed in my PhD work.

Version française

Ce travail de thèse porte sur l'étude des propriétés électroniques des structures et dispositifs semi-conducteurs à base de nitrure par une approche originale basée sur la spectroscopie d'émission d'électrons et la spectroscopie de photo-courant. Ce travail a été réalisé en étroite collaboration avec, d'une part, l'Université de Californie à Santa Barbara (UCSB), pour les aspects expérimentaux et, d'autre part, avec le Groupe de Physique des Systèmes Irréguliers du laboratoire PMC à l'Ecole Polytechnique et l'Université de Taiwan (NTU), pour les aspects théoriques.

L'industrie des nitrures s'est développée au cours des vingt dernières années avec l'invention des diodes électroluminescentes InGaN/GaN (DEL) qui a été récompensée par le prix Nobel en Physique en 2014. L'une des raisons de cette reconnaissance est liée à l'impact attendu des dispositifs à base de nitrures en termes d'économie d'énergie. Les lampes basées sur les DEL en GaN sont des sources lumineuses très prometteuses pour l'éclairage à faible consommation d'énergie. Par ailleurs, les composés en nitrures devraient permettre le développement de dispositifs de puissance plus petits, plus rapides, plus efficaces et plus fiables que leurs homologues en silicium, qui sont limités en tension et en fréquence. Ces dispositifs devraient également permettre une réduction importante des pertes dans la transformation et la distribution de l'électricité. Toutefois, leurs performances sont loin des limites intrinsèques qui devraient permettre d'atteindre les objectifs ciblés en termes d'efficacité énergétique.

Les différents problèmes rencontrés dans les matériaux et dispositifs en nitrures sont discutés dans le Chapitre 1 de ce manuscrit. Deux d'entre eux sont particulièrement critiques et mènent à une situation paradoxale où l'industrie GaN est en expansion, mais la conception des dispositifs repose toujours sur des approches empiriques. Le premier problème est que les propriétés de base des nitrures (paramètres de la structure des bandes, dynamique des porteurs...) sont encore mal connues. Le second est que les dispositifs incorporent des hétérostructures à base d'alliages ternaires qui présentent un fort désordre de composition. Mais l'effet du désordre de composition sur les propriétés et la performance des dispositifs n'est pas clairement identifié et n'est généralement pas pris en compte. L'objectif de mon travail était d'identifier, par des méthodes spectroscopiques directes, les mécanismes qui régissent les processus photoélectriques et la dynamique des électrons dans les semi-conducteurs III-N. Deux problèmes ont été abordés plus spécifiquement: le transport d'électrons chauds sous forte injection et le rôle du désordre d'alliage dans les dispositifs optoélectroniques à base de structures InGaN/GaN.

Le Chapitre 2 décrit l'étude de l'émission d'électrons à partir d'hétérostructures en nitrures et de DEL activées à affinité électronique négative. Les DEL consistent en une jonction GaN p-n contenant des puits quantiques d'InGaN dans la zone de déplétion. Sur la surface de la couche de GaN de type p est déposée une couche atomique de césium qui permet d'atteindre la situation d'affinité électronique négative apparente où le niveau de vide se situe au-dessous du minimum de la bande de conduction dans le cristal massif. Dans ces conditions, lorsque des porteurs sont injectés électriquement dans la jonction, les électrons qui échappent à la zone active peuvent être émis sous vide. Il est alors possible de mesurer le spectre des électrons émis qui présente des structures caractéristiques du processus électronique en compétition avec la recombinaison radiative des porteurs. Cette approche tout à fait unique a permis de démontrer l'apparition d'une contribution d'électrons chauds, dominante à forte injection et corrélée à la diminution de l'efficacité de l'émission de lumière. Cette contribution a été attribuée à la génération d'électrons chauds par recombinaison Auger dans les puits quantiques, et au transfert de ces électrons vers les vallées supérieures de la bande de conduction d'où ils sont émis.

Au cours de mon travail, j'ai réalisé des expériences complémentaires basées sur la spectroscopie de photoémission à faible énergie pour déterminer les paramètres de la bande de conduction GaN. Ces expériences ont confirmé directement l'existence d'une vallée latérale à environ 1 eV au-dessus du minimum de la bande de conduction. La détermination de la position de la première vallée latérale de la bande de conduction est cruciale pour comprendre le transport d'électrons chauds qui est, en fait, généralement gouverné par des procédés à plusieurs vallées. La valeur obtenue est cependant beaucoup plus faible que celles prédites par des calculs *ab initio* de la structure électronique GaN, mais est en accord avec la contribution des électrons chauds observés dans les expériences d'électro-émission et avec différentes mesures indirectes réalisées par d’autres techniques.

De plus, j'ai étendu l'étude des processus photoélectriques au domaine des faibles énergies d'excitation et à différents échantillons et structures. Une variété de données surprenantes a été recueillie. Par exemple, à une énergie d'excitation optique inférieure à la bande interdite et en excitant en mode continu, on observe une contribution d'électrons « super énergétiques » au courant émis. En mode pulsé, une contribution « super énergétique » peut également être générée (dans certaines conditions d’excitation) pour des énergies de photons à la fois inférieures et supérieures à la bande interdite. Ces mesures montrent que les processus photoélectriques dans les semi-conducteurs en nitrures sont complexes et encore partiellement compris, en particulier pour une densité de puissance

d'excitation élevée, y compris pour des énergies de photons inférieures à la largeur de la bande interdite de GaN mais correspondant à la lumière émise par les DEL. Ainsi, l'étude réalisée dans ce travail montre que les processus photoélectriques excités par l'électroluminescence interne du dispositif sont également susceptibles de générer des contributions d'électrons chauds. L'origine de ces contributions n'est pas encore identifiée. Les difficultés liées aux mesures spectroscopiques du transport électronique (électro-émission, photoémission en bande interdite, microscopie électrostatique) sur les nitrures sont analysées. Dans tous les cas, le problème principal est la dispersion des données avec les conditions d'excitation et les échantillons. En conséquence, l'identification de l'origine des phénomènes observés est incertaine et plusieurs interprétations sont possibles.

Le Chapitre 3 traite du problème des effets de localisation induits par le désordre d'alliage dans les dispositifs optoélectroniques incorporant des puits quantiques InGaN. Cette étude comprend à la fois une partie expérimentale et une partie théorique. Du point de vue expérimental, l'approche que j'ai développée consiste à mesurer la variation du photocourant dans des cellules solaires InGaN/GaN en fonction de l'énergie d'excitation. Dans ces dispositifs, l'efficacité d'extraction du photocapteur étant très proche de l'unité, la mesure du photocourant fournit un accès direct à l'absorption des puits quantiques. Pour une énergie d'excitation plus petite que la bande interdite dans les puits quantiques, les mesures montrent une queue d'absorption, appelée queue d'Urbach, qui est liée à la localisation des états électroniques par le désordre compositionnel de l'alliage. La variation de la queue d'Urbach avec la tension appliquée à la jonction montre un décalage vers les hautes énergies compatible avec la compensation de champ piézoélectrique dans les puits. Une description théorique de l'absorption dans des puits quantiques en alliage ternaire a été réalisée. Cette description est basée sur une approche de localisation dans des systèmes désordonnés qui permet pour la première fois de déterminer directement le paysage de localisation sans résoudre l'équation de Schrödinger associée, ce qui réduit considérablement le temps de calcul. Dans ce traitement, les fluctuations de composition d'alliage sont celles mesurées par tomographie par sonde atomique. Pour les différentes structures étudiées, correspondant à des compositions d'alliage des puits quantiques variant de 0 à 30%, les simulations de la queue d'Urbach sont en excellent accord avec les mesures de spectroscopie de photocourant. De plus, la modélisation est développée pour décrire complètement un dispositif en état de fonctionnement. L'application de cette théorie à la modélisation 3D de structures LED présentant des fluctuations de composition permet un calcul auto-cohérent des caractéristiques du dispositif qui inclut les effets quantiques.

Enfin, le manuscrit est complété par une liste de Références et une section d'Annexes qui fournit des informations supplémentaires sur différentes problématiques spécifiques abordées au cours de mon travail de doctorat.

1 PROBLEMS IN III-NITRIDE MATERIALS AND DEVICES

It is rather surprising that after decades of development of group-III nitrides (as a reference, the first high-brightness blue nitride LED was demonstrated in the early 1990's by Shuji Nakamura [1]) there is still an intense academic effort to truly understand the physics of nitride devices. Several problems are still unsolved as it will be outlined in the sections of this chapter.

One could think that III-N semiconductors are basically similar to other III-V's such as GaAs, simply differing by the values of their basic parameters such as lattice constant, band gap energy, refractive index, etc., which can be properly measured. However, nitride devices suffer from a panoply of uncontrolled structural, optical and electronic effects, such as threading dislocations, disorder-induced carrier localization, current crowding, polarization fields, etc. This concomitant ensemble of undesired phenomena occurring beyond the will of the semiconductor "designer" dramatically complicates the understanding of nitrides. It should be pointed out that the industry has already performed a sensational improvement of these devices, but probably more on an empirical basis rather than on a deep comprehension of the microscopic processes occurring in the devices under operation. I however believe that the on-going academic effort is worthy for at least two reasons: first, while it is possible to achieve appreciable performances of a device on a purely empirical optimization process, the ultimate efficiency limit is very unlikely to be attained without a fundamental understanding; second, a fundamental understanding of a device may always lead to evidence new

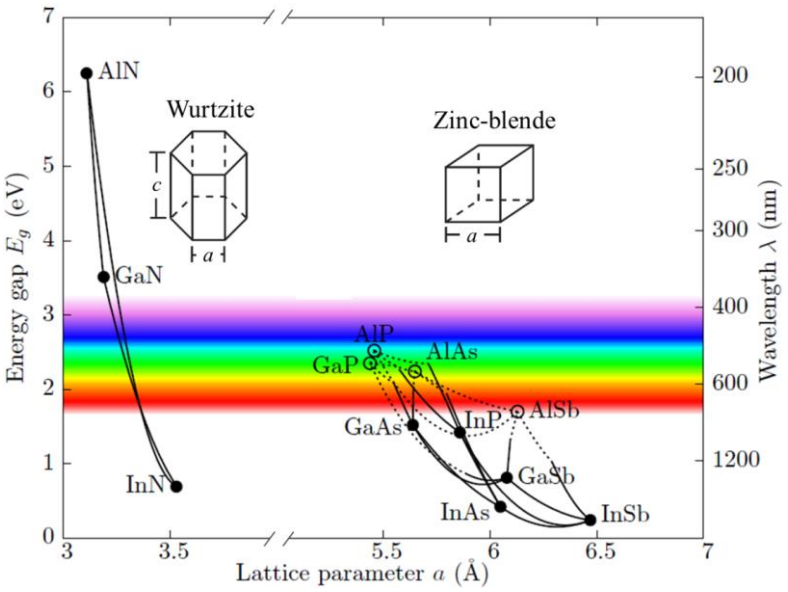

Figure 1 – Energy band gap of III-V semiconductor compounds as a function of their lattice parameter *a*. Solid and dotted lines correspond to direct and indirect gap ternary alloys, respectively. Adapted from M.A. Caro's PhD thesis [2] with permission.

phenomena, contributing this way to an expansion of the field that goes well beyond the technological optimization.

The aim of this chapter is to outline the main problems existing in nitrides, their identified causes and the possible implemented solutions. After an introduction on the key technologies enabled today by nitrides (Sec. 1.1), problems that stem from intrinsic material properties in nitride compounds, such as threading dislocations, p-type GaN conductivity, compositional disorder and polarization fields, will be discussed (Sec. 1.2). Then the problem of efficiency droop of nitride-based LEDs will be presented, whose phenomenology is identified while its origin is still debated (Sec. 1.3). Finally, the importance of the knowledge of conduction band parameters of nitrides, still poorly known, and their impact on device performances will be discussed (Sec. 1.4).

1.1 Context

Group-III nitrides are a class of semiconductor materials very suitable for optoelectronic and electronic applications. III-N compounds, such as GaN, InN and AlN, have a direct band gap in the wurtzite phase and the derived ternary alloy's band gap energy can span the whole range from the near IR ($E_{g,InN}$ = 0.7 eV) up to the mid UV ($E_{g,AlN}$ = 6.2 eV) while the lattice parameter remains in a rather narrow range. This gives to III-N compounds an exceptional versatility with respect to the other III-V semiconductor compounds, such as III-As, III-P and III-Sb, as shown in Figure 1.

Semiconductor devices based on nitride materials exhibit today phenomenal performances with applications extending in many branches of optoelectronics and electronics.

Among all, the most important application of III-N materials is commonly considered to be solid-state lighting based on nitride light-emitting diodes (LEDs). These devices decrease enormously the energy consumption for lighting compared to traditional incandescent bulbs providing a net reduction in cost and $C0_2$ emission. Special mention should be made of lighting in many parts of the developing world. About 1.6 billion people do not have electricity delivery. There, up to recently, light was mainly produced by kerosene lamps. For a lamp producing 10 lm and consuming 0.05 l h^{-1} of kerosene, the fuel volume over the 25,000 h lifetime of a competing LED lamp is 1250 l, at a cost of $1250. This is to be compared with a 1W LED lamp producing 60 lm, at an energy cost of $50 assuming a $2/kWh price, where the cost of the lighting system consisting of the lamp with its associated photovoltaic panel and battery is in the $10-100 range [3].

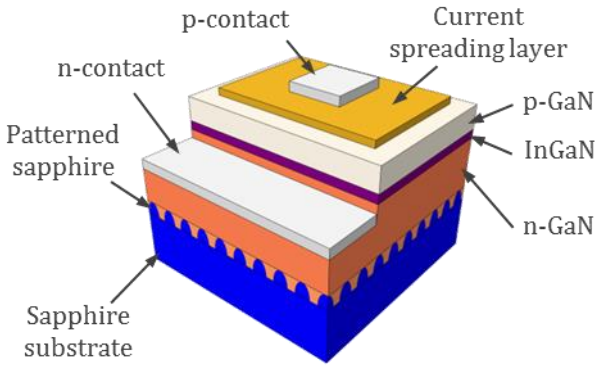

Figure 2 – Schematic of a typical InGaN/GaN LED structure grown on a patterned sapphire substrate.

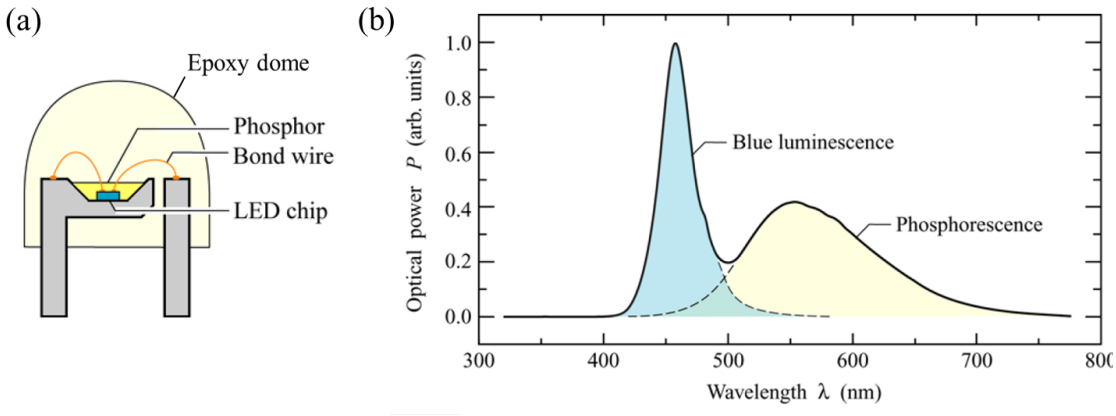

Figure 3 – (a) Schematic of an LED chip with phosphor coating for white light emission and encapsulated in an epoxy dome to enhance light extraction. (b) Typical luminescence spectrum of a phosphor-coated blue LED. Adapted from Ref. [4].

Six times more light is obtained at 4% of the energy cost (not counting the improved health benefits of suppressing fire risk and indoor pollution). The "benefit to mankind" brought by the invention of efficient blue LEDs was acknowledged in 2014 by the Nobel Prize in Physics awarded to Isamu Akasaki, Hiroshi Amano and Shuji Nakamura.

LEDs are semiconductor devices based on electroluminescence (EL) able to convert an injected electrical current into incoherent light within a narrow emission spectrum. A typical GaN-based LED device is depicted in Figure 2, showing the layered semiconductor structure grown on a sapphire substrate. For reasons that will be further

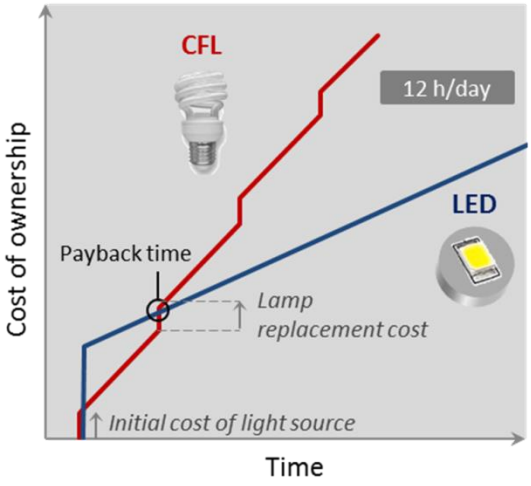

Figure 4 – Comparison of the cost of ownership as a function of time for CFLs and LED lamps for a daily use of 12 hours.

discussed, patterning of the substrate is used to enhance light extraction from the device, and a current spreading layer is employed to homogeneously distribute the injected current in p-GaN. Blue LEDs are a key element for solid-state lighting as white light can be obtained with phosphor coating of the LED device, as schematized in Figure 3a. Part of the blue luminescence will be absorbed by the phosphors and re-emitted as a broad yellow phosphorescence band. The exact shade or color temperature of the white light will depend on the specific spectrum of the blue LED and composition of the phosphor (Figure 3b). Another method to obtain white light from LEDs consists in mixing blue, green and red LEDs on a single module but this method has a higher cost and is more hardware-intensive, as it requires three LEDs and in particular a green LED, which usually suffers from poor efficiency, a problem known as the "green" gap.

White LEDs allow today solid-state lighting at high efficacy with a record value of 303 lm/W (Cree Inc., 2014). The cost of ownership (CoO) of LEDs, which includes the initial cost of the lamp bulb, the replacement costs and the cost of electricity required to deliver the desired lumen × hours, is even lower than that of compact fluorescent lamps (CFL), as shown in Figure 4 for a typical daily use of the light source of 12 h/day. Even though the initial cost of CFLs is lower, the higher conversion efficiency of LEDs (corresponding to a smaller linear slope in the diagram of Figure 4) and their longer lifetime reduce considerably their CoO leading to a short payback time for the adoption of LED lamps [5].

It is worth noting that solid-state lighting based on LEDs not only provides energy saving and cost reduction but has also the ability of improving our quality of life. Thanks to dimming and spectral control of the light source LEDs allow a dynamic lighting, which can be adapted to the different activities of the day (for instance, cool, fresh light to provide a good start to the day, warm dim light to facilitate relaxation at lunch time, etc.).

Other applications of nitride LEDs that are worth mentioning are plant growth based on UV and blue LEDs, which allow to regulate flowering time, biomass accumulation and stem elongation, and automotive headlights based on white LEDs, which can be assembled in all kinds of shapes and provide much focused rays.

Group-III nitrides constitute also the main source of solid-state semiconductor lasers with direct emission, i.e. not frequency-doubled, from the UV to the green range. Violet lasers used in the Blu-ray technology have enabled optical data storage with a 3× higher

information density than the one achieved on DVDs operating with red lasers, thanks to their shorter wavelength. Nitride lasers, in particular vertical cavity surface-emitting lasers (VCSELs), which can be formed in 2D arrays, hold great promise for high-power density displays and projectors [6].

Finally another field in which III-N materials have undergone dramatic progress in the last few years is power electronics [7]. Thanks to their wide band gap GaN-based high-electron mobility transistors (HEMTs) exhibit large breakdown voltages (with a record of 2.2 kV for HEMTs fabricated on Si [8]), low on-state resistances and high-switching frequencies. Moreover, the high sheet charge density of the two-dimensional electron gas (2DEG) allows reducing the transistor area so that more devices can be fabricated on a wafer. The superior performances of GaN HEMTs combined with their reduced cost and expected reduction of electricity losses may lead to displace in the future the corresponding Si power devices.

1.2 Problems in nitride compounds

Despite the remarkable performances of the aforementioned nitride technologies, several problems still exist in these devices setting an obstacle towards a deep understanding of the physics involved and their ultimate optimization. In the following I will give an overview of these problems. Although presented separately, the reader will have to keep in mind that these effects are often concurrent in nitride devices leading to complex optoelectronic systems.

1.2.1 Threading dislocations in GaN growth

The most widespread growth technique of GaN structures is hetero-epitaxial growth by metal-organic chemical vapor deposition (MOCVD) on lattice mismatched substrates such as c-plane sapphire ($\alpha - Al_2O_3$) and SiC (6H-SiC). To absorb strain originating during hetero-epitaxial growth, a GaN buffer layer is usually grown. Because of the large lattice mismatch (16% for GaN on sapphire and 3.5% for GaN on SiC) and different thermal expansion coefficients, threading dislocations (TD) with very large densities, typically ranging between 10^7 cm^{-2} and 10^{10} cm^{-2}, are formed (Figure 5). In principle, TDs may act as non-radiative recombination sites reducing the probability of radiative recombination, and as scattering centers decreasing the mobility of free carriers.

It is very surprising that with such high density of TDs GaN-based devices can still be highly efficient. Different explanations have been proposed for this. Hangleiter *et al.*

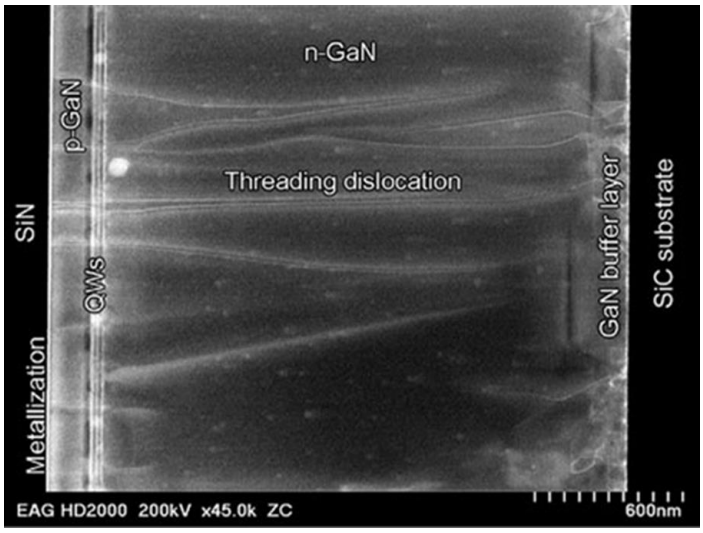

Figure 5 – TEM image showing threading dislocations in a GaN LED structure grown on SiC. Image from North Carolina State University, Ref. [9].

suggested that V-shaped pits nucleating on every TD form sidewall QWs with higher band gap energy that create a potential barrier around every defect and prevent the carriers from entering and recombining non-radiatively at the dislocation [10]. However, this effect seems to be a non-universal phenomenon that depends on the growth condition, as there have been reports showing that similar sidewall QWs can have lower band gap energy [11]. Another mechanism that has been proposed is carrier localization in radiative centers [12] due to random alloy fluctuations statistically occurring in nitride ternary alloys, such as InGaN. The importance of compositional disorder will be discussed in more details in Chapter 3.

There have been consistent efforts to reduce the TD density in nitrides [13]. Silicon-valley LED manufacturer Soraa was founded in 2008 by Shuji Nakamura, Steven DenBaars and James Speck based on the principle that GaN structures grown on bulk GaN substrates would ultimately outperform conventional LEDs grown on sapphire or SiC. Thanks to the developed GaN-on-GaN^{TM} technology, Soraa LEDs have dramatically reduced TD densities and can be operated at high current density with high efficiency [14]. Consequently, these LEDs can be 15 to 25 times smaller than conventional power LED devices leading to competitive chip prices despite the expensive bulk GaN substrate.

1.2.2 Poor conductivity of p-GaN

The elementary building block of the vast majority of semiconductor devices is the p-n junction in which different regions of the crystal structure are selectively doped with donors or acceptors. These impurities introduce reasonably shallow energy levels that lie in proximity of the conduction or valence band edge giving free carriers (electrons or holes) in the semiconductor.

Historically one of the major obstacles to the realization of nitride devices has been the growth of p-doped GaN. After initial attempts with Zn, Cd and Be the only working dopant for p-type GaN was established to be Mg. Nevertheless due to passivation by H, coming from precursors during the MOCVD growth, Mg acceptors could not be activated resulting in highly resistive layers ($10^6\ \Omega \cdot \mathrm{cm}$, Ref. [15]). In 1989 Akasaki and Amano at Nagoya University discovered that p-GaN could be activated by breaking Mg-H complexes with low-energy electron beam irradiation [16]. This method allowed to obtain a hole concentration of 2×10^{16} cm^{-3} which was still too low to fabricate devices. The breakthrough was made by Nakamura in 1992 at Nichia Corporation,

where he managed to activate p-GaN by means of post-growth thermal annealing above 700°C in N_2 ambient obtaining a hole concentration of 3×10^{17} cm^{-3} [15].

Despite decades of development, today Mg-doped p-GaN is still a poor conductor due to the large activation energy E_A of Mg acceptors which is ~170 meV [17]. The deep acceptor levels force to use high dopant concentrations N_A in p-GaN to obtain a sufficient hole concentration for practical applications. The hole concentration p can be estimated as (Ref. [18], p. 63):

$$\mathbf{p = \frac{N_A}{1 + 4 \cdot e^{E_A - E_F / k_B T}}} \qquad \mathbf{(1)}$$

where E_F is the Fermi energy with respect to the valence band maximum (VBM) and $k_B T$ is the thermal energy. Taking $N_A = 2 \cdot 10^{20}$ cm^{-3}, assuming $E_A - E_F = 118$ meV (Ref. [19], p. 39) at room temperature, p is $\sim 5 \cdot 10^{17}$ cm^{-3}, that is only 1 acceptor among 400 is ionized. For this hole concentration, assuming a hole mobility μ_h of 4 cm^2/V·s (Ref. [19], p. 43) the bulk resistivity of the p-GaN layer is calculated to be ~3 Ω ·cm from

$$\boldsymbol{\rho_{bulk} = (p \cdot e \cdot \mu_h)^{-1}} \qquad \mathbf{(2)}$$

The most important consequence of the poor conductivity of p-GaN is that the hole current injected in the p-layer of nitride devices tends to accumulate in proximity of the p-contact without spreading uniformly in the p-layer. This effect is known as current crowding and will be further discussed in Sec. 2.5.1 and Appendix 5.2. In order to contrast current crowding, a very thin indium tin oxide (ITO) layer is usually deposited on the surface of p-GaN. ITO allows spreading current homogeneously in the p-layer because of its high conductivity ($\rho_{bulk} \sim 5 \cdot 10^{-4}$ Ω ·cm) while absorbing only a small fraction of LED light thanks to its low absorption coefficient at the corresponding wavelength ($\alpha_{ITO} \sim 500$ cm^{-1}).

1.2.3 Compositional disorder in nitride ternary alloys

As already mentioned, by making ternary alloys between InN, GaN and AlN it is possible to span band gap energies ranging between 0.7 eV and 6.2 eV, which gives a large versatility in the design of nitride structures. Common building blocks of nitride devices are InGaN QWs and AlGaN barriers with In or Al compositions that can vary between few % to several tens of %. An intrinsic material property of ternary alloys is compositional disorder that is statistically determined. For instance, an $In_{0.1}Ga_{0.9}N$ layer

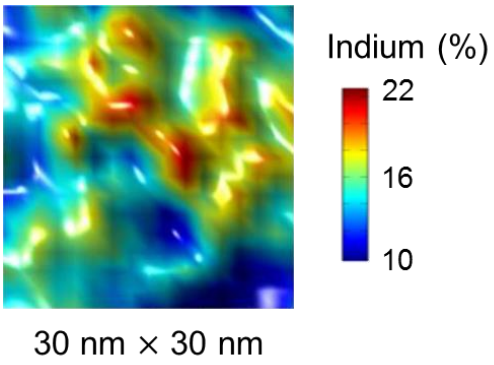

Figure 6 – 2D atomic map of indium atoms in the mid-plane of an InGaN/GaN QW measured by atom probe tomography [20]. For a mean In composition of 15% large compositional fluctuations are observed.

has a crystal structure similar to that of pure GaN but where N atoms are held at the same positions and the other atomic sites are occupied with a probability of 10% by In atoms and 90% by Ga atoms.

Compositional disorder can be characterized by atom probe tomography (APT), a destructive microscopy technique based on time-of-flight of ions evaporated from the sample and allowing to reconstruct a 3D atomic map of the specimen. Figure 6 shows a typical In composition map measured by APT corresponding to the mid-plane of an InGaN QW of a blue LED [20]. As it can be observed for an average In composition of 15% strong compositional fluctuations occur in the plane of the QW. Two essential pieces of information can be deduced from APT measurements of nitride ternary alloys [21]:

- Compositional disorder in InGaN layers is purely random, i.e. uncorrelated. APT allows to shed light on a long-lasting debate on the nature of disorder, random or correlated, in InGaN [22];
- The typical length scale of compositional disorder is of few nanometers, which makes its experimental characterization challenging.

APT measurements provide atomic maps of InGaN and AlGaN layers but do not explain how the observed compositional disorder may affect the optoelectronic properties of nitride devices. To address this issue it is necessary to describe and characterize the disorder-induced fluctuations occurring in the conduction and valence band of the material that are “seen” by the free charge carriers. This problem will be tackled in Chapter 3 by means of an original theoretical approach allowing us to

incorporate the effect of disorder in the simulations of nitride semiconductor structures without having to solve the complicated eigenvalue problem corresponding to the Schrödinger equation of the disordered system. Moreover this approach will be validated by an experimental characterization of disorder by light absorption measurements in InGaN layers of different compositions.

1.2.4 Polarization-induced electric fields in nitrides

Electric polarization plays a key role in determining the optical and electrical properties of nitrides. A distinction has to be made between spontaneous (P_{sp}) and piezoelectric (P_{pz}) polarizations. P_{sp} is due to the lack of inversion symmetry of the crystal structure and is strong in nitride crystals in the wurtzite phase. For instance, the spontaneous polarization constant of GaN is 0.03 C/m^2 [23] giving a surface-polarization charge

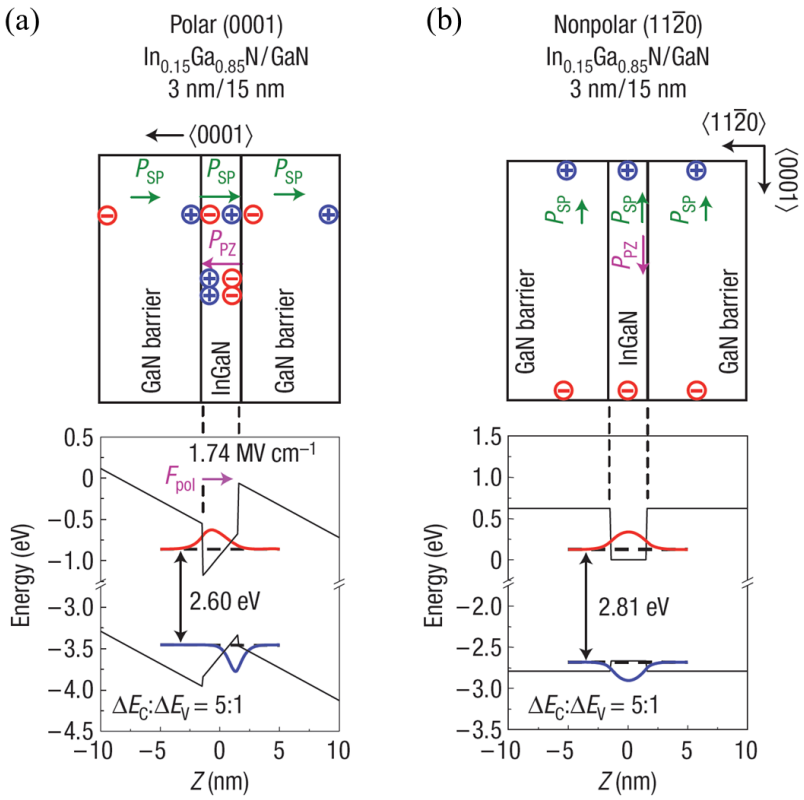

Figure 7 – Structures and simulated band diagrams of $In_{0.15}Ga_{0.85}N$/GaN QWs grown on (a) polar and (b) nonpolar crystal orientations. The resulting polarization in the InGaN layer in (a) is dominated by the piezoelectric polarization, which determines the direction of the electric field in the QW. Reproduced after Ref. [12].

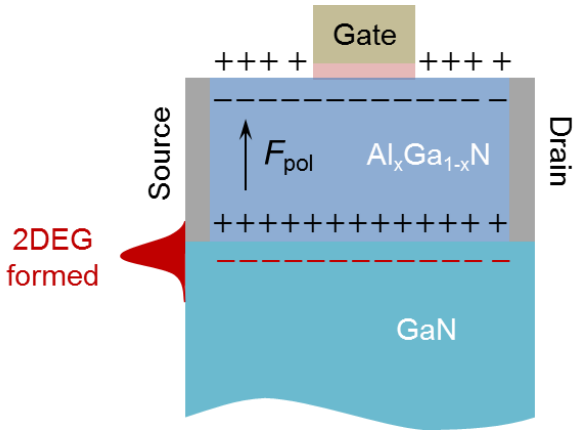

Figure 8 – Schematic of an AlGaN/GaN HEMT device. The 2DEG in the GaN channel is due to the polarization discontinuity at the AlGaN/GaN interface.

density of $2 \cdot 10^{13}$ cm^{-2}. P_{pz} is induced by the strain at the interface between two layers with different lattice constant. The piezoelectric coefficients of III-N's are an order of magnitude larger than other III-V semiconductors, such as GaAs, GaP and GaSb.

It is of particular interest to consider polarization effects along the [0001] direction of the wurtzite crystal since conventional nitride structures are epitaxially grown on c-plane along this axis. An example of polarization effects on the optoelectronic properties of InGaN/GaN QWs grown on different crystal directions is shown in Figure 7. In the structure grown on c-plane (Figure 7a) a strong polarization-induced electric field F_{pol} is present in the QW. Typical electric field values measured in similar InGaN/GaN structures are larger than 1 MV/cm for In compositions above 10% [24]. There are three important consequences due to the strong F_{pol}:

- The electron and hole wave functions are spatially separated.
- The QW emission energy undergoes a redshift (compare with the nonpolar structure with $F_{pol} = 0$ in Figure 7b). This effect is known as the quantum-confined Stark effect (QCSE).
- Increasing the carrier concentration in the QW will screen F_{pol} and cause a blue-shift of the QW emission energy.

It is clear from these points that the description of the steady-state operation of an optoelectronic device suffering from polarization-induced electric fields in the active region will be quite complicated. In particular, it should be noted that the spatial separation of the electron and hole wave functions reduces the oscillator strength of the e-h pair thus decreasing the recombination rate and the radiative efficiency of the

structure. Much effort has been dedicated to the growth of nitride LEDs along alternative orientations [25] with reduced (semipolar) or no (nonpolar, Figure 7b) polarization along the growth direction, in order to mitigate or eliminate these polarization effects.

However it is interesting to note that polarization effects are not always detrimental to nitride devices. For instance, the 2DEG in AlGaN/GaN HEMTs is induced by the discontinuity of polarization at the heterojunction (Figure 8). Therefore, unlike AlGaAs/GaAs HEMTs in which intentional modulation doping is required to create charges in the channel, polarization can be used in nitrides as a tool to design the 2DEG carrier density as a function of the thickness and composition of the $Al_xGa_{1-x}N$ barrier [26]. Note that the penetration of the wave function into the $Al_xGa_{1-x}N$ barrier causes scattering by random alloy disorder limiting the mobility of the 2DEG. This issue can be attenuated by the growth of a thin AlN layer at the interface confining the 2DEG in the channel.

1.3 Efficiency droop in nitride LEDs

LED efficiency droop is a complex problem in III-nitrides as it involves, among others, all the issues already discussed in this chapter. For this reason, it is one of the most debated topics in the LED community. An illustration of the droop phenomenon is given in Figure 9. In presence of droop, the optical output power of a nitride-based LED increases sublinearly with the injected current density (inset). The corresponding efficiency curve of the LED is represented by the continuous red line. The peak efficiency of the device occurs at low current density, while at higher injection the LED efficiency "droops". The most important consequence of droop is that currently LED bulbs are made of several LED chips allowing to operate each device at its peak efficiency and still obtaining a sufficient total luminous flux from the bulb, but at the expense of a much higher cost of the lamp. Understanding and solving the droop problem represents a major challenge in view of the application of LEDs to solid-state lighting as the requirement in terms of energy saving is to at least displace the quite efficient fluorescent, sodium, and high intensity discharge lamps used today in the main energy consuming lighting sectors, industrial, commercial and outdoors, with more

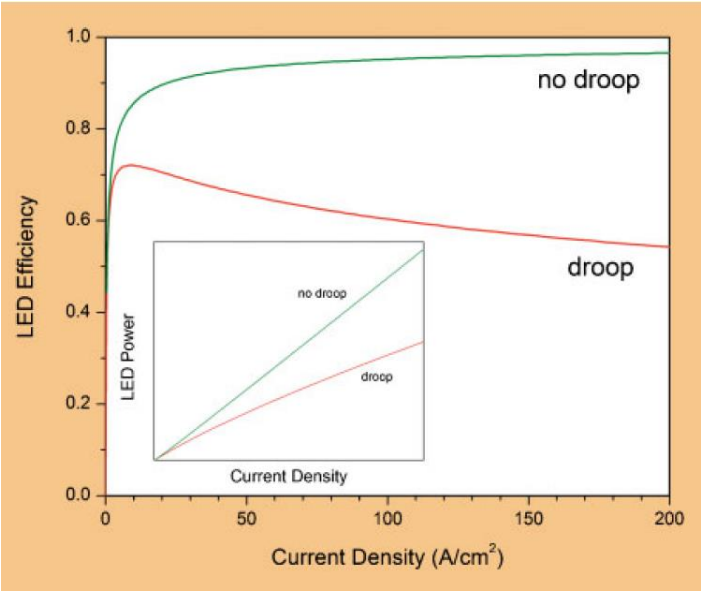

Figure 9 – Illustration of the effect of droop in a simulated nitride-based LED from Ref. [27]. In presence of droop, the LED efficiency curve (red curve) decreases at high current density, while the ideal trend calculated without droop (green curve) approaches the unity efficiency. The inset shows the corresponding optical powers of the LED exhibiting a sublinear increase with current density in the case of droop, and a linear dependence without droop.

efficient and better light quality lamps. To achieve this, LEDs have to perform at the physical limits of electricity-to-light conversion efficiency, requiring mastering of the intrinsic electrical and optical properties of the materials, and of the electromagnetic properties of the device structure. The goal is to obtain single-chip LED bulbs that are highly efficient at high current density ("no droop" limit shown as a green curve in Figure 9) and at the same time cost-competitive with the other commercial light sources.

The conversion efficacy of electricity into white light in LEDs (η_{LED}, lumens out/electrical power in) is mainly the product of five terms:

$$\boldsymbol{\eta_{LED} = \eta_{el} \times \eta_{inj} \times IQE \times \eta_{ext} \times LER} \qquad \textbf{(3)}$$

- η_{el}, the electrical efficiency, mainly associated with ohmic or contact losses (mostly related to p-GaN, as discussed in Sec. 1.2.2), which represents the fraction of electrical power not injected as e-h pairs;
- η_{inj}, the injection efficiency which describes the fraction of current injected into the light-emitting region;
- IQE, the internal quantum efficiency which describes the conversion of injected electron-hole pairs into photons inside the active part of the LED structure;
- η_{ext}, the light extraction efficiency which gives the fraction of photons emitted outside the LED to those generated inside;
- LER, the luminous efficacy of radiation of the emitted light (lm/W), which represents its visual efficiency, characteristic of the emitted spectrum, and is connected to the color rendering of the light source. A source at the peak of eye sensitivity (555 nm) yields by definition 683 lm/W, but is not white. Adding red and blue to the spectrum reduces lm/W. Depending on the technology used to generate white and on color quality, for instance as displayed by the CRI, the maximum LER is in the 300–400 lm/W range [28,29].

The product of the 3 middle terms gives the external quantum efficiency (EQE).

Much effort has been made to optimize the LED efficiency. In the first place the problem of light extraction was tackled. In principle only a small fraction of the light that is generated in a nitride LED can be directly extracted from the device. The reason for this is that the refractive index of AlInGaN compounds has a typical value of 2.4-2.5 which is often larger than those of the media surrounding the LED. For instance, in the simple case of a planar luminescent semiconductor slab, only the light propagating

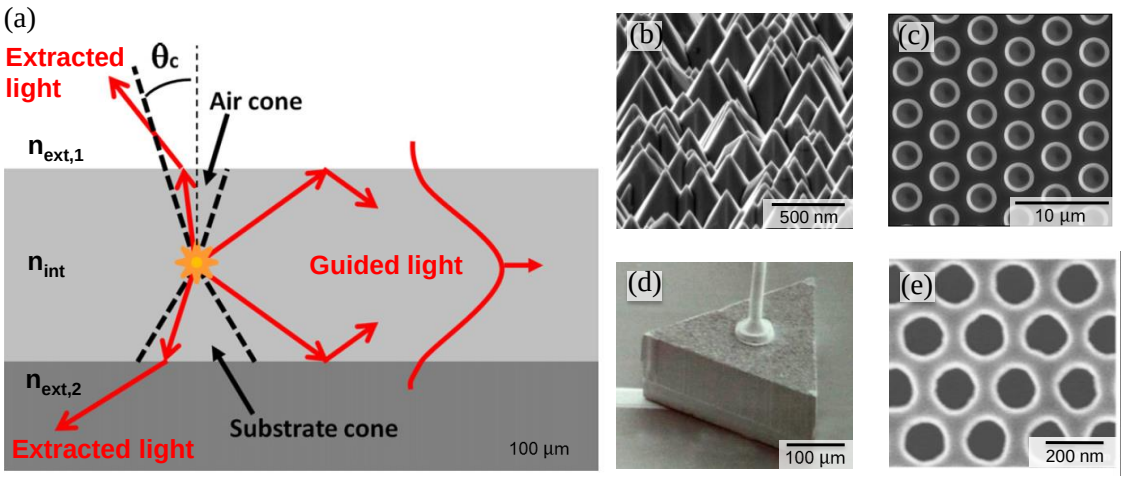

Figure 10 – (a) Diagram showing different possible paths for light propagation in a planar luminescent semiconductor slab embedded between a substrate and air. Only the light propagating within the air and substrate extraction cones may be directly extracted from the semiconductor. Adapted from Ref. [33]. (b)-(e) Various techniques of light extraction features for LEDs: (b) surface roughening [30]; (c) substrate patterning [34]; (d) side shaping [14]; (e) photonic crystal [35].

within a narrow cone defined by $\theta_c = sin^{-1}(n_{ext}/n_{int})$ is directly extracted (Figure 10a). The rest of the light is trapped as a guided mode in the semiconductor by total internal reflection and would usually end up being reabsorbed, dissipating its energy into heat.

In order to increase θ_c, LEDs are often encapsulated in hemispherical epoxy or silicone domes (see Figure 3a) with a refractive index of ~1.5, closer to the refractive index of the semiconductor than n_{air}. (UV LEDs are an exception. No epoxy or silicone dome is used in this case as this would cause strong optical absorption losses in the UV range.) Thanks to the geometry of the dome light rays extracted into the epoxy impinge at the surface almost perpendicularly and are transmitted into air.

In addition to this, various texturing techniques have been developed to improve light extraction from LEDs (Figure 10b-e). The two main approaches are surface roughening [30] and substrate patterning [31] aiming at randomizing the trajectory of trapped light. After some random propagation within the LED, the beam, if not absorbed, will strike the interface within the extraction cone. Side shaping [32] can lead to sizeable low loss side extraction when using transparent index-matched substrates. A light extraction method relying on wave optics rather than geometrical optics is based

on photonic crystals [33]. The main advantage is emission directionality, which does not seem yet a large enough advantage to offset the demanding fabrication technology. These techniques have led to a remarkable progress in the past decade increasing the light extraction efficiency in nitride LEDs from roughly 20% to over 85%.

The technological solutions developed in the last decade have led to remarkable progress in all components of the efficiency allowing to attain EQE's of 80+% in blue LEDs at peak efficiency [36], corresponding to low current densities of the order of 1-10 A/cm^2. However getting nearer the physical limits could lead to increasing by 60% the performance of LEDs in the market: the product of several efficiency factors in the 80+% range leads to today's overall efficiencies around 39% for warm-white phosphor-converted LEDs, with a 2020 target of 62% (Ref. [29] p. 34). Moreover, as already mentioned, solving the problem of LED droop by extending the high-efficiency performances to high current densities would allow decreasing the chip area and reduce the cost of the devices on the market.

Different non-radiative losses, specifically related to microscopic electronic processes occurring in the active region of the LED, may affect the efficiency of the η_{inj} and IQE terms appearing in Eq. (3) and cause droop (Figure 11). The main proposed droop mechanisms affecting η_{inj} (Sec. 1.3.1) and IQE (Sec. 1.3.2) will now be presented. Then the problem of the identification of the dominant mechanism for droop will be discussed (Sec. 1.3.3). Finally, remedial action for diminishing droop will be briefly reviewed (Sec. 1.3.4).

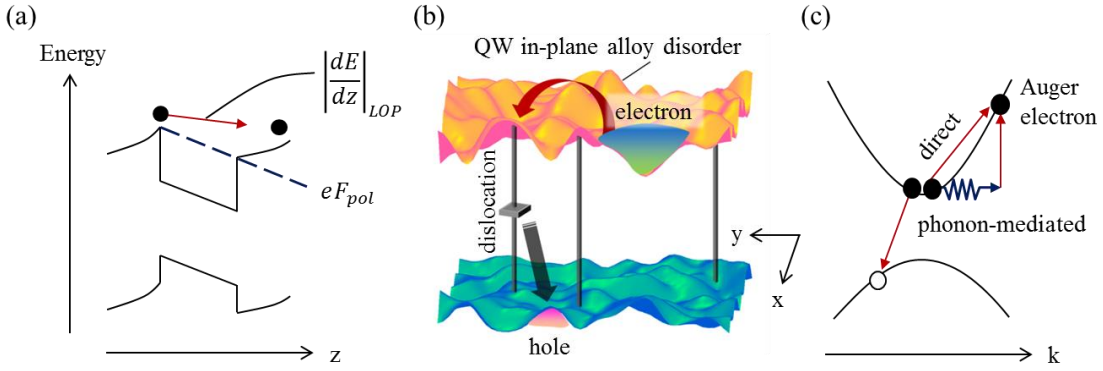

Figure 11 – Principle of different non-radiative microscopic electronic processes which have been proposed to explain droop: (a) carrier overflow; (b) defect recombination following band filling of localized states; (c) direct and phonon-mediated e-e-h Auger recombination.

1.3.1 Carrier leakage

Two main leakage mechanisms [37,38] have been proposed to reduce carrier injection efficiency in the active region of the LED and cause droop: carrier overflow and poor hole injection.

Poor hole injection may be caused by the low p-type doping efficiency of GaN and low hole mobility leading to unbalanced carrier injection in the active region of the LED. It has to be noted that a number of solutions have been implemented to inject carriers more efficiently and carrier injection efficiency is most often near 100% [39].

The principle of the carrier overflow mechanism from a semi-classical perspective is shown in Figure 11a. Due to the presence of a polarization-induced electric field in the QW of a polar InGaN/GaN LEDs, carrier capture by the QW will depend on a trade-off between the carrier energy-loss rate $|dE/dz|_{LOP}$ by longitudinal optical phonon (LOP) emission and the potential drop across the QW due to F_{pol}. Considering an electron velocity of 10^5 m/s, a LOP emission time and energy of 10 fs and 92 meV, respectively, and $F_{pol} = 1.7$ MV/cm, it is obtained $|dE/dz|_{LOP} \sim 92$ meV/nm being smaller than $eF_{pol} \sim 170$ meV/nm, which indicates that a fraction of the carriers is not captured by the QW. Carrier overflow is avoided by the use of multiple quantum well (MQW) structures, where electrons overshooting one QW are captured by the next ones. Then a new issue that may rise is asymmetric carrier injection in the different QWs which can be reduced by proper design of the structure [40].

A similar leakage mechanism is carrier escape from the QW which may be caused by inadequate carrier confinement in the active region. This mainly concerns electrons whose escape into the p-GaN layer next to the light-emitting QWs is avoided by using a wider band gap (AlGaN) electron blocking layer (EBL). Modeling along the ABC model, which fits the LED efficiency curve using a polynomial to represent different recombination rates (detailed description in Appendix 5.1), however disputes this at high injection.

1.3.2 Non-radiative recombination processes

Two other main mechanisms have been invoked to explain the origin of droop and are related to non-radiative recombination processes affecting the IQE: recombination on defects, following band filling of localized states, and Auger recombination.

A schematic describing the first mechanism is shown in Figure 11b: at high current density, band filling of localized states, induced by compositional disorder in InGaN QWs, may result in excess carrier injection into percolative delocalized states and carrier transport to non-radiative centers [41].

The second mechanism is Auger recombination, a three-particle process well-known in semiconductors in which an e-h pair recombines non-radiatively and its energy is transferred to a third carrier, either an electron (direct e-e-h process, as shown in Figure 11c) or a hole (direct e-h-h process). In usual carrier injection conditions, momentum conservation severely limits the efficiency of direct Auger recombination. However, the probability of Auger transitions may be enhanced by indirect processes involving phonons [42], which supply momentum to the excited hot-carrier, or by alloy disorder [43], which enables additional final states. It should be noted that the large polarization fields existing in nitrides further complicate the calculation of Auger rates due to the reduced e-h wave functions overlap. It seems that the non-radiative and radiative recombination mechanisms are diminished by the same overlap factor [44], which overall should not affect the IQE when expressed as a function of carrier density. These fields have however an indirect impact on IQE: since the diminished recombination rates cause an increase in carrier lifetime, the optimal carrier density (corresponding to the maximum IQE) is reached at a lower current density (going against the desired performance of high efficiency at high current density).

1.3.3 Identification of the dominant droop mechanism

There is a wide disagreement about the identification of the physical mechanism of droop. This is partly due to the fact that the usual methods to discriminate among the various mechanisms are based on the fitting of light vs. current curves, sometimes with the addition of the I-V characteristics. However, such measurements only indirectly probe the internal LED physical processes through space, time and energy-integrated quantities, not probing in details the microscopic electronic and optical processes. Moreover, the analysis of these measurements most often neglect phenomena such as carrier-induced changes in internal electric fields and inhomogeneity of carrier density which strongly impact the significance of the experimental data analysis. It also has to be noted that experimental studies are often performed in structures grown in academic laboratories, e.g. single QW (SQW) or double heterostructure (DH) LEDs, which might be quite different from commercial LEDs. This is because some phenomena are

considered as better controlled, avoiding for instance the problem of non-uniform carrier injection, however at the cost of very different carrier injection properties, where carrier overflow or leakage could be enhanced compared to industry's MQW structures. Many studies are performed on structures without EBLs, where indeed strong carrier leakage could occur. It should be kept in mind that commercial LED structures result from long and painstaking iterative optimization processes to limit extrinsic effects that can be solved by structure design, growth improvements and higher doping levels, effects often invoked by academics but which have possibly been already solved in industry.

We should finally mention that disagreements extend beyond data fitting to both experimental and theoretical results. Before 2007, the cause for droop was thought to be of extrinsic nature due to poorer injection efficiency or carrier delocalization towards non-radiative centers. This state of affairs changed dramatically when Shen *et al.*, from Philips Lumileds, announced in 2007 [45] that droop was due to an intrinsic effect occurring at high carrier density, the Auger effect, through an analysis which introduced the ABC model and which relied on carrier lifetime changes with carrier density. Beyond the ABC analysis, which holds significant inherent limitations as discussed in Appendix 5.1, other evidence for Auger recombination was brought along either based on experiments or theory.

PL and EL measurements were carried out on the same commercial samples [46,47]. The perfect similarities of the measured effects, in particular the coincidence of PL and EL measured lifetimes, led the authors to the conclusion that Auger is indeed the culprit for droop under LED electrical operation. While the ABC coefficients are measured to change with carrier density (see Figure 2 of Ref. [48]), the value of the C coefficient is in good agreement with the theoretical expectations (in the 10^{-31} $cm^6.s^{-1}$ range).

In 2011 Kioupakis et al. [42] provided theoretical backing to the Auger hypothesis, by showing the much higher rate of the indirect Auger effect as compared to the direct process. However, disagreement reigns in theoretical calculations of the Auger coefficient: some theoreticians calculate indirect phonon-assisted Auger recombination rates in the 10^{-31} $cm^6.s^{-1}$ range [44] while others obtain values in the 10^{-34} $cm^6.s^{-1}$ range, both for direct and indirect Auger transitions [49]. Recently Vaxenburg *et al.* [50] theoretically found significantly increased direct Auger rates in QWs when compared to bulk ones due to the size and shape of the confinement potential whereas the radiative recombination coefficient is unchanged, while Kioupakis *et al.* [44] claim that the

Auger and radiative recombination coefficients change similarly. It has also been modeled that the impact of a given Auger coefficient could be enhanced at a given injected current by carrier localization, current crowding and carrier leakage induced by the Auger process [51].

While transport measurements or integrated optical emission experiments cannot distinguish electron energies, well-designed optical spectroscopy experiments can trace hot carrier leakage in undoped or doped structures generated by the Auger effect. A PL experiment by Binder *et al.* [52] in a structure containing both UV and green QWs has shown hot carrier generation attributed to the Auger effect: when exciting green QWs with intense blue light, UV light emission can be observed from the adjacent larger gap QWs due to hot electron transfer associated with the Auger effect. These experiments are however carried out in specially designed nitride structures.

Iveland *et al*. [53] presented in 2013 an original technique based on electron emission spectroscopy allowing to directly measure the energy of vacuum-emitted electrons from commercial LEDs. In this experiment a commercial LED is operated in forward bias under standard electrical operation. A large fraction of electrons and holes injected into the QWs of the LED radiatively recombine. However, at high injection currents, a fraction of the carriers injected into the QWs with the highest carrier density recombine by an Auger process. Electrons with various energies, among which energetic Auger electrons, may travel towards the surface and be emitted into vacuum. The measurement of hot electrons emitted from the LED was then interpreted as the first direct observation of Auger-generated electrons in a semiconductor under electrical injection. Moreover, a linear correlation was observed between the Auger current and the non-radiative droop current suggesting that Auger recombination is the dominant droop mechanism in nitride LEDs. This new technique has been investigated in depth in the course of this thesis and will be presented in Chapter 2.

1.3.4 Remedial actions to diminish droop

The assignment of droop to an intrinsic mechanism indicates that remedies must address the mechanism itself, by reducing the carrier density for a given current density. In other words, droop cannot be solved by better quality materials or simple changes in designs, as would be for instance required if it was due to defects or carrier overflow. A number of possible tracks is briefly reviewed.

1.3.4.1 Larger active regions

Employing larger active regions is the most widely used technique so far. As already mentioned, LED lamps incorporate many LED chips as a given current will be spread over a larger surface. One can also diminish the volume carrier density by using thicker active layers. Gardner *et al.* demonstrated early that the use of a thick DH active layer could lead to higher onset of droop [54]. However, this solution does not seem to be implemented industrially, most certainly because the peak IQE is lower than for thin MQW active layers because of poorer materials quality. Another way to increase the active volume thickness is by increasing the number of QWs. There is however a limit to uniform carrier injection and it seems that this is reached by industry for 5 to 9 QWs.

1.3.4.2 Nanowire LED structures

Growing nanowires on substrate is very widely developed at the research laboratory level [55]. The most studied system relies on the vapor–liquid–solid or vapor-solid-solid growth mechanisms. The idea here is that due to their high aspect ratio, vertical core shell wires can have a developed sidewall QW active area larger than that obtained from planar QWs, in spite of the reduced wire coverage of the substrate. Additional advantage is the natural high η_{ext} due to the scattering of the emitted light by the wires acting as a diffraction grating.

1.3.4.3 Nonpolar and semipolar growth

The electric field due to spontaneous and piezo-polarization in polar c-plane materials is a major cause for the occurrence of droop at low currents: because of the lower recombination rates induced by the internal electric field, the current density at which the Auger effect becomes significant is decreased. Thus, by decreasing the field and shortening lifetime, LEDs grown with nonpolar or semi-polar orientations will have Auger recombination only set in at higher current densities for the same Auger coefficient. The present performance of nonpolar and semipolar materials is very promising: very low droop is observed with current densities up to 1000 A/cm^2 range [56,57]. The main drawback is the need for GaN substrates.

1.3.4.4 Laser lighting

Lasers provide an interesting alternative approach to control the effect of droop: as the carrier density is clamped at its value at threshold, any additional injected carrier could recombine radiatively through stimulated emission as Auger recombination current would also be clamped. It is to be remarked that present lasers do not show an improved

EQE with respect to LEDs. The loss mechanisms are quite different in both devices. For LEDs, besides droop IQE associated losses, the main factors are connected to η_{ext}, mostly in electrodes as propagation losses are very reduced due to the short path of light rays in high-extraction efficiency LEDs. In lasers, light propagates in long cavities (from several 100 μm to few mm) and propagation losses can be quite high. An added issue is the large resistive loss at the high currents at which lasers operate which significantly reduce the conversion efficiency compared to LEDs [58].

1.4 Conduction band structure and hot-electron processes in nitrides

Many GaN-based electronic devices operate in presence of strong electric fields. In such devices, conduction electrons may gain large kinetic energies and access higher minima of the conduction band (CB) by mean of phonon intervalley transfer, as schematized in Figure 12. (Note that in theoretical band structures the first satellite valley is called U and lies between the L and M points of the Brillouin zone. Often experiments do not have a determination in k-space and generally refer to it as the L-valley.) These upper valleys thus act as a high-energy channel for electron transport. It is then of primary importance to determine the energy position of the CB side-valleys which may strongly affect the performance of these electronic devices.

For instance, in high-field condition a phenomenon known as negative differential resistance (NDR) may occur in which an increase of the voltage applied to the device leads to a current decrease (Figure 13). NDR may be used in microwave applications and typically originates from intervalley transfer towards a satellite valley with heavier effective mass (Gunn effect). NDR may also be induced by excitation above an inflection point in the CB. The dominating NDR mechanism depends on the relative ordering between the energy position of the considered satellite valley minimum and the inflection point [59,60]. Huang *et al*. [61] reported the first direct evidence of NDR in GaN through a metal-semiconductor-metal structure with a threshold electric field of 190 kV/cm, much higher than in other III-V's such as GaAs (3 kV/cm) and InP (10

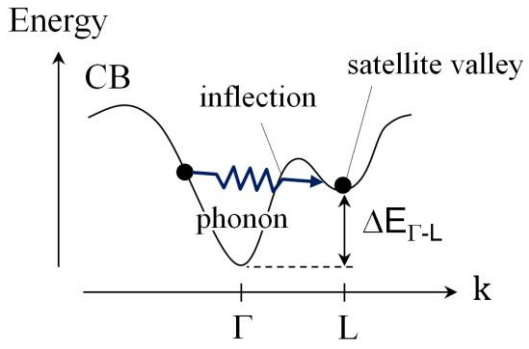

Figure 12 – Schematic showing intervalley transfer in k-space of a hot electron from the central Γ valley to the first satellite valley L in the conduction band of GaN. The process is mediated by a phonon which supplies momentum to the hot electron.

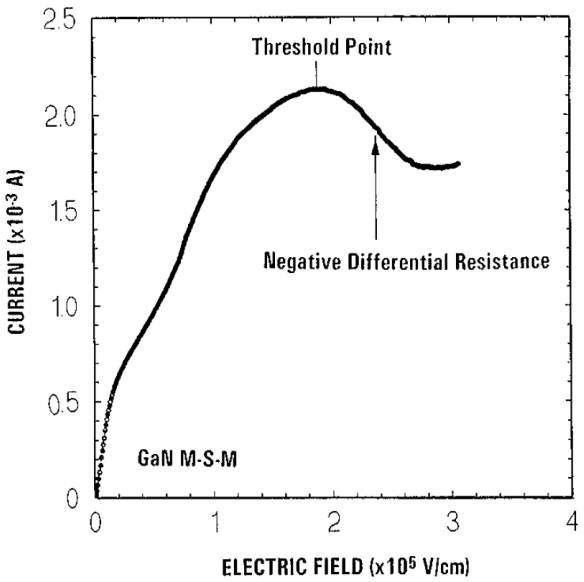

Figure 13 – Current-field characteristics measured by Huang *et al.* [61] in a GaN metal-semiconductor-metal (M-S-M) system exhibiting NDR. The electric field is assumed to be uniform between the M-S-M fingers and is directly converted from the voltage applied to the device.

kV/cm) likely due to the larger intervalley separation $\Delta E_{\Gamma,L}$. GaN-based Gunn diodes have been theoretically investigated as potential THz sources [62] but no clear experimental demonstration has yet appeared.

Another example of GaN-based electronic devices in which intervalley transitions may play an important role is AlGaN/GaN HEMTs, as revealed by EL microscopy. In these devices luminescence with photon energies well below the band gap of GaN can be observed at high drain-source voltage [63]. The luminescence signal appears at a threshold electric field of ~150 kV/cm and may be due to radiative intervalley transitions or scattering at ionized defects. In Ref. [63], the mechanism giving origin to EL in AlGaN/GaN HEMTs was attributed to optical transitions from different satellite valleys to the central Γ valley, though it was noted that important band structure parameters are considerably scattered between different band structure calculations and experimental studies.

Indeed, despite the rapid progress in GaN-based electronic devices, some of the fundamental properties of GaN are still poorly known. In particular, a considerable range of values is found in the literature for the energy of the first satellite valley in the conduction band of GaN. Very low values of 340 meV and 290 meV above the CB

minimum, were deduced respectively from BEEM measurements [64] and from PL spectroscopy [65]. Other experimental determinations provide significantly larger values. An intervalley energy separation $\Delta E_{\Gamma,L}$ of ~ 1.2 eV was obtained from photoexcited field emission on GaN nanorods [66]. Similar values are provided by pump-probe transient optical spectroscopy. Sun *et al.* [67] obtained a side-valley energy position of 1.34 eV in n-GaN. More recently Wu *et al.* [68] measured a $\Gamma \rightarrow$ L intervalley transfer onset occurring at an interband excitation energy of 4.51 eV which corresponds to a L-valley energy of ~0.85 eV above the CB minimum when assuming parabolic bands with effective masses of $m_e^* = 0.22\, m_0$ and $m_{hh,z}^* = 1.58\, m_0$ for electrons [69,70] and holes [71] respectively, and taking 92 meV as the intervalley phonon energy [72]. The unoccupied band structure of wurtzite GaN was studied by inverse photoemission spectroscopy [73], though only along the $\Gamma - A$ symmetry line in the bulk Brillouin zone. The A-valley was observed to lie at ~3.1 eV above the bottom of the CB but, according to theoretical band structures, it is not expected to correspond to the first satellite valley in k-space. Ellipsometry measurements may determine the band structure of the conduction band by exciting either shallow interband transitions (i.e. in proximity of the band gap) or deep interband transitions (i.e. from core levels such as Ga 3d in GaN). In the first case the determination of the CB depends on the specific assumption for the valence band dispersion, which can be taken from theoretical calculations (often unable to predict the correct E_g and therefore requiring a band gap renormalization) or experiments (such as angle-resolved photoemission spectroscopy). From shallow interband transitions Goldhahn *et al.* [74] concluded that the L valley is located at least ~2 eV above the Γ minimum, while Kim et al. [75] obtained a value of 1.4 eV. In the case of deep interband transitions the measured interband energies need a correction for the exciton binding energy of the hole created in the 3d level and the excited electron, which considerably affects the uncertainty on the energy estimation of the satellite valleys. For instance, Rakel *et al.* [76] wrote:

> *These results would indicate that the lowest p-like conduction bands are located just about 1 eV above the conduction-band minimum. [Note: the precise estimation for the first satellite valley is 0.8 eV.] Nevertheless, we assume these bands at a considerable higher position. It is known that quasiparticle and excitonic effects introduce an energy offset. For example, Aspnes et al. [77] have determined an exciton binding energy of 0.66 eV for In 4d transition in InAs.*

However Aspnes *et al*. [78] quoted a typical exciton binding energy of only 0.1 eV for Ga-V materials (such as GaAs, GaP and GaSb), which would seem more reasonable to apply to transitions from Ga 3d in GaN and would give a corrected energy separation of 0.9 eV for $\Delta E_{\Gamma,L}$.

It has to be noticed that experimental values are quite indirectly obtained and that theory provides remarkably higher values than the experiments. In GaN band structure obtained from ab initio calculations both Goano *et al.* [79] and Delaney *et al.* [80] predicted a value of 2.25 eV above the CB minimum for the energy position of the first satellite valley, while Wang *et al.* [81] and de Carvalho *et al.* [82] obtained respectively, 1.49 eV and 2.06 eV. Thus, in the absence of direct experimental determination, the position of the satellite valleys is still debated. A direct experimental access to the CB structure of GaN, based on photoemission spectroscopy (PES), will be presented in Sec. 2.3.

2 PHOTOELECTRIC PROCESSES IN III-NITRIDES BY ELECTRON EMISSION SPECTROSCOPY

The work by Iveland *et al*. [53] based on electro-emission spectroscopy explored a new technique to directly study the microscopic electronic processes occurring in nitride LEDs under standard electrical operation, as already mentioned in Sec. 1.3.3. The pioneer experiment was carried out at Ecole Polytechnique in collaboration with the University of California at Santa Barbara (UCSB) and, after its publication in Physical Review Letters, it had a significant impact on the nitride community (~260 citations 3 years after its publication, according to Google Scholar) because of the novelty of the experimental approach and the claim of identification of the droop mechanism as due to Auger recombination.

First, I will present the main conclusions of this pioneer experiment (Sec. 2.1). Exploring in depth this new experimental technique is one of the objectives of this chapter. At the same time this analysis will imply dealing with universal problems of III-nitride materials and devices, which are interesting also in view of applications and techniques that are different from electron emission spectroscopy. In Sec. 2.2 details on the experimental technique of low-energy electron emission spectroscopy and the materials studied in this chapter will be given. The conduction band structure of GaN will be studied by near-band-gap photoemission spectroscopy in Sec. 2.3 to assess the energy position of the first satellite valley, which may play an important role on hot electron transport of nitride devices. In Sec. 2.4 extensive photoemission studies of

GaN-based materials and InGaN/GaN LEDs will be presented, shedding light on the photoelectric processes that may be excited by LED light in LED electro-emission. Finally, in Sec. 2.5 the potential inhomogeneity across the electron emitting surface of an electro-emission device will be characterized, which has to be taken into account for establishing the correct energy reference of the electron spectra. Sec. 2.6 summarizes the conclusions of this work, and suggests some new perspectives for achieving a better understanding of the anomalous photoemission processes observed in nitrides.

2.1 LED electro-emission: the pioneer experiment

The idea behind the experiment of Iveland *et al*. is that an evidence of the occurrence of Auger recombination in an operating LED may be provided by the direct observation of hot carrier generation in the structure. In the AlGaAs materials system, hot carrier measurements were carried out by internal spectroscopy whereby voltage-controlled energy barriers were used to measure the kinetic energy of the electrons [83]. Such structures are at this time extremely difficult to implement in the nitride materials system because of growth constraints. Therefore, Iveland *et al*. resorted to measuring directly the kinetic energy of electrons. For that purpose, it was used an experimental approach reminiscent of the photoelectric effect, discovered by Hertz in 1887 and explained by Einstein in 1905. There, electrons are photoexcited and emitted out of a metal using UV light. Einstein explained this effect by assuming the quantization of light through photons which excite electrons at a well-defined kinetic energy. In 1914, Millikan measured the maximum kinetic energy of the escaping electrons as a function of exciting photon energy and precisely determined [84] Planck's constant *h*. Since that time, electron spectroscopy techniques have been developed to probe the electronic properties of solids. Among these techniques, angle resolved photoemission spectroscopy (ARPES) gives access to the valence band structure. Other techniques like Auger electron spectroscopy (AES) or electron energy loss spectroscopy (EELS) provide chemical information through the detection of specific processes which give rise to well-defined energy exchange between interacting particles within the material before the emission of an electron. Therefore, the electronic processes occurring within the material can in principle be identified by measuring the kinetic energy of the emitted electrons. Applying such an approach for probing the electron transport mechanisms in semiconductors is however not straightforward since the relevant conduction band region in usual compounds lies well below the vacuum level which prohibits electron

emission. But when covered with a Cs atomic surface layer, p-type semiconductors may exhibit the remarkable property of effective negative electron affinity (NEA), a situation where the vacuum level at the surface lies below the minimum of the conduction band (CBM) in the bulk, allowing emission of conduction electrons [85]. In this condition, electron emission spectroscopy gives access to the electronic properties over the whole CB and is thus well adapted to study hot-electron transport mechanisms.

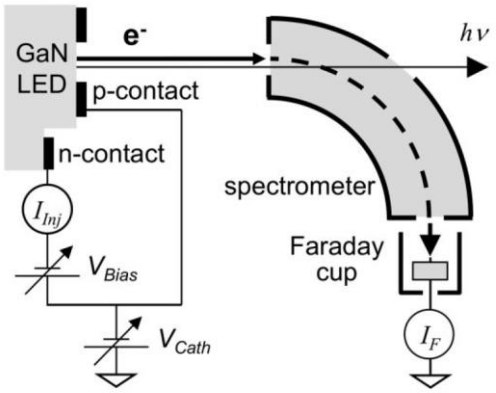

Figure 14 - Schematic of the experimental set-up used for LED electro-emission [53]: electrons are ejected into vacuum from a forward-biased LED. The kinetic energy of the electrons is analyzed in a cylindrical electrostatic deflector.

In the LED electro-emission (EE) experiment, schematized in Figure 14, carriers are injected electrically by biasing the junction. The electrons escaping from the active region into the top p-GaN layer can be emitted into vacuum from the surface activated to NEA and their energy distribution curve can be measured.

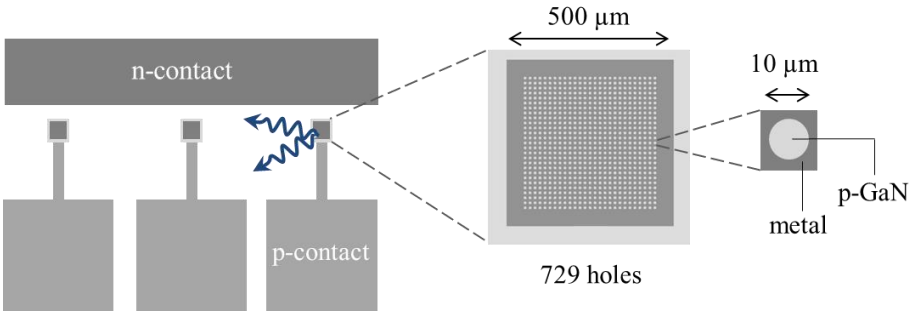

Figure 15 – Schematic representation of the contact geometry used in the LED sample studied in Ref. [53] by electro-emission. Three identical devices are present on the sample. The p-contact consists of an array of holes exposing p-GaN for electron emission into vacuum.

A commercial blue LED (Walsin Lihwa Co.) was studied in Ref. [53] with p- and n-contact specifically designed for EE (see Figure 15). In particular, the p-contact was fabricated with an array of holes exposing part of the p-GaN surface for electron emission.

When operating the device in forward bias, a substantial fraction of electrons and holes that are injected into the QWs recombine radiatively. However, at high injection currents, a fraction of the carriers injected into the QWs with the highest carrier density may recombine by an Auger process. In the e-e-h Auger process the energy of the electron-hole recombination promotes an electron to a high-energy CB state whereas in the e-h-h Auger process a hole is excited in a high-energy hole state (not measured by the EE technique). Electrons with various energies, among which energetic Auger electrons, may travel toward the surface and be emitted into vacuum. Measuring the energy of the emitted electrons should then give evidence of the Auger process, provided that some Auger electrons reaching the surface sustain a significant fraction of their high initial kinetic energy.

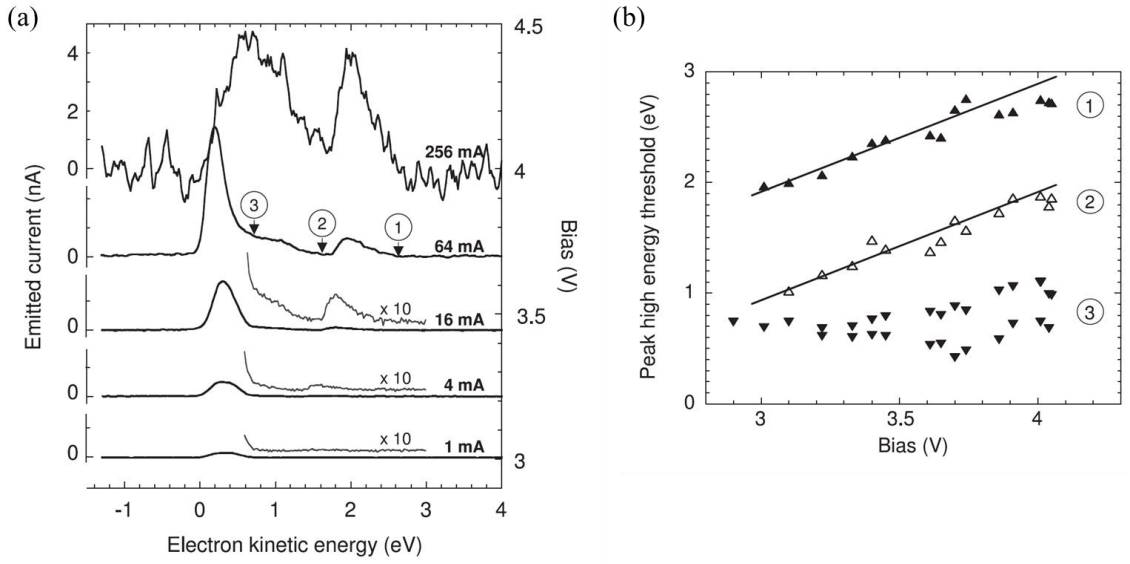

Figure 16 – (a) Measured energy distribution curves from Ref. [53] of electro-emitted electrons for different injection currents in the LED (for clarity, the baseline of each spectrum was shifted). The electron kinetic energy is referenced to the vacuum level of cesiated p-GaN. Labels ①, ② and ③ indicate the high-energy thresholds of three different electron peaks. (b) Bias-dependent shift of the high-energy threshold corresponding to the electron emission peaks shown in (a).

The EE spectra measured in Ref. [53] exhibited three distinct contributions (Figure 16a). At current below 1 mA, corresponding to a current density of 0.4 A/cm^2, a single low-energy emission peak (labeled ③) was observed. Two higher energy electron emission peaks appeared at 4 mA injected current and higher. The main peak (labeled ①) was ~1.5 eV above the low-energy peak. A somewhat weaker intermediate peak (labeled ②) was also observed at 0.3-0.4 eV above the low-energy peak. The relative intensities of these two high-energy peaks remained in the same ratio with increasing current, thus suggesting a common source.

Figure 17 summarizes the mechanisms at the origin of the three contributions as proposed in Ref. [53]. The high-energy peaks ① and ② were interpreted as Auger-generated electrons. However, their energy was not at the expected position: the initial kinetic energy of Auger electrons should be at ~2.25 eV above the CBM of bulk GaN

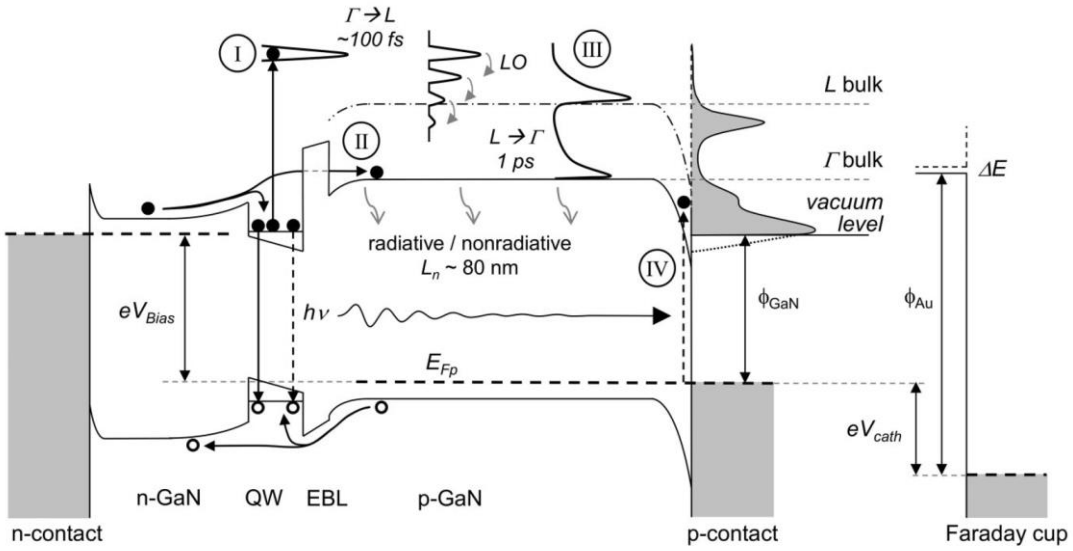

Figure 17 – Schematics of the emission of electrons from an LED in vacuum according to Ref. [53]: electrons originate from the QW with some high-energy ("hot") electrons generated by the Auger effect. After thermalization in the different accessible valleys of the CB, they give rise to high-energy peaks in the energy distribution of electrons emitted in vacuum. Thanks to negative electron affinity of the surface due to cesium deposition, electrons with energy below the bulk CB minimum can be observed, for example due to energy relaxation in the BBR or below-gap absorption excited by the LED light, as long as their energy is above the vacuum level. The active layer of the LED is shown as a single QW, but the actual sample has 8 QWs.

since Auger electrons are created in the InGaN QWs, with an energy close to 2.75 eV (for a 450 nm LED) above the ground state, which lies about 0.5 eV below the GaN bulk level. In the LED EE measurements, hot electrons with a maximum energy of ~1 eV above the CBM were observed. This was explained as follows: Auger hot carriers undergo partial energy thermalization while they travel from the QW to the surface rapidly emitting optical phonons, each time losing ~92 meV of kinetic energy. During this downwards cascade of phonon emission, they will transfer to a side conduction valley (called "L" for the sake of simplicity) as these valleys have much higher densities of states, due to their degeneracy and higher effective masses. As the transfer back to the central Γ-valley is quite slow, L electrons can reach the surface (peak ①), and their existence is a memory that these electrons were created with an initial high energy within the LED by the Auger effect. Those L electrons which have been returning into Γ, near enough the surface to survive non-radiative recombination in the p-material, are at the origin of the intermediate peak ② observed well above the low-energy photoemission peak. The separation between the Γ and L peaks, as deduced from the position of their high-energy threshold, is 0.95 ± 0.1 eV.

Then, the contribution of the so-identified Auger-generated current to the droop of the

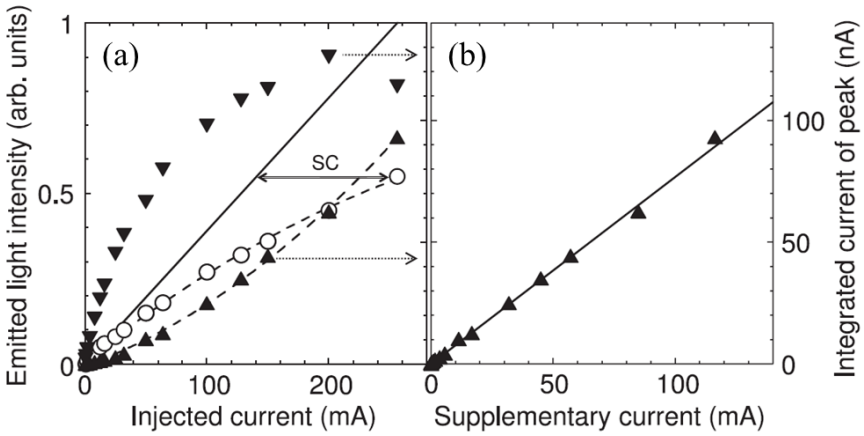

Figure 18 – (a) Plots of the integrated current over the high-energy peaks (upward triangles), low-energy peak (downward triangles) and of the optical output power (open circles) as a function of the injected current. The straight line is the expected optical output power in the absence of efficiency droop, obtained by a linear extrapolation from the maximum IQE value. "SC" labels the supplementary or droop current. (b) Plot of the integrated current over the high-energy peaks as a function of the droop current. Reproduced from Ref. [53].

LED was evaluated. For this purpose, the integrated intensity of the high-energy peaks, considered in a first approximation as proportional to the Auger recombination current (assuming linearity of the transport to the surface and extraction probability), was compared to the droop component of the injected current as deduced from the separately measured dependence of EQE on current (Figure 18a). The droop or supplementary current (labeled "SC") is the difference between the actual injected current and the current which would give the same optical output if the maximum IQE had been conserved.

The observed linear relation between the supplementary current due to droop in the EQE vs. current curve and the integrated current of the high-energy peaks interpreted as Auger-generated (Figure 18b) suggests that the two phenomena are the same, as other droop mechanisms are not expected to have the same dependence on injected carrier density. This result was the basis to claim that Auger recombination is the dominant droop mechanism in the studied commercial InGaN/GaN LED.

This analysis relies on the assumption that a high-energy electronic channel exists in bulk p-GaN at ~1 eV above the CBM, where hot Auger electrons created in the QWs of the operating LED may relax and accumulate, preserving a spectroscopic information on their generating process.

Actually, the energy position of the first satellite valley in GaN is not clearly established from the literature, as already detailed in Sec. 1.4. (Note that, in the experiment by Iveland *et al.* [53], the LED is operated close to flat band condition and electron transport in p-GaN is dominated by diffusion. Therefore, a high field is not present in p-GaN, but the Auger process is in principle sufficient to populate side valleys with hot electrons.) According to theoretical calculations the L-valley should lie over 2 eV above the CBM in GaN, which would not explain why an electron peak at only ~1 eV above Γ is observed in LED EE. On the other hand, the reported experimental values are scattered over a wide range, from few 100 meV to more than 1 eV. Moreover, the experimental determinations are rather indirect, as they rely on models, and their accuracy may be questioned.

It is therefore crucial to directly determine the energy position of the first satellite valley in the CB of GaN with a conclusive experiment. This issue will be addressed in Sec. 2.3, where another type of electron emission spectroscopy based on near-band-gap photoemission will be used to determine $\Delta E_{\Gamma,L}$ in GaN.

The low-energy peak ③ was suspected to originate from photoemission (PE) internally excited by the LED blue light through below-gap absorption in the BBR. This hypothesis was supported by the observation of a similar electron peak under external photoexcitation at a wavelength close to the peak of LED EL. However, photoemission processes in the LED were not investigated in detail in Ref. [53]. Such studies were carried out in the course of this work and will be presented in Sec. 2.4.

The energy scale of the EE spectra in Ref. [53] was referenced to the vacuum level of the cesiated p-GaN surface. Note that this reference is not convenient when comparing measurements on one or different samples, as the NEA (and therefore the work function of p-GaN/Cs) suffers from degradation with time and depends on the surface preparation (chemical cleaning, annealing, Cs exposure, etc.). After a careful calibration of the pass energy of the electron analyzer, which will be illustrated in Sec. 2.2.3, the electron energy can be referenced to the Fermi level of the p-contact. This convention will be used in the rest of this thesis (unless otherwise specified). It has to be noticed that if no potential drop occurs at the interface between the p-contact and p-GaN then the respective Fermi levels are aligned and the energy scale can be directly referenced to the electron emitting semiconductor. However, this was not the case in the sample studied in Ref. [53]: a rectification occurred at the metal/p-GaN interface, as signalled by the bias-dependent shift of the peaks ① and ② shown in Figure 16b. Non-ohmic voltage drops may considerably affect the accuracy of the spectroscopy and will be discussed in more details in Sec. 2.5.

2.2 Materials and methods

Electron emission spectroscopy experiments that will be presented in this chapter require in general to:

- Grow a sample structure adapted to the crystal or device property that needs to be measured;
- Process sample contacts designed for the specific electron excitation source, which may be electrical or optical;
- Prepare the sample surface for electron emission into vacuum;
- Measure the energy distribution of the emitted electrons by means of an electron spectrometer.

A general description of the different procedures is outlined in Sec. 2.2.1-2.2.3. Then the details on the different samples and experiments will be given along with each result presented in this chapter.

2.2.1 Sample structures and contact processing

The majority of the samples studied throughout this thesis by electron emission spectroscopy are GaN-based p-n junction structures grown on c-plane sapphire, either by industrial LED manufacturers (Walsin Liwha Co. and Seoul VioSys) or at UCSB. An InGaN/GaN MQW active region is present at the junction in the case of LEDs (5 and 8 QWs in Seoul and Walsin samples, respectively, with a thickness of 3 nm each), but is absent in some samples for control experiments or for the measurement of pure GaN crystal properties. An AlGaN EBL (30 nm and 40 thick in Seoul and Walsin

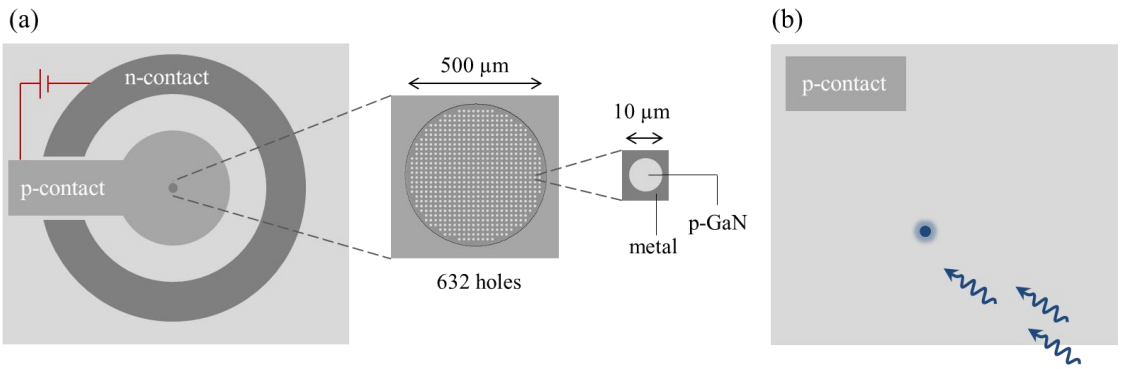

Figure 19 – Schematic of the contact geometry used in GaN-based samples processed for: (a) electro-emission; (b) photoemission.

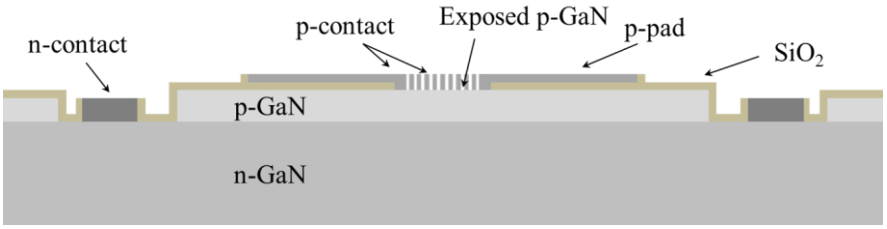

Figure 20 - Schematic profile of a GaN-based p-n junction device processed for electro-emission. A mesa etch allows the deposition of the n-contact. The p-contact has an array of apertures for electron emission and is contacted by a large isolated p-pad.

samples, respectively) may be present in the p-layer of some LEDs to reduce electron leakage from the active region under electrical operation. As in EE experiments hot electrons are expected to originate from the active region of the LED and be emitted into vacuum after transport in the p-layer of the diode, the thickness of p-GaN (typically 100-200 nm) may be an important parameter affecting hot electron relaxation.

Samples may be processed either for EE experiments (Figure 19a), in which the electron excitation source is internal and due to the bias applied to the device, or PE experiments (Figure 19b), where electron excitation is caused by an external light source, such as a laser or a lamp. In the latter case, only the p-contact (typically Pd/Au) is deposited on the sample and is used as a potential reference for energy analysis and to maintain charge neutrality during PE supplying the sample with carriers (note that the sapphire substrate is electrically insulating). Since the goal of the PE experiments is to study the photoelectric processes and the electronic properties of the semiconductor, the p-contact normally occupies a small fraction of the sample surface and lies in a corner of the sample to avoid unintentional PE from the metal.

The fabrication process of samples for EE is more elaborated and is carried out in the UCSB Nanofabrication Facility. A schematic of the typical structure profile is depicted in Figure 20. A mesa etch is required in order to deposit the n-contact, which can be achieved with a few photolithographic steps where a negative photoresist (PR) is spin-coated on the p-surface and then exposed to UV light through a mask. After development, the PR is removed from the region corresponding to the mask, allowing for dry etch into p-GaN (inductively coupled plasma etching). Then, the n-GaN is exposed and the n-contact (typically Ti/Ni/Al/Au, 10/100/100/200 nm) is successively deposited by e-bombardment metal evaporation. Similarly, the p-contact (typically

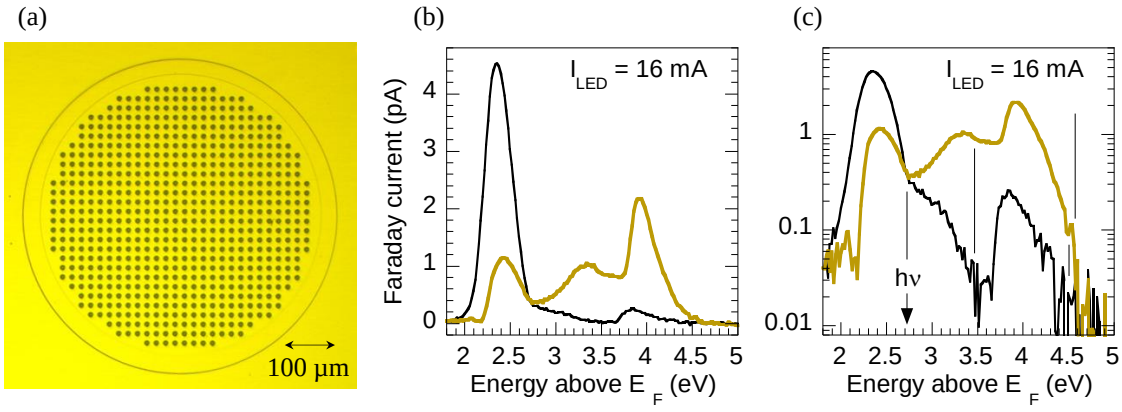

Figure 21 – (a) Optical microscope image of the holey p-contact of a sample processed for electro-emission with concentric contact geometry. (b) EDCs measured in electro-emission at an injected current of 16 mA for the Walsin LED with square electrodes studied in Ref. [53] (black curve) and a Seoul LED with concentric contacts (brown curve). (c) Same as (b) with logarithmic current scale.

Pd/Au, 10/100 nm) is deposited on the sample. It has a diameter of 500 µm and exhibits an array of 632 apertures (each one having a 10 µm diameter) for electron emission (Figure 21a). It is contacted by a large p-pad, isolated from p-GaN by a SiO_2 layer.

In principle, one could think of substituting the array of small apertures with a single large aperture of several 100 µm diameter. But in this case, to avoid large potential inhomogeneity across the electron emitting surface due to current crowding, a current spreading layer (for instance Pd) should be deposited on top of the large aperture. This may have the unwanted effect of attenuating (not uniformly) the hot electron distribution emitted from the semiconductor, even in the case of a thin spreading layer (few nm). Therefore, the array of small apertures constitutes in principle the most adapted design for the p-contact of EE samples.

A remarkable technological effort was carried out at UCSB to improve the emission efficiency of the devices by optimizing their contact geometry [86–88]. The concentric contact geometry shown in Figure 19a represents an evolution with respect to the square electrode design (Figure 15) employed in the pioneer experiment reported in Ref. [53]. The advantage of the concentric contact design is to create, when biasing the device, a more uniform electric field in the region between the p-contact and the circular collecting aperture of the electron analyser. This avoids distortion of the measured emitted electron spectrum and contributes to the increase of the signal-to-noise ratio in EDCs (and therefore to the reduction of the spectral acquisition time for a given signal-

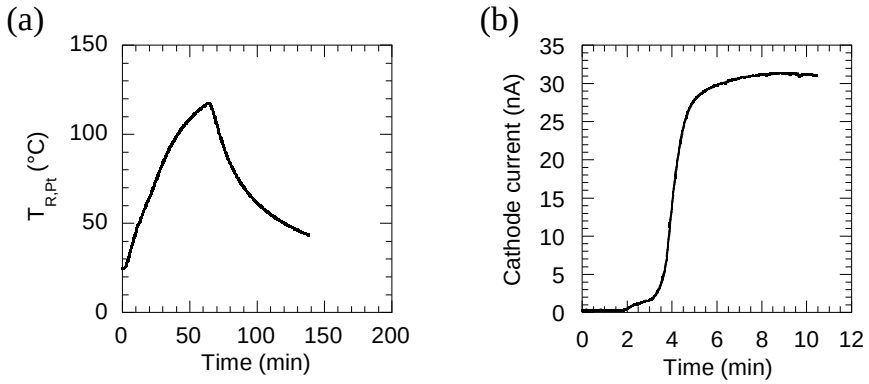

Figure 22 – Monitoring of the surface preparation in UHV and electron emission curves of an LED sample processed for EE. (a) Annealing cycle for vacuum cleaning of the surface monitored by a Pt resistance probe with temperature $T_{R_{Pt}}$. (b) Cs evaporation on the surface monitored by measuring the cathode current emitted from the LED at a current of 2 mA.

to-noise ratio). An EE spectrum measured from a Seoul LED with concentric contacts is shown in Figure 21b and can be compared with EE from the Walsin LED with square electrodes studied in Ref. [53]. Due to the slight difference in injection area related to the contact geometry, at an injection of 16 mA the current density is 8 A/cm^2 in the Walsin sample and 11 A/cm^2 in the Seoul sample. The specific features of the different peaks may depend on the characteristics of the diodes and the surface preparation, as it will be later discussed in this chapter. The main remark at this point is that for different contact geometries and different manufacturers three electron contributions are observed.

2.2.2 Surface preparation for low-energy electron emission

The preparation of a sample surface for low-energy electron emission consists of two major steps: 1) surface cleaning, as any impurity layer would be an obstacle to surface activation and electron emission; 2) surface activation to NEA.

The sample is chemically cleaned in a piranha solution (3:1 mixture of H_2SO_4 and 30% H_2O_2 solution in H_2O), then rinsed in distilled water and anhydrous ethanol. Prior to insertion in the vacuum load-lock chamber through a nitrogen glove box, the sample is treated in an HCl-isopropanol solution to eliminate the native oxide and form a passivation layer preventing the formation of a surface oxide [89]. The chemical treatment of the sample is performed under N_2 atmosphere in a glove box which is connected to the load lock of the ultra-high-vacuum (UHV) experimental chamber.

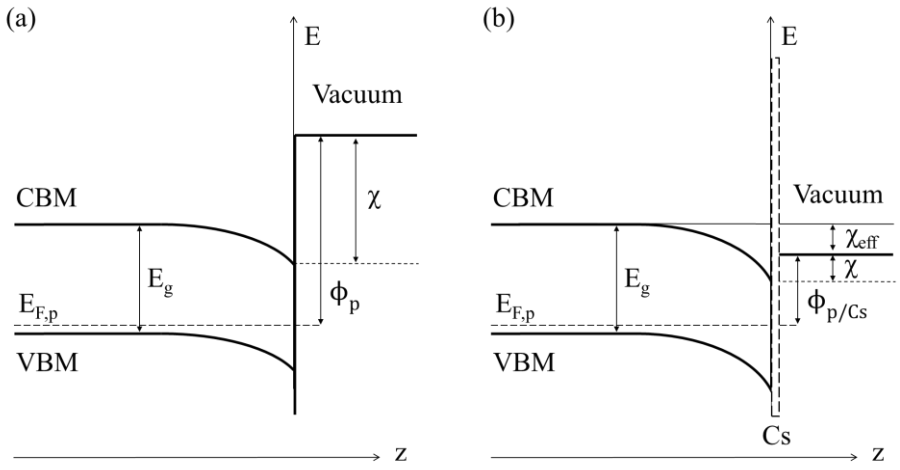

Figure 23 - (a) Band diagram of a typical p-type semiconductor near the surface. A potential energy barrier of height χ prevents electrons from escaping into vacuum. ϕ_p denotes the work function of the semiconductor; (b) Surface energy band diagram of a cesiated p-type semiconductor. The deposition of Cs lowers the electron affinity and increased band bending at surface leads to a condition of effective negative electron affinity χ_{eff}, allowing electrons at bulk CBM to leave the crystal.

Right after the chemical passivation treatment, the sample is introduced into the load lock and transfered into the UHV chamber, where the typical base pressure is in the low 10^{-11} Torr range. The sample is then annealed with a heater mounted on the backside of the sample holder. Typical annealing cycles are shown in Figure 22a where the temperature of a calibrated Pt resistance ($T_{R_{Pt}}$) is used for monitoring as a function of time. As the Pt probe is embedded in the sample holder its temperature does not directly correspond to that of the sample. From a calibration with a pyrometer it is found that

$$\mathbf{T_{sample}}\ (^{\circ}\mathbf{C}) \approx \mathbf{T_{R_{Pt}}}(^{\circ}\mathbf{C}) + \mathbf{180} \quad \text{for } \mathbf{T_{R_{Pt}}} \in [100, 400]^{\circ}\mathrm{C} \qquad \mathbf{(4)}$$

Note that a precise control of the annealing temperature is not needed as the only strict requirement is not to overcome the sample temperature threshold of typically 800°C at which the surface morphology is deteriorated and surface depletion of nitrogen atoms occurs [90]. The chemical passivation of the sample and the subsequent fast introduction procedure from N_2 atmosphere into vacuum allows using moderate annealing temperature. Typically, samples processed for EE are annealed only up to ~300°C (as in Figure 22a) to limit: 1) the increase in contact resistance suffered by the p- and n-contacts after the annealing, which may then cause a considerable shift of the

EDC spectra under forward bias operation (Figure 45a,b); 2) Au diffusion from the p-contact into the exposed p-GaN apertures. However, such issues are negligible in samples processed for PE, as the circulating current (usually in the range 1-100 nA) is much smaller than in typical LED operation (1-100 mA) and the Au contact is far from the electron emitting region. Consequently, annealing at 500-600°C can be carried out in these samples, which improves the surface cleaning.

The next step in the surface preparation is activation to NEA. The energy band diagram of the surface of a typical p-type semiconductor is shown in Figure 23a. Electron escape from the crystal is prevented by a surface potential energy barrier. The amount of energy required for an electron lying at the CBM to reach the vacuum level is called electron affinity χ, while the work function ϕ_p is defined as the energy required to bring an electron from the Fermi level to the vacuum level. The work function of a clean GaN surface is typically around 4 eV (Sec. 5.3; Ref. [91]). By depositing on the surface an ultra-thin layer of Cs, an alkali metal with low work function and low ionization potential (~1.8 eV and ~3.9 eV, respectively [92]), the electron affinity of the semiconductor is lowered. Due to Fermi level pinning at the middle of the energy gap, bands are bent downwards near the surface and the condition of so-called effective negative electron affinity is reached, in which electrons at bulk CBM can be emitted into vacuum.

Cs is evaporated on the surface of the sample using a cesium dispenser (SAES Getters) placed approximately 4 cm from the sample. The state of cesiation is monitored as a function of time (Figure 22b) by measuring the total electron current emitted from the sample which, depending on the type of sample, may be excited by EE (applying a bias on the device) or PE (shining light on the sample). Under Cs exposure the cathode current from the sample rapidly increases, then reaches a maximum, typically for a coverage of less than 1 monolayer [89]. Note that the achievement of the effective NEA condition in a wide band gap semiconductor such as GaN is easier than in narrow band gap semiconductors (as for instance GaAs), since a smaller reduction of the work function is needed in order to bring the vacuum level below the bulk CBM [93].

It is important to remark that the annealing temperature and cesiation condition may considerably affect some features of the measured EDCs. Both a degradation of cesiation and a different annealing temperature may cause a shift of the low-energy threshold of the different electron contributions, which consequently displaces the position of the peaks and changes their relative ratio. However, the high-energy

threshold of the different peaks is substantially unaffected by the surface condition. These effects have to be taken into account when comparing different electron emission measurements: ideally samples should always be annealed at similar temperatures and be measured few hours after cesiation.

It should be noted that the UHV chamber used for the electron emission spectroscopy experiments at Ecole Polytechnique was not equipped for surface characterization. Some *ex situ* low-energy electron diffraction (LEED) measurements of the p-GaN surface of bare photoemission samples were carried out at the FEMTOARPES facility of the synchrotron SOLEIL and exhibited a clear hexagonal diffraction pattern, while LEED characterization of processed electro-emission devices was prevented by the contact geometry of the samples.

2.2.3 Electron energy analysis

Once that a distribution of electrons is emitted into UHV, the electron energy can be analyzed by mean of an electron spectrometer. In this thesis work, electron emission experiments are carried out using a home-made low-energy electron spectrometer designed by Drouhin *et al*. [94] which sets the foundation of several PE experiments for the study of band structure and hot electron transport properties of semiconductors [95,96]. However, no EE spectroscopy experiment on a semiconductor device was ever conceived and carried out before the work of Iveland *et al*. [53] in 2013.

The spectrometer, schematized in Figure 24, consists of four main parts.

- A rotator, which is a 90° cylindrical deflection selector (CDS) consisting of two concentric cylinder sectors made of gold wires, equipped with an entrance aperture, collects and deflects the emitted electron beam. It hosts a hole which provides optical access to the sample surface and allows to excite the sample in PE experiments and to collect the emitted light when performing LED EE spectroscopy measurements.
- A collimation and deceleration electron optics is formed by a three-element cylinder lens.
- A selector, which is another 90° CDS, selects electrons with high-energy resolution (down to 20 meV). Two CDS are employed because the presence of the hole for light transmission would limit the energy resolution in the rotator.

- A Faraday cup, made of a shielded gold-covered anode, collects the energy-selected electron beam.

The electron analyzer is operated in constant pass energy mode. In this mode, the potentials of the analyzer electrodes are kept constant fixing the pass energy E_{sel} and the energy resolution ΔE. An EDC is obtained by measuring the current collected on the

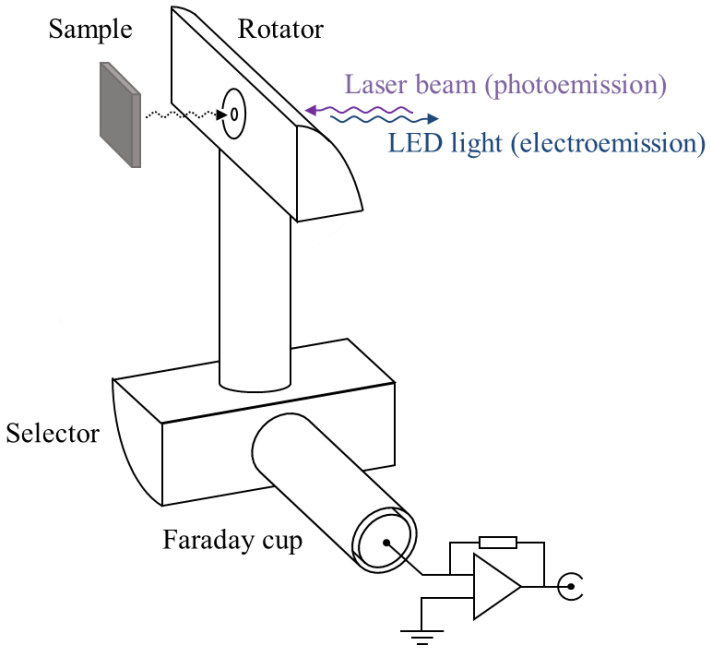

Figure 24 – Diagram of the electron spectrometer used in electro-emission experiments. The sample is mounted on a translation sample holder for alignment. The electron beam emitted into vacuum is 90°deflected in the rotator, then collimated and decelerated, and successively analyzed in energy by the selector. Finally, the selected beam is collected at the grounded Faraday cup. A hole in the rotator allows extracting light from an electro-luminescent device or shining light on a sample for photoemission.

Faraday cup at the analyzer exit slit as a function of the sample potential V_{cath} relative to the analyzer (Figure 25a). The sample holder allows taking several isolated contacts on the sample. The cathode potential V_{cath} is applied to the p-contact. (In EE measurements the junction bias potential is added to V_{cath} and applied to the n-contact, as shown in Figure 14.) To perform the energy assignment of the electron peaks appearing in an EDC, the energy of the electrons emitted into vacuum must be referenced to some energy level of the sample, as for instance the Fermi level of the p-contact $E_{F,m}$. For this purpose, the electron spectrometer has to be calibrated.

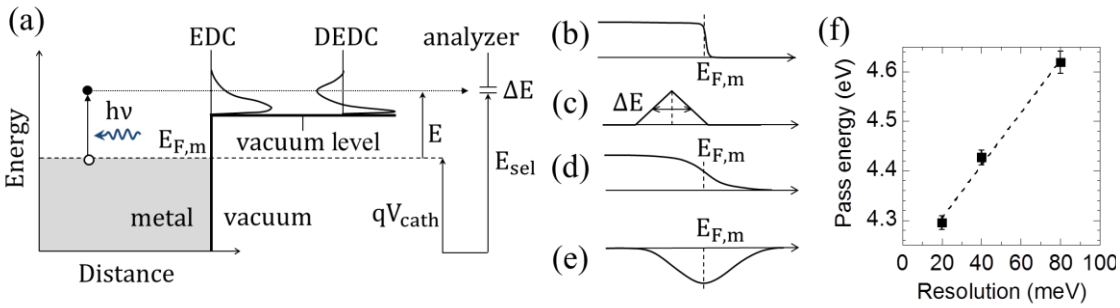

Figure 25 - (a) Schematics of the photoemission experiment carried out on a metal sample for the energy calibration of the spectrometer. The energy of ballistic photoelectrons excited from $E_{F,m}$ gives a distinguishable feature in DEDC spectra allowing to determine the pass energy of the analyzer; (b) Fermi-step distribution of a metal; (c) Triangular transmission function of the analyzer with FWHM determining the resolution of the spectrometer; (d) Fermi distribution of a metal broadened by the convolution with the spectrometer transmission function in (c); (e) Derivative of the Fermi distribution in (d); (f) Pass energy of the spectrometer calibrated on a gold sample at different energy resolutions.

The goal of the energy calibration is to determine E_{sel}. In order to measure a current of electrons emitted from the sample at an energy E with respect to the Fermi level of the p-contact $E_{F,m}$, a potential difference V_{cath} must be applied between the analyzer and the sample in order to satisfy the following relation:

$$\boldsymbol{E + qV_{cath} = E_{sel}} \qquad \textbf{(5)}$$

where $q < 0$ is the electron charge.

A photoemission energy calibration experiment is carried out on a metal sample (Figure 25a). In the case of a metal, the energy E of ballistic photoelectrons excited from $E_{F,m}$ is equal to the photon energy $h\nu$. (The case of an amorphous metal sample is considered, for which the crystal momentum is not conserved in electronic transitions. Thus, differently from the case of semiconductor crystals, all transitions with initial states at the Fermi level are allowed.) Then by taking the value of V_{cath} at which the ballistic photoelectrons are measured, E_{sel} can be obtained from Eq. (5) imposing $E \equiv h\nu$.

The high-energy edge of the photoemitted spectrum should reflect the Fermi distribution of the metal (Figure 25b). The energy width of the Fermi step is determined by the temperature but the measured Fermi distribution at the high-energy edge of the

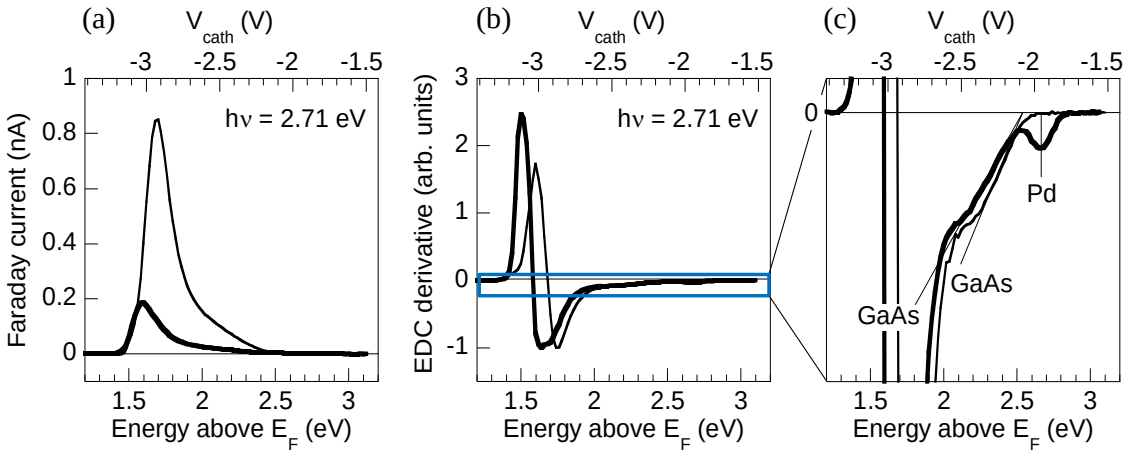

Figure 26 – (a) EDC and (b) DEDC spectra measured at $h\nu = 2.71$ eV on a GaAs sample before (thin curve) and after (thick curve) deposition of a 5 nm thick Pd layer. A zoom on the ballistic photoelectron contribution of the DEDC is shown in (c). The upper x-axis corresponds to the cathode voltage applied to scan the electron distributions, while the lower energy scale is referenced to the Fermi level of the p-GaAs surface and is obtained from V_{cath} using the calibrated pass energy of the spectrometer at $\Delta E = 80$ meV. Straight lines in (c) indicate the determination of the energies of ballistic photoelectrons.

photoemitted spectrum is broadened mainly due to the resolution of the analyzer (Figure 25b-d). Considering a triangular transmission function for the spectrometer with FWHM ΔE (Figure 25c), the inflection point of the EDC high-energy edge is not shifted and corresponds to the energy of ballistic photoelectrons excited from $E_{F,m}$. This feature is best identified on the EDC derivative (DEDC) appearing as a high-energy minimum (Figure 25e).

The pass energy of the spectrometer determined from the Fermi step position measured on a gold sample (400 nm-thick Au layer evaporated on a sapphire substrate) at different spectrometer resolutions is shown in Figure 25f. The experimental points correspond to the average of calibrations carried out at excitation photon energies of 1.92 eV, 2.41 eV, 2.54 eV and 2.61 eV. The dependence of E_{sel} on ΔE is due to the change of the spectrometer potentials at different resolutions, which may modify the path of the selected electrons. The intensity of the emitted cathode current may affect the energy selection due to charging effects in the electrodes of the analyzer. This effect has been evaluated in a wide range of cathode currents (from 50 nA to 2 µA) and is taken into account in the error bars reported in the calibration.

Differently from the case of a metal, in a semiconductor electronic transitions at above-band-gap photon excitation occur from a well-defined initial state in the valence band to a well-defined final state in the CB. The excess energy $h\nu - E_g$ is shared among electrons and holes according to their respective masses. The final energy E of the most energetic ballistic photoelectrons in a semiconductor can be calculated with a parabolic model as:

$$\boldsymbol{E = \left(h\nu - E_g\right) \cdot \frac{m^*_{hh}}{m^*_e + m^*_{hh}} + E_g - E_{F,p}} \qquad \textbf{(6)}$$

where E is referenced to the Fermi level of the semiconductor $\boldsymbol{E_{F,p}}$, and m^*_{hh} and m^*_e are the effective masses of heavy holes and electrons respectively.

In order to verify the energy calibration obtained from the metal, we measure the photoemission spectrum of a Zn-doped ([Zn] $\approx 10^{19}$ cm^{-3}) p-GaAs sample at hν = 2.71 eV and ΔE = 80 meV. The measured EDC is shown in Figure 26a (light line) where the upper x-axis corresponds to the cathode voltage applied to the sample to scan the energy distribution and the lower energy scale has been deduced from V_{cath} using Eq. (5) and the value of E_{sel} obtained from the previous energy calibration. The corresponding DEDC is shown in Figure 26b. In the case of a semiconductor crystal the energy of ballistic photoelectrons is determined by the high-energy threshold (HET) of the DEDC [97], which can be clearly observed in Figure 26c. The measured HET of 2.56 ± 0.08 eV is in perfect agreement with the ballistic energy E = 2.54 eV calculated from Eq. (6) using the following values taken from Ref. [98] for the different parameters: $m^*_{hh} = 0.50\ m_0$, $m^*_e = 0.063\ m_0$, $E_g = 1.42$ eV, $E_{F,p} = 20$ meV. (In the considered case the use of a more accurate non-parabolic model is not necessary as it would give a correction to the predicted value of E which is smaller than ΔE.) Moreover, after deposition of a 5 nm-thick Pd layer on the p-GaAs surface (EDC and DEDCs shown as thick curves in Figure 26) a high-energy peak appears in the DEDC due to ballistic electron emission from the metal at $E = 2.66 \pm 0.08$ eV in agreement with $h\nu$. These measurements validate the energy calibration of the low-energy electron spectrometer for electron emission experiments on metals and semiconductors.

One needs here to express one word of caution. In all the EDCs shown in this thesis with the x-axis label "Energy above E_F", the energy scale must be intended as referenced to the Fermi level of the wire connected to the p-contact. If no voltage drop occurs between this reference and p-GaN then the energy scale can be considered as

referenced to the Fermi level at the surface of the p-GaN layer. This is the case of the near-band gap PES studies presented in Sec. 2.3, where no appreciable surface or bulk PV effect occurs in p-GaN due to the low excitation intensities, and no bias is applied across the structure. On the other hand, the SPV effects observed in the PE studies of Sec. 2.4, and the rectifying p-contact of EE devices (characterized in Sec. 2.5) may produce a non-negligible energy shift so that the measured electrons emitted from p-GaN will appear at a higher apparent energy.

2.3 Conduction band structure of GaN by photoemission spectroscopy

To address the open question of the presence of a satellite valley at ~1 eV above Γ in the CB of GaN, of the most importance in the interpretation of the electro-emission spectroscopy experiment presented in Ref. [53] (see Sec. 2.1), near-band-gap PES will be used, which has already allowed the determination of several conduction band properties of different III-V semiconductors, such as GaAs [97] and InP [99], activated to NEA.

Contrarily to the usual x-ray and UV PES techniques, near-band-gap photoemission of NEA semiconductors is mainly sensitive to the empty states structure. Indeed, it can be considered that the optical excitation creates δ distributions at well-defined energies in the conduction band corresponding to heavy-hole, light-hole, and spin-orbit split-off band. Then electrons relax their energies by phonon scattering and a broad electron distribution forms, the detailed shape of which is determined by the hot-electron transport mechanisms in the CB. Therefore, the photoemitted electron spectrum contains very little information on the initial state of the optical transition. At best, very weak structures corresponding to the final state of the optical transitions from the three valence bands are sometimes observed but not in the case of GaN, except for the high-energy threshold of the spectrum which is characteristic of the final state of the optical transition from the heavy-hole band. When varying the excitation energy $h\nu$, the features which show up in the EDCs of the emitted photoelectrons can be unambiguously assigned either to the optical transition final states (allowing band dispersion measurement) or to the emission from side valleys at the bottom of which electrons accumulate during the relaxation process.

In the following the experimental study of the CB structure of wurtzite p-GaN by near-band-gap PES for excitation energies ranging from 3.10 eV to 5.79 eV is reported. In this energy range, two features associated with CB valleys are evidenced and are attributed to the Γ valley and to the first satellite valley (called L). A $\Gamma - \mathrm{L}$ intervalley energy separation of 0.90 ± 0.08 eV above the bottom of the CB is directly obtained, much lower than theoretical ones and in agreement with those recently estimated from optical spectroscopy experiments [68] and some ellipsometry measurements [76].

2.3.1 Experimental details

The sample is a wurtzite GaN p-n structure grown by MOCVD on a (0001) sapphire substrate processed for PE (Sec. 2.2.1). The top p-layer is 200 nm thick, larger than the absorption length for above band-gap excitation energies (the absorption coefficient is $\alpha > 7.5 \times 10^4$ cm^{-1} [100]). The acceptor (Mg) concentration is of 5×10^{19} cm^{-3} in the bulk and overdoped in the proximity of the surface. In this doping condition the width of the BBR near the p-surface is less than 10 nm.

The sample is chemically cleaned as usual (Sec. 2.2.2) and annealed at 580°C for ~90 min. The surface activation to NEA was controlled by monitoring the PE current under laser light excitation at $h\nu = 3.32$ eV. The cesiation procedure was completed with a maximum quantum yield (QY) of ~0.4% and the work function was lowered to about 2.3 eV, being stable for few days. The PES measurements were performed with a broadband light source (Energetiq EQ-99) coupled to a monochromator (J-Y H10-UV) with an output wavelength dispersion of ± 2 nm and a transmitted optical power ranging between 0.2 μW in the deep UV (200 nm) and 10 μW near the band gap of GaN (spot size on sample ~500 μm). The measurement at the highest excitation energy ($h\nu$=5.79 eV, λ=214 nm) was done using a UV bandpass filter (20 nm bandwidth), rather than with the monochromator, giving a transmitted optical power of 14 μW. The light beam was focused at normal incidence on the p-GaN surface. Photoemitted electrons were analyzed with the low-energy electron spectrometer as described in Sec.2.2.3 and the resolution was set at 80 meV.

2.3.2 Principle of near-band gap photoemission spectroscopy

Figure 27 shows schematics of the photoemission processes. Direct interband transitions excite electrons with a well-defined conduction energy. A small fraction of the photoelectrons is emitted without energy loss, yielding a quasiballistic hot-electron contribution (labeled B). This contribution extends up to the highest possible transition final state energy (related to transitions from the heavy-hole valence band) which defines the HET of the PE EDCs. Most of the photoelectrons undergo energy and momentum relaxation by phonon emission. In the bulk, relaxation produces electron accumulation at the bottom of the conduction valleys. For moderate light energy above the band gap, electrons are photoexcited in the Γ valley but if the transition final state energy lies above a satellite valley minimum, electrons can be efficiently transferred from Γ to the satellite valley by emitting a phonon. We remark that the L valley in

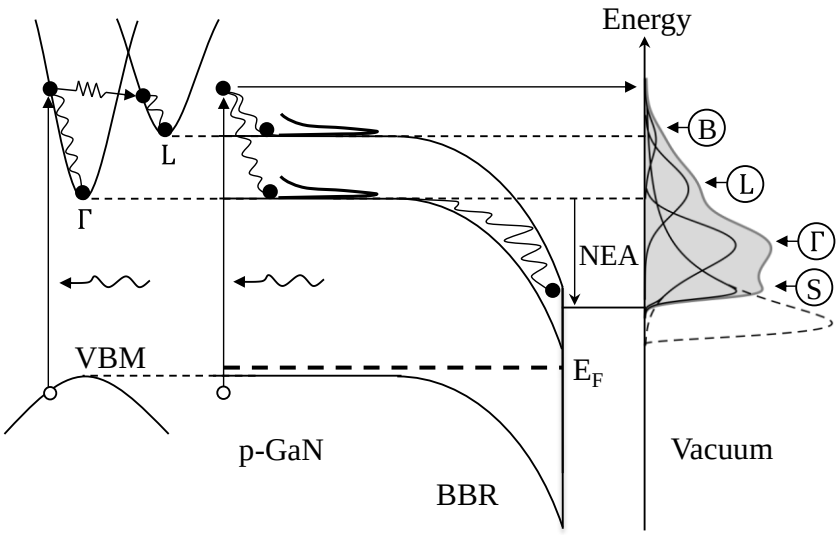

Figure 27 - Left: Reciprocal-space schematic of photoelectron excitation and intervalley transfer from Γ to L valley via phonon emission. Right: Real-space schematic of the photoemission processes occurring in *p*-GaN at above-band-gap excitation. Quasiballistic electron emission produces a high-energy peak (labeled B). Energy relaxation induces electron accumulation in the bulk at the bottom of the conduction band valleys (peaks _ and L). Relaxation in the BBR produces a low-energy peak (S). The energy distribution curve (shaded area) measured in vacuum exhibits characteristic features related to the different above processes. The vacuum level cuts the low-energy side of the EDC, in particular a considerable portion of the S peak (dashed line).

wurtzite crystals has a sixfold degeneracy giving a large final density of states (DOS) for intervalley transfers. Each populated valley acts as a source of thermalized electrons.

Partial energy loss during transit through the BBR prior to emission into vacuum broadens the valley contributions towards low energy. But the HETs of these contributions will point to the position of the valleys in the bulk. Note that the structures related to the CB valleys can easily be identified since their position is determined by the energy of the valley minimum and does not depend on the excitation energy (provided the photon energy is large enough to populate the considered valley). Prior to emission in vacuum, energy and momentum relaxation near the surface of electrons either photoexcited in the BBR (i.e., at lower energy than in the bulk) or backscattered at the semiconductor/vacuum interface results in the formation of a low-energy contribution (labelled S) which extends down to the bottom of the BBR in the crystal and is cut by the vacuum level in the emitted spectrum. We remark that with near-band-

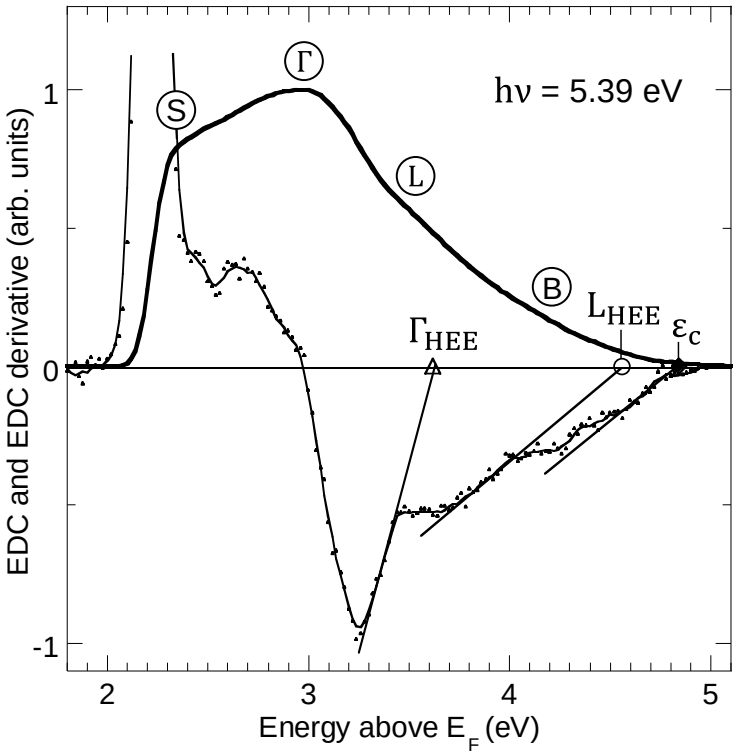

Figure 28 - EDC and corresponding DEDC measured at 5.39 eV excitation energy. The energy scale is referred to the GaN Fermi level. Four different contributions are observed labeled (S), (Γ), (L) and (B). The high-energy extrapolation of the Γ and L contributions is shown on the derivative (Γ_{HEE} and L_{HEE}) giving an energy separation between Γ and L of 0.92 ± 0.08 eV. Due to the overlap of different contributions, Γ_{HEE} and L_{HEE} slightly overestimate the bulk positions of the valleys. The high-energy threshold of the spectrum (ε_C) gives the energy of the optical transition final state in the bulk p-GaN.

gap excitation (of energy much lower than twice the band gap, a range sometimes called the "magic window" [101]) photoelectrons do not have enough kinetic energy for exciting the electron-hole pair by impact ionization so that the low-energy peak is not due to secondary electron emission as is usually the case in standard photoemission experiments.

2.3.3 Near-band gap photoemission spectroscopy of GaN

The normalized EDC measured on the p-GaN sample at 5.39 eV excitation energy is shown in Figure 28 along with its derivative. The EDC (bold line) exhibits a main peak (Γ) with a low-energy shoulder (S) and high-energy contributions (L, B). The different convoluted contributions to the photoemission spectrum are properly resolved when

performing a fine analysis of the DEDC [97]. The DEDC is measured by applying a 60 mV modulation to the cathode potential and detecting the related Faraday cup current modulation with a lock-in amplifier. Four contributions are clearly observed. The thermalization in the BBR gives rise to the low-energy positive peak. Then, three structures are resolved in the negative part of the DEDC. Two are originating from the electron population accumulated in the Γ and L valleys as will be discussed below. The HET of these contributions is evaluated as usual [97], by taking the extrapolation to zero of their high-energy slope (Γ_{HEE} and L_{HEE}). Finally, the quasiballistic emission contribution appears on the high-energy edge of the DEDC with HET ε_C.

Figure 29 shows a set of DEDCs recorded for different excitation energies ranging from 3.10 eV to 5.39 eV using the broadband light source coupled to the monochromator. The DEDC measured at $h\nu$ = 5.79 eV using the bandpass filter is plotted in violet. For the sake of clarity, the low-energy contribution is not shown. Electron emission is observed also for below-band-gap excitation, in agreement with previous observations by Pakhnevich *et al.* [102,103]. A detailed study of below-gap PE processes in GaN will be presented in Sec. 2.4.1. Beyond the low-energy peak, the spectrum only exhibits a quasiballistic contribution which shifts away from the low-energy contribution and its HET lies at $E_F + h\nu$. For excitation energies larger than the band gap of wurtzite GaN E_g = 3.44 eV [104], an intense peak is observed with an almost constant energy position. This contribution at fixed energy originates from the accumulation of electrons at the bottom of the Γ valley. On the high-energy side of the Γ peak, the quasiballistic contribution shows up as a shoulder which shifts with increasing $h\nu$. For $h\nu = 4.63$ eV, this hot-electron structure splits into two contributions: a fixed plateau (labeled L) which corresponds to electron accumulation in an upper conduction valley and a high-energy quasi-ballistic tail which goes on shifting with $h\nu$. These two electron contributions are more distinctly resolved at high excitation energy (e.g. $h\nu = 5.79$ eV) as the energy separation between the fixed L structure and the quasi-ballistic tail is larger.

2.3.4 Determination of the intervalley energy separation: Method #1

In Figure 30a, the extrapolated HETs of the structures observed in the DEDCs are plotted as a function of the excitation energy. For below-band gap excitation, the HET of the quasiballistic contribution ε_C closely follows the dashed line of unity slope, indicating that optical transitions occur in the BBR with initial states at E_F. For above-

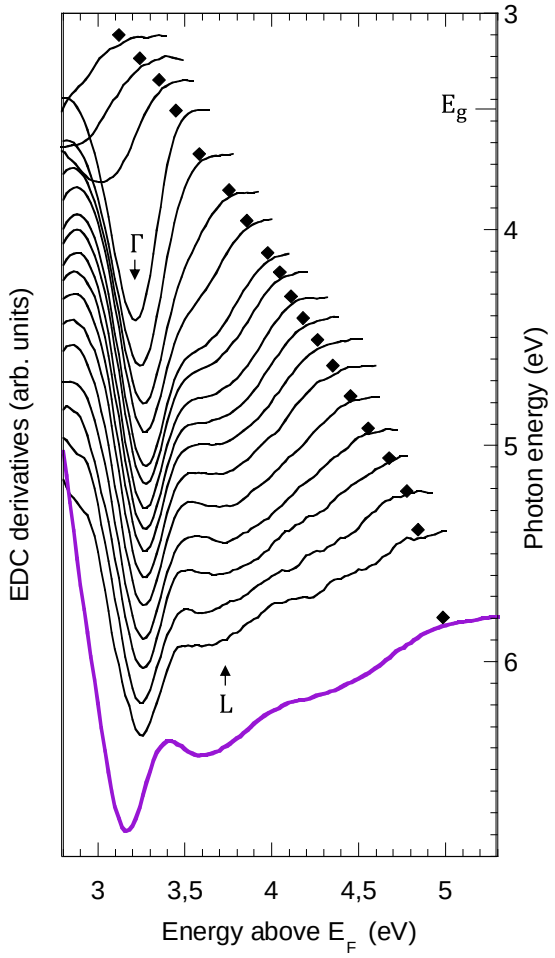

Figure 29 – Normalized DEDCs measured for different excitation energies: (in eV) 3.10, 3.21, 3.31, 3.45, 3.65, 3.82, 3.96, 4.11, 4.20, 4.31, 4.41, 4.51, 4.63, 4.77, 4.92, 5.06, 5.21, 5.39. The DEDC measured at $h\nu$=5.79 eV using a bandpass filter is plotted in violet. The baseline of the spectra is shifted according to light energy (right-hand scale). Above $h\nu$ = 4.63 ± 0.13 eV, the position of the L structure is fixed, while the high-energy threshold of the spectra (diamonds) shifts with the excitation energy.

band gap excitation, the variation of ε_C with $h\nu$ deviates from the line of unity slope because it corresponds to the final state of direct interband transitions from the heavy-hole band for which the excess energy, $h\nu - E_g$, is shared among electrons and holes according to their respective effective masses. The full line represents the calculated variation of the final state for optical transitions from the heavy-hole band, assuming parabolic bands with effective masses $m_e^* = 0.22m_0$ for electrons and $m_{hh,z}^* = 1.58m_0$ for holes. Taking E_F = 60 meV above the valence band maximum, this curve fits well with the experimental variation of ε_C up to $h\nu \sim$ 4.5 eV. The deviation between

calculation and experimental values observed at higher excitation energy is due to the nonparabolicity of the bands away from the Γ point [105,106]. The extrapolated HETs of the Γ and L contributions, Γ_{HEE} and L_{HEE}, exhibit fixed positions from which a Γ-L separation of $\Delta E_{\Gamma,L}$= 0.92 ± 0.08 eV is deduced, with an uncertainty that takes into account the spectrometer resolution. Note that, due to the overlap of the different contributions, the extrapolated HETs slightly overestimate the absolute bulk energy position of Γ and L (for instance Γ_{HEE} lies at 3.61 ± 0.08 eV above E_F ,while Γ is expected at 3.38 eV above E_F). A similar effect was also observed in GaAs at room temperature [97]. However, this should not significantly affect the measurement of the relative position of Γ and L.

2.3.5 Determination of the intervalley energy separation: Method #2

In the following a data analysis procedure is used which allows to independently determine the optical threshold for populating the L valley by phonon-assisted intervalley transfer. From the value of this threshold, the energy position of the L valley minimum is straightforwardly deduced. This procedure consists in tracking the intercepts of the high-energy slope of DEDCs with three arbitrary ordinates, Y_1, Y_2, and Y_3, as shown in Figure 31. (This analysis is effective

In the following analysis the data corresponding to the measurement with the bandpass filter are not included.) The variation of the intercept energies E_1, E_2, and E_3 versus photon energy is plotted in Figure 30b. The intercept energy E_1 remains constant since Y_1 only crosses the Γ structure for $h\nu \geq E_g$, while the intercept energy E_3 constantly increases with $h\nu$ since it corresponds to quasiballistic electron emission. The intercept energy E_2 initially increases with photon energy similarly to E_3, i.e., to the quasiballistic contribution. It then reaches a stable value indicating electron transfer and accumulation in the L valley. (Note that this data analysis procedure is effective for a roughly constant ratio of the peaks Γ and L of the DEDCs. Such ratio is almost constant for the set of measurements done using the monochromator (black curves), but is quite different for the DEDC obtained using the bandpass filter (violet curve). Therefore, the latter measurement is not considered in the present analysis, which however corresponds to a photon energy well above the optical threshold for intervalley transfer in the L valley. The reason why the L/Γ peak ratio is quite larger at $h\nu$=5.79 eV may be due to a more efficient population of the L valley at high photon energy, if a larger fraction of hot

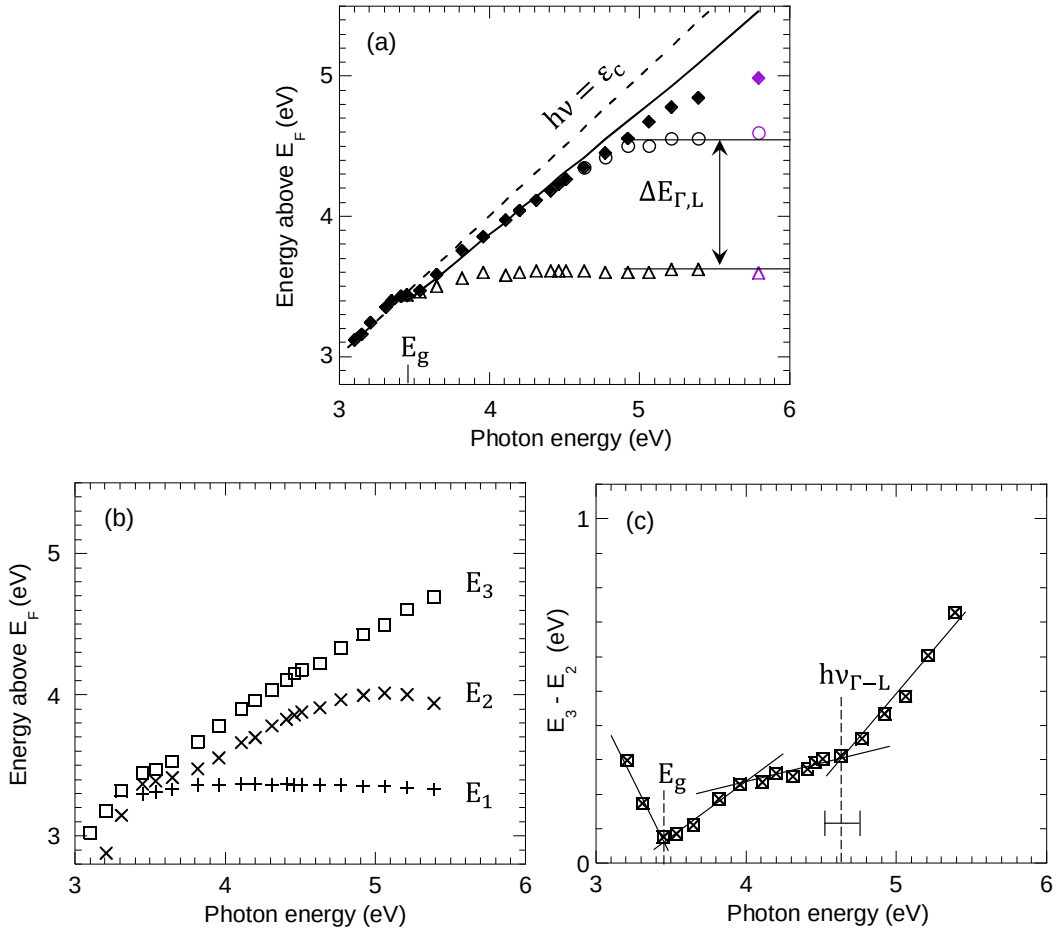

Figure 30 - Energy position above the GaN Fermi level of different features seen in derivative spectra as a function of the excitation energy. (a) High-energy extrapolation of different contributions in DEDCs: Γ peaks (Γ_{HEE}, triangles), L peaks (L_{HEE}, circles), and the high-energy threshold of DEDCs (ε_C, diamonds). The variation of the transition final state energy calculated from the parabolic band approximation (m_e^*= 0.22m0, $m_{hh,z}^*$= 1.58m0) is plotted as a full line. The extrapolations of the DEDC measured at $h\nu$=5.79 eV using a bandpass filter are plotted with violet markers. (b) Variation vs. $h\nu$ of E_1, E_2, and E_3, the intercept energies of DEDCs high-energy slopes with $Y_1 = -0.8$, $Y_2 = -0.4$, and $Y_3 = -0.1$ (in arbitrary units; see Figure 31). (c) Variation of $E_3 - E_2$ as a function of $h\nu$. The kinks indicated by the vertical dashed lines correspond to the photon energy threshold for populating the Γ and L valleys.

electrons is scattered to the L valley [107] or if direct interband transitions at the L point are allowed for this excitation.)

The difference between E_3 and E_2 is plotted in Figure 30c as a function of $h\nu$. Two kinks are observed at $h\nu$ = 3.45 eV and 4.63 eV corresponding to the excitation energies where the intercept energy E_2 deviates from the variation of E_3, which is characteristic of the ballistic electron behavior. The first kink at $h\nu = E_g$ is due to the transition from below to above-band gap excitation and corresponds to electron accumulation in Γ. The second kink at $h\nu$ = 4.63 ± 0.13 eV corresponds to electron transfer and accumulation in the L valley and directly gives the optical threshold $h\nu_{\Gamma,L}$ for the activation of the Γ-L intervalley transfer. The measured value of $h\nu_{\Gamma,L}$ is close to the one of 4.51 ± 0.05 eV determined by Wu *et al.* [68]. A more recent UV pump/IR probe spectroscopy experiment on UID GaN, similar to that carried out by Wu *et al*. but with higher precision in proximity of the Γ -L transition, gave $h\nu_{\Gamma,L} = 4.62 \pm 0.03$ eV (S. Marcinkevicius, KTH Sweden, private communication, 2016).

From the value of $h\nu_{\Gamma,L}$ measured by PES an independent determination of the energy position of the L valley can be obtained. Using the parabolic band approximation, the conduction final state energy for $h\nu$ = 4.63 eV is estimated to be 1.04 eV above Γ. Then, taking the intervalley phonon energy as 92 meV, it is deduced 0.95 ± 0.13 eV for the position of L above the CB minimum. This estimation can be refined by taking the measured value of the highest possible optical transition final state ε_C , i. e. the HET of the EDC, which accounts for the actual band dispersion including non-parabolicity. At $h\nu_{\Gamma,L}$ = 4.63 eV, we obtain ε_C = 4.35 eV above E_F, that is 0.97 eV above Γ. Considering the emission of an intervalley phonon of energy 92 meV, it is deduced 0.88 ± 0.13 eV for the position of the L valley above Γ, which is consistent with the value of $\Delta E_{\Gamma,L}$ that was obtained from the extrapolation of the Γ and L structures. Note that this procedure is quite robust and the result is unchanged when choosing other values of Y_1, Y_2 and Y_3 within a reasonable range (typically ±0.05 in the scale of Figure 31).

2.3.6 Concluding remarks

In summary, a photoemission spectroscopy study of wurtzite p-GaN was carried out to determine important CB parameters. With a fine tuning of the excitation energy, the derivatives of the photoelectron EDCs exhibit two structures with fixed energy positions that are attributed to the emission of electrons accumulated in two different CB valleys, namely the Γ valley and the first satellite valley, assumed to be L.

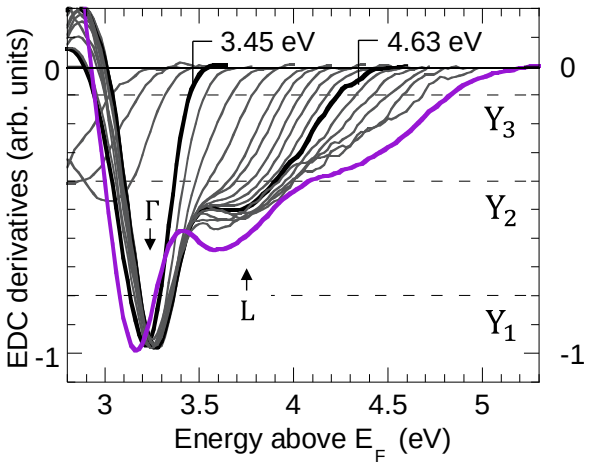

Figure 31 - Superimposed DEDCs from Figure 29. Y_1, Y_2 and Y_3 are arbitrary ordinates used to track the displacement of different DEDC features as a function of photon energy.

Some authors remarked that the observation of an accumulation point above the CB minimum in PE spectra could in principle also correspond to a local increase in the DOS of the Γ-valley [60]. However, it should be noted that such feature would play, in terms of hot electron transport, a similar role to that of a satellite valley. A conclusive identification of the nature of the observed accumulation point would be given by measurements with a resolution in k-space, such as angle-resolved photoemission spectroscopy (ARPES). ARPES spectra consist in maps E(θ) of the electron kinetic energy vs. the polar angle at which the electrons are emitted from the sample. A model based on energy and parallel momentum conservation may allow relating the maps E(θ) to the band structure ε(k) of the crystal. Moreover, by rotating the azimuthal angle ϕ, the dispersion along different crystallographic directions parallel to the surface plane may in principle be studied. ARPES measurements on p-GaN/Cs surfaces were attempted in collaboration with the group of Luca Perfetti at the FEMTOARPES facility of the synchrotron SOLEIL [108] but have not led to conclusive results yet due to the following encountered difficulty. PES of semiconductors activated to NEA requires applying a bias between the sample and the analyzer in order to collect the electrons emitted at low energy. This bias in turn creates an electric field region which perturbs the electron trajectory causing a distortion of the ARPES spectra. Future studies may bypass this problem using two-photon pump-probe ARPES [109,110], which would avoid the need of cesiating and applying a bias to the sample.

Concerning the influence of the Cs activation layer on the near-band-gap PES measurements two remarks can be done. First, the Cs activation layer does not modify the final state energy of the most energetic photoelectrons as the same spectral HET is measured in an uncesiated p-GaN sample ($h\nu$=4.9 eV, see Figure 97). Second, it is excluded that the observed optical threshold for the population of the high-energy state named "L" is due to transitions induced by surface states related with Cs, since the same $h\nu_{\Gamma,L}$ is observed in pump-probe experiments on unintentionally doped (and uncesiated) n-GaN.

From the PES measurements presented here, two independent determinations for the Γ-L separation were obtained: 0.92 ± 0.08 eV is directly measured as the distance between the high-energy extrapolation of the Γ and L structures, while 0.88 ± 0.13 eV is deduced from the excitation threshold at which the fixed L structure shows up. The above direct consistent measurements allow to establish the L valley position in wurtzite GaN at $\Delta E_{\Gamma,L}$ = 0.90 ± 0.08 eV above the CBM.

This value confirms previous indirect experimental estimates, described in Sec. 1.4, but contrasts with the much higher theoretical predictions provided by ab initio calculations. The large discrepancy between theory and experiments remains unsolved. My competences do not allow a critical analysis of the typical assumptions made in ab initio calculations, but one could think that the disagreement may originate from a mismatch between the ideal theoretical systems and the real nitride materials that are experimentally investigated. It also has to be noticed that the determination of the band structure of solids by ab initio calculation is known to be much more problematic for the conduction states than for the occupied states; for many materials, ab initio calculations indeed exhibit large discrepancies in the empty states energies while valence states energies are much more convergent.

In conclusion, the value of $\Delta E_{\Gamma,L}$ in GaN determined by PES is in agreement with the energy separation of the two high-energy peaks, labelled ① and ② in Figure 16a, observed in LED EE [53] ($\Delta E_{1,2}$ = 0.95 ± 0.1 eV). However, comparing the absolute energy position of the HETs of ① and ② with L_{HEE} and Γ_{HEE} determined by PES is not straightforward since these LED peaks exhibit very large shifts as a function of bias (Figure 16b), whose origin will be analyzed in Sec. 2.5.

2.4 Anomalous photoemission effects in GaN

In the above photoemission study of the p-GaN band structure, below band gap photoemission was shown to occur, leading to the emission of ballistic photoelectrons at energy $h\nu + E_F$, lower than the bulk CBM energy level. This phenomenon was already observed [102] but its origin is still not established. Possible photoelectric processes that could generate below-gap photoemission in p-GaN are Franz-Keldysh (FK) absorption in the strong electric field of the BBR, absorption from surface states or from impurity bands in the gap of the bulk crystal. It is important to identify the origin of below-gap photoemission because this process may play a role in the electro-emission of InGaN/GaN LEDs, since in these experiments light below the band gap of GaN is present due to radiative recombination in the quantum wells of the device. Here we will show through an extensive characterization that below band gap photoemission is a complex process that may produce "super-energetic" photoelectrons with emission energies well above the expected threshold $h\nu + E_F$ for excitation at $h\nu$ (Sec. 2.4.1). Then in order to study the influence of LED light in LED electro-emission experiments a combination of different electro-emission and photoemission experiments will be carried out (Sec. 2.4.2).

2.4.1 Below bandgap photoemission studies of cesiated p-GaN surfaces

In the present section the PE processes of bare p-GaN surfaces (i.e. without the p-contact grid, as in Figure 19b) are presented. The bare surface allows excluding any contribution due to metal PE in the EDCs. The main sample studied in the following is a p-n junction structure () grown on c-plane sapphire at UCSB by MOCVD and consists of: p+ GaN cap/p-GaN (1 µm, [Mg] = $2\cdot10^{19}$ cm^{-3})/AlGaN barrier (15 nm, [Mg] = $2\cdot10^{19}$ cm^{-3}, [Al] ~20%)/p-GaN (10 nm, [Mg] = $2\cdot10^{19}$ cm^{-3})/n-GaN (1 µm, [Si] = $5\cdot10^{18}$ cm^{-3}). The AlGaN EBL and the 1 µm thick p-GaN layer are used to prevent electron emission originating from possible absorption processes in the n-GaN layer. Experiments are performed on cesiated surfaces at below-gap excitation as a function of different parameters (such as exciting photon energy, excitation power, p-GaN surface) revealing the occurrence of a "super-energetic" photoemission process (Sec. 2.4.1). A few complementary measurements showing that a similar anomalous photoemission process may also occur in above-gap excitation are presented, while for a full account of these studies the reader is referred to Appendix 5.3. Finally, a summary of the various

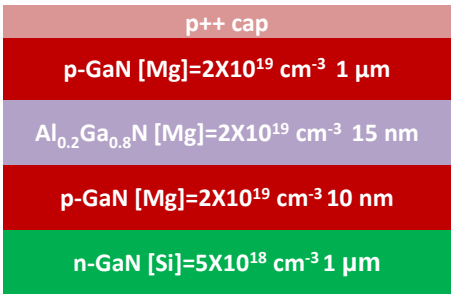

Figure 32 – Schematic of the main p-n junction structure studied in the below-gap photoemission spectroscopy experiments reported in this subsection.

observations related to the process creating "super-energetic" photoelectrons in p-GaN is given (Sec. 2.4.1.1).

In the first experiment, whose results are summarized in Figure 33, light from a Kr/Ar laser source (filtered to eliminate plasma emission from the laser) is shined on the cesiated p-GaN surface of the p-n junction structure described above at a photon energy of 2.71 eV, similar to the emission peak of blue LEDs. The main difference with respect to the below-gap PE measurements described in Sec. 2.3 and done with a weak excitation power of the order of 10 µW (focused lamp spot diameter ~500 µm) is that in the following study a larger laser power range is investigated, between ~100 µW and ~10 mW (with a focused beam diameter of ~200 µm).

PE spectra measured at different external optical powers $P_{ext,PE}$ (see Figure 41) shined on the sample are shown in Figure 33a-d. At a power of 0.10 mW a single contribution is observed with a HEE close to $h\nu + E_F$, thus exhibiting a behavior similar to that of "well-behaved" below-gap PE. However, increasing the power by only few 100 µW, a high-energy shoulder starts to appear and at 2.30 mW a distinct high-energy peak is clearly observed with a high energy tail extending over about 1 eV above $h\nu + E_F$. In other words, a considerable fraction of the spectrum (shadowed area of Figure 33c) is emitted well above the expected threshold for ballistic electron emission: these "super-energetic" photoelectrons, appearing at an optical power density of the order of 1 W/cm^2, originate from an unexpected and anomalous PE process in p-GaN which, to the best of the author's knowledge, has never been reported in the literature, at the exception of Ref. [111], which will be discussed later (Figure 37). A further increase of $P_{ext,PE}$ to several mW changes the relative ratio between the two contributions and slightly shifts the position of both peaks towards higher energy (Figure 33d), with a logarithmic dependence on power (Figure 33e).

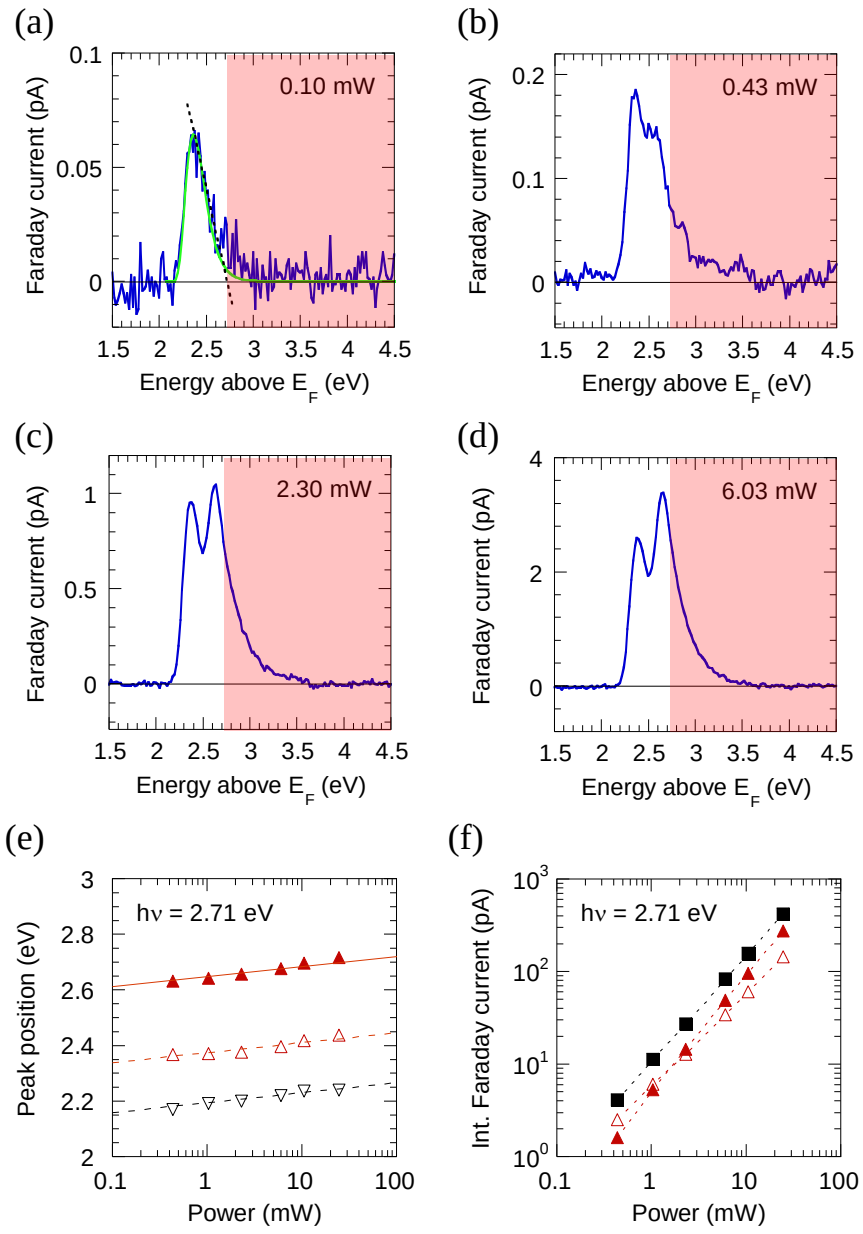

Figure 33 – (a)-(d) PE spectra measured at different excitation powers on the GaN p-n PE sample at $h\nu$ = 2.71 eV. The shadowed regions highlight the super-energetic fraction of the electron distribution emitted above $h\nu + E_F$. (e) Energy shift of the maxima of the low- (empty red triangles) and high- (filled red triangles) energy peaks as a function of power. The shift of the low-energy onset (vacuum level) is also shown (black triangles). Lines correspond to logarithmic fits. (f) Power dependence of the integrated current of the low- (empty triangles) and high- (filled triangles) energy peak, and entire spectrum (squares). Dashed lines are guides to the eye. To separate the two contributions the lineshape shown as a green curve in (a) is used for the low-energy peak.

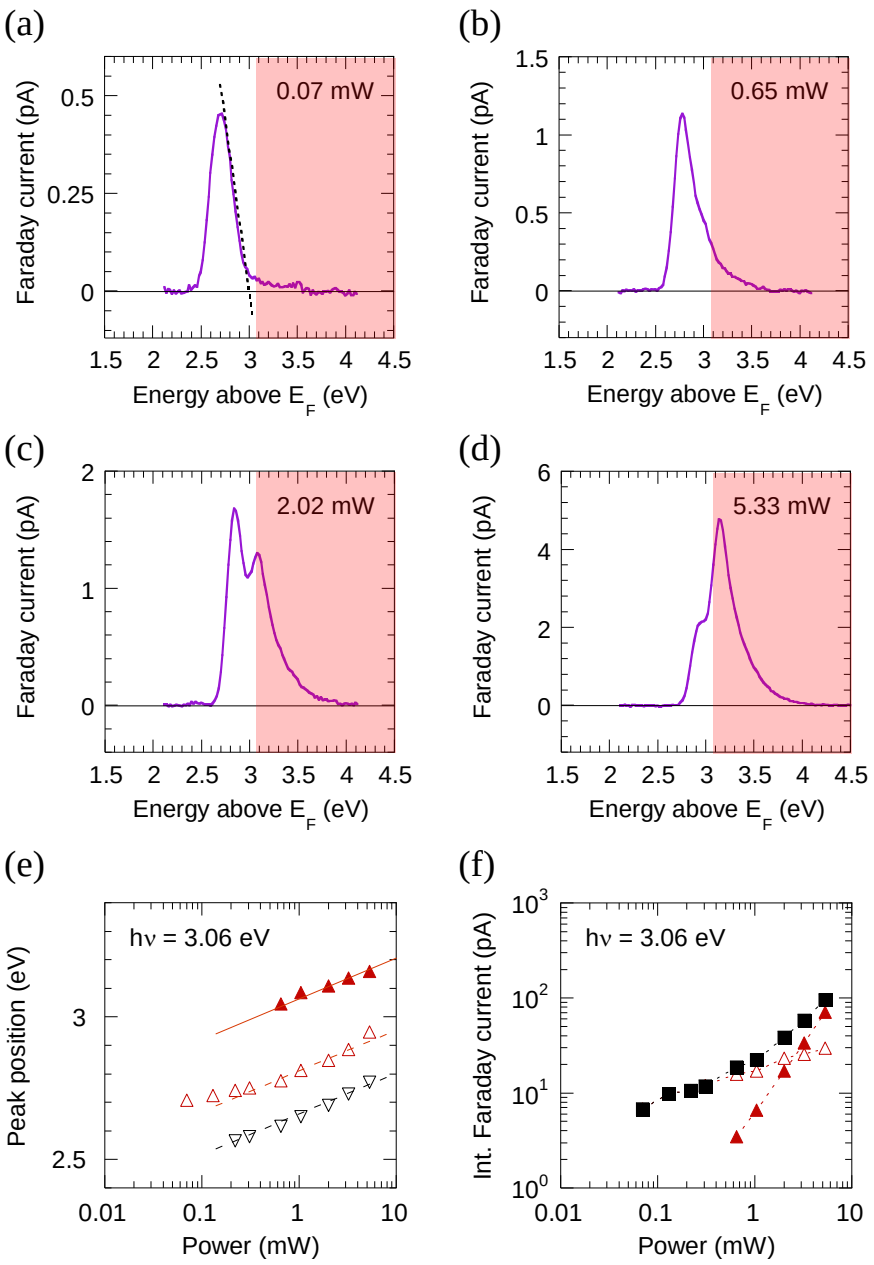

Figure 34 – (a)-(d) PE spectra measured at different excitation powers on the GaN p-n PE sample at $h\nu$ = 3.06 eV. (e) Energy shift of the maxima of the low- (empty red triangles) and high- (filled red triangles) energy peak as a function of power. The shift of the low-energy onset (vacuum level) is also shown (black triangles). (f) Power dependence of the integrated current of the low- (empty triangles) and high- (filled triangles) energy peak, and entire spectrum (squares). To separate the two contributions the EDC shown in (a) is used for the low-energy peak.

This logarithmic shift and the energy separation of the two peaks may be related to a SPV effect, which was observed in Ref. [112] to cause surface potential shift of several 100 meV in similar irradiation conditions as those used here. Assuming a lineshape for the low-energy peak (corresponding to the green curve of Figure 33a), a separation of the two contributions of the PE spectra can be estimated. The integrated current of each peak as a function of $P_{ext,PE}$ is shown in Figure 33f. The relative intensities of the two PE contributions change with power and the high-energy peak dominates at high $P_{ext,PE}$. The overall efficiency of these PE processes is small, corresponding to a QY of only 3-$5 \cdot 10^{-6}$, as calculated from the total emitted cathode current (measured analyzer transmission 1.5%) and the incident power on the sample (Eq. (7)) in the range between few 100 µW and few 10 mW.

Below-gap PE at hν = 2.71 eV can then be compared with similar measurements done on the same p-n junction sample at hν = 3.06 eV (larger than the emission photon energy of blue LEDs and still below the energy gap of GaN) and presented in Figure 34. (The annealing temperature during the surface preparation was not the same in the two series of measurements and is at the origin of the difference in the low-energy onset of the spectra, which however is secondary in terms of the present analysis.)

Qualitatively the same results are obtained at hν = 3.06 eV: at low power a single peak with HEE close to $h\nu + E_F$ is observed (Figure 34a), then increasing $P_{ext,PE}$ a super-energetic contribution appears (Figure 34b,c) and finally dominates the spectrum (Figure 34d). The two peaks shift towards high energy with an approximate logarithmic dependence on $P_{ext,PE}$ for both excitation photon energies (Figure 33e and Figure 34e). This shift follows the shift of the vacuum level. The slope of the logarithmic shift is about twice larger at hν = 3.06 eV, being coherent with a SPV effect which as well increases with hν in this range (see Fig. 2b in Ref. [112]). Correlatively, an increase in the electron emission yield with hν is observed, which is due to the difference in the intensity dynamics of the two peaks as a function of $P_{ext,PE}$ (Figure 33f and Figure 34f). Indeed, the intensity of the low-energy contribution increases sub linearly due to the SPV which progressively crops the low energy edge of the peak, while the intensity of the high energy peak increases super-linearly.

It has to be noticed that the shift (and quantum yield decrease) of the low-energy ("well-behaved") peak is only apparent and reflects the shift of the vacuum level. Therefore, its HET does not shift (although it is difficult to precisely follow its position as a function

of light power). This is consistent with a bulk state origin of this contribution to the photoemission spectrum. On the contrary, the high energy ("super-energetic") peak

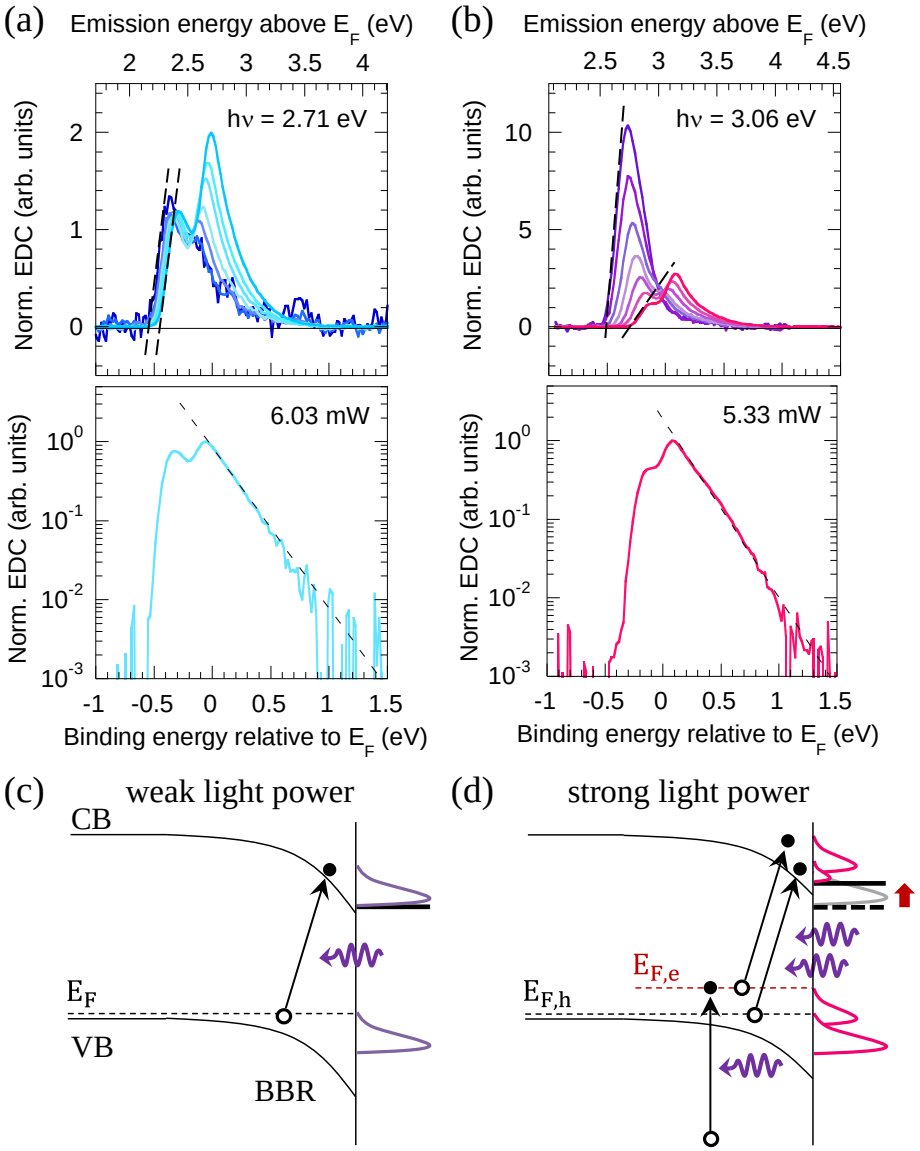

Figure 35 – PE spectra measured on the GaN p-n sample for two below-bandgap excitation energies and different powers. (a) *hν* = 2.71 eV, powers in mW: 0.20, 0.43, 1.04, 2.30, 6.03, 10.51, 24.80; (b) *hν* = 3.06 eV, powers in mW: 0.22, 0.31, 0.65, 1.04, 2.02, 3.24, 5.33. EDCs are normalized to the incident photon flux and are plotted as a function of the measured electron emission energy (top scale) and the deduced binding energy (bottom scale). Logarithmic plots of the spectra recorded for the two excitation energies at similar incoming power are also shown. (c)-(d) Schematics of the qualitative model proposed to describe the modifications of "well-behaved" below-gap PE spectra, as in (c), in presence of SPV effects (d).

entirely shifts with the SPV. Therefore, the separation between the HET of the low and high energy peaks is not fixed and changes as the SPV with light power and energy.

It also has to be noticed that, although the super-energetic peak extension is similar to the Γ-L separation measured in the above bandgap photoemission experiments, this similarity should be fortuitous. The behaviours of the super-energetic peak and of the L-valley feature are indeed different. While the super-energetic peak shifts with light power and energy, the energy position of the L-valley feature remains fixed. This indicates that the super-energetic electron photoemission and the L-valley feature are of different nature.

In Figure 35a,b the power series of the PE spectra measured at hν = 2.71 eV and hν = 3.06 eV are plotted as normalized to the incident photon flux. With such normalization, if the spectra were scaling linearly with the optical power all EDCs should perfectly overlap. Conversely the change in the series of spectra indicates that the electron distribution is modified according to the excitation condition. Two energy scales are shown: the emission energy (upper x-axis), which corresponds to the standard energy reference used throughout this thesis for the emitted electrons, and the binding energy (lower x-axis), which corresponds to the energy of the initial states, i.e. prior to photoexcitation, and is obtained by subtracting hν from the emission energy. Plotting the EDCs as a function of the binding energy is a common practice in x-ray and UV PES, mainly sensitive to the occupied (or initial) states, and the underlying assumption in presenting the spectra with this energy reference is that photoelectrons are rapidly emitted into vacuum after excitation with negligible energy relaxation in the CB.

From Figure 35a,b it can be noticed that the range of emission energy of the spectra measured at hν = 2.71 eV and hν = 3.06 eV varies considerably but the range of binding energies is essentially the same. This suggests that the two series of spectra originate from similar initial states: a low-energy distribution with negative binding energy observed even at low excitation power, and a high-energy peak that appears above E_F when increasing the power. A qualitative description of the photoelectric processes involved can be formulated on the basis of the work of Yablonovitch *et al.* [113], who studied the effect of SPV on the quasi-Fermi levels of an n-GaAs surface. At very low excitation power the PE process from the cesiated p-GaN surface can be schematized as in Figure 35c: the electronic states are at equilibrium and "well-behaved" photoexcitation takes place from initial states lying below E_F. However, at larger power,

minority carriers accumulation at the surface occurs (unless the surface recombination velocity of the photocreated e-h pairs is fast enough to compensate it) which tends to flatten the bands. This situation is best described by the hole and electron quasi-Fermi levels, $E_{F,h}$ and $E_{F,e}$, respectively, shown in Figure 35d. In this representation, the photoexcitation of electrons from $E_{F,e}$ could give rise to an additional contribution appearing at higher energy than that excited from $E_{F,h}$. (Note that the model assumes that the Fermi level of the p-contact of the sample, used as the energy reference in the EDCs, is at equilibrium with $E_{F,h}$.) The effect of SPV on the PE spectra of p- and n-GaP surfaces, covered by a 6 Å Ag film, was studied by Alonso *et al*. in Ref. [114]. In the case of the p-type surface the electron emission from the Ga 3d core level and from the ultra-thin silver layer was observed at higher energy than the emission from a gold reference and was attributed to SPV occurring in the BBR of the semiconductor. An important difference with respect to the result of Alonso *et al*. is that here both the "well-behaved" and the "super-energetic" contribution can be distinctly observed.

A feature of this scheme is that it can explain the simultaneous high-energy shift of the low- and high-energy peak observed at increasing excitation power (Figure 33e and Figure 34e). Indeed, as $E_{F,e}$ rises due to SPV, the position of the vacuum level should increase and, as schematized in Figure 35d, the first effect will cause a shift of the high-energy peak and the latter will cause an increase of the vacuum level position and a progressive cut of the low-energy peak. Moreover, as the SPV is larger at $h\nu$ = 3.06 eV, these effects are most noticeable in the spectra of Figure 35b. It has however to be noticed that the SPV-induced shift of the super-energetic peak is very moderate for $h\nu$ = 2.71 eV: it is of the order of 100 meV for an incident power densities ranging over two orders of magnitude between 0.03 and 3 W/cm^2.

These observations suggest that the emitted electron peaks originate from states in the gap. The low-energy contribution exhibits a rather fixed HEE at $h\nu + E_F$ while its low-energy cut-off by the vacuum level shifts with the SPV. This indicates that it is related to initial states which lie below the Fermi level and which are not anchored to the surface. Since the high-energy contribution shifts with power in the same way as the vacuum level it is very likely to originate from a surface state shifting with the surface potential.

It has to be noticed that the lineshape of the super-energetic peak is very specific and interestingly does not depend on the excitation energy (at least for the two laser energies

used here which differ by 0.35 eV one from the other) nor on light power. The high-energy tail exhibits, for both photon energy, an exponential decay (as shown on the logarithmic plots of the EDCs in Figure 35a,b) with a characteristic decay energy of about 200 meV (which is almost an order of magnitude larger than the lattice temperature). Note that, defining the HET in this case is somewhat problematic but with the present experimental sensitivity the tail is found to extend at least over more than 1 eV. In contrast, the low-energy edge appears to be quite sharp which indicates a well-defined onset which is not determined by the vacuum level cut-off (which lies well below the high energy peak onset for the two photon energies used here) but rather by the gap states from which electron are excited.

Another intriguing feature of this "anomalous" photoemission mechanism is its quite high efficiency considering that it is a nonlinear two-step process which requires populating electronic gap states lying well above the Fermi level from which will be emitted photoelectrons excited with below bandgap light of very moderate power density. It is not clear which absorption mechanism would generate enough electrons to explain the observed signals.

In principle, the emission process of super-energetic photoelectrons may be related to the filling of specific surface states characteristic of a given crystal orientation of GaN.

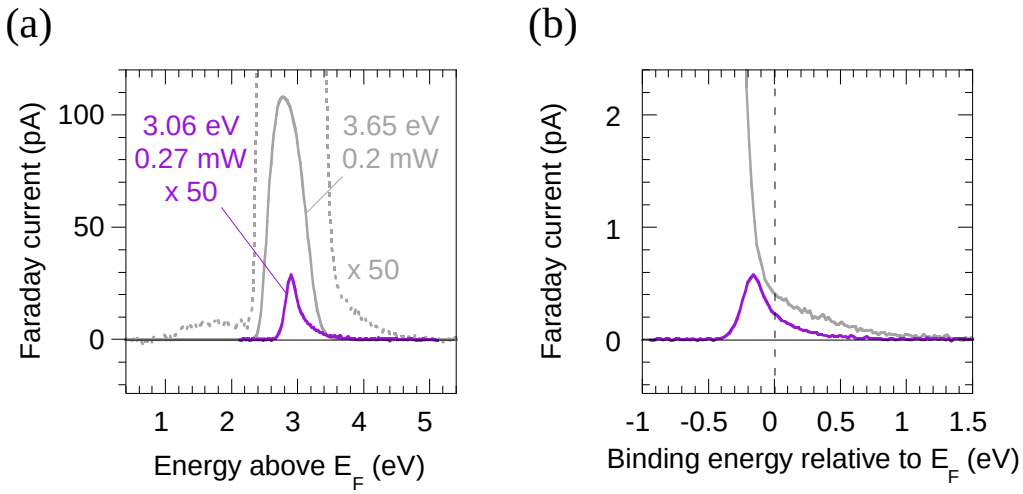

Figure 36 – PE spectra measured on a m-plane p-n PE sample at above- and below-gap excitation. EDCs are plotted as a function of: (a) the measured emission energy; (b) the deduced binding energy. In both measurements in (b) a high-energy tail of initial states extending above E_F can be observed, being at the origin of super-energetic PE in (a).

However, the same effect is observed in a non-polar GaN p-n structure grown on m-plane by MOCVD (200 nm thick p-GaN, [Mg] $\sim 2 \times 10^{19}$ cm^{-3} in the bulk and overdoped in proximity of the surface): in below-gap excitation (laser diode at $h\nu$ = 3.06 eV, 0.27 mW) a large fraction of the EDC extends above $h\nu + E_F$ (Figure 36a). Super-energetic electron emission can also be observed for above-gap excitation. Exciting at $h\nu$ = 3.65 eV (broadband light source + 340 nm filter with 11 nm passband bandwidth, 0.2 mW) the main peak, which originates from absorption in bulk p-GaN, exhibits a HET at 3.44 eV above E_F (Figure 36a), close to the value of 3.58 eV above E_F obtained by near-band gap PES at the same excitation (Figure 30a). (The small discrepancy may be due, in addition to the precision of the spectrometer, to a difference in the position of E_F within the band gap caused by the different p-type doping concentration of the two samples.) However, a super-energetic tail is observed ("×50" dashed gray line in Figure 36a), being much weaker than the main peak. In Figure 36b the PE spectra measured at above- and below-gap excitation are plotted as a function of the binding energy and it can be noticed that:

- the super-energetic tails extend over a similar binding energy range for both excitation energies, suggesting that these contributions possibly originate from the same initial states extending over about 1 eV above E_F;
- the intensity of the super-energetic contributions is almost the same for comparable excitation powers (differing by about a factor of 2), suggesting that the efficiency of the super-energetic photoemission process does not vary much between the considered below- and above-gap excitation. This is coherent with the interpretation of this phenomenon as caused by SPV, which is also expected to weakly vary among these values of $h\nu$ (Fig. 2b in Ref. [112]).
- the finite rejection of the electron spectrometer and the stray light due to scattering in the rotator (especially when using a rather broad beam) are however often responsible for small ghost contributions on the spectrum edges (on the low or high energy side), as can be seen in Figure 36b on the spectrum recorded with above bandgap excitation; these contributions are orders of magnitude smaller than the main photoemission peak but comparable with the super-energetic feature, making uncertain the evidence of a superenergetic feature for CW above bandgap excitation.

To the best of the author's knowledge, the only observation of anomalous PE effects in p-GaN/Cs that was reported in the literature so far is that of Yater *et al.* [111]. The EDCs obtained in two different measurements at above-gap excitation using a pulsed laser (Nd:YAG, 5 ns pulses, 15 Hz repetition rate, $h\nu$ = 3.49 eV) are reproduced in Figure 37. Yater *et al*. commented as follows:

> *In some measurements, a single peak was present (open circles) while in others a double-peaked distribution was observed (filled circles). In the latter case, the two peaks exhibited different behavior in subsequent measurements, with the lower-energy peak remaining fairly stable while the higher-energy peak shifted upwards over time. The cause of this anomalous behavior needs to be better understood. Specifically, we need to examine whether other features (such as surface or gap states) are being probed by the laser and whether the pulsed nature of the laser is affecting the electron generation and transport processes in the material.*

A feature of the spectra that was not explicitly discussed by the authors, but probably is the most surprising, is that a large portion of the spectra extends above $h\nu + E_F$ (here highlighted as the shadowed region in Figure 37), i.e. it is super-energetic. However, it has to be noticed that the spectra of Figure 37 exhibit a very symmetric line shape while a sharp low energy cut off by the vacuum level is usually expected. No information is given in Ref. [109] on the resolution of the spectrometer which could help understanding the observed line shape and width. Moreover, one should note that the

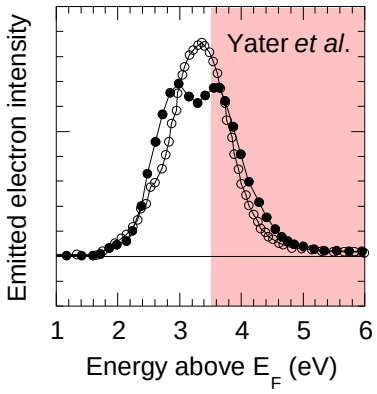

Figure 37 – PE spectra reproduced from Ref. [111] for pulsed above-gap excitation at $h\nu$ = 3.49 eV of a p-GaN/Cs surface. In the same conditions some measurements presented two peaks (filled circles) and others a single peak (empty circles). In both cases super-energetic PE was observed (shadowed region).

excitation conditions used in Ref. [111] are different from those of the present experiments, which employed CW laser sources in below-gap PE and a CW broadband light source in above-gap PE. Therefore, on the basis of our measurements, it can be stated that super-energetic photoemission can be observed for light excitation sources in CW operation but it is not clear if the origin is the same than the phenomena reported by Yater *et al.*, also keeping in mind the different lineshapes. Extensive PE experiments carried out with a pulsed laser in above-gap excitation are presented in Appendix 5.3, but for an uncesiated p-GaN surface.

The dependence of super-energetic PE on the doping concentration of p-GaN is studied on a series of four p-n samples grown by MOCVD with the structures schematized in Figure 38b. Three samples only differ in the Mg concentration (labeled "low", "mid", "high") of the 1 µm thick surface p-GaN layer, while the fourth one has a 10 nm p+ cap on top of the 1 µm thick p-GaN layer doped at the "high" level. The PE experiments are carried out exciting with a laser diode at $h\nu$ = 2.82 eV and a power of ~8 mW. The measured spectra are shown in Figure 38a. In all the samples, super-energetic photoelectrons are observed (shadowed region) indicating that the underlying process has not a sharp activation in the studied range of [Mg] and is always allowed. Of the three samples without p+ cap, the one with "low" doping gives the highest super-energetic PE signal, and increasing [Mg] progressively reduces the signal, as obtained

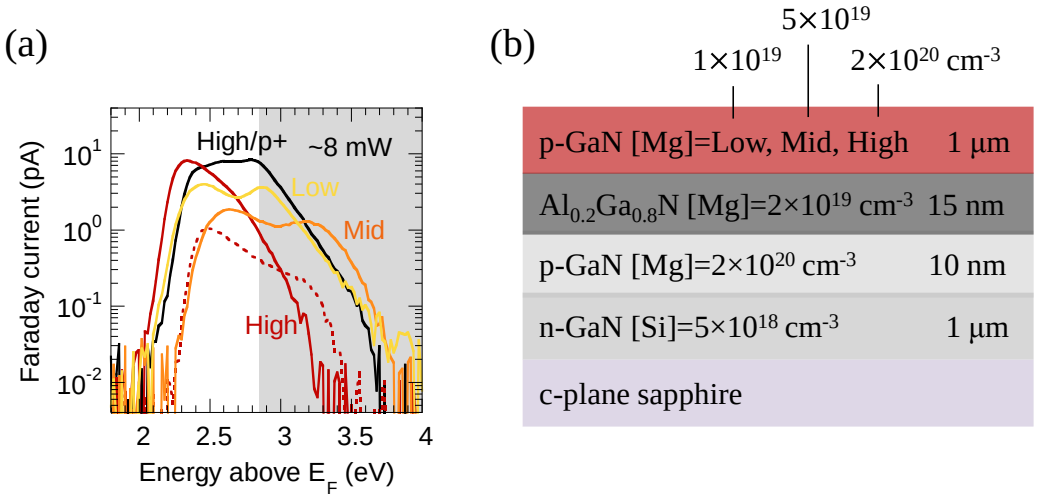

Figure 38 – (a) PE spectra measured at $h\nu$ = 2.82 eV and a power of ~8 mW on four p-n PE samples with the basic structure shown in (b) and differing in the "low", "mid", or "high" doping level and by the possible presence of a p+ cap. In all samples super-energetic PE is observed (shadowed region).

from the "mid" and "high" doping samples. However, the sample with "high" doping level and p+ cap exhibits the highest overall super-energetic signal. Therefore, no quantitative conclusions can be drawn on the net influence of the doping concentration on the efficiency of super-energetic PE. Moreover, the double peak shape is not always observed as shown for the highly-doped sample without cap.

Finally, one may wonder whether the super-energetic PE process is affected by the sample growth source and if it would occur also in commercial grade samples. To verify this, PE with laser excitation at $h\nu$ = 3.06 eV, below the band gap of GaN but above the band gap of the InGaN QWs, is carried out on a LED sample grown by Seoul VioSys (100 nm thick p-GaN) processed for PE. The series of EDCs measured at different powers in the range 0.1-0.9 mW is shown in Figure 39a. The lower x-axis corresponds to the cathode voltage applied between the p-contact of the sample and the analyzer in order to scan the electron energy distribution. The higher x-axis corresponds to the supposed electron emission energy above E_F obtained as usual from Eq. (5) using V_{cath} and taking E_{sel} = 4.62 eV for the set spectrometer resolution of 80 meV. As it will be explained, in this particular experiment the electron emission energy deduced from Eq. (5) is not correct.

At low excitation power a single peak is observed and increasing the power a second peak appears. This is reminiscent of the results obtained in the same experiments carried out on a p-n junction structure and shown in Figure 34a-d. However, all the EDCs lie below the HET expected for "well-behaved" below-gap PE exciting electrons to final states at $h\nu + E_F$ (marked as a dashed line). Moreover, increasing the excitation power, instead of observing a super-energetic contribution as in the p-n experiments (Figure 34a-d), the EDCs shift towards low energies. This is an artefact that is simultaneously due to the large access electrical resistance of p-GaN and to a photovoltage (PV) occurring in the active region of the LED. The first effect is illustrated in Figure 39d: upon photoemission, to maintain the charge balance in the sample, a hole current needs to be supplied to the photoexcited spot on the semiconductor, which is several mm away from the p-contact in these experiments. Due to the poor conductivity of p-GaN the path of minimum resistance passes through the highly conductive n-GaN layer (dashed trajectory in Figure 39d). The second effect is explained in Figure 39e: upon photoexcitation at a photon energy above the band gap of the InGaN QWs of the LED (a single QW, instead of 5, is drawn for simplicity) a PV builds up, leading to an energy difference $e\Delta V_{PV}$ between the quasi-Fermi levels in p- and n-GaN in correspondence of

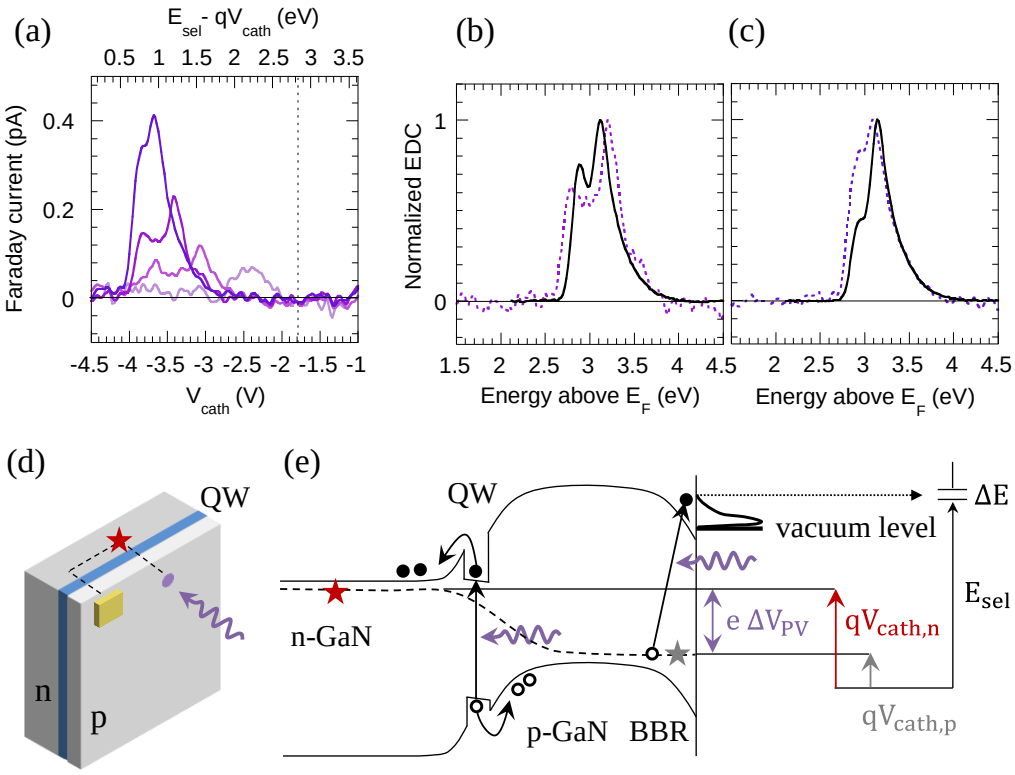

Figure 39 – (a) PE spectra measured on a LED PE sample excited at $h\nu$ = 3.06 eV. Powers in mW (from weakest to strongest spectrum): 0.10, 0.33, 0.60, 0.90. EDCs are plotted both as a function of the applied cathode voltage and the apparent electron emission energy as calculated from Eq. (5). (b)-(c) Comparison of PE spectra measured at $h\nu$ = 3.06 eV on the LED PE sample (dashed lines) and the p-n PE sample (full lines, already shown in Figure 34). EDCs are normalized to their maximum. LEDs curves are shifted by ~2 eV to correct for bulk PV. Excitation power in mW: (b) LED 0.6, p-n 3.24; (c) LED 0.9, p-n 5.33. (d) Schematic of the path of minimum resistance (dashed line) followed by the hole current supplied from the p-contact to the photoemitting spot in a LED structure upon excitation several mm far from the p-contact. (e) Schematic of the effect of bulk PV in an LED structure producing a potential difference across the junction in correspondence of the photoexcited region. The cathode voltage for the EDC measurement then depends on whether it is applied to n- or p-GaN.

the photoexcited region. As a combination of these two effects, the cathode voltage is applied between the analyzer and the quasi-Fermi level in n-GaN ($V_{cath,n}$) and, due to $e\Delta V_{PV}$, is more negative than if it were referenced to the quasi-Fermi level in p-GaN ($V_{cath,p}$). Ultimately this leads to an apparent shift of the EDCs towards lower electron emission energy and the magnitude of the shift increases with the strength of the PV.

Such shift does not occur in the previous PE experiments carried out on simple p-n structures because: 1) in excitation below the band gap of GaN the only sizeable absorption occurs at the surface and not at the junction; 2) in excitation above the band gap of GaN all the absorption occurs in the p-GaN layer, as this is typically at least 200 nm thick, more than the absorption length of above-gap light in p-GaN. Therefore, in neither case a PV is created at the junction of p-n structures.

The EDCs measured from the LED can be compared with those obtained from a p-n junction (Figure 34a-d). It is found that the PV correction shift to be applied to the LED spectra is $e\Delta V_{PV} \sim 2$ eV in order to match the energy range of the p-n spectra. The lineshapes obtained at different excitation powers in the LED and p-n structure (0.6 mW and 3.2 mW, respectively, in Figure 39b and 0.9 mW and 5.3 mW, respectively, in Figure 39c) are very similar, confirming that the same super-energetic PE process occurs also in commercial grade LED samples.

2.4.1.1 Summary of the observations on super-energetic photoemission in p-GaN

To summarize, an anomalous photoemission process generating "super-energetic" photoelectrons with emission energies well above the expected maximum threshold $h\nu + E_F$ for excitation at $h\nu$ was observed and characterized through extensive studies on different p-GaN surfaces. Results obtained in above-gap photoemission of pristine p-GaN surfaces are reported in Appendix 5.3. Here below are summarized the main characteristic of the process observed with below bandgap excitation.

- Electron emission energy: appearance as a broad peak which may extend beyond 1 eV above $h\nu + E_F$;
- Light source: observed exciting with CW laser (diodes, Kr/Ar, Ti:sapphire);
- Photon energy: observed for below-bandgap photoexcitation;
- Excitation power: observed for a power density in the range 0.1-1 W/cm^2 (photon irradiance 10^{17}-10^{18} s^{-1} cm^{-2}) with a logarithmic shift of the peak as a function of power;
- p-GaN surface: observed on cesiated surfaces grown on c- and m-plane, grown at UCSB and industrially, with Mg acceptor doping levels from $1 \cdot 10^{19}$ cm^{-3} to overdoped (p+ cap). No quantitative conclusions could be drawn on the influence of [Mg] on the intensity of the peak.

Several features of the process are an indication of SPV. A tentative scheme was proposed to explain the generation of super-energetic photoelectrons on the basis of an intrinsic multi-photon process associated with SPV effects causing a non-equilibrium between the electron and hole quasi-Fermi levels at the p-GaN surface.

In the following section, the possible occurrence of the observed super-energetic photoemission process in LED electro-emission experiments as potentially excited by the internal device electro-luminescence will be investigated by means of combined electro-emission and photoemission studies.

2.4.2 LED light effects in LED electro-emission

The fact that LED EE is carried out in standard LED operation, i.e. under electrical injection, obviously implies that LED light is present in the device during the experiments. Then, all the possible photoelectric effects occurring in the structure need to be characterized as these may contribute to the measured EE spectra.

The InGaN/GaN LED studied in Ref. [53] emits light in the blue range, well below the band gap of GaN. Different mechanisms could possibly produce below-gap photoemission (i.e. photoemission excited by photons of energy smaller than the band gap of the semiconductor) in the structure (see Figure 40).

- Absorption in the p-contact, could contribute to photoemission as in the usual photoelectric effect. (PE from the n-contact is not considered as in the geometry of the LED EE experiments this contact does not face the collecting aperture of the electron analyzer.) Due to the thickness of the p-contact (~100 nm), photoelectrons excited by LED light from the p-GaN/p-contact interface will not be emitted into vacuum due to their short inelastic mean free path (few nm [115]) caused by electron-electron collisions in the metal. Photoemission from the metal may occur if LED light shines on the surface of the p-contact, for instance due to reflections in the vacuum chamber.
- Franz-Keldysh effect, which corresponds to below band gap absorption caused by the overlap of the electron and hole wave functions in the presence of an

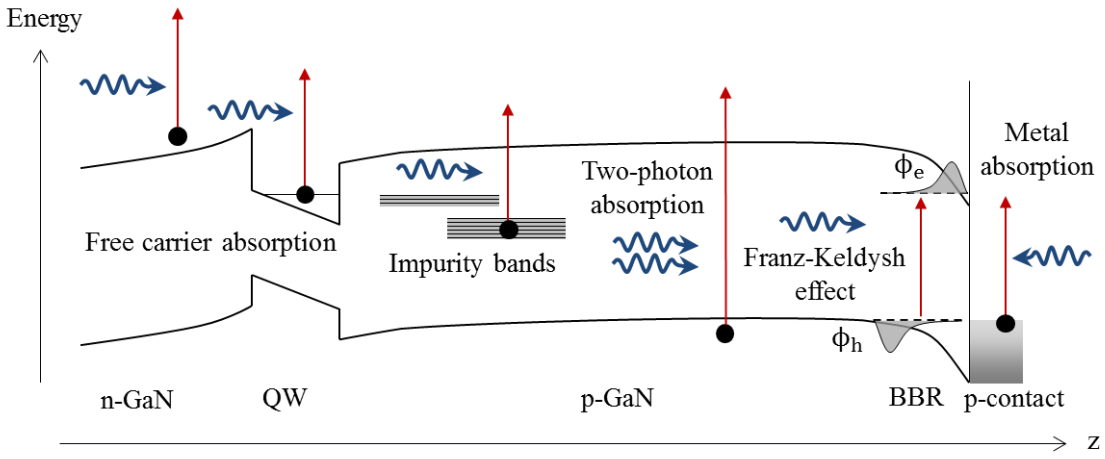

Figure 40 – Diagram showing different below-gap absorption mechanism that may occur in an InGaN/GaN LED structure excited by LED light. Not all the processes have a sizeable probability, as discussed in the text.

electric field, is likely to be produced by LED light in the strong electric field of the BBR (of the order of several MV/cm, taking the amplitude of the band bending as $\sim E_g/2$ and the depletion width of the BBR as few nm). Moreover, in this surface region photoelectrons have a high escape probability into vacuum, if excited above the vacuum level.

- Absorption from impurity bands can be induced in the band gap of p-GaN by acceptors and point defects. Impurity-related transitions are typically observed in Mg-doped GaN by luminescence in the red, blue and UV range [116]. However, photoemission from impurity bands may only occur if the corresponding states, normally empty, are populated by some mechanism. In addition to gap states in the bulk, surface gap states may also lead to below-gap photoemission. Different surface states may be observed in GaN, depending on the surface preparation condition [117].
- Free carrier absorption in n-GaN or in the QW region can be envisaged. Such excitation would lead to very low electron densities as, for concentrations of ~10^{18} cm^{-3}, the free carrier absorption coefficient is in the cm^{-1} range (as determined from measurements in laser structures and as calculated from first principles in Ref. [118]). This would give absorption probabilities in the 10^{-4} range for a micron thick n-layer. In addition, such hot electrons photocreated in the n-layer would have to traverse the active region and the EBL (if any) before reaching the p-layer, while sizeable electron reflections are to be expected at each interface. Moreover, free carrier absorption from electrons injected in the QWs, at densities in the 10^{18} cm^{-3} range, should be much smaller given the few nm thick QWs (note that using the bulk free carrier absorption cross section [118] combined with the total thickness of the active region only provides a rough estimate of the absorbance of the QWs). Excitation from leaking electrons in the p-layer is also negligible due to the very small space-averaged density of such electrons. It should be remarked that light would only go through these absorbing layers a few times (typically 2.5 average round-trips) in commercial LEDs with light-extracting features [119].
- Two-photon absorption is very unlikely to occur in LED EE as it would require light intensities in the GW/cm^2 range, many orders of magnitude above light power densities in LEDs.

The low-energy peak observed in Ref. [53] was suspected to be due to photoemission internally excited by LED light, which may be caused by the first three mechanisms described here. But, in addition to this, can LED light excite hot electrons in the structure through the "super-energetic" photoemission process studied in Sec. 2.4.1? If this is the case, then Auger recombination would not be the only viable mechanism to generate the high-energy peak observed in EE. To address this question, a combination of different EE and PE experiments was carried out. In these studies, the LED is electrically injected to produce EE, and an external laser source, close to the peak wavelength of the LED, may be simultaneously shined on the sample to mimic LED light and produce PE.

Schematics of the experimental configurations corresponding to the studies of Sec. 2.4.1-2.4.2 are shown in Figure 41. For a quantitative comparison of the PE signal measured from the different experiments, the internal optical power in the p-GaN layer potentially producing PE can be estimated as:

PE on PE sample $$\boldsymbol{P_{ext,PE} \cdot T_{rot} \cdot (1 - R)} \quad (7)$$

PE on EE sample $$\mathbf{P_{ext,EE} \cdot T_{rot} \cdot (1 - R) \cdot f_{ap}} \quad (8)$$

EE $$\mathbf{P_{LED} \cdot f_{ap} = I_{LED} \cdot h\nu/e \cdot IQE(I_{LED}) \cdot f_{ap}} \quad (9)$$

where $P_{ext,PE/EE}$ is the external optical power shined on a PE/EE sample, respectively. This power is reduced in Eq. (7), (8) by the beam transmission through a fine grid in the rotator hole of the electron analyzer (T_{rot} =75%) and by the reflectance of the p-GaN surface (R~19% for below-gap excitation [120]). In Eq. (8) an additional geometric factor, f_{ap} =25%, corresponding to the filling ratio of the p-GaN apertures in the injection area of the p-contact is present. P_{LED} is the internal optical power of the LED which can be calculated from the injected current I_{LED}, the emission energy hν~2.8 eV and the relative quantum efficiency curve of Figure 92, measured from the blue LED studied in Ref. [53], where a peak IQE of 76% is obtained from an ABC fit (Eq. (80)). Perfect injection in the active region ($\eta_{el} = \eta_{inj} = 1$) and a homogeneous distribution of LED light over the injection area are assumed.

The excitation intensities Q in p-GaN corresponding to the different experiments are:

PE on PE sample $$\boldsymbol{Q_{int,PE} = P_{ext,PE} \cdot T_{rot} \cdot (1 - R)/[\pi \cdot (\phi_{spot}/2)^2]} \quad \mathbf{(10)}$$

PE on EE sample $$\boldsymbol{Q_{int,EE} = P_{ext,EE} \cdot T_{rot} \cdot (1 - R)/[\pi \cdot (\phi_{spot}/2)^2]} \quad (11)$$

EE $$Q_{LED} = P_{LED}/[\pi \cdot (\phi_{inj}/2)^2] \quad (12)$$

where ϕ_{spot}=200 μm is the typical focused laser spot diameter and ϕ_{inj}=500 μm is the diameter of the electrical injection area of the LED. Note that the geometrical factor f_{ap} does not affect the intensities.

By imposing equality among the internal powers of Eq. (7)-(9) the following relation between I_{LED} and $P_{ext,PE/EE}$ is obtained:

$$I_{LED} = \frac{P_{ext,PE} \cdot T_{rot} \cdot (1-R)}{\frac{h\nu}{e} \cdot IQE(I_{LED}) \cdot f_{ap}} = \frac{P_{ext,EE} \cdot T_{rot} \cdot (1-R)}{\frac{h\nu}{e} \cdot IQE(I_{LED})} \quad (13)$$

which is plotted in Figure 41.

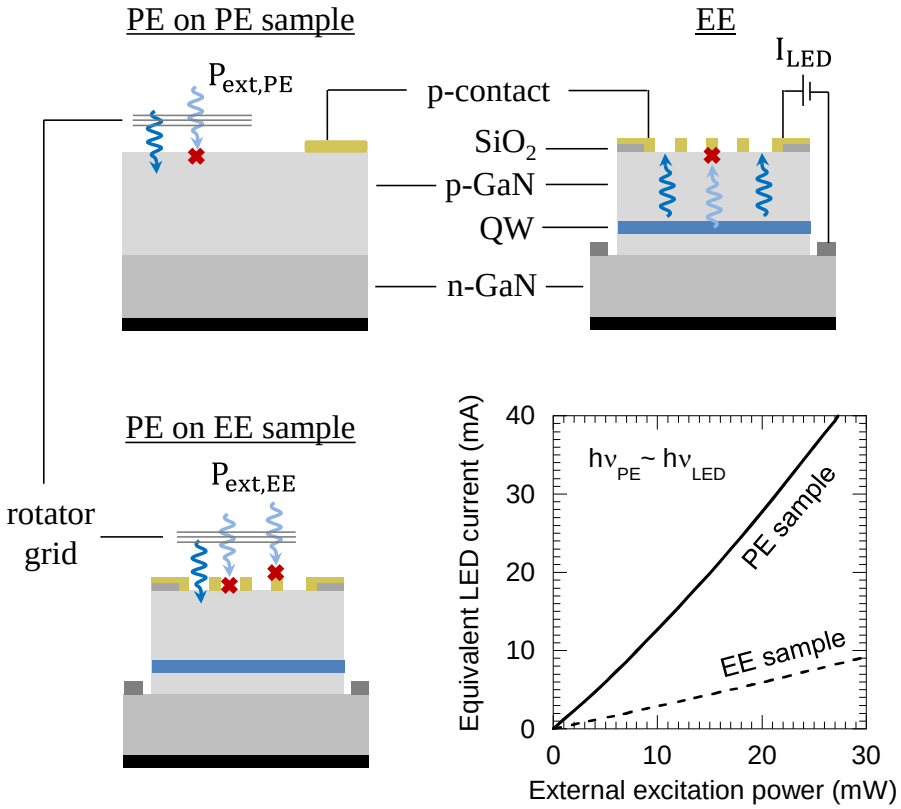

Figure 41 – Schematics of different experiments carried out to study the PE processes excited by LED light in LED EE. The plot shows the current to inject in an LED EE device to generate an internal optical power in p-GaN potentially producing PE equivalent to that created by external photoexcitation on a PE or EE sample. The relations are calculated from Eq. (13). Different optical losses (red crosses), such as reflection at the p-GaN surface and absorption by the p-contact, may occur, thus reducing the effective optical power potentially producing PE.

If nonlinear phenomena play a role in PE (such as SPV effects scaling logarithmically with the optical intensity), then not only the internal powers but also the intensities have to be compared. From Eq. (10)-(13) it follows:

$$\boldsymbol{Q_{int,PE} = f_{ap} \cdot \left(\frac{\phi_{inj}}{\phi_{spot}}\right)^2 \cdot Q_{LED} \sim 1.6 \cdot Q_{LED}} \quad \textbf{(14)}$$

$$\boldsymbol{Q_{int,EE} = \left(\frac{\phi_{inj}}{\phi_{spot}}\right)^2 \cdot Q_{LED} \sim 6.3 \cdot Q_{LED}} \quad \textbf{(15)}$$

implying that, at a given internal power, in "PE on PE sample" experiments the mimicked optical intensity reproduces quite closely that of EE experiments, while in "PE on EE sample" experiments the discrepancy is larger.

Let us now draw a comparison between the two electron peaks observed in below band gap photoemission of p-GaN at hν = 2.71 eV (Sec. 2.4.1) and the two high-energy peaks seen in the EE of blue LEDs, i.e. the peaks labeled ① and ② in Ref. [53]. (Note: the low-energy peak ③ observed in LED EE is attributed to metal PE, as it will be later discussed.) From the relation between the equivalent LED current and the external excitation power plotted in Figure 41 ("PE sample" curve) it can be deduced that a choice of $P_{ext,PE}$ in the range 1-23 mW represents, in terms of the internal optical power in p-GaN potentially contributing to PE, the condition achieved in the LEDs for I_{LED} in the interval 1-32 mA, which is the one typically studied in EE with the LED in CW operation. Moreover, the excitation intensities in the "PE on PE sample" experiment and in LED EE are very similar (Eq. (14)).

- Appearance. At an excitation power larger than few mW two distinct peaks are observed in PE on p-GaN and, in agreement with the equivalence relation plotted in Figure 41 ("PE sample" curve), two peaks emitted from p-GaN also appear in LED EE at an injected current of few mA.
- Relative energy position. The HET of the PE spectrum lies well above the threshold $h\nu + E_F$ of "well-behaved" below-gap PE. Super-energetic emission may indeed extend over an energy range which exceeds $h\nu + E_F$ by about 1 eV or more. This is comparable with the energy separation of 0.95 ± 0.1 eV observed between the HETs of peaks ① and ② in LED EE. However, as already emphasised, the separation of the well-behaved and super-energetic peaks observed in below bandgap PE depends on excitation power while the separation between the two high energy peaks in LED EE experiments remains constant when the injected current is increased.

- Absolute energy position. The HET of the PE spectrum at $P_{ext,PE}$ = 2.30 mW lies at ~3.6 eV above E_F, while the HET of peak ① depends on the I-V characteristic of the LED (see Figure 46, Figure 47a) due to the rectifying character of the p-contact, an effect that will be analyzed in Sec. 2.5.
- Peak shift vs. excitation. In below bandgap PE, the super-energetic peak was shown to shift towards high energies at increasing $P_{ext,PE}$ (Figure 33e) with a logarithmic dependence on excitation, while the well-behaved peak remained fixed but was progressively cropped from the low energy side. In Sec. 2.4.1, the PE super-energetic peak was attributed to electron photoexcited from surface gap states and its shift to SPV. In LED EE the two high energy peaks were shown to shift towards high energy with increasing I_{LED}: Iveland *et al.* [53] observed a linear shift with the voltage applied to the device (i.e. ~a logarithmic shift with I_{LED} considering that at high bias voltage $V \propto \ln I$, Figure 16b.). This shift was however not attributed to a SPV but to a potential drop at the rectifying p-contact (Sec. 2.5).
- Peak intensity vs. excitation. The relative intensities of the two PE contributions change with power and the most energetic peak dominates at high $P_{ext,PE}$ (Figure 42a). In LED EE the relative ratio of the peaks ① and ② was reported in Ref. [53] to be constant as a function of I_{LED} within the measurement precision. However, in the subsequent EE measurements performed in the course of this thesis on different LEDs (as, for instance, the one reported in Ref. [87]) the intensity ratio of peaks ① and ② exhibits appreciable change as a function of I_{LED} (Figure 42b).

The two peaks observed in below-gap PE of p-GaN exhibit some common features with the two high-energy peaks measured in LED EE but also some noticeable differences in particular when considering their energy separation and its evolution with the injection/excitation conditions. Therefore, the two below bandgap PE peaks can not be straightforwardly related to the two EE high energy features. In order to evaluate if below-gap PE processes affect LED electro-emission upon excitation by the internal device electro-luminescence, experiments combining EE and PE in LEDs were then performed.

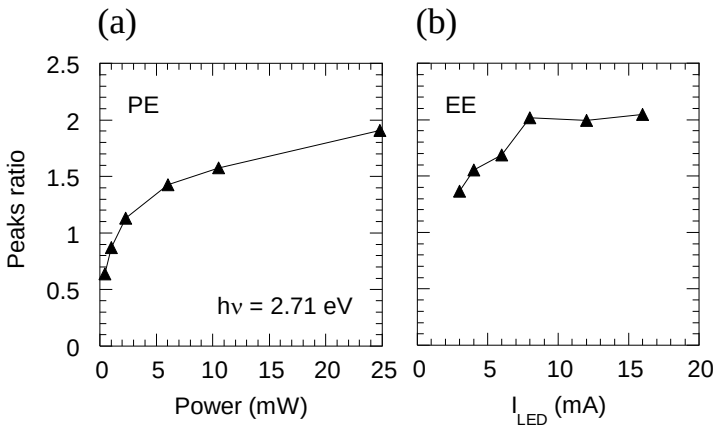

Figure 42 – Intensity ratio of the two high-energy peaks observed in (a) below-gap photoemission of bare p-GaN/Cs (Sec. 2.4.1), and (b) LED electro-emission (corresponding to the device reported in Ref. [87]), as a function of optical power and LED current, respectively.

In the following, a Seoul LED processed for EE, annealed and cesiated as described in Sec. 2.2.2 is studied. The sample has 5 QWs with a thickness of 3 nm each, the p-GaN layer is 200 nm thick with a Mg acceptor concentration of $\sim 2 \cdot 10^{20}$ cm^{-3} and no EBL is present in the structure. The peak emission wavelength of the LED EL (measured at 16 mA) is 441 nm (hν = 2.81 eV) with a FWHM of 17 nm. The EDCs measured in EE at an injected current of 1 mA and 16 mA are shown as solid lines in Figure 43a,b. As in the sample studied by Iveland *et al*. [53] (Figure 16a), at 1 mA a single low-energy peak is observed, while at 16 mA two additional high-energy peaks are observed with a separation between the HETs of ~0.96 eV.

The low-energy peak scales slightly sub-linearly with I_{LED} (compare the "×16" peak at 1 mA with the low-energy peak at 16 mA) as LED light does due to droop, which may be an indication of photogeneration. Moreover, this peak is not observed to shift as a function of I_{LED} (contrarily to the high-energy peaks), which suggests that it follows the energy reference of the p-contact (see Sec. 2.5.1). These observations indicate that the low-energy peak is generated by PE induced by LED light at the p-contact (Au/Pd).

To test this hypothesis, PE measurements using the 2.71 eV line of a Krypton/Argon laser are carried out on a Au sample at $P_{ext,EE}$=0.3 mW. The photoemission peak emitted from the metal (Figure 43d) exhibits a Fermi step-like high-energy edge with an inflection point at 2.68 eV (determined as in Sec. 2.2.3), close to the exciting photon energy. Its EDC lineshape resembles the low-energy peak observed in LED EE (Figure

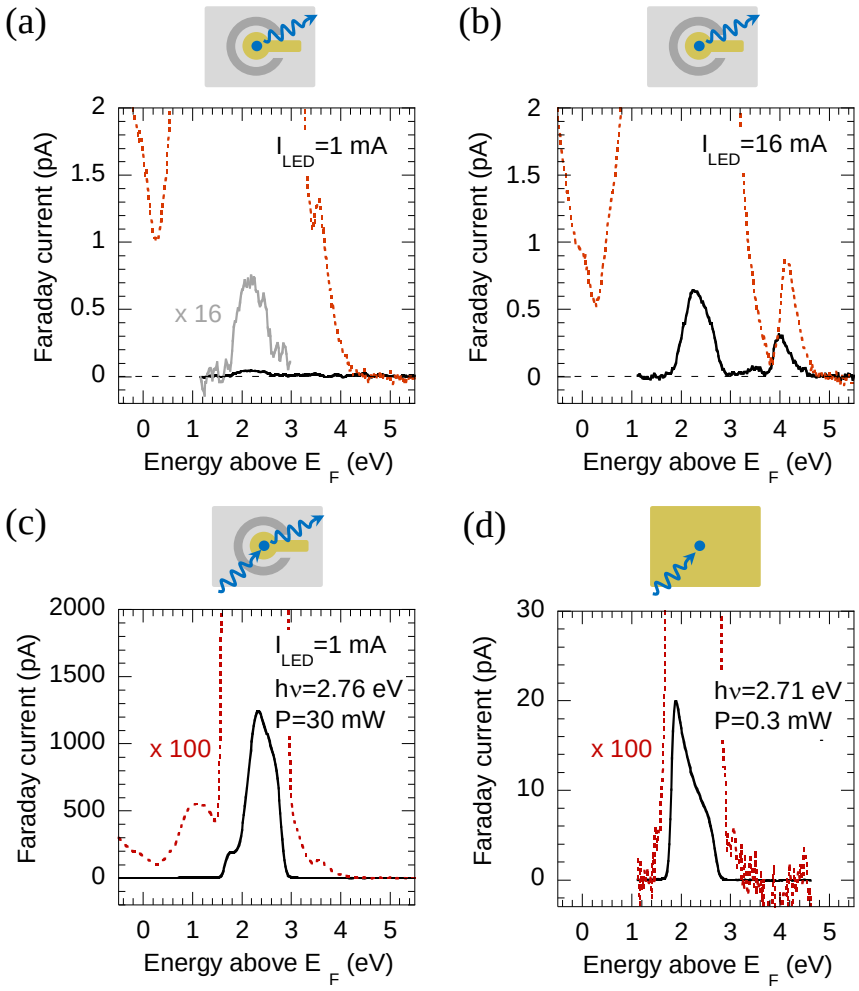

Figure 43 – PE and EE experiments carried out on an LED (Seoul, 200 nm thick p-GaN, no EBL) and gold sample to identify the photoelectric contributions to the LED EE. External PE excitation is at hν = 2.76 eV and $P_{ext,EE}$=30 mW in (a), (b), (d), and at hν = 2.71 and $P_{ext,EE}$=0.3 mW in (c). Schematics of the experiments correspond to the EDCs shown as solid lines in (a)-(d). (a) LED EE at 1 mA and 3.03 V bias (solid black line), and with simultaneous PE (dashed red line). (b) LED EE at 16 mA and 3.97 V bias (solid black line), and with simultaneous PE (dashed red line). (c) PE+EE at 1 mA and 3.03 V bias. (d) PE of the Au sample.

43a,b) apart from a difference in the onset of the peak which is due to a disparity in the surface activation condition of the two samples.

For all the above reasons the low-energy peak observed in EE is ascribed to photogeneration from the p-contact by LED light excitation (while in Ref. [53] it was rather suspected to be due to LED light-excited PE from the BBR of the semiconductor). Then it has to be verified whether LED light may also create the high-

energy contributions observed in EE. For this purpose, a light beam (laser diode) at hν = 2.76 eV and power $P_{ext,EE}$=30 mW is shined on the aperture array of the LED EE sample, which is simultaneously operated either at 1 mA or 16 mA (corresponding to an applied bias of 3.03 V and 3.97 V, respectively). The EDCs measured in concurrent PE and EE are then compared with those generated by EE alone, to study the modification of the spectra induced by the additional "mimicked" LED light. From Eq. (13) it is deduced that the equivalent LED current corresponding to the considered $P_{ext,EE}$ is 9 mA, indicating that the optical power in the apertures due to the laser excitation and LED operation should be of the same order of magnitude in the PE+EE experiment.

The EDC measured in PE+EE at 1 mA is shown in Figure 43c. The main intense peak exhibits a Fermi-step with an inflection point at 2.77 eV. Its lineshape is very similar to that of the low-energy peak observed in LED EE (Figure 43b). This peak is attributed to metal PE excited by laser light shining on the p-contact and appears much more intense (~2000x) than the low-energy peak observed in LED EE because of the different illuminating conditions: in PE+EE the laser beam impinges directly on the p-contact, while in EE only a small fraction of the emitted LED light is back-reflected in the UHV chamber onto the p-contact. (Note that the quantum yields of metal PE in the excitation condition corresponding to Figure 43c,d are very similar.)

Several peaks, weaker by orders of magnitude than the main peak, appear out of the energy window corresponding to the metal photoemission, as it can be seen in the dashed curve of Figure 43a,c. Considering the large difference in the signal level of the different contributions to the PE+EE spectrum, care should be taken for their interpretation. On the low-energy side, successive shoulders are observed which are presumably "ghost" peaks created by space charge effects in the analyzer [121] due to the large emitted cathode current (~2 μA). Such features are not observed on the metal PE spectrum of Figure 43d obtained at a much smaller optical excitation power. On the high-energy side of the main peak a distinct peak appears which was not observed in LED EE alone (Figure 43a). Increasing I_{LED}, this peak progressively shifts towards higher energies. In PE+EE at 16 mA (dashed line in Figure 43b) the peak holds a position close to that of the high-energy peak observed in LED EE (solid line in Figure 43b) but is more intense than in LED EE alone. After subtraction of the large background due to metal PE and of the EE signal it is found that this contribution is essentially unchanged in the two PE+EE experiments, except for the energy shift of ~0.5 eV. The shift with I_{LED} indicates that: first, this contribution is not an artefact due

to space charge effects, as these should not change with I_{LED} since the total emitted cathode current is dominated by the intense metal PE excited by the laser and is substantially unaffected by the EE signal; second, the considered high-energy contribution is likely to be photocreated in the exposed p-GaN apertures since $E_{F,p}$ in the semiconductor is expected to shift towards high energies with respect to $E_{F,m}$ in the metal at increasing I_{LED}, as discussed in Sec. 2.5.1 (Figure 45a,b).

The important conclusion of these experiments is that adding external light at the LED emission wavelength to an LED EE experiment can create and enhance a high-energy contribution in the EDCs. This result indicates that it is possible to photogenerate a high-energy peak similar to the one observed in LED EE alone. It should be remarked, however, that the illumination condition in the EE and PE experiments is different as the light impinges on the p-GaN surface from the interior and exterior side of the sample, respectively. The arrangement of the electron emission spectroscopy setup does not allow at the moment to easily excite the sample with a laser beam impinging on the substrate of the LED, which explains the choice of the excitation configuration used here. Excitation from the interior and from outside could lead to different results: the photovoltages could be more uniform across the sample when exciting from inside compared to the photovoltage only created in the apertures when exciting from the outside. The energy map could be significantly altered.

According to Ref. [53], the high-energy peak observed in LED EE is generated by an Auger process occurring in the QWs of the LED under electrical injection. Then it may be argued that the photocreation of the high-energy peak observed in the present PE+EE experiment is ultimately due to an increase of the carrier concentration n in the QWs due to optical interband absorption of the laser beam, which would consequently enhance the Auger rate $C \cdot n^3$ (C being the Auger coefficient in the ABC model). This is excluded for the following reasons: 1) the optical interband absorption at the considered $h\nu$ is small, leading to a small perturbation of the carrier generation term in the QWs, as calculated below; 2) a high-energy peak can be photogenerated in PE+EE also exciting at a photon energy well below the band gap of the blue-emitting QWs (namely in the green and red range), as it will be shown; 3) a high-energy peak can be photoexcited also in a simple p-n junction without QWs in a similar PE+EE experiment (Appendix 5.4.2).

Concerning the first aforementioned point, the total carrier recombination rate in the QWs can be written at steady state as

$$\frac{\mathbf{dn}}{\mathbf{dt}} = -\mathbf{R} + \mathbf{G} = \mathbf{0} \qquad \textbf{(16)}$$

where R is the carrier recombination rate (equal to $An + Bn^2 + Cn^3$ in the ABC model) and G is the carrier generation rate. Under electrical injection (as in EE) the generation rate is given by

$$\mathbf{G_{el}} = \frac{\mathbf{I} \cdot \boldsymbol{\eta}_{\mathbf{el}} \cdot \boldsymbol{\eta}_{\mathbf{inj}}}{\mathbf{A_{inj}} \cdot \mathbf{d_{active}} \cdot \mathbf{e}} \qquad \textbf{(17)}$$

where I is the current injected over an area A_{inj} and d_{active} is the total thickness of the QW layers.

Under optical excitation (as in PE) the generation rate is given by

$$\mathbf{G_{photo}} = \frac{\mathbf{P} \cdot \boldsymbol{\alpha}(\mathbf{h\nu}) \cdot \mathbf{l}_{\boldsymbol{QW}} \cdot \mathbf{N}}{\mathbf{A_{spot}} \cdot \mathbf{d_{active}} \cdot \mathbf{h\nu}} \qquad \textbf{(18)}$$

where P is the optical power of the beam at $h\nu$ with spot size A_{spot}, and $\alpha(h\nu) \cdot l_{QW}$ is the absorptance of each of the N QWs which should be independent of their thickness l_{QW} [122] (neglecting the dependence of the electron-hole overlap on l_{QW}).

Then, in a PE+EE experiment the total carrier generation term is $G = G_{el} \cdot (1 + G_{photo}/G_{el})$, where the relative weight of the perturbation due to the optical excitation is given by

$$\frac{\mathbf{G_{photo}}}{\mathbf{G_{el}}} = \frac{\mathbf{P} \cdot \boldsymbol{\alpha}(\mathbf{h\nu}) \cdot \mathbf{l}_{\boldsymbol{QW}} \cdot \mathbf{N}}{\mathbf{A_{spot}} \cdot \mathbf{h\nu}} \cdot \frac{\mathbf{A_{inj}} \cdot \mathbf{e}}{\mathbf{I} \cdot \boldsymbol{\eta}_{\mathbf{el}} \cdot \boldsymbol{\eta}_{\mathbf{inj}}} \qquad \textbf{(19)}$$

For the PE+EE experiment described above, taking P = 18 mW (after transmission through the rotator hole and the p-GaN surface), I = 16 mA, $\alpha(2.85\ \text{eV}) \cdot l_{QW} \sim 0.1\%$ [123] and $\eta_{el} \cdot \eta_{inj} = 1$, it is obtained G_{photo}/G_{el} = 1%. This indicates that the laser excitation only adds a small perturbation to the generation term due to electrical injection. Since the high-energy peak observed in PE+EE at 16 mA is enhanced by a factor 3× with respect to EE alone (Figure 43b), it seems unlikely that this electron peak originates from an electronic process occurring in the QWs, such as Auger recombination, but seems to be rather directly generated by a photoelectric process. It should be remarked that, even though the carrier density in the active region should not be significantly increased by the laser excitation in the PE+EE experiment,

the carrier distribution among the different QWs, which is predicted to be quite inhomogeneous in simulations of LED electrical injection (cf. Figure 85), may be modified, possibly inducing a difference in the injection condition of EE and PE+EE experiments.

To investigate the origin of the latter process, an excitation spectroscopy of the high-energy peak observed in PE+EE is carried out, namely by varying the exciting photon energy of the laser beam above and below the band gap of the QWs. Before the experiment, the sample is re-annealed at higher temperature ($T_{R_{Pt}}$~260°C for 20 min) to enhance the overall electron emission efficiency and then re-cesiated. After this treatment, the high-energy peak is clearly observed in LED EE already at I_{LED} = 2 mA (Figure 44a). (It should be noted that the high-temperature annealing caused a partial degradation of the I-V curve of the device increasing the forward voltage by ~1 V. Such degradation, if occurring at the p-contact, may affect the absolute energy position of the electron contributions emitted from the semiconductor. However, at a low current such as 2 mA the effect of this degradation on the position of the high-energy peak appears to be secondary.)

The PE+EE spectroscopy experiment is carried out at an injection of 2 mA and, differently from the previous PE+EE experiment shown in Figure 43, the photoemission signal is singled out by synchronous lock-in detection in phase with the optical excitation. The measured PE spectra with the LED operated in forward bias and for Kr/Ar laser excitation in the red-blue range are shown in Figure 44b. EDCs are normalized to the incident photon flux. (The corresponding laser power is ~10 mW for excitation in the green-blue range and ~50 mW in the red range.) As it can be observed, a high-energy peak can be photogenerated for all excitation energies, even below the band gap of the InGaN QWs, and extends in the same energy region of the high-energy peak observed in LED EE alone. Moreover, at $h\nu$ = 1.92 eV (red curve) the intense peak due to metal PE appears at lower energy (because its high-energy inflection point shifts with $h\nu$) revealing an intermediate photoexcited contribution which may correspond to the intermediate energy peak (called ② in Ref. [53]) typically observed in EE (not distinguishable at 2 mA in Figure 44a; see Figure 43b). However, this intermediate contribution can in fact be observed with all excitation energies (except that it is progressively swamped by the metal PE peak when increasing $h\nu$) and the position of its HET seems to remain constant (close to 3.3 eV above E_F) which is not compatible with a photoexcitation process.

The intensity of the high-energy peak measured in PE+EE is plotted in Figure 44c as a function of the exciting photon energy. Considering the peak as proportional to the absorption probability of the photoelectric process from which is generated, then the absorption mechanism scales exponentially with $h\nu$ with an inverse slope of 160 meV. Absorption in the QWs is excluded as the inverse slope of the exponential Urbach tail in InGaN is, despite compositional disorder effects, much smaller, typically around

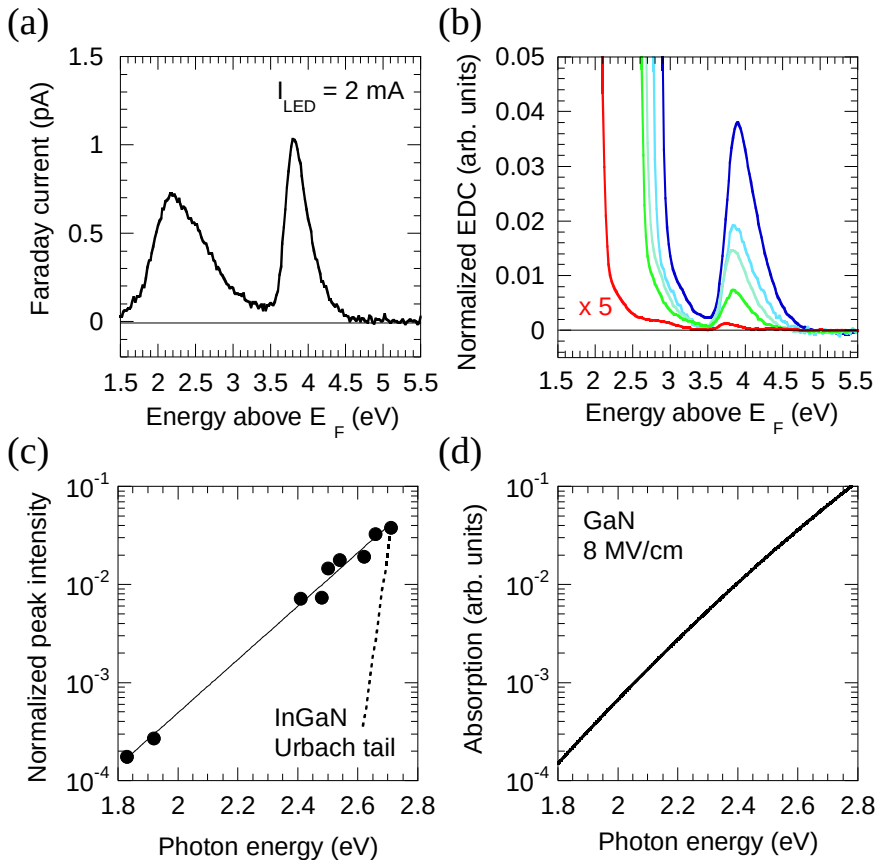

Figure 44 – (a) LED (Seoul, 200 nm thick p-GaN, no EBL) EE at 2 mA and 4.3 V bias after re-annealing at $T_{R_{Pt}}$~260°C. (b) PE+EE spectroscopy at I_{LED} = 2 mA and lock-in detection synchronized with laser excitation. EDCs are normalized to the incident photon flux and measured at photon energies of: 1.92 eV (red), 2.41 eV (green), 2.50 eV (blue-green), 2.62 eV (light blue), 2.71 eV (blue). (c) Intensity of the high-energy peak observed in PE+EE experiments, as those shown in (b), as a function of the exciting photon energy. The dispersion is fitted by an exponential (solid line). The typical slope of Urbach tails in InGaN is also shown for comparison (dashed line). (d) Theoretical Franz-Keldysh absorption in GaN for an electric field of 8 MV/cm giving a nearly exponential decay at low photon energy similar to that fitted in (c).

20 meV (dashed line) as measured by photocurrent spectroscopy in Chapter 3.

Instead the photoelectric process may be due to a Franz-Keldysh effect occurring in the strong electric field of the p-GaN surface BBR. (Note that the creation of "super-energetic" photoelectrons, well above $h\nu + E_F$, by means of FK absorption still requires the occupation of initial states above E_F (Figure 35d).) In the bulk limit FK absorption [124] is given by

$$\boldsymbol{\alpha(h\nu) \propto \frac{e|\vec{E}|}{\Delta E} \cdot \left[\frac{h\nu - E_g}{\Delta E} \left| Ai\left(-\frac{h\nu - E_g}{\Delta E} \right) \right|^2 + \left| Ai'\left(-\frac{h\nu - E_g}{\Delta E} \right) \right|^2 \right]} \qquad \textbf{(20)}$$

where $\Delta E \equiv \left(e|\vec{E}|\right)^{2/3} \cdot (\hbar^2/2m)^{1/3}$ depends on the reduced mass of electrons and holes $m = (1/m_e + 1/m_h)^{-1}$ and Ai is the Airy function Ai. From Eq. (20) it is found that for an electric field of 8 MV/cm (and taking $m_e = 0.22m_0$, $m_h = 1.58m_0$, $E_g =$ 3.4 eV for bulk GaN) the Franz-Keldysh absorption curve (Figure 44d) fits the exponential scaling of the high-energy peak with $h\nu$.

Such value of $\vec{E}$ corresponds well to the expected order of magnitude of the electric field in the BBR. The width of the BBR may be estimated from the 1D Poisson equation

$$\boldsymbol{\frac{d^2V}{dz^2} = -\frac{\rho_s(z)}{\varepsilon_s}} \qquad \textbf{(21)}$$

where V is the electric potential in the BBR, z is the distance from the surface, $\boldsymbol{\rho_s}$ is the charge density near the surface and $\boldsymbol{\varepsilon_s}$ is the dielectric permittivity of the semiconductor. Considering a width W depleted from carriers, $\boldsymbol{\rho_s}$ is the net ionized acceptor charge density $-e \cdot N_A^-$. Then the integration of Eq. (21) gives

$$\boldsymbol{V_z = V_{BB} \cdot \left(1 - \frac{z}{W}\right)^2} \qquad \textbf{(22)}$$

where $V_{BB} = e \cdot N_A^- W^2/2\boldsymbol{\varepsilon_s}$ corresponds to the band bending amplitude at surface, reported to be about 1.5 V in GaN [125]. Since the acceptor level lies below E_F at the p-GaN surface due to the band bending, the acceptors can be considered as nearly all ionized in the BBR. Then for the p-GaN acceptor concentration of the LED ($2 \cdot 10^{20}$ cm^{-3}) and using the GaN dielectric permittivity $\boldsymbol{\varepsilon_s}$ = 9.7 ε_0, the depletion width of the BBR may be estimated to be 3 nm. This would give an average electric field, in a first linear approximation, of V_{BB}/W~5 MV/cm, not too far from the fitted value of $\vec{E}$ for FK absorption.

Finally, it is noted that the photocreation of the high-energy peak was reproducible in PE+EE experiments carried out on several LED samples at Ecole Polytechnique, and at UCSB using a similar electron spectrometer.

In conclusion, a combination of PE and EE experiments has shown that a high-energy peak somewhat similar to that observed in LED EE can be photogenerated by external light irradiation, exciting both at the same photon energy of the LED and below, for incident optical powers estimated to be comparable to that of the LED under electrical operation in EE. The direct photocreation is unlikely to occur in the QWs of the LED, neither by an optically-enhanced electronic process such as Auger recombination nor by optical absorption, and is rather ascribed to a photoelectric process occurring in p-GaN. Complementary PE+EE experiments carried out in simple p-n junctions devices (without QWs) support this interpretation (Appendix 5.4.2). Several common features but also some significant differences have been observed between the two high-energy peaks measured in LED EE and in below-gap PE of p-GaN, which do not allow to conclude on the origin of these phenomena. In particular, the absolute energy position of these peaks cannot be directly compared because of energy shifts which depend on the current injected in the LEDs or on exciting power in p-GaN PE experiments. In the next section the origin of these spectral shifts will be addressed and their magnitude will be quantified by measuring the potential profile across the electron emitting surface of the LED.

2.5 Potential inhomogeneity in electro-emission devices

While super-energetic photoemission, discussed in Sec. 2.4, was found to be an intrinsic effect due to photoelectric processes occurring in p-GaN, in the present section an extrinsic effect that is device-dependent (more specifically, determined by contact processing) and which also has important consequences on electro-emission spectroscopy will be investigated.

After an introduction on the possible mechanisms leading to potential inhomogeneity in LEDs and which may induce a spectral shift in EE (Sec. 2.5.1), the energy position of the high-energy peak observed in a set of different devices will be analyzed as a function of their electrical characteristics (Sec. 2.5.2). It will be shown that devices fabricated from the same epilayer but having different forward voltages exhibit large energy shifts in the position of the high-energy peak. To identify the origin of this effect a characterization of the potential inhomogeneity across the electron emitting apertures of the devices will be carried out by local measurements using an atomic force microscope (AFM) with a conductive tip (Sec. 2.5.3). Finally, remedial actions to restore an equipotential electron emitting surface will be presented (Sec. 2.5.4).

2.5.1 Is the LED electron emitting surface equipotential?

In electron emission spectroscopy knowing the energy reference of the electron emitting surface is a prerequisite for the interpretation of the measured spectra. However, this may not be straightforward in LED EE experiments. It should be reminded that in the sample of Ref. [53] the p-contact was designed with an array of holes (Figure 15) allowing to expose part of the p-GaN surface for electron emission from the semiconductor into vacuum. Then, while the energy reference in the measurements is easily fixed to the Fermi level of the p-metal $E_{F,m}$, referencing the spectra to the (quasi-)Fermi level of p-GaN $E_{F,p}$ at the surface of the electron emitting apertures may not be simple. (Note that not only the semiconductor but also the metal, due to PE excited by LED light, emits electrons.) There are several factors, as schematized in Figure 45, which may cause a misalignment $e \cdot \Delta V$ between $E_{F,m}$ and $E_{F,p}$ across the electron emitting surface.

- A rectifying contact usually forms at the p-GaN/metal interface (see Sec. V in Ref. [126]) due to the typical low hole concentration in p-GaN and large Schottky barrier height (1.4 eV was reported in Ref. [127] for a p-GaN/Pt contact, as the p-electrode of the sample studied by Iveland *et al.* [53]). When

current is injected in the LED, as in standard forward-bias operation, the metal/p-GaN Schottky barrier is reversely biased and a non-ohmic potential drop forms at the metal/semiconductor interface (Figure 45a,b). The misalignment among $E_{F,m}$ and $E_{F,p}$ is due to the insulating character of the depleted BBR.

- Surface photovoltage (SPV, Figure 45c,d) can be caused by the trapping of photoelectrons at the exposed p-GaN surface. Photoelectrons, created by LED light as described in Sec. 2.4.2, may accumulate either at the surface of the CB, due to the downward band bending, or in surface states causing a partial screening of the BBR field. (Note that photoelectrons emitted into vacuum do not contribute to SPV.) Depending on photon energy and light intensity, SPV may push surface levels up with respect to the contact reference ($E_{F,m}$) as much as ~1 eV in p-GaN [112].
- Current crowding in proximity of the p-contact may cause a potential inhomogeneity in the apertures opened in the p-contact. Due to the bulk resistivity of p-GaN the injected hole current may tend to flow towards the junction perpendicularly to the p-GaN/metal interface with an inhomogeneous spreading within the exposed p-GaN apertures. Consequently, the voltage drop at the junction below the p-contact will be larger than within the aperture regions. Assuming the low-resistive n-GaN layer of the structure as equipotential, current crowding in p-GaN will result in a potential difference between $E_{F,m}$ and $E_{F,p}$ (Figure 45e,f). In this case both surface and bulk states are pushed up in the apertures with respect to the contact reference. An analytical model of current crowding in p-GaN developed for a contact geometry with apertures, as used in EE experiments, is presented in Appendix 5.2.

As a consequence of all the described processes, since the energy reference in the EE measurements is fixed at $E_{F,m}$, an electron emitted from a p-GaN aperture into vacuum will be observed at an apparent energy higher than its actual energy in the semiconductor (i.e. when referenced to $E_{F,p}$). It should be remarked that the energy shift $e \cdot \Delta V$ varies with the injected current with a dependence that is determined by the specific mechanism. A rectifying contact should give a potential drop that varies logarithmically with current (as in a Schottky diode at a reverse bias larger than the breakdown voltage). SPV varies logarithmically with light intensity [112], as already mentioned. Taking the LED optical power as proportional to the current (neglecting

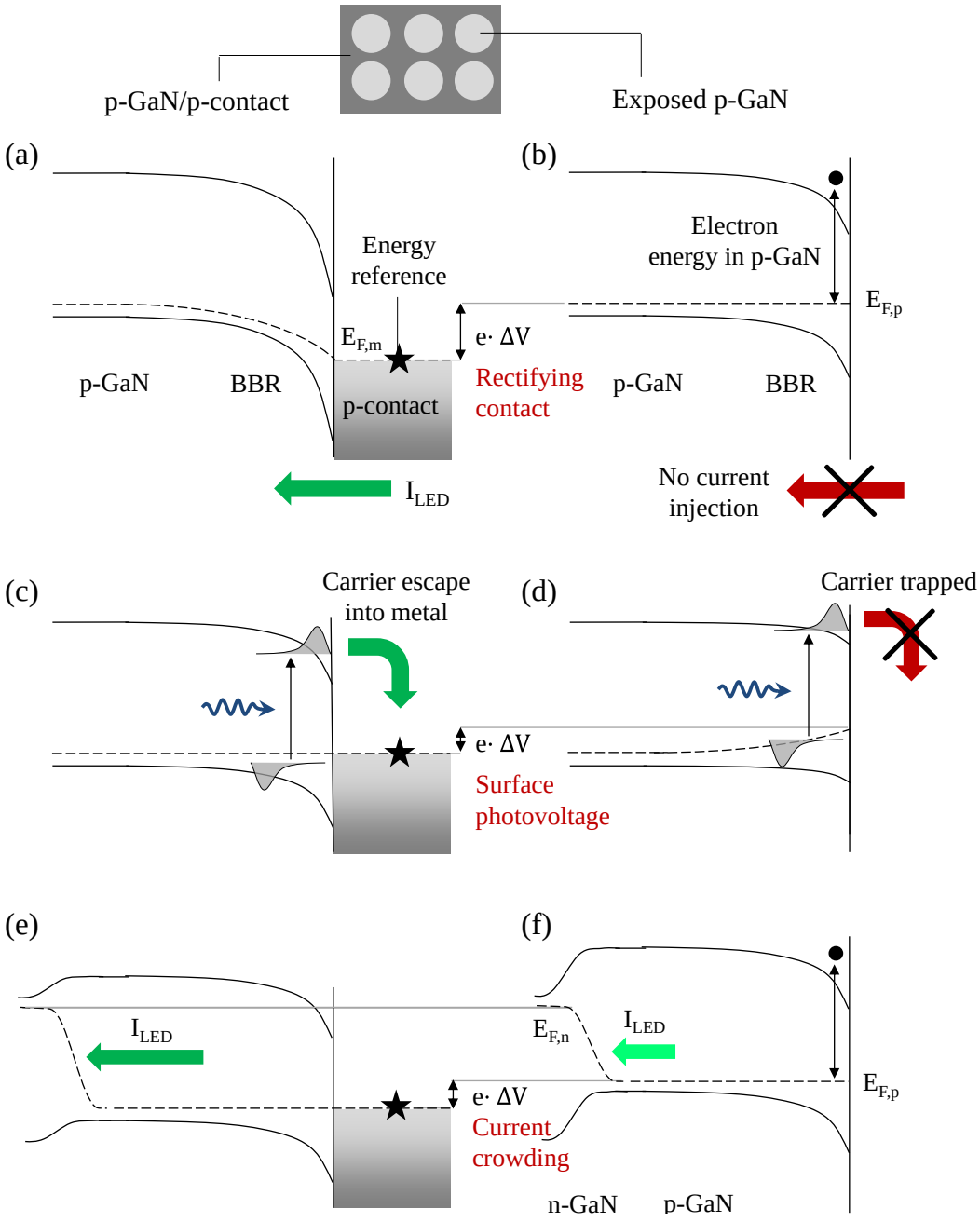

Figure 45 – Diagram representing different mechanisms causing a potential difference between the Fermi level of the p-contact and the Fermi level at the surface of an exposed p-GaN aperture when current is injected in the LED: (a-b) rectifying p-GaN/metal contact; (c-d) surface photovoltage excited by LED light; (e-f) current crowding close to the p-contact due to the resistive p-GaN layer.

droop in a rough approximation), then also SPV excited by LED light should have an approximate logarithmic dependence on current. Instead the potential drop due to current crowding in p-GaN is expected to vary ~linearly with current (Figure 96c) from the model derived in Appendix 5.2.

Iveland *et al*. [53] observed a shift of the high-energy electron peaks that varied linearly with the voltage applied to the junction, i.e. ~logarithmically with the current injected in the LED (considering that at high voltage $V \propto \ln I$), as it can be observed in Figure 16b. This shift was attributed to a potential drop in the rectifying p-contact, providing supplementary energy (with respect to $E_{F,m}$) to the electrons emitted from bulk p-GaN. On the basis of the previous qualitative considerations, a rectifying p-contact and/or SPV effects are expected to be responsible for such a shift of the electron peaks with current. Current crowding effects seem to be negligible also due to the small $e \cdot \Delta V$ predicted from the model in Appendix 5.2 (Figure 96c), well below the magnitude of the observed peak shifts. In addition to this, it should be remarked that the shift of the peaks ① and ② confirms that these electrons are emitted from p-GaN (with $E_{F,p}$ shifting with respect to $E_{F,m}$), in agreement with the conclusions of Sec. 2.4.2. Conversely, the low-energy peak ③ holds a ~fixed energy position, as expected for emission from the p-contact.

Energy shifts need to be properly characterized as some low-energy electrons may appear as "hot" in the EE spectra if the shift in the energy reference is not properly taken into account. Such characterization will be carried out in Sec. 2.5.3.

2.5.2 Device-dependent shift of the high-energy peak in LED electro-emission

In the following the position of the high-energy peak measured in LED EE from a set of 10 distinct devices is compared. All devices are blue LEDs grown by Walsin Lihwa Co. (8 QWs) or Seoul VioSys (5 QWs) and fabricated at UCSB for EE experiments with square electrodes (Figure 15) or concentric contact geometry (Figure 19a), respectively. Some devices are fabricated from the same epilayer and with the same type of contacts, while others differ in the thickness of the p-GaN layer (100 nm, 200 nm or 500 nm), in the possible presence of an EBL, or a SiO_2 layer masking the p-pad surface to reduce metal PE [87].

In Figure 46 the EE curves measured from the different devices at I_{LED} = 16 mA are shown. All LEDs produced essentially three electron contributions. The EDCs are normalized to the intensity of the high-energy peak and the baseline of the spectra is shifted by the forward bias V_f applied to the LED. The relative intensity of the high- and intermediate-peak varies among the structures without any correlation with the p-GaN layer thickness. This is in contrast with what one would expect if these electrons were

originating from the active region and then diffusing through p-GaN till the surface, as proposed in Ref. [53], therefore producing more thermalized than hot electrons from thicker p-layers. (It should be noted that in the Walsin sample with a p-GaN thickness of 500 nm (cyan curve) the two high-energy contributions can only be distinguished by taking the derivative of the EDC. This spectrum is quite similar to that measured in the Seoul 100 nm with EBL sample (violet curve), both having an intense intermediate peak, a weak high-energy shoulder and low-energy contribution, and a low forward voltage.)

The fact that nominally identical structures, i.e. with the same epilayer, exhibit an appreciable shift in the position of the high-energy peak is a clear indication of an extrinsic effect related to the contact processing of each device. The position of the high-energy peak shows a correlation with V_f (Figure 47a). A maximum shift as large as ~1 eV is measured among the different devices. LEDs with larger V_f are suspected to suffer from larger non-ohmic losses at the p-GaN/p-contact interface which, as

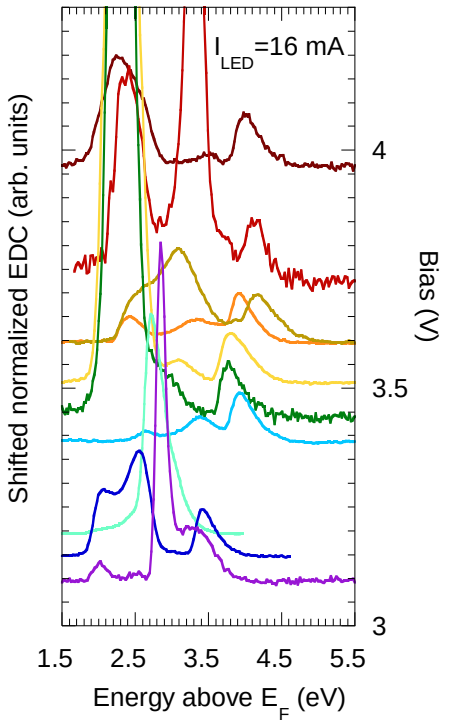

Manufacturer	$t_{p\text{-}GaN}$ (nm)	EBL	SiO_2
Seoul	200		
Seoul	100	✓	
Seoul	100	✓	✓
Seoul	100		
Seoul	100		
Walsin	200	✓	
Seoul	100		✓
Walsin	500		
Seoul	100	✓	
Seoul	100	✓	

Figure 46 – EE spectra measured from different LEDs at an injected current of 16 mA. EDCs are normalized to the intensity of the high-energy peak and the baseline is shifted by the applied forward bias. The samples reported in Ref. [53] and [87] correspond to the spectra plotted as green (3.45 V) and light blue (3.39 V) curves, respectively.

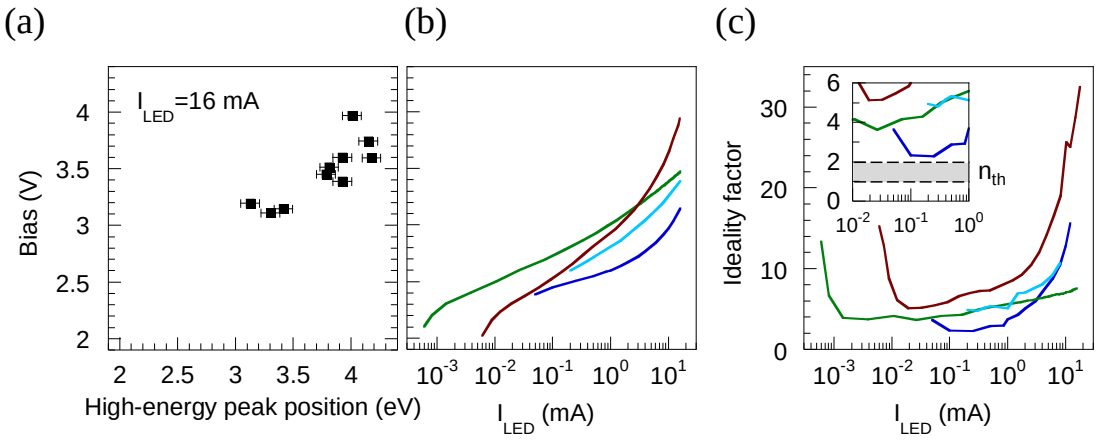

Figure 47 – (a) Position of the high-energy peak measured in EE at a current of 16 mA from different LEDs as a function of the forward bias applied to the device (from Figure 46). (b) Voltage-current characteristics and (c) ideality factors of different LEDs whose EDCs are plotted in Figure 46 using the same colors. The samples reported in Ref. [53] and [87] correspond to the spectra plotted as green and light blue curves, respectively. The inset in (c) shows the minimum ideality factor, expected to be close to (far from) the theoretical values predicted by the Sah-Noyce-Shockley theory in the case of devices with ohmic (rectifying) contacts.

discussed in Sec. 2.5.1, can cause an apparent shift towards high energies of the electrons emitted from the p-GaN apertures.

A large V_f is in general related to a large ideality factor. Shah *et al.* [128] presented a model of nitride diodes based on an electrical equivalent circuit of different diodes in series, corresponding to the p-n junction, unipolar heterojunctions and metal-semiconductor junctions, each having an associated ideality factor. In the high-voltage approximation ($V > 3kT/q$), the applied bias can be written as the voltage dropped across the different diodes of the circuit:

$$\mathbf{V = \sum_i V_i = \frac{kT}{q} \sum_i [n_i \cdot (\ln I - \ln I_{S,i})]} \qquad \mathbf{(23)}$$

where n_i and $I_{S,i}$ are the ideality factor and the reverse saturation current of the i-th diode. From Eq. (23) it follows

$$\mathbf{\ln I = \frac{q/kT}{\sum_i n_i} V + \frac{\sum_i n_i \ln I_{S,i}}{\sum_i n_i}} \qquad (24)$$

which shows that the ideality factors of the different junctions add up to the total ideality factor of the device, $n = \sum_i n_i$. Note that the second summand of Eq. (24) is constant in the linear regions of the $\ln I\,(V)$ curves, where the different n_i's are constant.

Figure 47b shows the measured voltage-current characteristics of four LEDs whose EDCs are plotted in Figure 46 (same colors). The samples studied in Ref. [53] and Ref. [87] correspond to the green and light blue curves, respectively. Note that in Ref. [53] and here a 23 Ω access resistance in series with the diode was removed from the I-V curve of the device. The derived ideality factor of the devices, calculated as $n = q/kT\ (d\ln I/dV)^{-1}$, is plotted in Figure 47c. As it can be observed the devices with the largest V_f also exhibit the largest n. At low and high currents, the device performance is

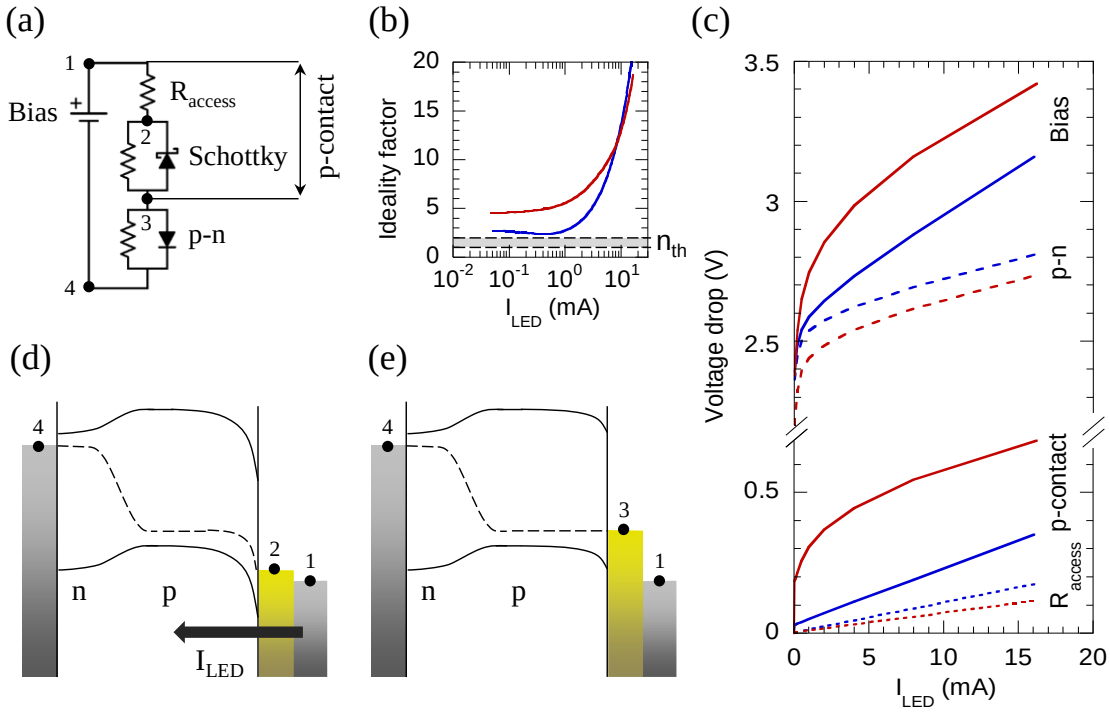

Figure 48 – (a) Equivalent electrical circuit model of the LED. Depending on the Schottky barrier height the p-contact may exhibit more ohmic or rectifying behavior. Labels 1-4 correspond to different nodes of the circuit at which the potential can be probed by c-AFM measurements. (b) Ideality factors and (c) voltage drop across different elements of the circuit measured by c-AFM for two LED devices processed with the EE geometry and metal pillars in the apertures (as in Figure 49). In (d) and (e) a schematic band diagram of the structure is shown, respectively, for the area of the p-contact where current injection occurs and for the regions occupied by the pillars where no current is injected.

dominated, respectively, by a shunt and a series resistance which cause large values of n. However, in the intermediate range of currents (~0.01-1 mA) the diodes dominate the device characteristics: the I-V curve exhibits a nearly exponential behavior and the ideality factor is almost constant. In this region the $n(I)$ curve reaches a minimum (inset of Figure 47c), which is meaningful for the characterization of the diode [129].

The device with low V_f has a minimum value of the ideality factor of ~2, close to the predictions of the Sah-Noyce-Shockley theory giving $n_{th} = 2$ and $n_{th} = 1$ in the case of a p-n junction dominated, respectively, by SRH recombination in the space charge region and diffusion in the neutral region of the junction [130]. Conversely, the devices with large V_f exhibit minimum n values of ~4 and ~5 appreciably larger than n_{th}. According to the previous model this can be attributed to other diodes in series with the p-n junction, whose ideality factors add up to n_{th}. In the following it will be shown that this effect is specifically due to the rectifying character of the p-contact, which acts as a Schottky diode in series with the p-n junction.

2.5.3 Characterization

An equivalent electrical circuit model of the LEDs studied here is schematized in Figure 48a. The p-contact is represented by an access resistance, essentially determined by the contact resistance of the wire connection to the p-contact, in series with a reverse-biased Schottky diode at the metal/p-GaN interface. Unipolar heterojunctions, such as the EBL, are considered as incorporated into the GaN-based p-n structure. The other resistors in the circuit determine the amount of leakage in the diodes and in particular, in the case of the Schottky barrier, the more or less ohmic behavior of the junction. (Note that in the derivation of Eq. (23), (24) such resistors are considered large enough to be neglected.) A bias is applied across the entire circuit.

In order to characterize the voltage drop across the different elements, the potential at the nodes 1-4 shown on the circuit has to be measured. In particular, $V_{1,3}$ is directly responsible for the shift of the electron peaks emitted from the semiconductor in EE. For this it can be considered that in the regions of current injection below the p-contact the band diagram of the structure can be schematized as in Figure 48d: a bias $V_{1,4}$ is applied across the device and a current I_{LED} flows in the circuit, the access resistance of the connection at the p-contact determines $V_{1,2}$, and the metal-semiconductor junction is reverse-biased. However, in the apertures of the p-contact of the EE devices no current is locally injected, no voltage drops at the p-GaN/p-contact interface and the band

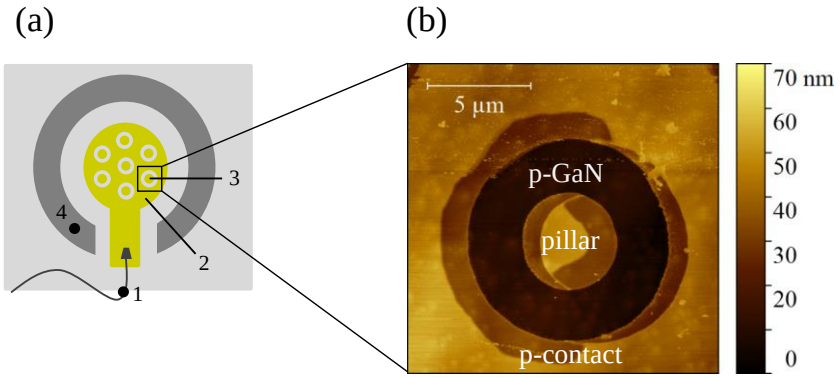

Figure 49 – (a) Schematic of the EE geometry of the p-contact of LEDs adapted for local potential measurements. In each aperture of the p-contact (632 in total, here only a few are drawn for simplicity) a 5 µm-diameter Pd/Au pillar has been deposited. Labels 1-4 correspond to the nodes of the equivalent circuit of the LED shown in Figure 48a. (b) Topography image measured by AFM showing a single p-GaN aperture in the p-contact with the lithographically defined pillar at the center.

diagram of the structure in these regions corresponds to Figure 48e. Therefore, by probing the local potential in the apertures (node 3) the voltage drop across the p-contact can be determined as $V_{1,3}$ (and implicitly the one across the Schottky barrier as $V_{1,3} - V_{1,2}$). For this purpose, the EE contact geometry is slightly modified by the addition of 5 µm-diameter metal pillars in the center of each aperture by photolithography (Figure 49). Metal pillars facilitate the measurement of the local potential in air, whereby exposed p-GaN would form an oxide layer. Both the p-contact and pillars are deposited as Pd/Au 15 nm/15 nm layers; the total thickness of the pillars is 30 ± 10 nm due to the shadowing effect of the deposition. As already discussed in Sec. 2.5.1, $V_{2,3}$ may not only be due to the rectifying character of the p-contact but also to current crowding and SPV upon LED operation. While crowding was already considered to give a negligible contribution on $V_{2,3}$ in EE according to the calculations of Appendix 5.2, the latter mechanism is expected to produce sizeable effects on the basis of the results of Sec. 2.4.1. However, it has to be considered that the presence of the metal pillars in the apertures of these modified EE devices may strongly reduce the local SPV. Therefore, the results of the measurements carried out in the following are expected to mainly originate from the rectifying character of the p-contact on $V_{2,3}$ and not from SPV.

The potential measurements on the devices are carried out by electrostatic force microscopy (EFM) and conductive atomic force microscopy (C-AFM) using an electrically conductive n-doped Si tip (spring constant 2.8 N/m) covered with 20 nm of PtIr. The setup is used in two different modes:

- Sequential imaging of the topography by AFM and potential map by EFM: in every line scan, the sample topography is measured by AFM in tapping mode, then the tip is retracted few nm far from the sample to freely oscillate in EFM mode and repeat the line scan to measure the potential. This method allows to acquire an image of the potential distribution across the surface of the sample which, however, is only qualitative, as it will be explained;
- Local probe of the potential by C-AFM: the C-AFM tip is brought in electric contact at different points on the metal surface of the sample and the local potential is directly measured.

Two LED samples are studied with the I-V characteristics shown in Figure 48c (in blue, Walsin 8 QWs, 100 nm p-GaN, with EBL; in red, Seoul, 5 QWs, 100 nm p-GaN, no EBL). The corresponding ideality factors are plotted in Figure 48b. Once again the device with lower V_f exhibits a smaller n value (~2 blue curve, ~4 red curve), being close to n_{th}.

First of all the potential distribution across part of the current injecting region and a single pillar is mapped by EFM. A dynamic voltage difference $V_{ac} \sin \omega t$, where V_{ac} is of the order of 1 V (with respect to the sample metallic layer) and the angular frequency ω matches the lowest eigenmode of the cantilever (77 kHz), is applied between the scanning tip and the sample, which behave as the plates of a capacitor with capacitance C. In these conditions an electrodynamic force F is exerted on the tip and by lock-in detection of the tip deflection the term depending on ω can be obtained

$$\mathbf{F} = \frac{\mathbf{1}}{\mathbf{2}} \frac{\mathbf{\partial C}}{\mathbf{\partial z}} (\mathbf{V_{dc}} - \mathbf{V_s}) \cdot \mathbf{V_{ac}} \mathbf{\sin \omega t} \qquad (25)$$

where $\mathrm{V_{dc}}$ is the difference between the tip potential and the local sample potential at the tip position, $\mathrm{V_s}$ is the difference in the work functions of the sample and the tip, and $\partial \mathrm{C}/\partial \mathrm{z}$ is the partial derivative of the capacitance of the sample-tip system with respect to the tip altitude as referenced to the surface of the sample. In EFM mode, the feedback electronics yields, at each point of the AFM image, the value of $\mathrm{V_{dc}}$ which brings F to zero. In other words, the $\mathrm{V_{dc}}$ map yields the local value of $\mathrm{V_s} + \Delta \mathrm{V}$, $\Delta \mathrm{V}$ being the

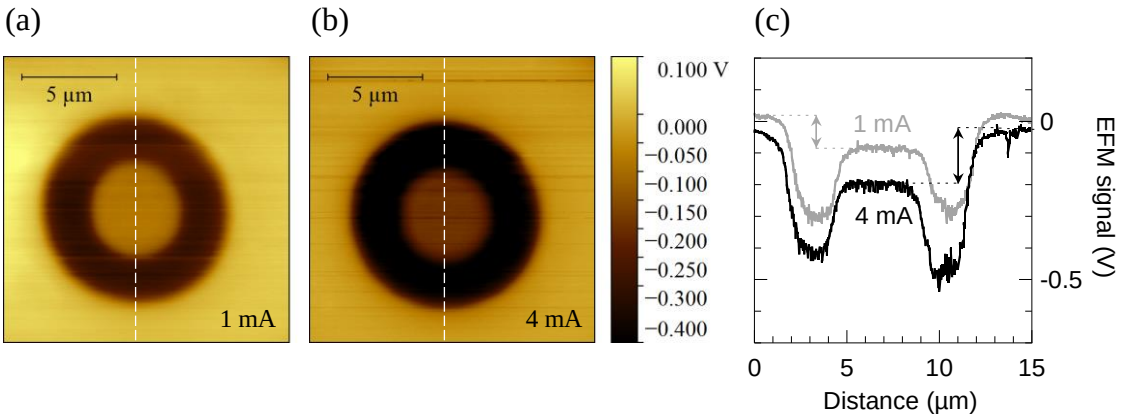

Figure 50 – Measured EFM maps revealing the inhomogeneity in EFM signal (related to Eq. (25)) among the p-contact and a pillar occurring in an LED with a rectifying p-contact upon current injection at: (a) 1 mA and (b) 4 mA. The EFM signal profile along the dashed lines of (a) and (b) is plotted in (c) showing that the inhomogeneity increases with current.

difference between the local potential and that applied to the metallic layer. However, extracting the value of V_{dc} is not straightforward because F may include contributions from the entire cantilever and not only from the tip. Therefore, the EFM measurement may provide ΔV values lower than expected, but the right quantitative trend of the potential distribution across the sample surface.

The EFM maps measured on the LED sample with higher V_f at I_{LED} of 1 mA and 4 mA are shown in Figure 50a and b, respectively. As it can be observed the EFM signal is rather uniform in the p-contact and in the pillar, exhibiting two different values in the two regions, which is ascribed to ΔV. (Note that, with respect to Eq. (25), V_s and $\boldsymbol{\partial C/\partial z}$ hold the same values in these two areas, as the pillar and the p-contact are fabricated with the same metal and have the same height. This is not the case for the exposed p-GaN annulus, which is not considered in the comparison.) Moreover, increasing the injected current in the LED, the difference in the EFM signal between the pillar and the p-contact increases indicating that a potential drop occurs at the p-GaN/metal interface (Figure 50c).

To quantify the potential drop across all the elements of the equivalent circuit at a given injected current in the LED, the local potential is measured by C-AFM at the nodes 2 and 3, i.e. at a point on the surface of the p-contact and of the pillar, respectively, while the potential at the nodes 1 and 4 is fixed by the applied bias. From these measurements the I-V characteristics of the different elements are directly obtained, as shown in Figure

48c. Both samples have an access resistance of the order of 10 Ω. Most importantly, the sample with $n \sim n_{th}$ exhibits, as expected, a nearly ohmic p-contact and the lowest voltage drop at the p-GaN/metal interface. Conversely, the p-contact of the sample with larger n clearly shows a rectifying character and a large voltage drop at the Schottky barrier. After removal of the p-contact contributions, the intrinsic I-V characteristics of the two p-n structures is very similar. The turn-on voltage of the Walsin sample is slightly larger than that of the Seoul sample (by ~70 mV), which may be due to the larger number of QWs in the active region and to the presence of the EBL.

The most important conclusion of this section is that the energy position of the high-energy peak observed in LED EE is strongly affected by the rectifying or ohmic behavior of the p-contact. The nature of the p-GaN/metal interface can be identified by deriving the ideality factor of the device. In EE experiments, the potential drop at the rectifying p-contact causes a high energy shift for electrons originating from bulk p-GaN. In addition, the surface potential across the apertures opened in the p-contact might be inhomogeneous. This potential inhomogeneity may be the source of a high-energy shift in the apparent energy (referred to the p-contact) of emitted electrons that originate from surface states. In EE experiments such energy shift should add up to that induced by SPV effects. The surface potential in the apertures of the p-contact of EE devices can be characterized by EFM and C-AFM. It is found to be lower than that at the p-contact, where current injection occurs. Shift of the aperture potential of a few 100 meV with respect to the p-contact potential were measured. The fact that, in well-behaved devices with low V_f and ohmic contacts, the high-energy peak observed in LED EE appears at much lower energy than in LEDs with rectifying contacts (Figure 47) might lead to re-evaluate the previously stated [5,87,131] agreement between the absolute energy position of this hot electron peak and the bulk position of the L valley in GaN.

2.5.4 Remedial actions

As an attempt to improve the ohmicity of the p-contact of EE devices, after vacuum annealing an ultrathin (1-2 nm) Pd spreading layer was deposited in UHV on top of the electron emitting region of the p-contact (inset of Figure 51a). The spot diameter of the deposited Pd layer is ~3 mm covering the entire apertures region. The spreading layer was deposited on two blue LEDs, one with V_f=3.15 V and the other with V_f=3.97 V at

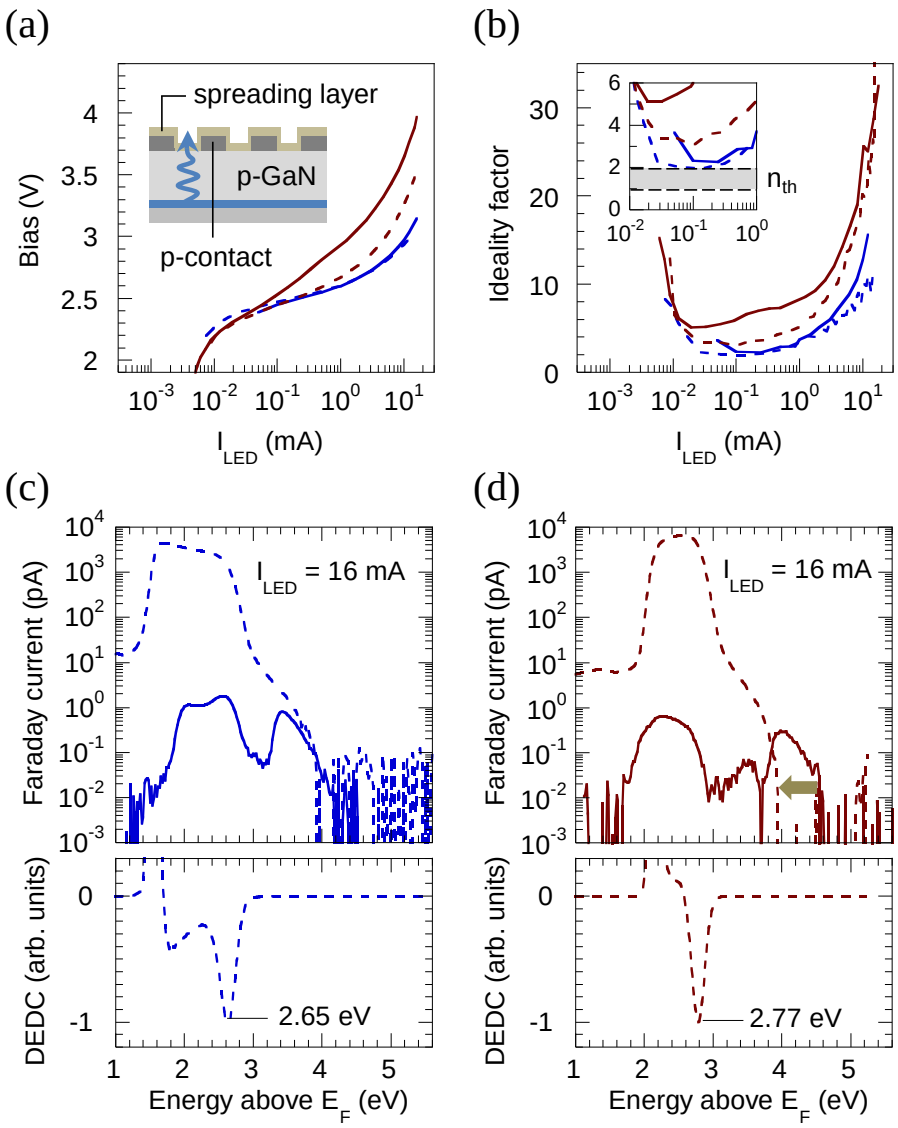

Figure 51 – Influence of a spreading layer deposition on the p-contact of two LED EE samples affecting their: (a) voltage-current characteristics; (b) ideality factors; (c) and (d) EE spectra. Both the curves measured prior (continuous lines) and after (dashed lines) deposition are plotted. Two devices are studied: one fabricated with an ohmic p-contact (blue lines) and the other fabricated with a rectifying p-contact (dark red lines), as determined from their minimum ideality factors, close or larger than the theoretical values for an ideal p-n junction.

16 mA, whose EDCs, I-V and n curves prior to deposition were shown in Figure 46 and Figure 47b and c (blue and dark red curves, respectively).

In Figure 51a,b the influence of the Pd spreading layer on the electrical characteristic of the two LEDs is studied by comparing the measurements prior (continuous lines) and after (dashed lines) deposition. The I-V curve of the sample with an initial low V_f was

substantially unchanged and the corresponding minimum ideality factor remained very close to the theoretical value of 2 predicted for a p-n junction dominated by carrier recombination in the space-charge region. Conversely, for the sample with an initial high V_f the spreading layer led to a considerable decrease in the forward voltage and the minimum ideality factor was lowered from ~5 to ~3 indicating the formation of a better ohmic contact.

The effect of the spreading layer on the EE curves of the two LEDs measured at 16 mA is shown in Figure 51c,d (dashed lines). Both samples exhibited a huge increase in EE signal (over 3 orders of magnitude). The main contribution of both spectra presents a high-energy inflection point (best seen on the DEDCs, cf. Figure 25) around 2.7-2.8 eV, in agreement with the peak EL energy of the LEDs, and is due to PE of the spreading layer excited by the internal light of the LEDs. Note that the dominant contribution to this signal must come from direct intense photoexcitation of the Pd layer deposited inside the p-GaN apertures (inset of Figure 51a), rather than from weak indirect reflections on the p-contact. From these observations, it can be inferred that, after deposition of the spreading layer, the voltage drop across the p-contact upon current injection in the LED is negligible (otherwise the high-energy inflection point would not be observed at $h\nu + E_F$) and the Fermi level in the apertures region is at equilibrium with that of the reference. In these conditions, on the high-energy side of the main peak, still a broad high-energy shoulder is observed (dashed line). This high-energy contribution is ascribed to electron emission from the semiconductor being related to the high-energy peak observed prior to Pd deposition (continuous line): its HET is observed to shift towards lower energy in the sample with an initial rectifying contact (arrow in Figure 51d) due to the improved ohmic character, while in the sample already fabricated with ohmic contacts the HET essentially does not shift (Figure 51c). This high-energy contribution may originate from super-energetic PE from p-GaN excited by the internal LED light, a phenomenon investigated in Sec. 2.4 and that will be examined in further details in Sec. 2.5.5 in the framework of LED EE.

It can be remarked that even though the issues of potential inhomogeneity across the electron emitting surface appear to be solved after the deposition of the spreading layer, still no Auger electrons are observed in the electro-emission of these devices neither at their expected ballistic energy (~5.6 eV above E_F [131]) nor at the L-valley energy. This may be explained by the relaxation of hot electrons due to electron-electron scattering in the metal spreading layer prior to emission into vacuum. However, it was

verified by complementary PE measurements on a control sample that hot photoelectrons excited in p-GaN at 5 eV above E_F are transmitted through a 1 nm Pd spreading layer with an attenuation factor of ~10. Therefore, an Auger current signal supposed to be emitted with a peak current of few 100 fA from a given LED sample without spreading layer should still be above the signal-to-noise ratio, at a typical noise level of 10 fA, after deposition of an ultrathin Pd layer. Other possible effects preventing the emission of Auger electrons in LED EE will be discussed in Sec. 2.6.1.1-2.6.1.3. Finally, it should be noted that the deposition of a spreading layer on LED EE samples, even though it can lead to an interesting analysis of the influence of potential inhomogeneity on EE, it cannot be considered as a practical solution to the issue of rectifying contacts in electro-luminescent samples since the EE spectrum is then almost completely dominated by the strong PE signal of the spreading layer. In the future the processing of EE devices will aim at the fabrication of ohmic contacts, which could be rapidly characterized by the inspection of their ideality factors.

2.5.5 Electro-emission of an LED with ohmic contacts

Given the results presented in the previous sections, it is clear that the interpretation of LED EE can be somewhat complicated by the electrical characteristic of the device under analysis. To minimize these effects, an available device with ohmic contacts, whose I-V chacteristic and ideality factor correspond to the blue curves of Figure 47b,c (Seoul 100 nm p-GaN with EBL), was selected to be analyzed, so that at low injected current (few mA) any shift in electron energy due to the applied bias can reasonably be neglected.

The light output power and EQE of the blue LED are shown in Figure 52b: the peak EQE corresponds to a current density of ~1 A/cm^2 and the droop regime begins at an injected current of few mA. The measured EDCs exhibit, as usual, three electron peaks (labelled ①,②,③ in Figure 52a). It was already concluded in Sec. 2.4.2 that the peak ③ is photoexcited by LED light at the p-contact. To get rid of this metal contribution, an external light beam mimicking the LED EL (Kr/Ar laser, $h\nu$ = 2.71 eV, 0.3 mW) is shined on a region of the p-contact without apertures and the measured EDC is subtracted, after proper normalization, from the LED EE spectrum measured at 1 mA (Figure 52c). The residual spectrum (gray curve in Figure 52c) is expected to be due to emission from the semiconductor and exhibits two contributions, corresponding to peaks ② and ①: a low-energy one emitted below $h\nu + E_F$ and a high-energy one

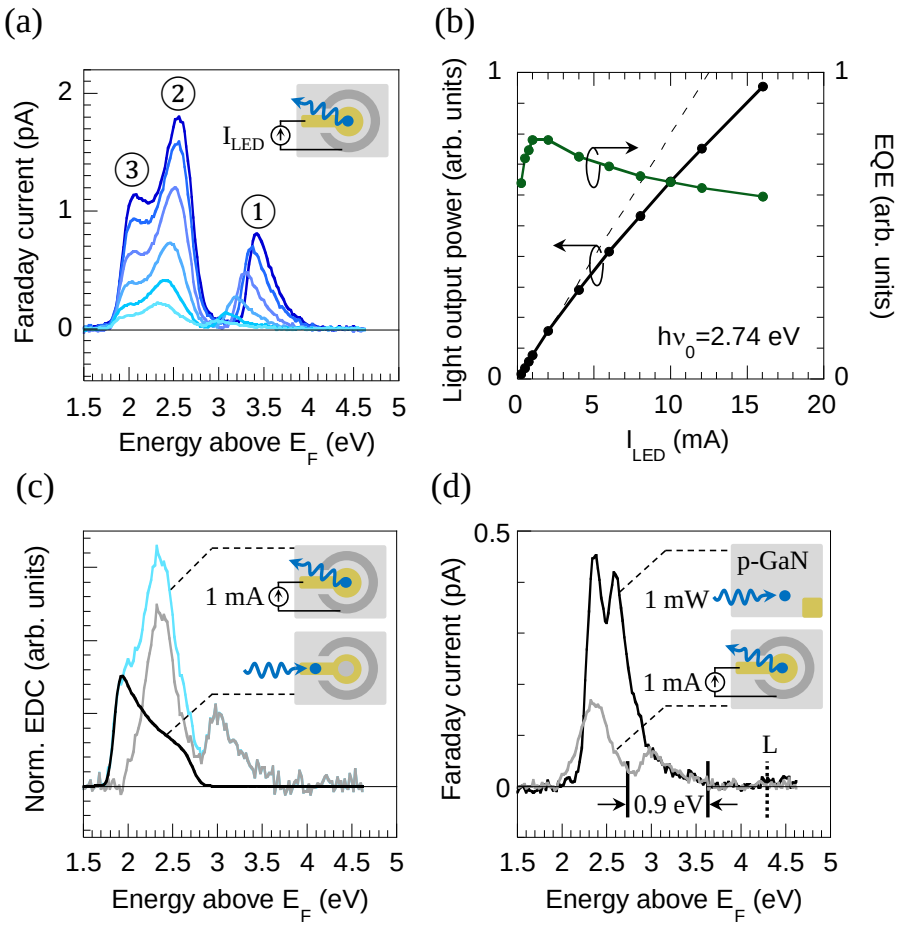

Figure 52 – (a) EE spectra measured as a function of the injected current (from bottom top, in mA: 1, 2, 4, 8, 12, 16) in an LED (Seoul, 100 nm p-GaN with EBL) with an ohmic p-contact, whose I-V characteristic and ideality factor are shown in Figure 47b,c as blue curves. (b) Light output power and external quantum efficiency of the LED. The dashed line is the expected optical power in the absence of droop, extrapolated from low currents. (c) Plotted in black is the PE spectrum photoexcited on a region of the p-contact without apertures at $h\nu$ = 2.71 eV. After subtraction of this metal contribution from the EE spectrum at 1 mA (light blue curve) the residual LED EE spectrum is obtained (gray curve). (d) Comparison of the residual spectrum at 1 mA from (c) with a below-gap PE spectrum measured on a bare p-GaN surface exciting at $h\nu$ = 2.71 eV and a power of 1 mW (from the series of measurements of Figure 33).

emitted above this threshold, which is reminiscent of the super-energetic photoemission process previously observed on bare p-GaN surfaces.

The residual spectrum from LED EE at 1 mA is compared in Figure 52d with the PE spectrum measured on a bare p-GaN surface exciting at $h\nu$ = 2.71 eV (Kr/Ar laser) with

an external power of 1 mW (series of PE measurements shown in Figure 33). The choice of the excitation power used for the comparison is based on the LED current-PE power equivalence curve of Figure 41 ("PE sample" curve). A remarkable qualitative and quantitative agreement is observed among the two spectra:

- Qualitatively, both spectra exhibit two electron peaks, a similar spectral width and the same spectral HET. On the basis of the observations of the PE

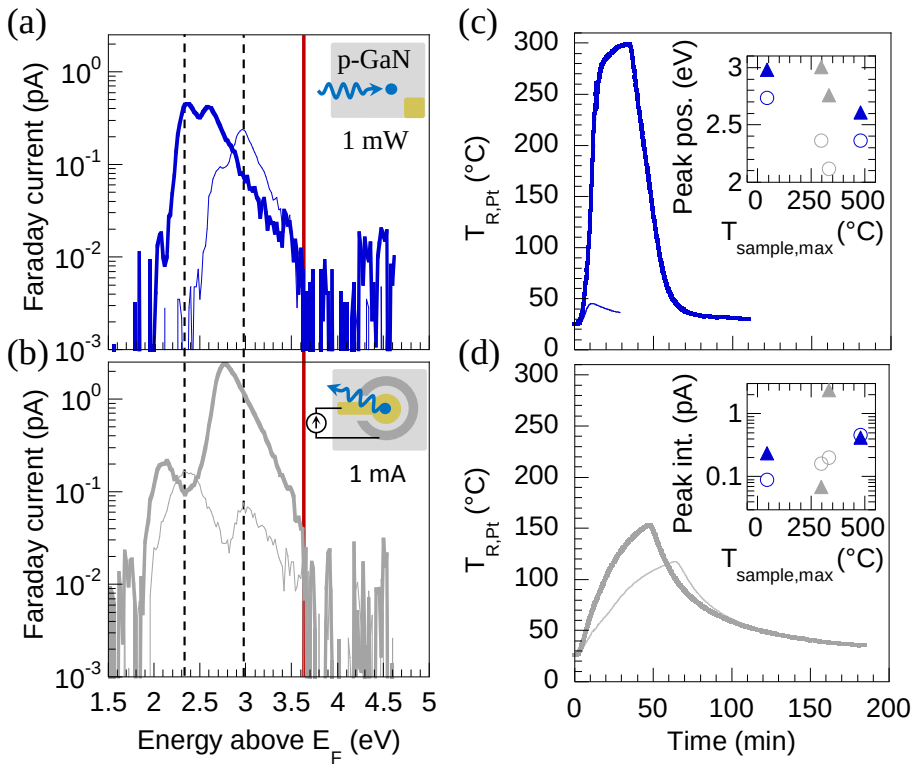

Figure 53 – Influence of surface preparation on the PE and EE spectra of Figure 52d. (a) Below-gap PE spectra measured on a p-GaN sample exciting at $h\nu$=2.71 eV and 1 mW. (b) EE spectra measured at I_{LED}=1 mA (the low-energy metal PE contribution was subtracted as in Figure 52c). The vertical lines extending in (a) and (b) are guides to the eye for the spectral HET (red line) and different peak positions (dashed lines) of the EDCs. The surface preparations leading to the EDCs shown in (a) and (b) are shown in (c) and (d), respectively, where the higher (lower) temperature annealing cycles correspond to thick (thin) curves. The insets in (c) and (d) show the position of the peak maxima and their intensities as a function of the maximum annealing temperature of the sample (triangles for the high-energy peaks, circles for the lower energy peaks; blue symbols for PE, grey symbols for EE).

measurements (Figure 33a), it can be assumed that the HET of the peak at lower energy is at $h\nu + E_F$ giving an energy separation between the two peaks of ~0.9 eV. Once again, it should be noted that the HET of the spectrum lies well below the energy position of the L valley in bulk p-GaN, as determined by near-band gap PES (marked "L" in Figure 52d), and therefore direct emission of electrons accumulated at the bottom of the L valley in the bulk can be excluded in both experiments;

- Quantitatively, considering that the measurements are carried out on different samples with different surface preparation and that the LED current-PE power equivalence is only an estimation, the difference of a factor 2× in the integrated current is reasonable.

It should be remarked that the efficiency of the below-gap PE process (defined as the number of emitted electrons per incident photons transmitted into p-GaN), as measured in Sec. 2.4.1, is very small, being of the order of ~10^{-6}. Assuming that the PE efficiency is close to the light fraction absorbed in the p-GaN layer (i.e. supposing that for each absorbed photon in p-GaN a photoelectron is emitted into vacuum with a surface escape probability close to unity – this evaluation neglects multi-photon transitions), it could be deduced that the photon losses occurring in p-GaN due to the considered photoelectric mechanism play a negligible role in the droop of the LED.

Finally, we note that the lineshape of the two contributions and, in particular, the position and intensity of the maxima of the two peaks (but not their HETs), are influenced by the surface preparation, both in PE and EE experiments, as it may be expected for peaks that are generated at the surface of the semiconductor. Moreover, it should be remarked that EE devices may have a surface presenting more impurities than simple PE samples due to the photolithography processing of the contacts. As an illustration of these effects, the EDCs measured in PE and EE corresponding to different annealing cycles shown in Figure 53c,d (in particular, for different maxima of $T_{R_{Pt}}$, where the corresponding $T_{sample,max}$ is obtained using Eq. (4)), are shown in Figure 53a,b. As a general trend, it can be observed that increasing the maximum annealing temperature the energy positions of all peaks decrease (inset of Figure 53c), while the corresponding peak intensities increase (inset of Figure 53d). However, independently of the specific surface preparation, in EE and PE excitations corresponding to similar optical power at the p-GaN surface (Figure 41) all the EDCs exhibit two common

features, namely the presence of two peaks and the same spectral HET, and for this reason can be expected to originate from the same mechanism, namely a below-gap PE process. The exact microscopic process responsible for the observed dependence on surface preparation of the spectral lineshape of the EDCs remains to be determined. In Sec. 2.6 future studies will be proposed allowing to test different hypotheses for the origin of these peaks.

2.6 Discussion and perspectives

In the present section, the main results reported in this chapter will be summarized and the specific difficulties related to different spectroscopic measurements of electronic transport in nitrides will be discussed. In all cases the main problem is to determine the correct energy reference, which is central in spectroscopy studies. As a consequence, the identification of the origin of the observed phenomena is uncertain and several interpretations are possible. Future studies which may allow testing the different hypotheses and identify the origin of the electron peaks will be proposed.

2.6.1 Discussion

Several spectroscopic techniques, mainly consisting of different electron emission techniques, were employed in the studies presented in this chapter to characterize the electronic transport and the photoelectric processes occurring in nitride materials and devices.

Near-band gap photoemission spectroscopy allowed the determination of important parameters of the conduction band of GaN (Sec. 2.3). The intervalley energy separation between the conduction band minimum Γ and the first satellite valley, named L, acting as a high-energy accumulation point for hot electrons, was established to be $\Delta E_{\Gamma,L} = 0.90 \pm 0.08$ eV. Moreover, the dispersion of the final state energies of ballistic photoelectrons as a function of the exciting photon energy was measured showing the effect of nonparabolicity of the bands away from the Γ point. Further insights into the position of the satellite valley in the Brillouin zone of the crystal could be given in the future by measurements with a resolution in k-space, such as angle-resolved photoemission spectroscopy (ARPES).

Below-gap photoemission studies of different GaN-based samples (Sec. 2.4.1) revealed the existence of an anomalous photoemission process capable of generating "super-energetic" photoelectrons with emission energies well above the expected maximum threshold $h\nu + E_F$ for excitation at $h\nu$. Several features of this process suggest the concomitant occurrence of a photoexcitation mechanism from surface states and of a surface photovoltage effect in the p-GaN layer upon intense illumination. The dependence of this process on several factors, such as light source, photon energy, optical power, p-GaN doping concentration and sample temperature, was characterized. However, the origin of these anomalous contributions is still not completely identified.

A combination of electro-emission and below-gap photoemission measurements in nitride LEDs showed that different photoelectric processes may be excited in the structures by the internal LED electro-luminescence (Sec. 2.4.2), leading to the photocreation of a low-energy peak emitted from the metallic p-contact and hot electrons emitted from p-GaN. But, in the excitation configuration of these experiments, the photoemission quantum yield of the metal is orders of magnitude larger than that of the semiconductor. As a consequence, in such PE+EE studies the electron spectrum is dominated by an intense peak due to metal PE, while the emission from the semiconductor appears as a much weaker high-energy contribution, which therefore cannot be easily characterized.

Electro-emission measurements of different LEDs showed that the absolute energy position of the hot electron peak is correlated with the electrical characteristic of the device (Sec. 2.5.2), with values scattered over a large range of ~1 eV for the considered ensemble of samples. This dispersion of values is ascribed to a different degree of potential inhomogeneity in the electron emitting surface of the devices, which is directly related with the ohmic/rectifying character of the p-contact.

Electrostatic force microscopy and conductive atom force microscopy measurements aimed at characterizing the surface potential in the LEDs as a function of the current injected in the device (2.5.3). A problem associated with the first technique is that the measured potential may include contributions from the entire cantilever and not only from the tip, complicating significantly the quantitative determination of the local potential. On the other hand, the second type of measurements requires the processing of ad-hoc contacts of the LED devices, namely the deposition of metal pillars inside the apertures of the p-contact, making the comparison with electro-emission measurements not straightforward.

With the exception of near-band gap photoemission spectroscopy, where both the optical excitation power and the current flowing between the p-contact and the semiconductor were relatively low, the common issue observed in all types of spectroscopies, whether arising from intense optical excitation or sizeable current injected in a device, concerns the difficulty in establishing the correct energy reference at the surface of the semiconductor. This in turn impacts the electron spectroscopy and thus the origin of the different observed phenomena cannot be easily identified. In particular, several interpretations concerning the origin of the electron peaks emitted in LED electro-emission are possible. In addition to the Auger interpretation described in

Sec. 2.1, a combination of anomalous photoemission processes internally excited by LED light in p-GaN and a spectral shift due to the rectifying character of the p-contact of some devices could explain the appearance of hot electrons in LED electro-emission spectra (Sec. 2.5.5), and could also appear concurrently to Auger generated electrons. The dominant process among these still has to be identified, and possible experiments to test the different hypotheses will be suggested.

If we accept the hypothesis that no Auger electrons are observed and that EE spectroscopy is not sensitive to droop-related electronic processes, an important question can be raised: assuming that Auger recombination is the dominant droop mechanism, as pointed out by an increasing number of experiments [45,46,48,52,132,133], why no Auger electrons are measured? Different physical mechanisms which may prevent their observation in EE are listed below.

2.6.1.1 h-h-e Auger recombination dominates?

As the EE technique does not allow to measure holes, if the h-h-e process producing a

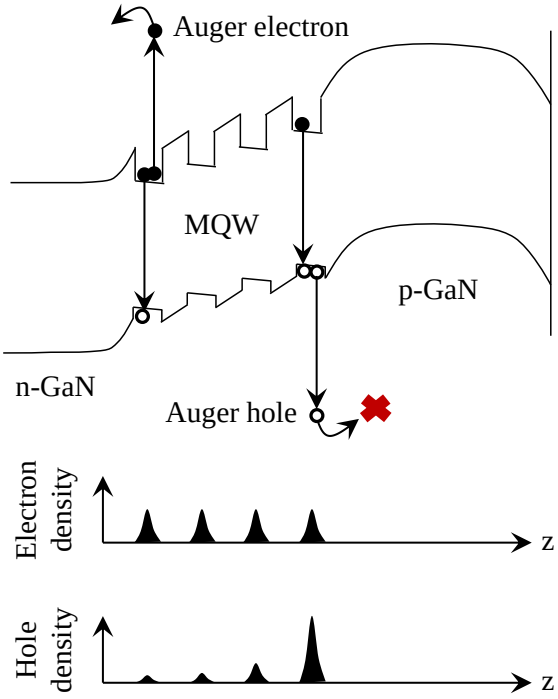

Figure 54 – Schematic of a MQW LED structure with a strongly inhomogeneous hole distribution among the different QWs due to localization. In this condition the dominant Auger process in the QW closest to the surface is of h-h-e type, therefore generating hot Auger holes which cannot be measured by the EE technique.

hot hole was the dominating mechanism of Auger recombination then possibly no Auger signal may be detected in LED EE.

In terms of the Auger coefficients, Kioupakis *et al.* [43] obtained by first-principles calculations, taking into account the influence of alloy disorder on the final states of Auger transitions, that in $In_{0.25}Ga_{0.75}N$ the h-h-e and e-e-h Auger coefficients have almost the same value (2-4·10^{-31} cm^6/s for h-h-e depending on the resolution of the k-grids, and 3·10^{-31} cm^6/s for e-e-h). A different theoretical approach allowing to calculate the influence of carrier localization on the Auger coefficients as based on a new theory of localization (Chapter 3) is currently under study. The principle is the following: strong spatial confinement due to disorder increases the range of k-vectors constituting a localized wave packet. Since in an Auger transition final states have large k-vectors, and because of momentum conservation [134], the scattering rate of the process can be enhanced by localization. Then, as holes are typically more localized than electrons, due to their heavier effective mass, the h-h-e Auger coefficient is expected to be considerably larger than the e-e-h Auger coefficient. Preliminary studies suggest that this hypothesis is correct.

On the experimental side, Galler *et al.* [135] combined photoluminescence measurements of SQW structures with different background electron or hole densities with an ABC model to deduce that the e-e-h Auger process dominates in InGaN. However, it should be considered that in MQW structures, such as the LEDs studied here by EE, carrier distribution among the different QWs can be very inhomogeneous due to disorder-induced localization. Calculations based on the localization landscape theory (Chapter 3) predict a rather uniform electron concentration but a strongly inhomogeneous hole distribution. Such conditions may lead to a large h-h-e Auger rate, proportional to p^2n, in the QW closest to the p-GaN layer and therefore produce hot carriers not detectable in EE (Figure 54). In this case future EE measurements of a SQW structure could avoid this issue and lead to a larger population of Auger electrons in the p-GaN layer potentially contributing to emission into vacuum.

2.6.1.2 Internal electric fields prevent electron emission?

As it was shown by EFM measurements, the electron emitting apertures of LED EE devices suffer from surface potential inhomogeneity, namely the potential is lower (therefore the electron energy is higher) in the p-GaN apertures with respect to the regions of the p-contact where current injection occurs (cf. band diagram in Figure

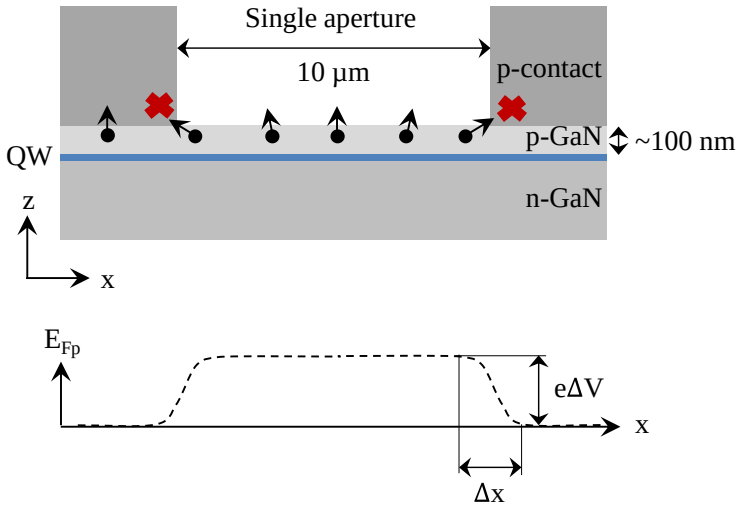

Figure 55 – Schematic of a single aperture in the p-contact of LED EE devices. Due to a surface in-plane inhomogeneity in the position of the quasi-Fermi level, the velocity of electrons reaching the surface of the p-GaN layer will have a component parallel to the plane which can drift them below the p-contact and prevent their emission into vacuum.

48d,e). Such potential gradient may induce an electric field parallel to the p-GaN layer increasing the drift velocity of the electrons reaching the surface and possibly "hiding" some carriers below the p-contact, where these would be absorbed by the metal without emission into vacuum (Figure 55). But, unless the parallel electric field is sufficiently strong along the entire aperture, this drift effect will only influence the Auger electrons reaching the surface close to the aperture edges and lead to a small reduction of the Auger current emitted from the aperture. As an estimation, it can be considered that the potential energy difference $e\Delta V$ between the aperture and the p-contact due to a Schottky barrier and/or SPV is of the order of 1 eV, then taking the length of the transition region Δx=2 µm [136] and the electron mobility as 300 $cm^2/V \cdot s$ [137], a parallel drift velocity of ~10^4 m/s is obtained, much smaller than the thermal velocity of few 10^5 m/s (at 300 K) and affecting only ~20% of the electron population generated inside the aperture. Such effect seems thus to be negligible.

2.6.1.3 Short hot-electron mean-free-path in p-GaN?

Another possible explanation which may prevent the observation of Auger electrons in EE could be related with the mean free path of hot electrons. If the Auger electrons generated in the active region of the LED thermalize to the bottom of the conduction band on a distance appreciably shorter than the thickness of the p-GaN layer, then it

would be possible that no hot electrons originating from the QWs can be observed at the p-GaN surface.

There are few experimental determinations of the minority carrier diffusion length (L_d) in p-GaN [138–141] corresponding to the mean free path of thermalized electrons (see Figure 56a) but, to the best of the author's knowledge, no experiment aimed at extracting the mean free path of hot electrons in p-GaN.

According to Spicer's theory of photocathodes based on the "three-step model" of PE [101] from a measurement of the PE QY of a NEA photocathode at different excitation energies $h\nu$ it is possible to extract the escape length (L_e), or mean free path, of hot electrons using the following relation:

$$\mathbf{QY} = \frac{\boldsymbol{\alpha_\phi} \cdot \mathbf{P_e}}{\mathbf{1} + \frac{\mathbf{l_\alpha}}{\mathbf{L_e}}} \qquad \mathbf{(26)}$$

where all quantities depend on $h\nu$, α_ϕ is the absorption probability above the vacuum level being ~1 for $h\nu$ larger than the work function of the photocathode, P_e is the escape probability at the surface/vacuum interface typically ranging between 30% and 60% in high-yield cathodes [142] and $\boldsymbol{l_\alpha}$ is the optical absorption depth. The QY of the p-n junction structure described at page 78 (notably, 1 µm thick p-GaN layer and [Mg] = $2\cdot10^{19}$ cm^{-3}, which should correspond to a hole concentration of few 10^{17} cm^{-3} [19]) was measured at several above-gap excitation energies and plotted in Figure 56b. The excitation power is of the order of 1 µW (focused lamp spot diameter ~500 µm). The initial hot electron energy after photoexcitation was deduced using a parabolic model with $m_e^* = 0.22m_0$ and $m_{hh,z}^* = 1.58m_0$, observed in Sec. 2.3.4 to be accurate up to $h\nu \sim 4.5$ eV. Taking $\boldsymbol{l_\alpha}$ from Ref. [100] and assuming $\boldsymbol{P_e}$ to be constant with $h\nu$, being 30% or 60%, the escape length curves of Figure 56b are obtained. By definition, $L_e(h\nu = E_g) \equiv L_d$ and, by averaging the values derived from the two estimations of $\boldsymbol{P_e}$, a minority carrier diffusion length of 27 ± 11 nm in the p-GaN layer is deduced, close to the determination of 21.3 nm in p-GaN (hole concentration $1\text{-}2\cdot10^{17}$ cm^{-3}) of Ref. [139].

However for hot electrons the discrepancy between the two L_e curves increases as the dependence on $\boldsymbol{P_e}$ becomes much more important. Let us assume the value of L_e=26 nm, obtained for hot electrons at 1 eV above the CBM using $\boldsymbol{P_e}$=60%, as the mean free path of Auger electrons in p-GaN. Then an estimation for the Auger current expected to be measured on the Faraday cup in LED EE can be given. The sample studied in Figure

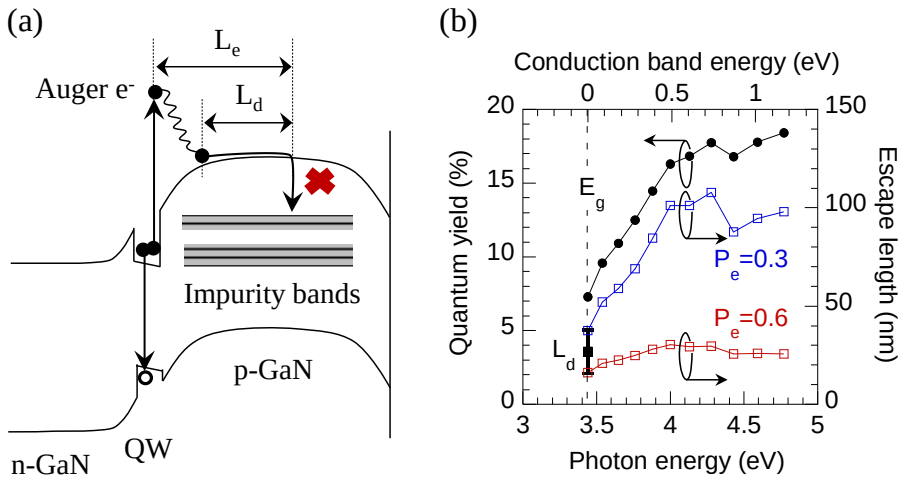

Figure 56 – (a) Schematic of Auger electron transport in the p-GaN layer of an LED. If the escape length of the hot electron (L_e) is much shorter than the thickness of the p-layer, a large fraction of Auger electrons will recombine before reaching the p-surface. Also shown the diffusion length of a thermalized electron (L_d). (b) PE QY measured on a p-n junction sample as a function of $h\nu$. The CB energy of the photoexcited hot electrons is deduced using a parabolic model (Sec. 2.3.4). Also shown the escape length curves calculated from Eq. (26) using different parameters for the surface escape probability P_e. A value of L_d = 27±11 nm is obtained for the minority carrier diffusion length in p-GaN ([Mg] = $2 \cdot 10^{19}$ cm^{-3}).

52a,b is considered, having a distance t=130 nm between the active region and the p-surface (taking the total thickness of the EBL and p-GaN layer, where electrons are assumed to have the same L_e=26 nm). The expected Faraday current I_F due to Auger electrons at I_{LED} = 16 mA can be estimated as:

$$\mathbf{I_F = I_{droop} \cdot e^{-\frac{t}{L_e}} \cdot \frac{1}{2} \cdot f_{ap} \cdot QY \cdot T_{an}} \qquad \mathbf{(27)}$$

where I_{droop} = 4 mA (Figure 52b), the $1/2$ factor accounts for the Auger emission in the direction opposite to the surface, f_{ap} =25% is the filling factor of the p-GaN apertures in the p-contact, a QY of 20% is assumed (Figure 56b) and the electron analyzer transmission is 0.5%.

From Eq. (27) it is obtained I_F = 3 nA, which would definitely be measurable by our electron analyzer (assuming a spectral width of few eV as usual). For comparison, it can be considered that the integrated Faraday current corresponding to the EDC of Figure

52b measured at I_{LED} = 16 mA is 70 pA. On the other hand, fixing our detection limit to $\boldsymbol{I_F}$ = 1 pA it can be calculated, maintaining all other parameters unvaried, that a mean free path shorter than 10 nm would be sufficient to make the Auger current undetectable. Therefore, a precise measurement of L_e is needed to reach a conclusion. There are currently other measurements in progress to determine L_e: 1) a p-n junction series of samples with different thicknesses of the p-GaN layer but the same [Mg] and crystal quality is under study. From the measurement of the cathode current in EE, L_d should be obtained; 2) local injection by scanning tunneling microscopy (STM) on the p-surface of GaN-based structures has already shown that electrons can diffuse in the p-GaN layer and reach an underlying QW recombining radiatively [143]. At the moment, measurements attempting to inject the electrons in the p-GaN layer along the growth direction and using the QW luminescence as a detector for the extraction of the electron mean free path are in progress. The advantage of this technique with respect to that mentioned at point 1) is that the injection energy of the electrons can be controlled by applying a bias between the STM tip and the sample, thus allowing in principle to measure L_e for hot electrons.

In addition to these experiments, as according to Eq. (27) I_F should decrease exponentially with t, LEDs with etched p-GaN layers are also being currently studied by EE, which should lead to an increase in the Auger emission signal, if this is limited by the mean free path of hot electrons in p-GaN.

2.6.2 Future studies and perspectives

Some experiments are proposed in order to test the different hypotheses concerning the origin of the electron peaks emitted in LED electro-emission.

Comparing a device having a large diameter single aperture in the p-contact, e.g. of the order of 2 mm, with a device having the usual p-contact grid should allow to strongly change the balance between electro-emission and parasitic below band gap photoemission. The large aperture device should favor parasitic below-gap PE, because of the large exposed p-GaN surface, and at the same time it should disadvantage Auger electron emission, because of a reduced emitting surface near the contact edge due to current crowding, from where Auger recombination is expected to emerge. Moreover, this sample would allow to externally photoexcite below-gap photoemission in p-GaN without exciting photoemission from the metal (considering the typical laser spot size of 200 μm).

InGaN/GaN LEDs with QWs emitting at other wavelengths than in the blue range, for instance a UV and a green LED, could be studied. First of all, such devices should have different droop behavior and thus different Auger electron emission signals. Moreover, the transport of Auger electrons should be mediated by the different conduction band valleys and therefore the Auger-related emission energy should not depend on the LED emission energy (providing that the recombination energy is large enough to excite Auger electrons above the side valleys of GaN). In contrast, parasitic below-gap photoemission should change.

Finally, let us give some overall considerations on the EE spectroscopy technique going beyond the study of nitride LEDs for the understanding of the origin of droop. EE spectroscopy has a decisive advantage over usual transport experiments based on electrical measurements as it allows extending the spectroscopic tool to the whole range of conduction band states. This technique is in its infancy as, apart from basic studies on cold cathodes [144], it has started developing only in 2013 after the pioneer work of Iveland *et al.* [53] and its applications to other devices still have to be explored. To verify that in a well-known semiconductor system an Auger emission current can be detected, GaAs/AlGaAs LEDs could be studied in EE, where the Auger coefficient is expected to be of the same order of magnitude of that in GaN [145]. Electro-luminescent devices may not be ideal from the point of view of EE spectroscopy as the photoelectric processes that may occur at the surface could affect the EE spectrum. However, it should be considered that the threshold for well-behaved PE is $h\nu \geq \phi$, where $h\nu$ is the photon energy of the EL device, typically not larger than the gap of the cap p-layer, and ϕ is the work function of the p-surface activated to NEA, usually around 2 eV. Thus, in narrow-gap semiconductors where $h\nu < \phi$, the hot electron spectroscopy should not be compromised (excluding the existence of super-energetic PE processes). Lastly it would be also interesting to carry out EE spectroscopy of commutation devices, where the intensity of EL should be negligible, for instance to study the transport properties of unipolar transistors or the tunneling transmission through barriers in polar and semipolar heterostructures, with the caveat of having a p-type surface in order to achieve the condition of effective NEA.

3 LOCALIZATION LANDSCAPE THEORY OF DISORDER IN NITRIDES

This chapter focuses on the study of localization effects induced by compositional disorder in optoelectronic devices incorporating heterostructures constituted by ternary alloys, such as InGaN QWs. An overview of the origin of compositional disorder in nitrides and its characterization by APT was given in Sec. 1.2.3. The effect of compositional disorder on the properties and performances of nitride devices is still not clearly identified. The following studies involve an experimental and a theoretical part. On the experimental side, the developed approach consists in measuring the variation of photocurrent in InGaN/GaN solar cells structures as a function of the excitation energy. In these devices, as the photocarrier extraction yield is close to unity, the photocurrent measurement give a direct access to the QW absorption. For an excitation energy smaller than the band gap energy of the QWs, the measurements exhibit an absorption tail, known as Urbach tail, that is related to the disorder-induced localization of the electronic states. The dependence of the Urbach tail with the bias applied to the junction shows a shift towards high-energies (blue-shift) compatible with the compensation of the piezo-electric field in the QWs. A theoretical description of absorption in the QWs composed by ternary alloys is also given. This description is based on an approach to localization in disordered systems recently developed by Marcel Filoche at Ecole Polytechnique and coworkers [146,147], allowing for the first time to determine the

localization landscape solving a linear problem rather than the eigenvalue Schrödinger equation associated with the system. In this treatment, the compositional fluctuations of the alloy that are taken as an input in the calculations have the statistical properties of APT data. For the different studied structures, in which the alloy composition constituting the QWs varies between 0 and 30%, the simulations of the Urbach tail are in excellent agreement with the photocurrent spectroscopy measurements. In addition to this, a novel method to model nitride LEDs is introduced, accounting for quantum disorder effects into the classical Poisson and drift-diffusion equations through the localization landscape theory. Simulations are developed jointly with the group of Yuh-Renn Wu at the National Taiwan University. This model can not only solve the carrier dynamics with quantum effects self-consistently but provide a much faster solver compared to those based on the Schrödinger equation, significantly reducing the computation time and so giving access to simulations of entire devices. The current-voltage characteristics and efficiency droop modeled by 3D simulation of a full LED structure with compositional material fluctuations represent well the experimental behavior of high quality blue LEDs.

The following sections will present:

- The elements of the localization landscape theory allowing to compute the localization and transport properties in disordered semiconductor structures (Sec. 3.1);
- The experimental characterization of compositional disorder by biased photocurrent spectroscopy measurements in nitride solar cells allowing to validate the new theoretical approach (Sec. 3.2);
- The application of the localization landscape theory to the modeling of nitride LEDs (Sec. 3.3).

3.1 Theory and modeling

Alloy semiconductors are ubiquitous in many modern semiconductors devices because of the impact of heterostructured materials on device performances (see e.g. Ref. [148]). The main property used is the band gap difference between the materials associated in the heterostructures. However, due to the large lattice mismatch between pure compound semiconductors which would lead to highly defective materials if employed as such, one has to associate binary compounds and alloys of binary compounds, leading to ternary alloys, eventually quaternary alloys, to obtain materials with sufficiently nearby lattice constants to obtain growth of high quality materials. One thus retains part of the band gap discontinuities between the binary compounds which allows to confine carriers in double heterostructures or QWs [149,150]. An additional useful property is the modulation of the refractive index which proved to be a beneficial effect of crucial importance to achieve room-temperature CW lasers, opening the way to optical telecommunications systems. Many other properties are impacted by alloying, some of them not desirable: for instance, the compositional fluctuations induce an additional scattering mechanism for charge carriers which diminishes the carrier mobilities.

GaN-based compounds maybe display the largest variety of properties of heterostructures and alloys. In addition to the usual ones, they also have, due to their large ionic composition and crystalline structure (most often wurtzite along the c-axis), spontaneous and piezoelectric fields, which impact strongly electrical and optical properties [23]. They also exhibit significant effects of the intrinsic spatial compositional fluctuations of their alloys. The random indium content in InGaN multiple quantum well (MQW) structures can vary locally from 10% to 23% within a few nanometers, for an average composition value of 17% [20]. These fluctuations can induce a strong modification of carrier spatial distributions, of recombination rates, and of the overall light emission efficiency of the device. They have long been invoked as being responsible for the short carrier diffusion lengths which in turn lead to high emission efficiencies in spite of the high density of defects still present in the best grown heterostructures [151].

Accounting for carrier localization induced by the local material disorder in semiconductor materials and devices is a daunting task. Classically, it requires solving the Schrödinger equation (both for electrons and holes) for random realizations of the disordered potential, and determining the energies and the spatial structure of the

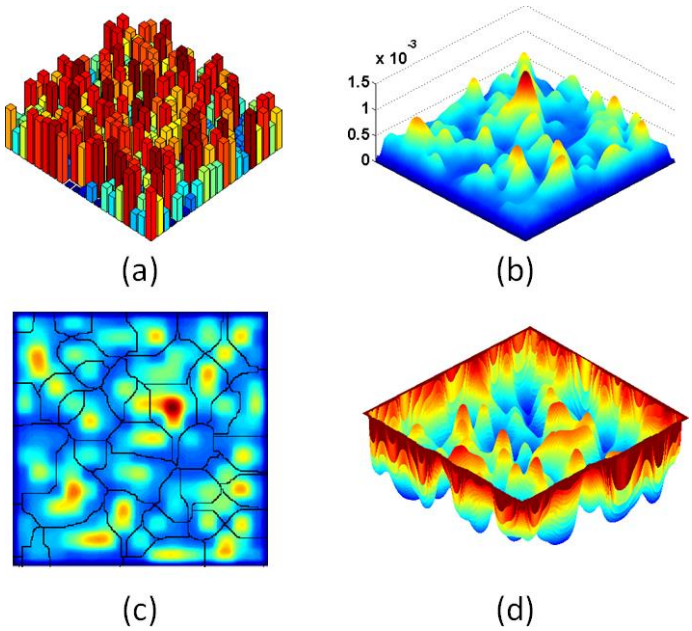

Figure 57: The localization landscape theory: (a) 3D representation of the original disordered potential V. (b) 3D representation of the landscape u solving Eq. (29). (c) The valley lines of the landscape u (black lines) delimit the various localization regions. (d) Effective localization potential $W \equiv 1/u$. The valley lines of u are now the crest lines of W, and the localization subregions outlined in (c) are the basins of W.

localized quantum states. Actually, this problem relates to the famous Anderson localization phenomenon [152] for which many questions remain open, despite more than 50 years of research. One of the most puzzling aspects of this phenomenon is the origin of the strong spatial confinement of the one-particle quantum states, attributed to destructive interferences occurring between different propagation pathways in the disordered potential. A recent theory has been proposed, allowing to accurately predict the localization regions of the carriers, and the DOS in the disordered potential created by the fluctuations of material composition, without having to solve the Schrödinger equation [146,147]. This groundbreaking theory is based on a new mathematical tool, the localization landscape, which is the solution to a Schrödinger-like equation with uniform and constant right-hand side.

In the following the implementation of this tool into semiconductor materials and its use in a semi-classical transport model of semiconductor devices will be presented. It will be shown how the formalism of the localization landscape enables to efficiently predict in semiconductor structures the wave functions and eigenenergies of the confined states,

the overlap between electrons and holes, the DOS, and the carrier distribution. This implementation conserves a local formulation, adding only to Poisson and transport equations a new PDE, and accelerates the computation time by several orders of magnitude compared to the Schrödinger-Poisson-transport type approach. Later in this chapter this approach will be applied to the specific case of nitride semiconductors, one showing experiments and theory of the Urbach tail of InGaN quantum wells (Sec. 3.2), the other on the simulation of full LED structures (Sec. 3.3).

3.1.1 The localization landscape theory

Let us start by presenting the main features of the localization theory exposed in Ref. [146,147]. In this theory, the precise spatial location of quantum states in a potential $V(\vec{r})$ can be predicted using the solution $u(\vec{r})$ of a simple associated Dirichlet problem, called the localization landscape. While the quantum states and the energies of particles with mass m are respectively the eigenfunctions and the eigenvalues of the Hamiltonian of the system defined as

$$\widehat{\mathbf{H}} = -\frac{\hbar^2}{2m}\mathbf{\Delta} + \boldsymbol{V} \qquad \textbf{(28)}$$

the landscape u is defined as the solution of

$$\widehat{\mathbf{H}}\boldsymbol{u} = -\frac{\hbar^2}{2m}\mathbf{\Delta u} + \boldsymbol{Vu} = \mathbf{1} \qquad \textbf{(29)}$$

the boundary conditions being either Dirichlet, Neumann, or periodic. In this theory, the localization subregions, i.e. the regions of lower energy solutions of the Schrödinger equation, are delimited by the valley lines of the graph of u, see Figure 57a,b. This property directly derives from a fundamental inequality satisfied by any eigenfunction ψ of $\widehat{H}$ with eigenvalue E, normalized so that its maximum amplitude is equal to 1 (see Ref. [146] for the proof):

$$|\boldsymbol{\psi}(\vec{\boldsymbol{r}})| \leq \mathbf{E}\ \mathbf{u}(\vec{\boldsymbol{r}}) \qquad \textbf{(30)}$$

In other words, the small values of u along its valley lines [146] constrain the amplitude of ψ to be small along the same lines and, as a consequence, localize low energy eigenfunctions inside the regions enclosed by these lines. But, as we will now see, more spatial information can be extracted from the localization landscape u.

3.1.1.1 The effective localization potential

Not only $u(\vec{r})$ controls the eigenfunctions, but also the function $W(\vec{r}) \equiv 1/u(\vec{r})$ (homogeneous to an energy) can be interpreted as a confining potential that is related for instance to the exponential decay of the Anderson localized states, even far from their main localization subregion. This property can be proved by transforming the original Schrödinger equation through the introduction of an auxiliary function ψ_1 such that $\psi \equiv u\,\psi_1$. A straightforward computation yields:

$$-\frac{\hbar^2}{2m}\left[\frac{1}{u^2}\,\mathbf{div}(u^2\nabla\psi_1)\right] + W\psi_1 = E\psi_1 \qquad (31)$$

One can see in this equation that the auxiliary function $\psi_1 = \psi/u$ thus obeys a Schrödinger-type equation in which the original potential $V(\vec{r})$ has disappeared. Instead, a new function $W(\vec{r})$ now plays the role of "effective confining potential". The valleys of u, which are the boundaries of the localization subregions [146], also correspond to the crest lines of W, and thus appear as barriers to the auxiliary function ψ_1, which is then localized in the valleys of W, see Figure 57c.

Actually, W is proved to play exactly the role of an effective potential thanks to the following identity satisfied by any quantum state $|\psi\rangle$:

$$\langle\psi|\,\widehat{H}|\psi\rangle = \frac{\hbar^2}{2m}\left\langle u\vec{\nabla}\left(\frac{\psi}{u}\right)\middle| u\vec{\nabla}\left(\frac{\psi}{u}\right)\right\rangle + \langle\psi|\,\widehat{W}|\psi\rangle \qquad (32)$$

This identity shows not only that the energy E of any quantum state $|\psi\rangle$ can never be smaller than the one it would have in a potential $W(\vec{r})$, but also that, according to Agmon's inequality [153,154], the quantity $W - E$ can be used to build an Agmon distance $\rho_E(\overrightarrow{r_1}, \overrightarrow{r_2})$ that will control the decay of $\psi(\vec{r})$ in the regions where $E < W$. This distance is defined as

$$\rho_E(\overrightarrow{r_1}, \overrightarrow{r_2}) = min_\gamma\left(\int_\gamma \sqrt{(W(\vec{r}) - E)_+}\,ds\right) \qquad (33)$$

where the minimum is computed on all paths γ going from $\overrightarrow{r_1}$ to $\overrightarrow{r_2}$. The control on the amplitude $\psi(\vec{r})$ of an eigenfunction centered in $\vec{r}$ of energy E is expressed through the inequality

$$|\psi(\vec{r})| \leq e^{-\rho_E(\overrightarrow{r_0}, \vec{r})} \qquad (34)$$

The localization landscape therefore provides an estimate of the decay of the quantum state away from its main existence region. This tunneling effect is more commonly

known in quantum mechanics as a result of the Wentzel-Kramers-Brillouin (WKB) approximation, of which the Agmon distance is the mathematical generalization holding for any potential satisfying Agmon's inequality. This estimate can be used for instance to assess the overlap between several localized states.

3.1.1.2 Eigenvalue and eigenfunction estimates

The landscape u provides an estimate of the state amplitudes and also enables us to assess the energies of the localized states. In each of the subregions bounded by the valley lines of the localization landscape u, the local fundamental eigenfunction and its corresponding energy can be accurately determined from u itself. The local ground state estimate that will now be derived is practically more exploitable than Eq. (33), (34), which require the minimization of a path integral being computationally demanding in dimensions larger than 1. To show that, the landscape u, satisfying $\widehat{H}u = 1$, has to be decomposed on the quantum states ψ:

$$\mathbf{u} = \sum_i \boldsymbol{\alpha_i}\, \boldsymbol{\psi_i} \quad \textbf{with } \boldsymbol{\alpha_i} = \langle \boldsymbol{u}|\boldsymbol{\psi_i}\rangle = \int \boldsymbol{u}(\vec{\boldsymbol{r}})\boldsymbol{\psi_i}(\vec{\boldsymbol{r}})\, \boldsymbol{d^3 r} \qquad \textbf{(35)}$$

These decomposition coefficients α_i can be computed using the self-adjointness of the Hamiltonian:

$$\boldsymbol{\alpha_i} = \langle \boldsymbol{u}|\boldsymbol{\psi_i}\rangle = \frac{\mathbf{1}}{\boldsymbol{E_i}}\langle \boldsymbol{u}|\widehat{\boldsymbol{H}}\boldsymbol{\psi_i}\rangle = \frac{\mathbf{1}}{\boldsymbol{E_i}}\langle \widehat{\boldsymbol{H}}\boldsymbol{u}|\boldsymbol{\psi_i}\rangle = \frac{\mathbf{1}}{\boldsymbol{E_i}}\langle \mathbf{1}|\boldsymbol{\psi_i}\rangle \qquad \textbf{(36)}$$

From the two above equations, one can make three main remarks. First, the lower energy quantum states contribute more to the landscape u than the high-energy ones (because E_i grows in the denominator of Eq. (36). Secondly, in a given localization subregion, the low-energy states (ψ_i) entering the decomposition of Eq. (35) are essentially the local quantum states of this subregion. Thirdly, in each subregion, the fundamental state has a bump-like shape, while the higher energy ones, by orthogonality, take positive and negative values which cancel out so that the scalar products $\langle 1|\psi_i\rangle$ of Eq. (36) almost vanish. Note that this cancellation also occurs for the high-energy delocalized states of the system. As a consequence, in each localization subregion Ω_m, the following relation is deduced:

$$\boldsymbol{u} \approx \frac{\left\langle \mathbf{1}\middle|\boldsymbol{\psi}_{\mathbf{0}}^{(\boldsymbol{m})}\right\rangle}{\boldsymbol{E}_{\mathbf{0}}^{(\boldsymbol{m})}}\boldsymbol{\psi}_{\mathbf{0}}^{(\boldsymbol{m})} \qquad \textbf{(37)}$$

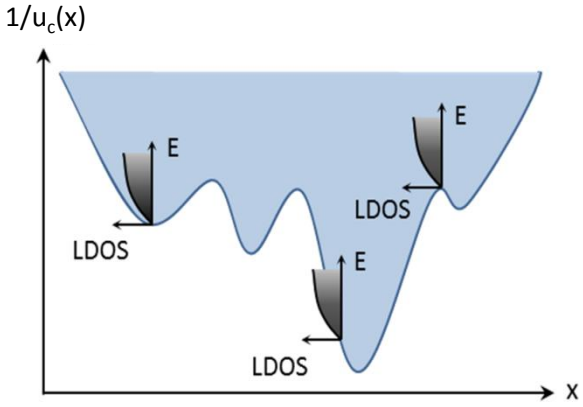

Figure 58: Local density of states (LDOS) deduced from the effective potential $W \equiv 1/u_c$.

which, after L2 normalization of u in Ω_m, shows that the local fundamental state $\psi_0^{(m)}$ is almost proportional to u:

$$\boldsymbol{\psi_0^{(m)} \approx \frac{u}{\|u\|}} \qquad \textbf{(38)}$$

Inserting Eq. (38) into identity (32) and using the fact that $W = 1/u$ allows us to evaluate the fundamental energy $E_0^{(m)}$ from the landscape only:

$$\boldsymbol{E_0^{(m)} = \left\langle \psi_0^{(m)} \middle| \widehat{H} \middle| \psi_0^{(m)} \right\rangle \approx \frac{\langle u | \widehat{W} | u \rangle}{\|u\|^2} = \frac{\langle u | 1 \rangle}{\|u\|^2} = \frac{\iiint_{\Omega_m} u(\vec{r}) d^3 r}{\iiint_{\Omega_m} u^2(\vec{r}) d^3 r}} \qquad \textbf{(39)}$$

The localization landscape provides therefore a direct estimate of the fundamental energy in each of the localization subregions.

3.1.1.3 The density of states

Finally, the prediction of the localized energies extends to the prediction of the density of states (DOS). We detail here the general case of a 3D system as well as the specific case of a 1+2D-system exhibiting two-dimensional translation invariance.

3.1.1.3.1 3D DOS

Due to the uncertainty principle, $\Delta x \Delta k \approx 2\pi$, each 3-dimensional one-particle quantum state spreads in phase space $(\vec{r}, \vec{k})$ on a volume of order $(2\pi)^3$. As a consequence, the number of energy states below a given energy E (also called the counting function $N(E)$) is asymptotically equivalent to $v(E)/(2\pi)^3$,where $v(E)$ is the volume in phase space determined by $H(\vec{r}, \vec{k}) \leq E$. This asymptotic behavior is the so-called Weyl's law.

In a 3-dimensional semiconductor, the Hamiltonian of an electron in the conduction band reads:

$$\boldsymbol{H(x,k) = \frac{\hbar^2 k^2}{2m_e^*} + E_c(\vec{r})} \qquad \textbf{(40)}$$

where E_c is the conduction band energy and m_e^* is the effective electron mass. The counting function deduced from Weyl's formula is therefore:

$$\boldsymbol{N(E) = \frac{2}{(2\pi)^3}\iiint_{H(\vec{r},\vec{k})\leq E} d^3r\, d^3k = \frac{2}{(2\pi)^3}\iiint_{\vec{r}}\left(\iiint_{\frac{\hbar^2k^2}{2m_e^*}\leq E-E_c(\vec{r})} d^3k\right) d^3r} \qquad \textbf{(41)}$$

The factor 2 appearing in the first numerator accounts for the spin degeneracy, and the integral within parentheses on the second line is simply the volume of a ball in k-space. The counting function can therefore be written as a space integral of a local counting function $N_1(E,\vec{r})$:

$$\boldsymbol{N(E) = \iiint_{\vec{r}} N_1(E,\vec{r})\, d^3r} \qquad \textbf{(42)}$$

with

$$\begin{aligned} \boldsymbol{N_1(E,\vec{r})} &= \boldsymbol{\frac{2}{(2\pi)^3}\frac{4\pi}{3}\left(\sqrt{\frac{2m_e^*(E-E_c(\vec{r}))}{\hbar^2}}\right)^3} \\ &= \boldsymbol{\frac{1}{3\pi^2}\left(\frac{2m_e^*}{\hbar^2}\right)^{\frac{3}{2}}[E-E_c(\vec{r})]^{\frac{3}{2}}} \end{aligned} \qquad \textbf{(43)}$$

Differentiating this expression with respect to E gives the local density of states $LDOS(E,\vec{r})$:

$$\boldsymbol{LDOS(E,\vec{r}) = \frac{1}{2\pi^2}\left(\frac{2m_e^*}{\hbar^2}\right)^{\frac{3}{2}}\sqrt{E-E_c(\vec{r})}} \qquad \textbf{(44)}$$

One recovers here the classical expression of the local density of states for conduction electrons in a semiconductor.

In a disordered system, Eq. (32) shows that $W(\vec{r})$ acts as an effective potential on the particle. Subsequently, W controls the distribution of energies for localized states in each localization subregion. One of the main consequences of this control, as shown on several examples in Ref. [147], is that W can be used to accurately estimate the density of states. Practically, this is achieved by replacing the original potential (here E_c) by W in the LDOS:

$$\boldsymbol{LDOS(E,\vec{r}) = \frac{1}{2\pi^2}\left(\frac{2m_e^*}{\hbar^2}\right)^{\frac{3}{2}}\sqrt{E - W(\vec{r})}} \qquad \textbf{(45)}$$

This expression physically means that at each point $\vec{r}$, the local density of states is equal to the one of an infinite medium with identical material composition and a parabolic band whose minimal energy would be $W(\vec{r})$ (see Figure 58). In the classical view of the local band approximation, $\vec{r}$ represents in fact a small volume compared to the typical size of the system, but large enough so that it can contain the local electronic states.

One needs here to express one word of caution. While the counting function $N(E)$ can be understood as the actual number of states below energy E over the spatial region of integration, the "local" density of states $LDOS(E,\vec{r})$ cannot be understood as the actual number of states at point $\vec{r}$ as soon as the spatial fluctuations of this $LDOS$ occur on a scale smaller than the typical spatial extension of the electronic states. It should rather be considered as a useful tool for assessing physical quantities.

This remark is of particular importance when this $LDOS$ is integrated over all possible energies to compute the local carrier density $n(\vec{r})$:

$$\boldsymbol{n(\vec{r}) = \int_{W(\vec{r})}^{+\infty} \frac{1}{1 + e^{\frac{E-E_F}{k_B T}}} LDOS(E,\vec{r})\,dE} \qquad \textbf{(46)}$$

This carrier density is apparently a local quantity at point $\vec{r}$, as in the classical drift-diffusion model, but thanks to the effective potential W appearing in the LDOS, it now also encompasses the quantum confinement induced by the material disorder. This expression is much more accurate than what could be estimated from the classical similar expression with $E_c(\vec{r})$ instead of $W(\vec{r})$. As such, this local quantity can be easily implemented into a Partial Differential Equation model such as a drift-diffusion solver with Poisson-transport-continuity equations, instead of solving the eigenfunctions of the Hamiltonian.

3.1.1.3.2 1D DOS

The procedure described above for 3D states can be applied similarly to 1D systems. In this case, the counting function reads:

$$\boldsymbol{N(E) = \frac{1}{\pi}\int_z \left(\int_{\frac{\hbar^2 k^2}{2m_e^*} \le E - W(z)} dk\right) dz = \frac{2}{\pi}\int_z \sqrt{\frac{2m_e^*(E - W(z))}{\hbar^2}}\,dz} \qquad \textbf{(47)}$$

and the local density of states is:

$$\boldsymbol{LDOS(E,z) = \frac{1}{\pi}\sqrt{\frac{2m_e^*}{\hbar^2}}\frac{1}{\sqrt{E-W(z)}}} \quad \textbf{(48)}$$

If one considers a 3D system with translational invariance in the two other directions x and y, such as a quantum well, then the quantum states are products of 1D and 2D states in the z direction and the (x,y) plane, respectively. The 3D density of states can thus be deduced from the above 1D density of states along z by convoluting it with the 2D LDOS:

$$\boldsymbol{LDOS_{3D}(E,z) = \int_{W(z)}^{E} LDOS_{2D}(E-E_1) \times \left(\frac{1}{\pi}\sqrt{\frac{2m_e^*}{\hbar^2}}\frac{1}{\sqrt{E_1-W(z)}}\right)dE_1} \quad \textbf{(49)}$$

$LDOS_{2D}$ being the 2D density of states for free particles, which is constant and equal to $m_e^*/2\pi\hbar^2$ (we do not count the spin degeneracy here as it is already included in the 1D LDOS). This finally gives the 3D density of states:

$$\boldsymbol{LDOS_{3D}(E,z) = \frac{1}{4\pi^2}\left(\frac{2m_e^*}{\hbar^2}\right)^{\frac{3}{2}}\int_{W(z)}^{E}\frac{dE_1}{\sqrt{E_1-W(z)}} = \frac{1}{2\pi^2}\left(\frac{2m_e^*}{\hbar^2}\right)^{\frac{3}{2}}\sqrt{E-W(z)}} \quad \textbf{(50)}$$

One can notice that the above expression is exactly identical to the 3D local density of states obtained in Eq. (45), except that here W depends only on z.

3.1.1.3.3 The potential reference

One needs here to underline a peculiarity of the localization landscape. When solving the Schrödinger equation, the potential $V(\vec{r})$ experienced by the quantum particle can be defined up to a constant value K. The resulting energies are then shifted by the same constant K. However, this invariance does not hold for the landscape u. If one considers u being the solution to Eq. (29), then the solution u_K corresponding to the same potential shifted by a constant K satisfies:

$$\boldsymbol{-\frac{\hbar^2}{2m}\Delta u_K + (V(\vec{r}) + K)u_K = 1} \quad \textbf{(51)}$$

If the constant K is much larger than the typical energies of the quantum states, then $Ku_K \approx 1$. Therefore, the corresponding effective potential $W_K = 1/u_K$ is very close to K. Inserting the effect of the potential shift on the energies into Eq. (30), the amplitudes of the quantum states are controlled by the landscape through the following inequality:

$$|\boldsymbol{\psi}(\vec{\boldsymbol{r}})| \leq (\mathbf{E}+\mathbf{K})\mathbf{u}_{\boldsymbol{K}}(\vec{\boldsymbol{r}}) \qquad \textbf{(52)}$$

In the situation where Ku_K becomes very close to 1, this inequality is almost trivially satisfied. In other words, the constraint on ψ exerted by the localization landscape u_K becomes weaker. This means that the constant K has to be chosen in order to be as small as possible, in such a way that the Hamiltonian remains a positive operator (a condition of applicability of the localization theory). As a consequence, in semiconductor structures where one encounters large, smooth variations of potential superimposed on small scale random potentials, one should resort to solving the localization landscape piecewise in regions over which the variation of the potential V is of the same order of magnitude than the energies of the quantum states.

3.1.2 The transport model

3.1.2.1 The new self-consistent approach

In this section, we elaborate on the simulation framework, including the implementation of the localization landscape theory into Poisson and drift diffusion equations. In the classical picture, Poisson and drift-diffusion equations are solved self-consistently to obtain the converged electrostatic potential φ and the quasi Fermi levels E_{Fn} and E_{Fp}:

$$\begin{cases} \boldsymbol{div}\left(\boldsymbol{\varepsilon_r}\vec{\boldsymbol{\nabla}}\boldsymbol{\varphi}\right) = \dfrac{\boldsymbol{q}}{\boldsymbol{\varepsilon_0}}\left(\boldsymbol{n}-\boldsymbol{p}-\boldsymbol{N_D^+}-\boldsymbol{N_A^-}+\boldsymbol{\rho_{pol}}\right) \\ \boldsymbol{div}\left(\vec{\boldsymbol{J}}_{\boldsymbol{n}}\right) = \boldsymbol{R}+\boldsymbol{G_n} \\ \boldsymbol{div}\left(\vec{\boldsymbol{J}}_{\boldsymbol{p}}\right) = -\boldsymbol{R}+\boldsymbol{G_p} \\ \vec{\boldsymbol{J}}_{\boldsymbol{n}} = \boldsymbol{n}\boldsymbol{\mu_n}\vec{\boldsymbol{\nabla}}\boldsymbol{E_{Fn}} \\ \vec{\boldsymbol{J}}_{\boldsymbol{p}} = \boldsymbol{p}\boldsymbol{\mu_p}\vec{\boldsymbol{\nabla}}\boldsymbol{E_{Fp}} \\ \boldsymbol{n}(\vec{\boldsymbol{r}}) = \displaystyle\int_{E_c}^{+\infty} \frac{\mathbf{1}}{\mathbf{1}+\boldsymbol{e}^{\frac{\boldsymbol{E}-\boldsymbol{E_{Fn}}}{\boldsymbol{k_BT}}}}\boldsymbol{LDOS_n}(\boldsymbol{E},\vec{\boldsymbol{r}})\boldsymbol{dE} \\ \boldsymbol{p}(\vec{\boldsymbol{r}}) = \displaystyle\int_{-\infty}^{E_v} \frac{\mathbf{1}}{\mathbf{1}+\boldsymbol{e}^{\frac{\boldsymbol{E_{Fp}}-\boldsymbol{E}}{\boldsymbol{k_BT}}}}\boldsymbol{LDOS_p}(\boldsymbol{E},\vec{\boldsymbol{r}})\boldsymbol{dE} \end{cases} \qquad \textbf{(53)}$$

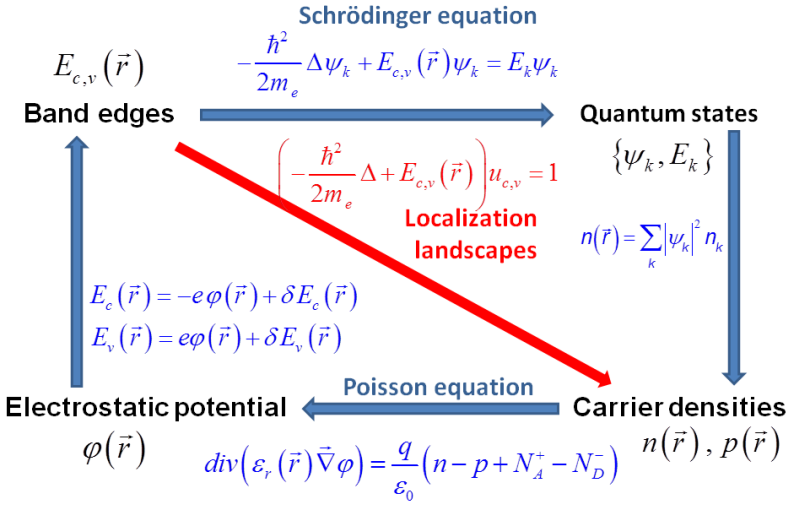

Figure 59: Schematic structure of the new self-consistent Poisson-landscape model allowing to bypass solving the Schrödinger equation.

$LDOS_{n,p}$ are the bulk local densities of states for electrons and holes, respectively; ρ_{pol} is the polarization charge which appears in some semiconductors such as nitrides where electric polarization effects are important; n and p are the free electron and hole carrier densities; N_A^- and N_D^+ are the activated doping densities of acceptors and donors; $\vec{J}_n$ and $\vec{J}_p$ are the electron and hole currents, respectively; R is the recombination rate which includes all types of recombination processes (SRH, radiative, Auger), and $G_{n,p}$ are the carrier generation rates.

In order to account for quantum effects, one has classically to solve the Schrödinger equation using $E_c(\vec{r})$ and $E_v(\vec{r})$ as potentials for electrons and holes respectively. The carrier densities are then deduced from the electron and hole wavefunctions, $\psi_{e,i}$ and $\psi_{h,j}$, and their corresponding energies, $E_{e,i}$ and $E_{h,j}$ through summation with Fermi-Dirac distribution:

$$\begin{cases} \boldsymbol{n(\vec{r}) = \sum_i \left(\frac{1}{1 + e^{\frac{E_{e,i} - E_{Fn}}{k_B T}}}\right) \left|\psi_{e,i}(\vec{r})\right|^2} \\ \boldsymbol{p(\vec{r}) = \sum_j \left(\frac{1}{1 + e^{\frac{E_{Fp} - E_{h,j}}{k_B T}}}\right) \left|\psi_{h,j}(\vec{r})\right|^2} \end{cases} \quad \textbf{(54)}$$

In the absence of currents, these carrier densities enter Poisson equation which in turn modifies the electrostatic potential. This is the usual self-consistent Poisson-Schrödinger scheme, depicted by the blue cycle in Figure 59. Introducing the

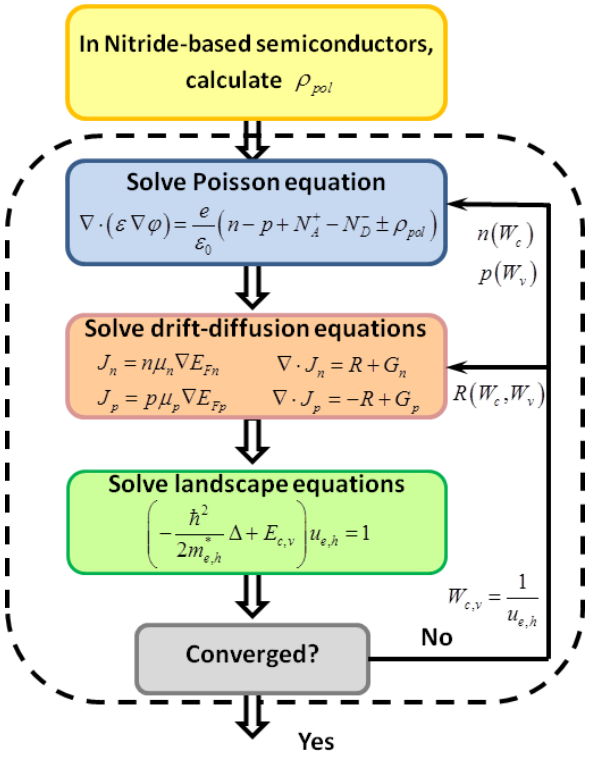

Figure 60: Flow chart solving the Poisson and drift-diffusion equations by applying the localization landscape theory.

localization landscape u allows to bypass solving the Schrödinger equation. From the electrostatic potential, we deduce two localization landscapes u_c and u_v, hence two effective potentials W_c and W_v. According to the theory, these landscapes provide direct estimates of the density of states $LDOS_n(\vec{r})$ and $LDOS_p(\vec{r})$, and of the carrier densities (Eqs. (47),(48)). This bypass is depicted by the red arrow in Figure 59.

Including transport equations into the Poisson-Schrödinger scheme adds another level of complexity. The carrier densities now enter Poisson and transport equations, from which one deduces the electrostatic potential and the quasi-Fermi levels. This loop results in lengthy, time-consuming and possibly unstable simulations that can take days of computing for a complex 3D structure with compositional disorder. Introducing the landscapes enables us to accurately assess not only the local carrier densities, but also the recombination rates through the overlap between electron and hole states in the localization subregions (see following subsection). These quantities are used to solve Poisson and drift-diffusion equations. This makes the localization theory easily compatible with a classical drift-diffusion approach. The schematic flow chart of the entire self-consistent simulation process is displayed in Figure 60.

One has to underline that in this model, the current densities still take their classical drift-diffusion form expressed in Figure 60. Yet, the carrier densities entering the expression of the currents are computed using the effective confining potentials W_c and W_v which shape the spatial structure of the quantum states. As a consequence, the tunneling effect of a quantum state through a local potential barrier created by fluctuations of the material composition is inherently included in the model. However, hopping processes between different quantum states are not accounted for in the current densities of the proposed model, which should be the topic of future extensions of this work.

3.1.2.2 Computing generation/recombination processes

The final subsection of the modeling section is dedicated to the computation of the generation and recombination processes in direct gap semiconductors using the localization landscapes, the focus being in particular on optical interband transitions, namely absorption and emission. Typically, the computation of these processes in quantum-confined semiconductor structures requires the knowledge of the eigenenergies and eigenfunctions of the quantum states, which determine respectively the energy of the transitions and the overlap between the electrons and holes. As derived in Sec. 3.1.1.2, these quantities can be in fact directly assessed from the localization landscape. It should be noted that due to the integrals appearing in Eqs. (38) and (39), these relations cannot be implemented into a local formulation, such as a self-consistent Poisson-drift-diffusion-W loop, but can be evaluated after convergence is reached for the simulated system.

We consider in the following the case of a homogeneous quantum well (QW), for which the classical absorption/emission expressions are rewritten using the localization landscape theory. The extension to the case of QWs with in-plane disorder is briefly outlined, while more details will be given in Sec. 3.2.

3.1.2.2.1 Absorption

The quantum mechanical expression of the absorption coefficient α of a QW of thickness L as a function of photon energy $h\nu$ is [155]:

$$\boldsymbol{\alpha(h\nu) = \frac{C}{L} \cdot g_{2D} \sum_{i,j} \Theta(h\nu - E_g - E_{e,i} - E_{h,j})\, I_{i,j}} \qquad \textbf{(55)}$$

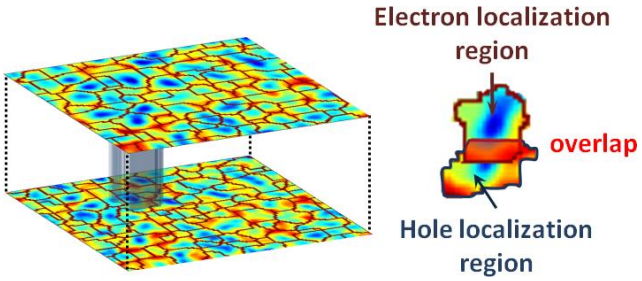

Figure 61: Overlap regions are defined as intersections between electron and hole localization subregions. (Left) superimposed electron and hole landscapes. (Right) Example of one overlapping region defined as the intersection of an electron and hole localization subregion.

where the prefactor $C = \pi e^2 \hbar |p_{cv}|^2 / m_0^2 c\, n_r \varepsilon_0 h\nu$ depends on the real part of surrounding refractive index n_r and the interband momentum matrix element p_{cv}. Considering a narrow photon energy range (close to the bandgap), we neglect the $k-$dependence of p_{cv} and the $h\nu$ dependence of C, and treat this prefactor as a constant; $g_{2D} = m_r \pi \hbar^2$ is the joint density of states (JDOS) of a 2-D system including the spin degeneracy with $m_r = (1/m_e^* + 1/m_h^*)^{-1}$ being the reduced effective mass. The summation is performed over all electron and hole states (labeled i and j, with $i = j = 0$ being the fundamental states) with eigenenergies $E_{e,i}$ and $E_{h,j}$. The overlap factor is determined by the electron and hole eigenstates $\psi_{e,i}$ and $\psi_{h,j}$ as:

$$\boldsymbol{I_{i,j} = \frac{\left|\langle \psi_{e,i} | \psi_{h,j} \rangle\right|^2}{\left\|\psi_{e,i}\right\|^2 \left\|\psi_{h,j}\right\|^2}} \qquad \textbf{(56)}$$

Our approach here is to use the localization landscape theory to assess the absorption coefficient directly from the maps of u_c and u_v computed for electrons and holes using Eq. (29), where V corresponds to the conduction and valence band potential, respectively. The valleys of the landscapes (which are also the crest lines of the $W_{c,v}$ potentials) partition the domain into localization subregions. Note that in the case of a homogeneous QW, only one localization subregion exists for each type of carrier, determined by the confinement along the growth direction, while in the case of a disordered QW several subregions can be found (Sec. 3.2).

In each subregion the eigenfunctions of the fundamental states, $\psi_{e,0}$ and $\psi_{h,0}$, and the corresponding eigen-energies, $E_{e,0}$ and $E_{h,0}$, can be calculated using Eqs. (38) and (39).

From the estimation of the eigenstates, the overlap factor $I_{0,0}$ of Eq. (56) can then be directly computed. To account for all interband transitions, Weyl's law can be used to estimate the system DOS instead of summing over all possible i, j as in Eq. (64). In Sec. 3.1.1.3 it was shown that in a 3D system with confinement along one direction and translational invariance along the others, Weyl's law predicts an LDOS exactly identical to that of the bulk case. Therefore, to compute the JDOS of the homogeneous QW the following well-known expression for bulk is used considering an effective bandgap $E_g + E_{e,0} + E_{h,0}$:

$$\boldsymbol{JDOS_{3D}(h\nu) = \frac{\sqrt{2}m_r^{3/2}}{\pi^2\hbar^3}\sqrt{h\nu - E_g - E_{e,0} - E_{h,0}}} \qquad \textbf{(57)}$$

Finally, the absorption coefficient of the homogeneous QW can be rewritten as:

$$\boldsymbol{\alpha(h\nu) = \frac{2}{3}\cdot C \cdot JDOS_{3D}(h\nu) I_{0,0}} \qquad \textbf{(58)}$$

where all quantities can be derived from the landscapes without solving the Schrödinger equation. (The factor 2/3 in Eq. (58) and the absence of the $1/L$ prefactor appearing in Eq. (55) are due to the use of the bulk expression of the JDOS in the absorption coefficient [155].)

The procedure for determining the absorption coefficient in the case of a disordered QW remains essentially the same. When superimposing the maps of the two landscapes, one can define the subregions which are the intersections between the various localization subregions for electrons and holes (Figure 61). For each of these electron-hole "overlapping" subregions a local value of α can be computed using Eq. (58). The overall absorption coefficient of the disordered QW is obtained by summing over all electron and hole subregions, Ω_m and Ω_n, as:

$$\boldsymbol{\alpha(h\nu) = \frac{2}{3}\cdot C \cdot \sum_{m,n} JDOS_{3D}^{(m,n)}(h\nu) I_{0,0}^{(m,n)}} \qquad \textbf{(59)}$$

where the JDOS and overlap factors depend on the fundamental state and corresponding energy of the considered subregion, namely $\psi_{e,0}^{(m)}$ and $E_{e,0}^{(m)}$ for electrons, and $\psi_{h,0}^{(m)}$ and $E_{h,0}^{(m)}$ for holes.

Such an accurate accounting of carrier localization in a disordered material is crucial for a precise assessment of the below-gap absorption processes. A detailed study on this topic is presented in Sec. 3.2.

3.1.2.2.2 Emission

While in the previous derivation of optical absorption the conduction and valence bands were considered as completely empty and filled, respectively, in the case of optical emission the occupation of the states depends on the specific injection conditions of the QW. Assuming that the quasi-Fermi levels for electrons and holes are known, the electron and hole distributions $n(z)$ and $p(z)$ in the QW can be determined using Eq. (46). The radiative recombination rate then reads

$$\mathbf{R}_{int} = \int \boldsymbol{B_0 n(z)\, p(z) dz} \qquad \textbf{(60)}$$

corresponding to the transition energy $E_g + E_{e,0} + E_{h,0}$ calculated from the landscapes as in Sec. 3.1.2.2.1. If the transition is homogeneously broadened, then a Lorentzian function must be used to determine the emission spectrum of the QW as:

$$\mathbf{R}_{sp}(\boldsymbol{h\nu}) = \frac{\frac{\boldsymbol{\Gamma}}{\boldsymbol{2\pi}}\boldsymbol{R_{int}}}{(\boldsymbol{h\nu - E_g - E_{e,0} - E_{h,0}})^2 + (\frac{\boldsymbol{\Gamma}}{\boldsymbol{2}})^2} \qquad \textbf{(61)}$$

Once again in the case of a disordered QW the emission spectra have to be summed over all possible transitions between localized states to produce the inhomogeneously broadened luminescence spectrum of the QW.

The localization landscapes can also be used to compute non-radiative recombination processes which may be strongly affected by disorder. In Auger recombination the confinement increases the carrier momentum compared to free carriers, leading to a better overlap with the wavefunction of the final high-energy carrier, and thus an enhanced transition probability.

Let us consider for instance the h-h-e Auger process: an electron and a hole recombine and transfer their energy through Coulomb interaction to a second hole which becomes highly energetic. Using the Fermi Golden Rule, one expresses the recombination rate in one overlapping region:

$$\frac{\boldsymbol{1}}{\boldsymbol{\tau}} = \frac{\boldsymbol{2\pi}}{\hbar}\left|\boldsymbol{M_{if}}\right|^2 \boldsymbol{\rho(E_f)} \qquad \textbf{(62)}$$

where $\rho(E_f)$ is the density of final states and M_{if} is the matrix element defined as:

$$\boldsymbol{M_{if}} = \sqrt{\boldsymbol{2}} \iint \boldsymbol{dr_1\, dr_2 \psi^*_{h,0}(r_1)\psi^*_{h,0}(r_2)} \times \boldsymbol{V(r_1, r_2)\psi_{e,0}(r_1)\varphi_{h,f}(r_2)} \qquad \textbf{(63)}$$

r_i being the initial and final positions, and V the Coulomb interaction potential. $\psi_{h,0}(r_1)$ and $\psi_{h,0}(r_2)$ are the initial states of the two holes, while $\psi_{e,0}(r_1)$ is the initial electron state. Finally, $\varphi_{h,f}(r_2)$ is the final state of the second hole.

After dividing the entire system into the aforementioned overlapping regions, the above integral is computed over each region separately. For instance, in the above integral, the final hole wavefunction $\varphi_{h,f}$ is assumed to be a simple plane wave of wavevector k_f, while the initial states are approximated by the local landscapes in the considered overlapping region (see Sec. 3.1.1.2). All these local integrals can then be assembled to build maps of the Auger recombination times in the whole system. The influence of compositional disorder on Auger recombination tackled by the localization landscape theory is currently under study.

3.1.3 Applications of the landscape theory to simple 1D heterostructures

In the following sections, we study successively 1-D superlattice (SL) structures to

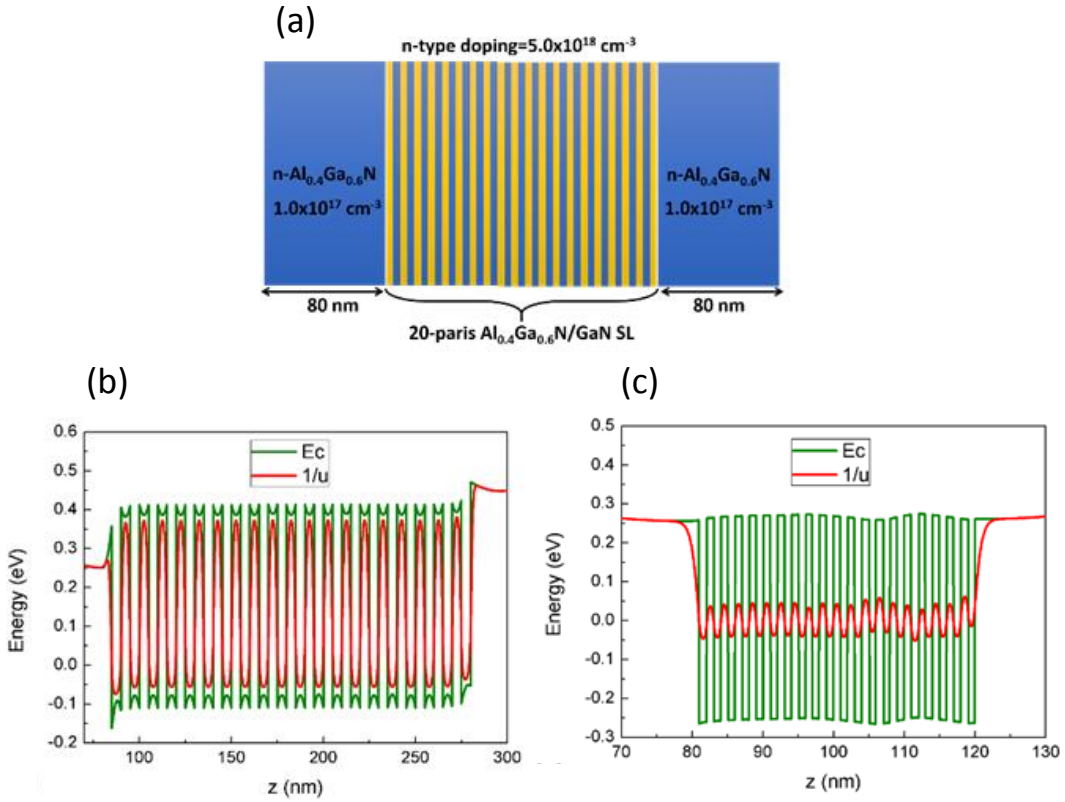

Figure 62: (a) Schematic structure of 20-period $Al_{0.4}Ga_{0.6}N$/GaN SLs. (b) and (c) are the conduction band potential (E_c) and effective quantum confining potential ($1/u_c$) for 5nm/5nm and 1nm/1nm m-plane SLs.

show how the localization landscape theory can be implemented to compute the DOS. Then, we apply our model to the simulation of a disordered superlattice (DSL). Finally, a 1-D single quantum well (SQW) structure is simulated to compare the carrier distributions computed by the classical Poisson equation, the Poisson-landscape model (localized landscape theory), and the Poisson-Schrödinger equation, respectively. All modeled structures presented in the following are 1-D with homogeneous layers. A full 3-D modeling of carrier transport in a semiconductor device including the effect of compositional disorder will be presented later (Sec. 3.3).

3.1.3.1 Density of states

3.1.3.1.1 Periodic superlattice

AlGaN/GaN superlattice (SL) structures are widely used in commercial LEDs to improve lateral current spreading [156]. However, modeling SL structures still remains a challenge for classical Poisson-drift-diffusion solvers. In the classical picture, the resistance experienced by carriers is determined by the barrier height. In SLs, this leads to an overestimation of its value. Schrödinger-based solvers can model SLs, accounting for wave function coupling and tunneling effects. However, this approach cannot be applied in the case of multidimensional devices to study current crowding effect of disordered systems, due to the high demand of computation time. We show here that the localization landscape theory allows us to overcome this constraint.

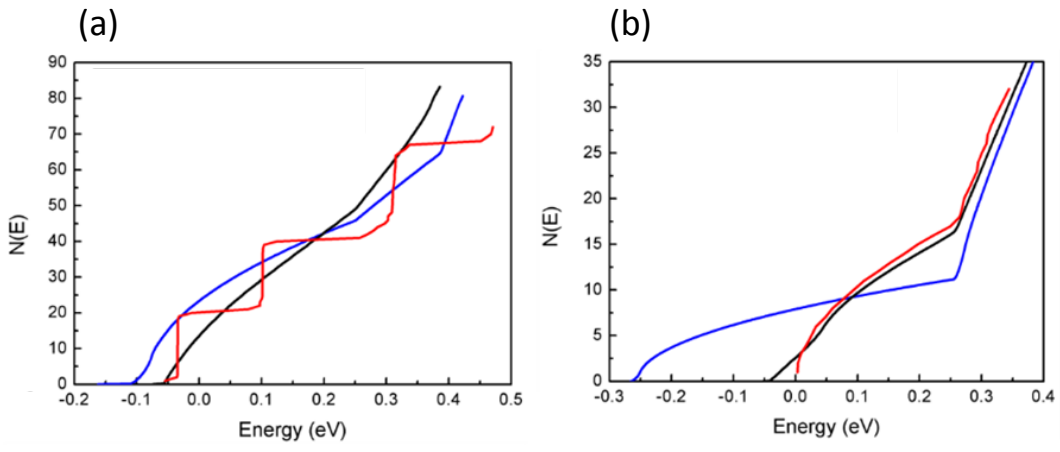

Figure 63 - (a) and (b) are the counting functions computed from the Schrödinger equation (red curves), or using Weyl's law with $1/u_c$ (black curves) or E_c (blue curves) for the 5nm/5nm and 1nm/1nm m-plane SLs corresponding to Figure 62b,c.

We model a 20-pairs n-type m-plane $Al_{0.4}Ga_{0.6}N$/GaN SL structure with flat band conditions at both ends, as shown in Figure 62a, to analyze the electron transport behavior. Two structures with different periodicities, 5 nm/5 nm and 1 nm/1 nm QW/barrier thickness, are simulated. A nonpolar m-plane orientation is considered at first to study the intrinsic transport properties of SLs as described by the landscape model. In the thicker SL (5nm/5nm), quantum effects are weaker and $1/u_c$ deviates only slightly from E_c, as shown in Figure 62b. On the other hand, in the thinner SL (1nm/1nm) $1/u_c$ is significantly different from E_c, as shown in Figure 62c. This difference translates into a lower semi-classical barrier setting the effect of stronger quantum tunneling.

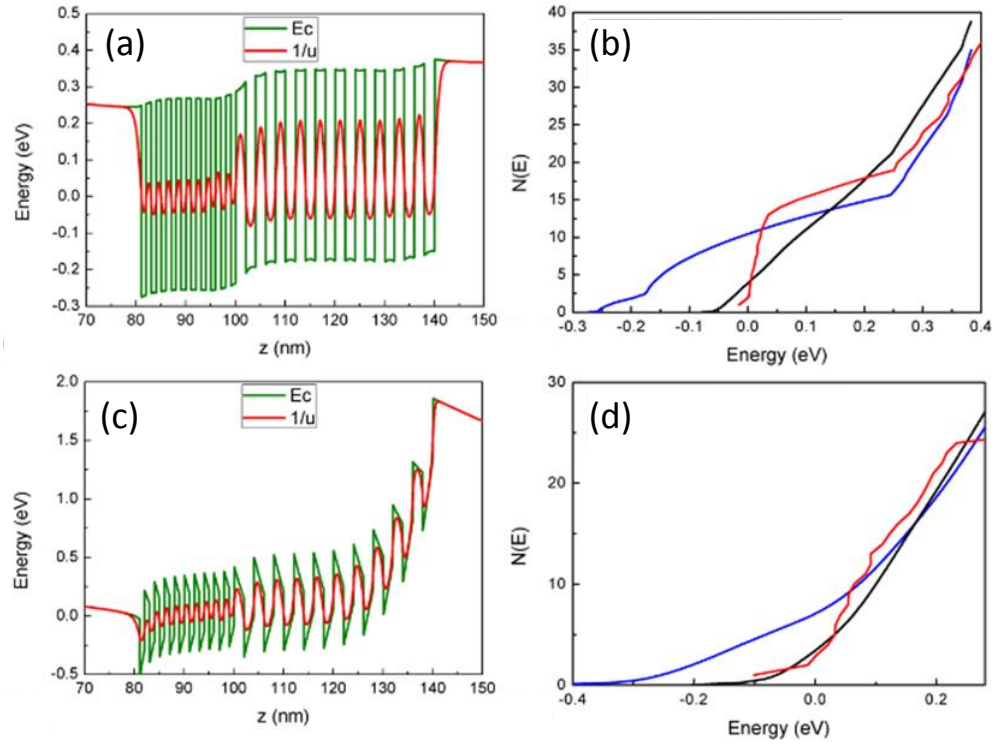

Figure 64 - Conduction band potential (E_c, green curves) and effective quantum confining potential ($1/u_c$, red curves) for (a) m-plane and (c) c-plane double period SLs. (b) and (d) display the corresponding counting functions computed from the Schrödinger equation (red curves), or using Weyl's law with $1/u_c$ (black curves) or E_c (blue curves).

For large SL thicknesses, quantum effects are weak and classical, landscape, and Schrödinger-based models give very similar number of available states, as displayed in Figure 63a. As the SL thickness becomes smaller, the classical counting function, computed from the original conduction band edge E_c, loses its accuracy compared to the sum of all subband states obtained from the Schrödinger equation, especially for lower energy states. However, $1/u_c$ provides a very good approximation compared to the

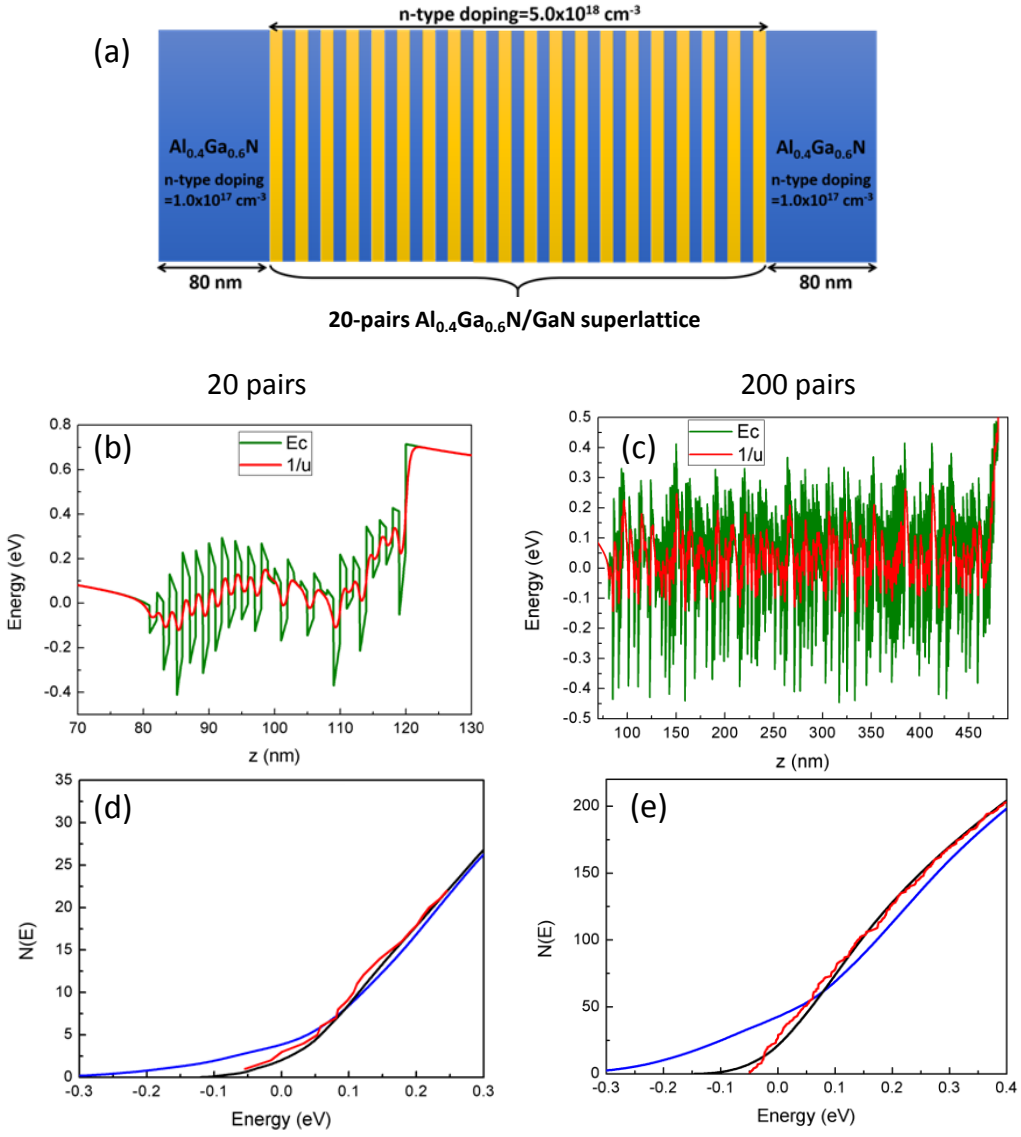

Figure 65 - (a) Schematic structure of a 20-pairs disordered superlattice. The disorder lies in the fluctuations of the well material composition across the structure. (b), (c) Conduction band potentials, and (d), (e) counting functions for 20-pairs and 200-pairs disordered c-plane SLs, respectively. The counting functions are computed from the Schrödinger equation (red curves), or using Weyl's law with $1/u_c$ (black curves) or E_c (blue curves).

Schrödinger solution, as one can observe in Figure 63b. One can also observe that in this last case, the $1/u_c$ -approximation of the counting function becomes positive about 50 meV earlier than the actual counting function of the Schrödinger equation. This slight discrepancy comes from the fact that, by definition, the$1/u_c$ -approximation of the counting function is continuous while the actual counting function is step-wise. Therefore, to reach a value close to 1 at an energy corresponding to the fundamental energy of the system, the approximate counting function has to become positive at a smaller energy.

To test further the landscape model, we analyze more complicated structures such as 20-pairs n-type SL with double periods composed of 10-pairs 1nm/1nm and 10-pairs 2nm/2nm SLs, respectively, including m-plane and c-plane cases. Figure 64a,c show the conduction band edge E_c and $1/u_c$ for m-plane and c-plane conditions. Here again, the difference between E_c and $1/u_c$ increases as the period become smaller, exhibiting stronger tunneling effects. The counting functions displayed in Figure 64b,d show the quality of the approximation provided by $1/u_c$, regardless of the structure complexity. We found the c-plane case exhibits a better agreement with the Schrödinger model due to distinct potential energy distributions. As randomness and inter-coupling increase in the system, the prediction of $1/u_c$ becomes closer to the solution of the Schrödinger equation. This last result was in fact already partly demonstrated in Ref. [147] for very random systems. These results confirm that $1/u$ can be used to model carrier transport and account for quantum effects in complicated systems.

3.1.3.1.2 Disordered superlattice

To illustrate the efficiency of the landscape model in the case of disordered systems, we compute the band structure and the density of states in nitride c-plane disordered SLs. Two types of SLs are investigated: the first is composed of 20 pairs of well/barrier layers, while the second is composed of 200 pairs. In both cases, wells and barriers have 1 nm thickness. The barrier material is $Al_{0.4}Ga_{0.6}N$ and the well material is $Al_xGa_{1-x}N$, where x is randomly and independently determined in each well, using a uniform law between 0 and 0.4.

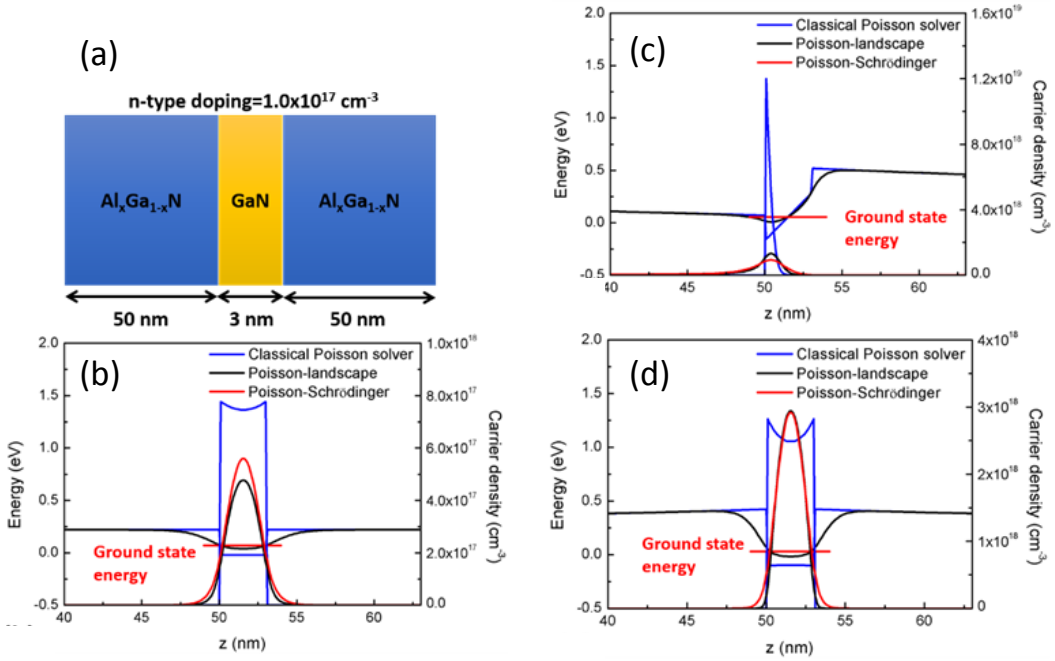

Figure 66 - (a) Schematic structure of the $Al_xGa_{1-x}N$/GaN SQW, where x is variable. (b) Potential energy and carrier distribution for m-plane and $x = 0.2$. (c) Potential energy and carrier distribution for c-plane and $x = 0.2$. (d) Potential energy and carrier distribution for m-plane and $x = 0.4$. The carrier distributions are obtained solving the Poisson equation, Poisson-landscape theory, and Poisson-Schrödinger equation, respectively. The Fermi level is located at zero energy as the reference.

For each type of SL, the conduction band potential and the counting function are computed (Figure 65b-e). In both cases, although the edge of the conduction band E_c now exhibits large fluctuations across the structure due to the compositional disorder, the quantum coupling between wells translates into a much smoother effective potential $1/u_c$. The minimum value of $1/u_c$ is significantly larger than E_c and can be interpreted as a local fundamental energy from the expression of the local density of states in Eq. (48). Looking at the counting functions (Figure 65d,e), we observe the very good agreement between the actual couting functions and its approximation obtained using $1/u_c$.

Finally, we still see the same slight discrepancy of the take-off energy between both functions that was observed in the periodic case. This discrepancy, which comes from

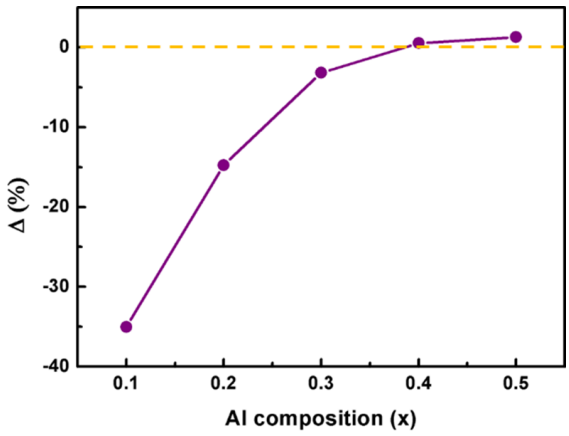

Figure 67 - Relative difference between the predictions of the peak carrier distribution by the Poisson-landscape and Poisson-Schrödinger models for various Al compositions of the $Al_xGa_{1-x}N$/GaN SQW structure corresponding to Figure 66.

the different natures of the two functions (continuous vs. stepwise), appears to be of the same order of magnitude independently on the number of wells in the structure.

3.1.3.2 Carrier distribution

To study and compare in detail the carrier distributions predicted by the different models, a 1D single QW is used. The structure is composed of a 3 nm active GaN layer, enclosed between two barriers of $Al_xGa_{1-x}N$, where $x = 0.2$ will be the reference case. The m-plane and c-plane case (without and with the polarization charge induced at the interface) are both discussed. The detailed dimension and material doping level are shown in Figure 66a, where the electron effective mass of $Al_{0.2}Ga_{0.8}N$ and GaN are 0.214 m_0 and 0.20 m_0, respectively. The doping is assumed to be fully activated to ensure the same activation condition for comparison.

Carrier density distribution is solved through three different methods: (1) the classical Poisson model solving the Poisson equation for the charge distribution of ionized donors across the SL structure; (2) self-consistent Poisson-landscape approach; and (3) self-consistent Poisson-Schrödinger approach. Figure 66b displays the computed carrier distribution and the potential energy for the m-plane case with a symmetric potential energy by the three methods. We can see that the carrier distribution obtained from the classical Poisson solver is almost constant across the well and dropping sharply outside, not accounting for the quantum nature of the electron. The Poisson-Schrödinger solver shows a very different result: the carrier distribution is more confined in the center of

the well and extends smoothly outside of it, revealing the wave function shape of the carrier. When using the landscape model, the effective quantum potential $1/u_c$ exhibits a smoother behavior than the original conduction band. The carrier density computed after replacing the original conduction band edge E_c with $1/u_c$ appears very similar to that computed from the Schrödinger equation.

In Figure 66c, we evaluate the c-plane case with an asymmetric potential profile induced by the polarization charge. The carrier distribution computed by the classical Poisson equation is sharp and mostly located at the minimum of the conduction band. This does not match the result obtained from the Poisson-Schrodinger solver. This excessively large carrier density located at the interface might be the reason why some numerical studies of GaN-based polar QWs using Poisson and drift-diffusion solvers adopt only ~50% of the theoretical polarization charge [157], in order to reproduce a carrier distribution consistent with Schrödinger equation. Here again, the Poisson-landscape model results in a smoother carrier distribution, as shown in Figure 66c, much closer to the Schrödinger solution.

In the case of a deeper m-plane QW with $x = 0.4$, carrier distributions computed with the Poisson-landscape and Poisson-Schrödinger models are also in good agreement, as displayed in Figure 66d. To quantify this agreement, a series of Al composition from 10% to 50% is simulated. For each simulation, the relative difference of peak carrier densities between the Poisson-landscape and Poisson-Schrödinger models, named Δ, is computed. According to Figure 67, Δ becomes smaller when the carriers are well localized within a deeper potential (larger Al composition) and almost vanishes above 40% Al composition.

From this result it can be concluded that the localization landscape model matches very well the solution of the Schrödinger equation when the system is strongly localized. Even in systems with a lower degree of localization (here, small x) the prediction of the Poisson-landscape model gives an acceptable agreement with the exact Poisson-Schrödinger solution and provides an overall description of the carrier distribution much more accurate than the result of a classical Poisson solver.

3.1.4 Conclusions

In this study the localization landscape theory [146,147], so far a mathematical method, was applied to the framework of semiconductors. It was shown how to use the resulting localized states, energies and density of states, into Poisson and drift-diffusion equations

to model the carrier transport of SL structures and carrier localization of disordered media in nitride-based systems. In principle, this method is not restricted in modeling nitride-based devices but can expand to other semiconductor materials, and to any electronic or optoelectronic properties requiring the knowledge of electron (and hole) quantum states. As it will be shown in real modeling exercises (Sec. 3.3), the computation speed of the landscape model is much faster than a conventional Schrödinger solver (Appendix 5.6), which is highly desirable to make 3D models of real-world devices.

According to the localization landscape theory, where a Schrödinger equation for the wave function is replaced by a Dirichlet equation for the landscape u, $W \equiv 1/u$ acts as an effective quantum classical confining potential seen by localized states, which can be taken into account for analyzing carrier localization and statistics in localization subregions. Using W in Weyl's law provides a good approximation of the density of states, carrier concentrations and spatial distributions compared with Schrödinger equation solutions, especially in the case of strong localization. Besides, as seen here in 1D cases, and shown to play a decisive role in the 3D modeling of LEDs (Sec. 3.3), the landscape theory simulates to an excellent approximation two major impacts of quantum mechanics, namely the reduction of barrier heights (the tunnel effect) and the raising of energy ground states (the quantum confinement effect).

3.2 Urbach tails of disordered InGaN quantum wells

The absorption edge in semiconductors is usually characterized by a long energy tail with an absorption coefficient α exponentially varying with photon energy and temperature along the Urbach tail rule [158]

$$\boldsymbol{\alpha(h\nu, T) = \alpha_0 \cdot e^{(h\nu - E_1)/E_0(T)}} \qquad \textbf{(64)}$$

where α_0 is a constant, E_1 determines the onset of the tail, usually the band gap energy E_g in semiconductors, and E_0 is the Urbach energy. Note that Urbach tails were proposed in 1953 essentially as a phenomenological description of thermally activated below-gap absorption (see e.g. Ref. [159] and references therein) and in Urbach's original expression $E_0 = kT/\gamma$, γ being a constant. Several attempts have since then been made trying to derive a universal theory [160,161]. By extension, exponential absorption edges are also called Urbach tails although they might not be associated with thermally activated phenomena. A variety of phenomena, intrinsic or extrinsic, have been invoked, and sometimes demonstrated, as physical mechanisms leading to Urbach tails such as the FK effect associated with the random electric fields of impurities, defect-induced smearing of band edges [162] and phonon-assisted absorption [159]. The impact of compositional alloy disorder on thermally activated Urbach tails has been clearly identified in $InAs_xSb_{1-x}$ [163] while in the case of amorphous Si Cody *et al.* could characterize both the effects of structural disorder and thermal disorder [164].

In the InGaN alloy system, very large Urbach energies E_0 of few hundreds of meV have been observed [165–167], attributed to phase separation of the InGaN alloy. This is to be contrasted with the luminescence linewidth in LED materials which is most often quite smaller, of the order of 100 meV or less. The Urbach energy observed in pure GaN is 12 meV [168] or 15 meV [169]. As will be shown in the present study, the Urbach tail of high quality $In_xGa_{1-x}N$ quantum wells (QWs) has Urbach energies in the range 15-30 meV and is determined by the disorder introduced by the random In compositional fluctuations.

Understanding disorder phenomena in nitride ternary alloys, such as InGaN and AlGaN, is of utmost importance as they constitute the core of several modern optoelectronic devices thanks to their wide tunability of energy bandgap. It is indeed well established by APT that these alloys exhibit random composition fluctuations on a typical length scale of a few nm [20]. Although APT provides imaging of the compositional disorder with atomic resolution, the relation between the measured atomic maps and the resulting

energy fluctuations occurring near the band gap edge of the alloy, where all physical phenomena of devices occur, is not straightforward and was not established. A direct characterization of the effects of compositional disorder on the optoelectronic properties of InGaN layers is also needed to verify any model of the disorder effects induced by the compositional random fluctuations.

Several theoretical studies indicate that compositional disorder in nitride ternary alloys is large enough to induce carrier localization which, in turn, may strongly influence the carrier transport, optical properties and efficiency of a device. In the case of nitride LEDs, simulations of I-V characteristics including random alloy fluctuations in the InGaN QWs and AlGaN barriers predict a voltage threshold which is almost 1 V lower with respect to the case of a homogeneous active region, in better agreement with the experimental values for actual devices, due to percolation in the disordered layers [170–172]. Atomistic calculations by Schulz *et al.* [173] show that low-band electron and hole states produce a strong inhomogeneous broadening of luminescence spectra of $In_{0.25}Ga_{0.75}N$/GaN QWs. First-principle calculations of non-radiative Auger rates in nitride semiconductors by Kioupakis *et al.* [43] indicate that indirect Auger recombination mediated by alloy disorder may play an important role in determining the efficiency loss of nitride optoelectronic devices.

On the experimental side, besides the Urbach tail measurement mentioned above, a well-known effect often interpreted as an evidence of carrier localization induced by disorder in InGaN QW layers is the “S-shaped” emission shift of the peak energy of photoluminescence observed as a function of temperature [174,175]. This phenomenon indicates relaxation of the carrier ensemble at low temperatures towards deeply localized centers, signaled by a red-shift of the emission energy, but does not provide information on the disorder effects impacting device operation.

In contrast, optical absorption spectroscopy should provide a more direct access to the disorder-induced energy fluctuations near the band edge, as it is directly linked to the electronic densities of states. In the present study the role of compositional disorder in a series of $In_xGa_{1-x}N$ QW structures of different In content is characterized by means of biased photocurrent spectroscopy (BPCS). Assuming that the collection efficiency of photocurrent is independent of photon energy, BPCS measurements are representative of optical absorption spectra [176]. For instance, in GaAs/AlGaAs QWs a series of distinct excitonic peaks could be observed by Collins *et al*. using BPCS, indicating that excitons, after photocreation, are ionized and transport through the structure

contributing to photocurrent [177]. To the extent that the optical interband matrix element has a weak dependence on photon energy in the narrow energy range of the Urbach tail, then below-gap absorption is determined by the joint density of states (JDOS) of the disordered system weighted by the overlap integral between the envelope functions of the localized states [155]. The contribution of internal piezoelectric fields on the absorption spectra can be evaluated by comparing data collected with different external applied biases. Previous photocurrent studies were carried out in InGaN/GaN QW structures under applied bias but did not aim at characterizing disorder-related effects on below-gap absorption [178,179].

In the present study the effect of compositional disorder in InGaN layers with different In content is characterized by analyzing their Urbach tails as measured by BPCS. QWs emitting from the violet ([In]=11%) to the green ([In]=28%) range exhibit small values of the Urbach energy, typically around 20 meV, while a much larger broadening would be expected from the fluctuations of the calculated random potential corresponding to the alloy disorder. An independent absorption model is derived on the basis of the localization landscape theory that takes into account the “effective” potential seen by localized states in disordered systems without having to resort to the Schrödinger equation [146,147].

The description of the samples and details on the experimental setup are given in Sec. 3.2.1. In Sec. 3.2.2 the main results of BPCS for $In_xGa_{1-x}N$ QW structures with In composition ranging between 0% and 28% will be presented. It will be shown that three different regions may be identified in the photocurrent spectra corresponding to different absorption mechanisms. The focus will be on the experimental characterization of Urbach tails as a function of In composition, applied bias, sample temperature and type of device incorporating InGaN QWs. In Sec. 3.2.3 theoretical models will be derived to study the effect of electric fields and compositional disorder on Urbach tails. First the influence of the polarization-induced QW electric field on the optical transition matrix element by means of the FK effect at below-gap photon energies will be evaluated. Then the absorption model based on the localization landscape theory will be introduced and its predictions will be compared to the measured Urbach tails giving an insight into the effect of compositional disorder in InGaN layers. Calculations of type-II well-barrier transitions will be presented in the Appendix 5.5 to model an additional absorption mechanism observed in the below-gap responsivity of near-UV emitting QWs.

3.2.1 Experiment

3.2.1.1 Samples

The samples are a series of $In_xGa_{1-x}N$/GaN multiple QW (MQW) solar cells grown by metal-organic chemical-vapor deposition (MOCVD) on (0001) sapphire substrates with mean In content ranging between 6% and 28% measured by x-ray diffraction with a PANalytic MRD PRO diffractometer. The structures are schematized in Figure 68a and consist of a 1 µm unintentionally doped GaN template layer, a 2 µm Si-doped n-GaN layer ([Si]=6x10^{18} cm^{-3}), a 10 nm highly Si-doped n$^+$-GaN layer ([Si]=2x10^{19} cm^{-3}), a), a 10 period undoped MQW active region with 2 nm $In_xGa_{1-x}N$ QWs (the QW thickness measured by XRD slightly increases with [In] in the different solar cells: 1.6 nm for 6%, 1.7 nm for 11%, 1.8 nm for 17%, 1.9 nm for 22% and 2.1 nm for 28%) and 7 nm GaN barriers, a 40 nm highly Mg-doped p$^+$-GaN layer ([Mg]=5x10^{19} cm^{-3}), a 30 nm Mg-doped p-GaN layer ([Mg]=2x10^{19} cm^{-3}) and a 15 nm highly Mg-doped p$^+$-GaN contact layer. The n- and p- layer adjacent to the active region are δ-doped to reduce the polarization fields in the QWs. APT experiments were performed to confirm the random distribution of In atoms in the InGaN layers in the different samples. Specimens were prepared with a FEI Helios 600 dual beam FIB instrument following standard procedure. APT analyses were performed with a Cameca 3000X HR Local Electrode Atom Probe (LEAP) operated in laser-pulse mode with a green laser (532 nm). The laser pulse

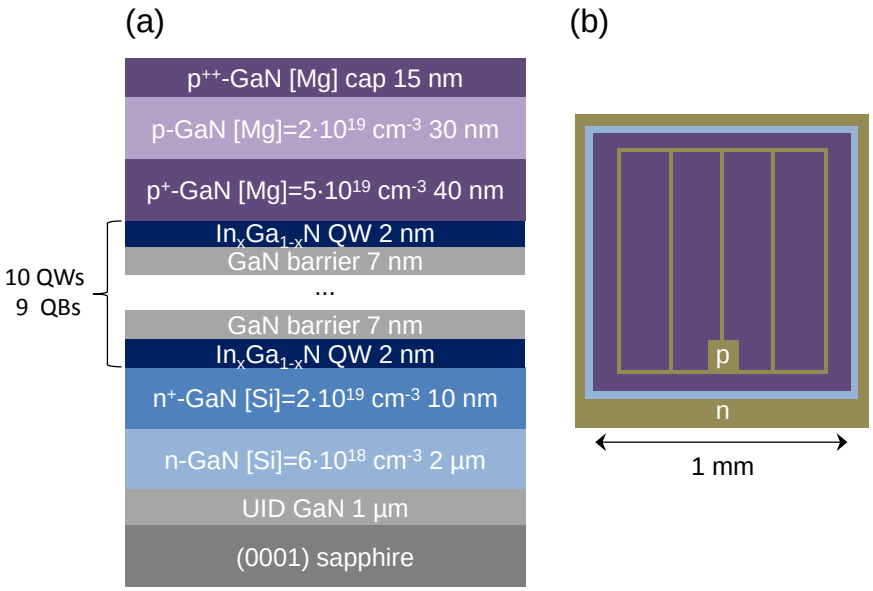

Figure 68 - (a) Schematic of the InGaN/GaN solar cell structures grown by MOCVD. (b) Contact geometry of the processed devices.

energy was 1 nJ and a detection rate of 0.005 atoms per pulse was set during each sample analysis. APT 3D reconstruction was carried out using commercial software IVAS^{TM}. Statistical distribution analysis were performed on sampling volumes of 30x30x2 nm^3 taken in the center of each InGaN layers and for each samples. The random distribution of In in each InGaN layers was confirmed by the success of the χ^2 test between experimental distributions and the binomial distribution predicted for random alloys.

A UV LED with pure GaN QW layers is also studied for comparison. This sample is grown by molecular beam epitaxy (MBE) on a semipolar $\{20\bar{2}1\}$ GaN substrate and its structure consists of an AlGaN buffer layer, a Si-doped n-$Al_{0.20}Ga_{0.80}N$ layer, a 5 period undoped MQW active region with 5 nm GaN QWs and 6 nm $Al_{0.12}Ga_{0.88}N$ barriers, a Mg-doped p- $Al_{0.20}Ga_{0.80}N$ layer and a highly Mg-doped p^+-GaN contact layer. The samples are processed by standard contact lithography and the final devices consist of 1 mm x 1 mm mesas, 30/300 nm Pd/Au p-contact grids on the top of each mesa with a center-to-center grid spacing of 200 µm, and a 30/300 nm Al/Au n-contacts around the base of each mesa (Figure 68b).

For comparison, commercial-grade LEDs produced by Nichia Corporation are also investigated: a UV LED (NCSU275 U395), in which the glass window has been removed to avoid partial absorption in the UV range of the exciting optical beam in BPCS measurements and in which the parallel protection device has been unwired to apply a wider range of reverse biases to the device; a bluish-green LED (NCSE 119AT), in which the silicone dome and the parallel protection device have not been removed (note: chemical removal of the silicone dome with Dynasolve solvent leaves the features of BPCS spectra substantially unchanged but considerably degrades their signal-to-noise ratio.)

3.2.1.2 Experimental set-up

The BPCS set-up consists of an Energetiq EQ-99 light source coupled to a TRIAX 180 monochromator with an output wavelength bandwidth of 2 nm (corresponding to about 15 meV in the range of interest of the present study). It should be remarked that for such value the convolution of an exponential decay with the Gaussian spectral line shape of the exciting beam does not affect the slope of the Urbach tail (i.e. the measurement of E_0). The spot size of the optical beam on the sample was ~1 mm^2, being comparable with the area of the mesas of the devices.

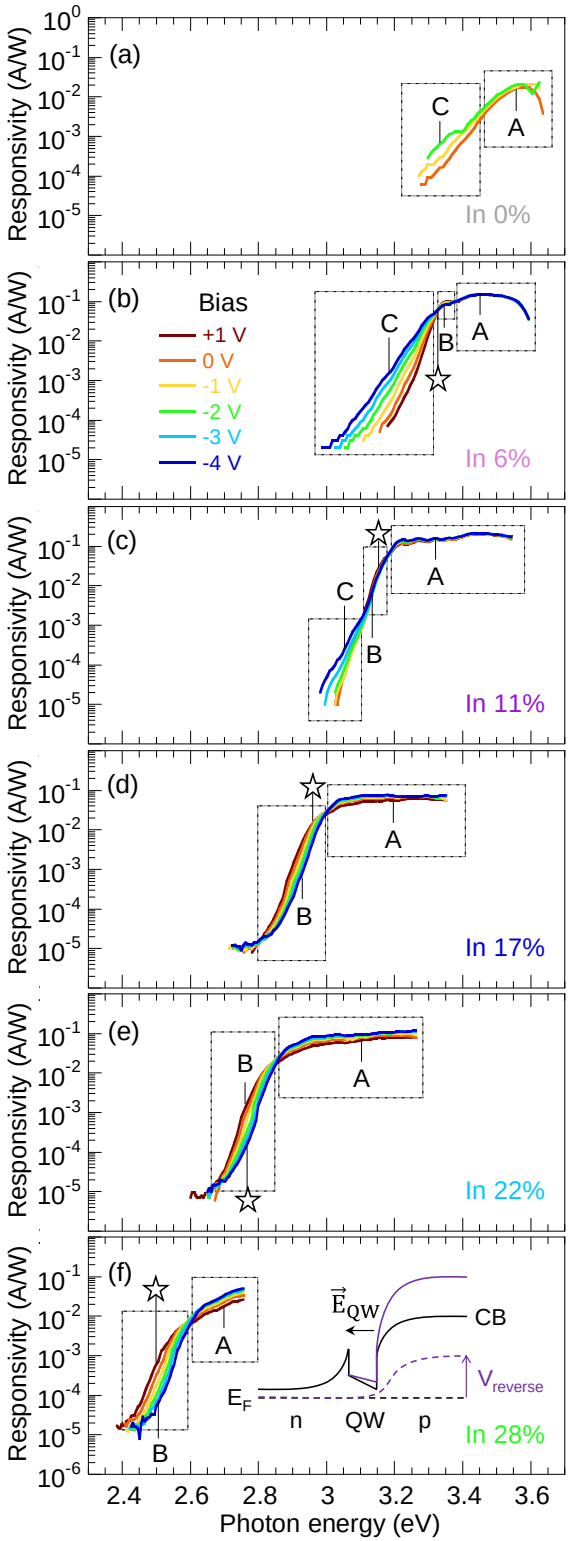

Figure 69: Responsivity measurements by BPCS of (a) m-plane UV GaN/AlGaN LED, and (b)-(f) c-plane $In_xGa_{1-x}N$/GaN solar cells with In composition ranging between 6% and 28%. The PL peak energy of the solar cells measured at 0 V is marked as stars. The schematic in (f) shows the conduction band diagram of a c-plane InGaN/GaN QW structure in which the QW electric field is partly compensated by $V_{reverse}$.

The samples were biased with a Keithley 2400 current-voltage source. The optical beam was modulated with a chopper wheel at a frequency of 82 Hz and the photocurrent signal was measured with a Princeton Applied Research 5209 lock-in amplifier. Low-temperature measurements were carried out in a JANIS SHI-4 closed cycle cryostat.

3.2.2 Results

BPCS measurements were carried out on the series of $In_xGa_{1-x}N$ QW structures with In composition varying between 0% and 28%, covering the UV to green range of the

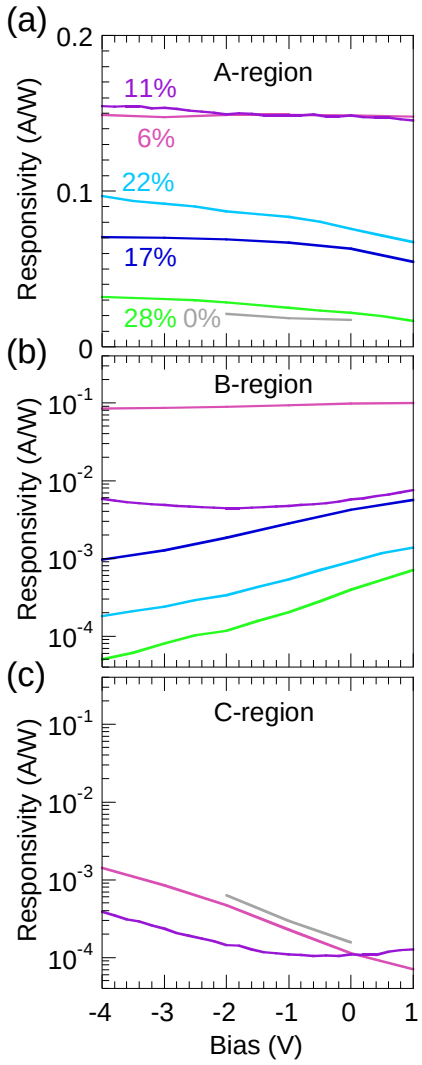

Figure 70: (a)-(c) Change in responsivity measured by BPCS as a function of applied bias at exciting photon energies belonging to the A, B, C regions of the spectra for $In_xGa_{1-x}N$ QW structures with different In composition. The photon energies corresponding to the different curves are marked as "A", "B", "C" in Figure 69.

spectrum, and for applied biases varying from +1 V to -4 V (where the negative sign indicates a reverse bias). The results are presented in Figure 69. The responsivity is obtained normalizing the photocurrent measured at a given photon energy to the incident optical power on the sample. Three different regions, named “A”, “B” and “C” (enclosed in Figure 69 by dashed boundaries), can be identified in the series of spectra according to their bias dependence. The bias dependence in these three regions is shown more in detail in Figure 70, where the responsivity at some fixed energy value is recorded for a continuous variation of the applied bias from -4 to +1 V. The specific energy values chosen for each sample are indicated in Figure 69. The photoluminescence (PL) peak energy of the solar cells measured at a bias of 0 V with different above-gap excitation laser sources is marked as stars in Figure 69.

The A-region is characterized by a weak increase in responsivity at increasing reverse bias (Figure 70a), is observed for all In compositions (Figure 69) and corresponds to absorption above the band gap of the QWs, E_g, which is defined similarly to Ref. [176]

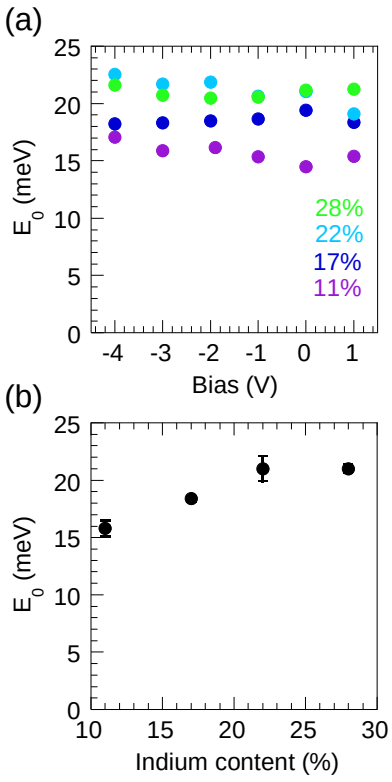

Figure 71: (a) Dependence on applied bias of the Urbach energy E_0 determined in the B-region of BPCS spectra for InGaN QW layers with different mean In content. (b) Mean values of E_0 averaged over the applied biases and plotted as a function of the mean In content of the corresponding InGaN/GaN solar cell.

as the transition energy between the exponential onset of the Urbach tail and the saturation region, corresponding to the intersection of the BPCS curves at the boundary between the A- and B-region (Figure 69b-f). A detailed description of the carrier escape mechanism from the QWs for excitation in the A-region was given in Ref. [180] according to which both tunneling and thermionic emission are expected to contribute, considering a barrier thickness of 7 nm as in our structures. No, or very little, disorder-induced effects are expected for this process, so the A region will not be discussed in the following.

The B-region is identified by an exponential decrease in responsivity at increasing reverse bias (Figure 70b), corresponding in the photocurrent spectra to an Urbach tail undergoing a blue-shift (Figure 69). Let us recall that in c-plane wurtzite InGaN/GaN structures $\vec{E}_{QW}$ points towards the substrate, as shown in the schematic of Figure 69f [24]. Increasing the reverse bias then partly compensates $\vec{E}_{QW}$ leading to a blue-shift in the absorption edge. The B-region appears in the spectra for In=6% and its energy range progressively extends at larger In concentrations. We remark that the PL peak energy of all the $In_xGa_{1-x}N$/GaN solar cells lies in the B-region which then is associated with transitions occurring in the QWs. Below-gap absorption processes giving origin to the B-region may depend on compositional disorder and QW electric field, as it will be further analyzed in Sec. 3.2.3.

None of these effects are expected to significantly affect below-gap absorption in semipolar GaN QWs, due to the reduced internal electric fields and absence of alloy fluctuations, explaining why the B-region is not observed in this sample (absorption curves in Figure 69a).

Finally, the C-region, in contrast with the B-region, is characterized by an exponential increase in responsivity at increasing reverse bias (Figure 70c) and is most clearly observed in the UV diodes. We interpret it as being due to type II well-to-barrier transitions, as detailed in the Appendix 5.5.

We remark that the B- and C-region originate from competing mechanisms of below-gap absorption which dominate, respectively, at high and low In concentration. The sample with [In]=11% corresponds to the intermediate case in which the two mechanisms have comparable efficiencies as may be observed in the deviation from the typical responsivity trend of the B- and C-region at large and small reverse bias, respectively (purple curves in Figure 70b and c).

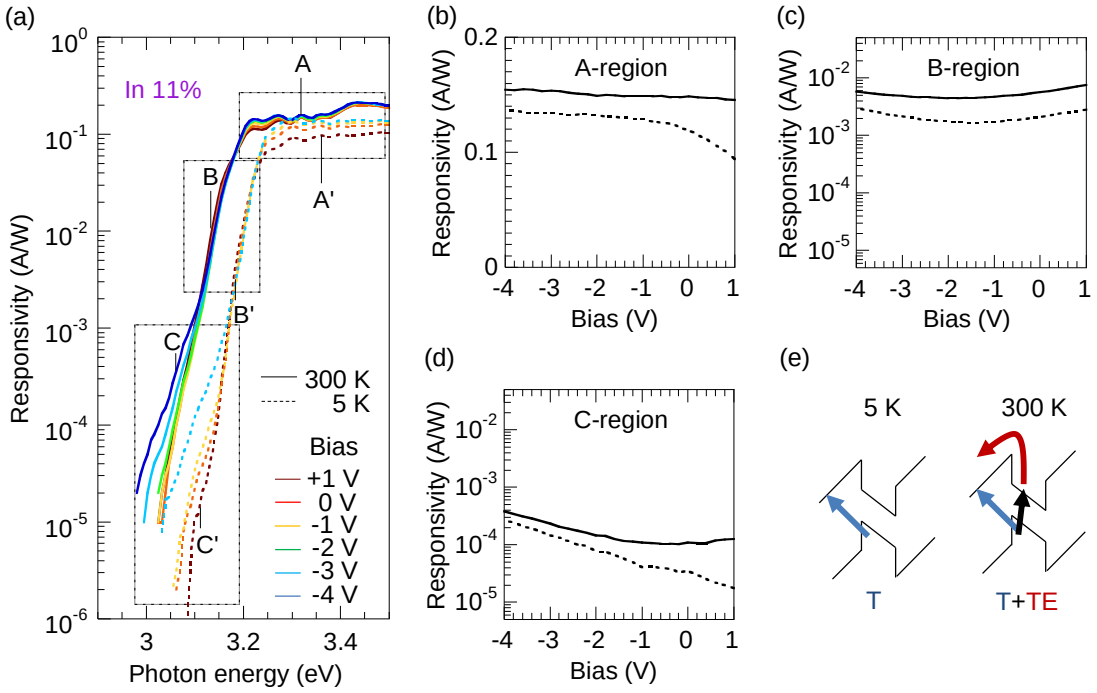

Figure 72: (a) Responsivity measurements by BPCS of an $In_{0.11}Ga_{0.89}N$/GaN solar cell at 300 K (continuous lines) and 5 K (dashed lines) as a function of applied bias. The low temperature curves are blue-shifted due to the increase in bandgap energy. The A, B, C regions are enclosed by dashed boundaries. (b)-(d) Change in responsivity as a function of applied bias at 300 K (continuous lines) and 5 K (dashed lines) for exciting photon energies belonging to the different regions and marked in (a) as A, B, C and A', B', C', at 300 K and 5 K, respectively. (e) Different mechanisms of carrier extraction from the QW. At low temperature tunneling outside the QW (T) may occur via type-II transitions. At room temperature, in addition to tunneling, absorption in the QW followed by thermionic emission (TE) may also occur.

In the following the dependence of the Urbach tail observed in the B-region will be examined as a function of different factors, such as bias, In composition, sample temperature and type of device, specifically solar cells or LEDs both incorporating InGaN QWs.

Urbach energies are fitted in a typical interval of photon energies ranging from $E_g - 150$ meV to $E_g - 20$ meV for samples with mean In composition varying between 11% and 28%. If carrier collection by BPCS were substantially dependent on the energy of the confined states in the QW, then one would expect that for a larger reverse bias

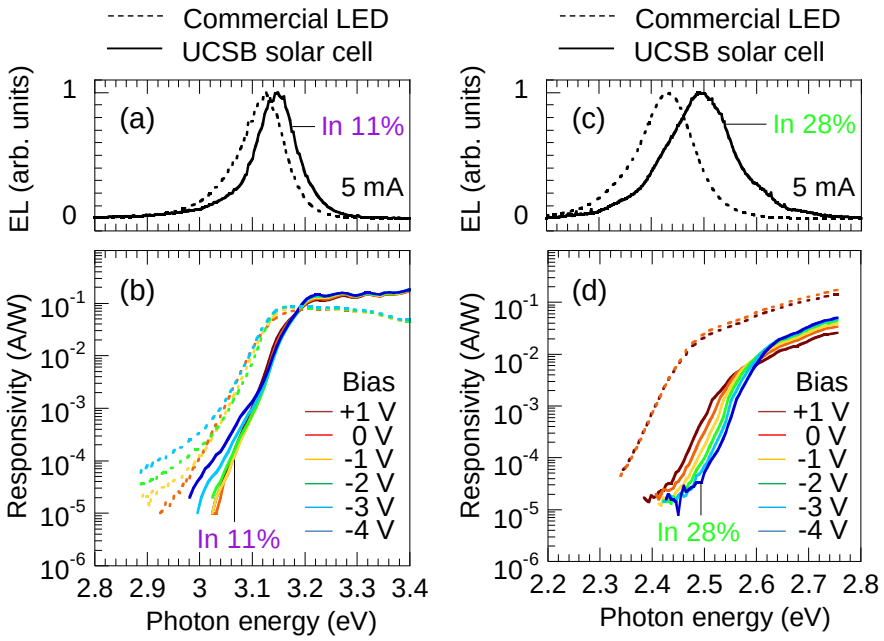

Figure 73: (a),(b) EL spectra measured at 5 mA injection and BPCS measurements of an $In_{0.11}Ga_{0.89}N$/GaN solar cell (continuous lines) and a commercial UV LED (dashed lines). (c),(d) EL spectra measured at 5 mA injection and BPCS measurements of an $In_{0.28}Ga_{0.72}N$/GaN solar cell (continuous lines) and a commercial bluish-green LED (dashed lines).

applied to the solar cells the extraction efficiency of low- localization energy carriers would increase, while that of high- localization energy carriers would remain roughly constant, thus changing the slope of the measured Urbach tails. In contrast, the experimental fact that the E_0 values appear to be almost independent on the applied bias (Figure 71a) indicates that carrier collection is only weakly sensitive to the exciting photon energy in the B-region, corroborating our hypothesis of the responsivity spectra as proportional to optical absorption. The average of E_0 taken over the different applied biases and denoted as $< E_0 >$ in Figure 71b varies weakly with In concentration for QWs emitting from the violet to the green range with the typical value being around 20 meV.

In Figure 72a BPCS measurements of the sample with [In] = 11% at room temperature and at 5 K can be compared. The increase in band gap energy at low temperature causes the photocurrent spectra to shift towards higher photon energy. But the bias dependence of the three different regions remains essentially unaffected (Figure 72b-d), except for the C-region in the low-bias range, a feature that is discussed in the Appendix 5.5.

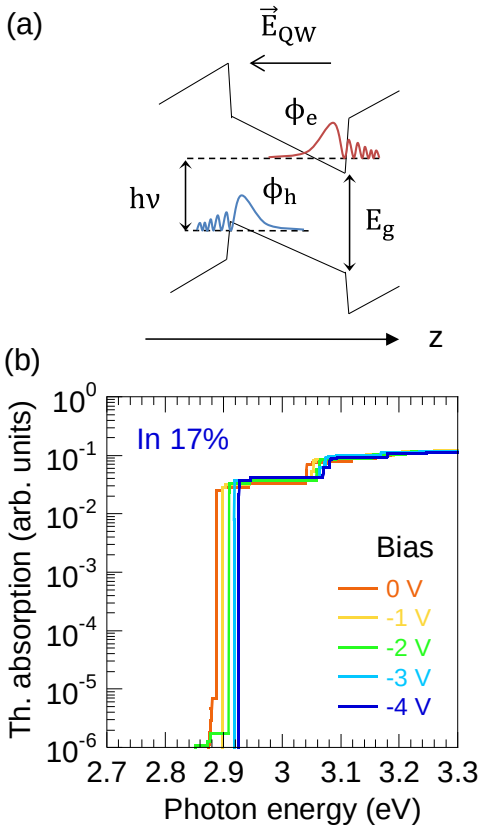

Figure 74: (a) Schematic of QCFK absorption in a QW. In presence of an electric field $\vec{E}_{QW}$ below-gap absorption at energy $h\nu < E_g$ is allowed by the overlap of the electron and hole wave functions. (b) Simulation of QCFK absorption curves for an $In_{0.17}Ga_{0.83}N$/GaN MQW solar cell structure as a function of the applied bias. Compositional disorder is not taken into account in these simulations.

Remarkably, the slope of the Urbach tail is substantially unchanged by the sample temperature: $\langle E_0 \rangle$ is 15.8 ± 0.7 meV at 300 K and 14.7 ± 0.9 meV at 5 K, in agreement with the interpretation of the Urbach tail as being related with compositional disorder, a structural property of the QWs that is temperature independent [181], therefore not due to phonon broadening.

Next we compare BPCS of UCSB solar cells with commercial LEDs to verify whether commercial-grade wafers and a different optimization of the optoelectronic devices, i.e. luminescence in LEDs vs. carrier collection in solar cells, may give rise to different features in the photocurrent spectra. Two commercial LEDs with electroluminescence (EL) spectra similar to those of two UCSB solar cells with [In]=11% and 28% are investigated (Figure 73a,c). The corresponding sets of BPCS measurements exhibit

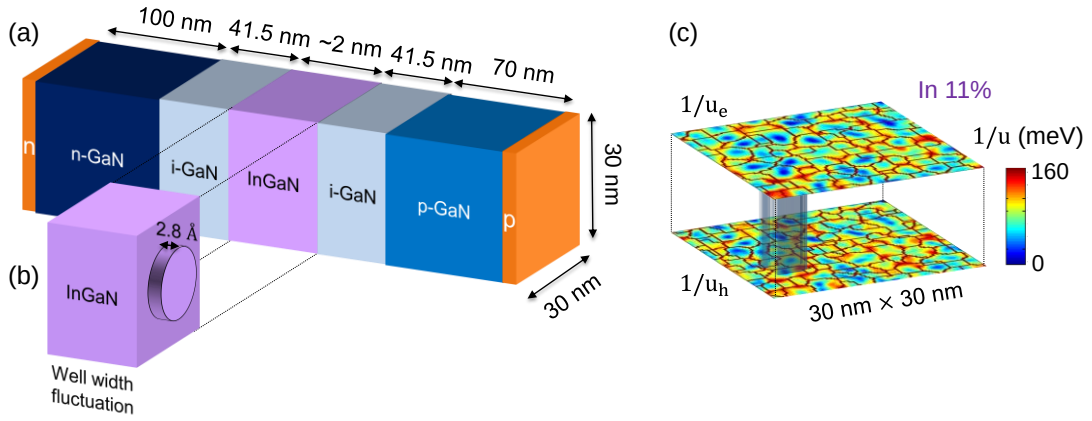

Figure 75: (a) Schematic of the typical InGaN/GaN QW structure used in the 3D absorption model. (b) The simulated InGaN QW incorporates a disk that is one monolayer thick representing a well width fluctuation. (c) « Effective » electron and hole landscapes obtained from the localization landscape theory for an $In_{0.11}Ga_{0.89}N$/GaN structure at 0 V and computed self-consistently with the Poisson-drift-diffusion equations. The maps shown here correspond to 2D cuts of the 3D landscapes in the middle plane of the QW.

strong similarities, apart from a small energy shift likely due to the difference in QW composition. In particular, in the case of UV devices (Figure 73b) the same A, B, C regions characterized by their bias dependence, as previously discussed, are observed. Green-emitting devices also exhibit common features related to the A and B regions (Figure 73d), though the application of a negative bias to the commercial green LED is severely limited by a Zener diode in parallel with the diode. The Urbach energies of the commercial devices are 21.4 ± 1.1 meV and 20.5 ± 0.5 meV for the UV and green LED, respectively, being closely in the range of E_0 measured in the UCSB solar cells. This indicates that E_0 is essentially unaffected by any possible difference in material quality. The overall close response in the measured spectra of the different devices suggests that BPCS allows carrying out a spectroscopy of intrinsic optoelectronic properties of InGaN QWs.

3.2.3 Theoretical model

In this section the possible absorption mechanisms giving origin to the Urbach tail of the B-region are analyzed by means of different models. Considering the strong polarization-induced electric fields present in c-plane InGaN/GaN QWs, typically of the

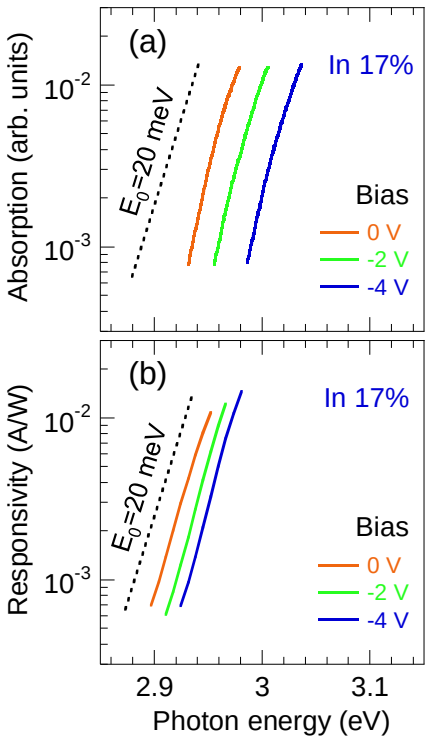

Figure 76: Urbach tails of $In_{0.17}Ga_{0.83}N$/GaN structures: (a) predicted from the 3D absorption model including compositional disorder and QW electric field, and (b) experimentally measured by BPCS. Curves correspond to different applied biases to the structure. The dashed line is shown as a reference and corresponds to an Urbach energy of 20 meV.

order of few MV/cm in the range of [In] considered here, the first hypothesis that is formulated is that the measured Urbach tails originate from the FK effect (Figure 74a).

Since we are dealing with QW structures, we should consider the quantum-confined Franz-Keldysh (QCFK) effect [124], shown schematically in Figure 74a, which corresponds to the FK effect in the limit of thin slabs of material. The absorption curve of an ideal QW should exhibit a step-like increase with photon energy due to the discrete nature of the allowed interband transitions. As a consequence of the symmetry breaking caused by the electric field, the major effect of the QCFK effect is to change the selection rules in the QW and permit "forbidden" transitions.

To evaluate the influence of $\vec{E}_{QW}$ in below-gap absorption we simulate the absorption curves of the $In_{0.17}Ga_{0.83}N$/GaN MQW solar cell structure as a function of bias using a 1D Schrödinger-Poisson-drift-diffusion solver [182,183] that assumes *homogeneous* QWs, i.e. without compositional disorder. The polarization fields of are calculated from

the spontaneous and piezoelectric polarizations of nitride QW. The quantum mechanical expression of the absorption coefficient of Ref. [124] is used, taking into account both transitions from the heavy hole and light hole bands. The simulated absorption spectra are shown in Figure 74b. The blue-shift of the absorption edge at increasing reverse bias due to the partial compensation of $\vec{E}_{QW}$ is quantitatively well reproduced in the simulations. Nevertheless the simulated curves exhibit a step-like increase due to the small thickness of the QW layers [124] indicating that QCFK alone is not sufficient to explain the observed experimental broadening of the absorption edge. Based on low temperature measurements discussed in Sec. 3.2.2 phonon broadening of the absorption edge has already been excluded. The main other mechanism of broadening is compositional disorder. Therefore to properly describe the Urbach tails of InGaN layers we develop a 3D absorption model incorporating both the effects of the electric field and compositional disorder in the QW.

In principle, to compute the absorption coefficient of a QW, solving the Schrödinger equation is necessary to obtain the localized eigenstates and corresponding eigenenergies needed to calculate the electron-hole overlap and energies of the different interband optical transitions [155]. In addition to this, when simulating biased devices, such as the solar cells considered in this study, also the Poisson and drift-diffusion equations have to be solved to account for the charge distribution and carrier transport. Note that solving the coupled Schrödinger-Poisson-drift-diffusion equations for a 3D device structure incorporating compositional disorder can be very demanding in terms of computational resources [172]. Here an alternative approach based on the localization landscape theory [146] is employed.

A schematic of the typical simulated InGaN/GaN QW structure is shown in Figure 75a. The size of the simulated domain is 30 nm × 30 nm × 255 nm. For the ease of computation the MQW region of the measured InGaN/GaN solar cells is substituted by an equivalent intrinsic layer with a single QW. Since the 10 QWs of each solar cell are nominally identical with very similar electric field conditions, the single QW model represents a fair approximation of the MQW structure in terms of the absorption spectrum. For each solar cell, the simulations are repeated for 10 different random configurations of the indium map and finally averaged to produce an average absorption curve. The indium atoms are first randomly distributed in the QW on an atomic grid with spacing a=2.833 Å corresponding to the average distance between cations in GaN. Then at each grid site the local In composition is averaged via the Gaussian averaging

method (broadening parameter fixed to $2a$). By taking the plane-averaged values of the resulting In composition an In profile along the growth direction is obtained, whose maximum defines the In concentration and whose FWHM defines the thickness of the QW. In the following simulations four solar cell structures are modeled with InGaN QWs having an In composition of 12%, 18%, 22%, 28% and a corresponding FWHM of 1.6 nm, 1.8 nm, 1.8 nm and 2.1 nm. These values allow to align the threshold of the simulated absorption spectra with that of the experimental curves, while remaining within ~1% of the In content and 0.1 nm of the QW thickness values determined by XRD in the experimental structures. Moreover, to include in the simulations the fluctuations in the width of the QWs, we consider in the process of random In atoms generation a circular region with one additional monolayer (Figure 75b), similarly to Ref. [173]. The disk occupies roughly 1/3 of the entire QW area.

All the material parameters needed in the simulations are assigned according to the local composition, as it will be detailed in Sec. 3.3.1. The new self-consistent Poisson-drift-diffusion-$1/u$ approach presented in Sec. 3.1.2.1 is used to solve the Poisson and drift-diffusion equations self-consistently with Eq. (29) accounting for quantum effects of disorder. For each given bias applied to the simulated solar cell the 3D localization landscapes are computed. As an example, 2D cuts of the "effective" potentials of electrons and holes, $1/u_e$ and $1/u_h$, in the middle of the QW of an $In_{0.11}Ga_{0.89}N$/GaN structure at 0 V are shown in Figure 75c, where the network of localization subregions is highlighted (thick lines). We shall now see how to exploit the localization landscapes to compute absorption in these structures.

In Sec. 3.1 the localization landscape theory was applied to the framework of semiconductors to derive a model accounting for quantum effects in disordered materials. In particular it was shown that the landscape u allows estimating in each localization subregion Ω_m the fundamental localized eigenfunction and its corresponding eigenenergy (Eqs. (38) and (39)).

Moreover, the following expression for the absorption coefficient of a disordered QW was derived

$$\boldsymbol{\alpha(h\nu) = \frac{2}{3} \cdot C \cdot \sum_{m,n} JDOS_{3D}^{(m,n)}(h\nu) I_{0,0}^{(m,n)}} \qquad \textbf{(65)}$$

where $C = \pi e^2 \hbar |p_{cv}|^2 / m_0^2 c\, n_r \varepsilon_0 h\nu$ is a prefactor depending on the real part of the surrounding refractive index n_r and the interband momentum matrix element p_{cv}, and

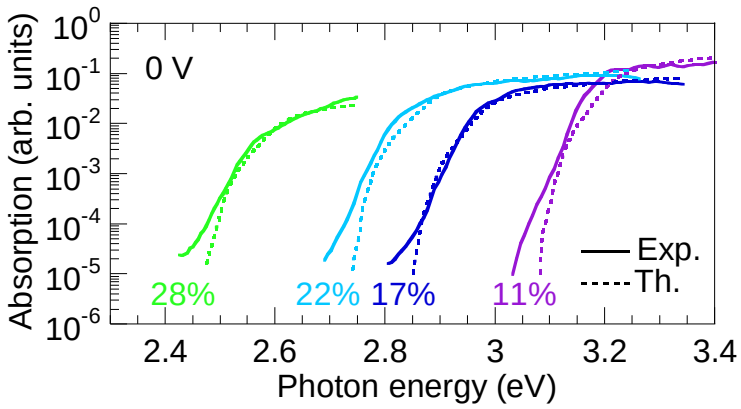

Figure 77: Absorption curves for InGaN/GaN structures of different In composition at 0 V predicted by the 3D theoretical model incorporating compositional disorder and QW electric field (dashed line). The responsivity curves measured by BPCS of InGaN/GaN solar cells of different In composition at 0 V are also shown (continuous lines).

the summation is over all electron and hole subregions (labeled m and n, respectively). Superimposing the maps of the two landscapes (Figure 75b), several subregions which consist in intersections of the localization subregions of electrons and holes can be defined. The joint density of states of each of these electron-hole "overlapping" subregions is given by

$$JDOS_{3D}^{(m,n)}(h\nu) = \frac{\sqrt{2}m_r^{3/2}}{\pi^2\hbar^3}\sqrt{h\nu - E_g - E_{e,0}^{(m)} - E_{h,0}^{(n)}} \qquad (66)$$

where $m_r = (1/m_e + 1/m_h)^{-1}$ is the reduced effective mass, and $E_{e,0}^{(m)}$ and $E_{h,0}^{n}$ are the fundamental localized states of the m-th electron and n-th hole subregions. The overlap factor is determined by the electron and hole fundamental eigenstates as

$$I_{0,0}^{(m,n)} = \frac{\left|\langle \psi_{e,0}^{(m)} | \psi_{h,0}^{(n)} \rangle\right|^2}{\left\|\psi_{e,0}^{(m)}\right\|^2 \left\|\psi_{h,0}^{(n)}\right\|^2} \qquad (67)$$

The simulations presented in the following corresponding to different mean [In] of the QW are obtained by averaging the absorption curves calculated from the landscape model using 10 different random configurations of the indium map. Urbach tails computed from the 3D absorption model for an $In_{0.17}Ga_{0.83}N$/GaN structure at different applied biases are shown in Figure 76a and b can be compared with the experimental

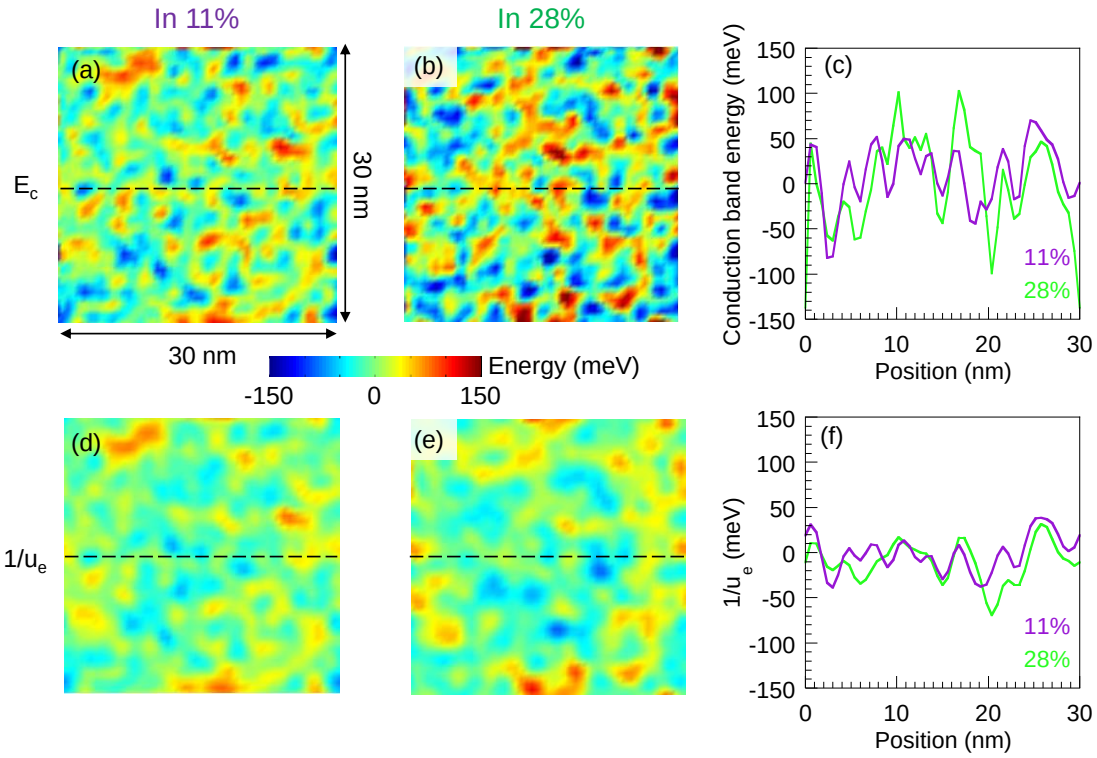

Figure 78: (a)-(b) Simulated conduction band potential maps of InGaN QWs with different In composition. (c) 1D cuts along the dashed lines of the E_c maps showing the fluctuating potential. (d)-(e) Electron energy landscapes calculated from the localization landscape theory based on the E_c maps shown in (a)-(b). (f) 1D cuts along the dashed lines of the energy landscapes $1/u_e$. The amplitude of the fluctuations is much reduced with respect to that of the corresponding E_c potentials.

Urbach tails measured by BPCS of the $In_{0.17}Ga_{0.83}N$/GaN solar cell in Figure 76b. The 3D nature of the model allows reproducing both the broadening and the bias-dependence of the experimental Urbach tails which are mainly defined by the in-plane compositional disorder and the QW electric field along the growth direction, respectively. In Figure 77, the simulated absorption curves of the InGaN/GaN solar cells at 0 V for a mean In composition ranging between 11% and 28% can be compared with the corresponding experimental measurements. Note that the absorption model only considers optical transitions occurring within the QW which give origin to the A- and B-region observed in the experiments, while type-II well-to-barrier transitions responsible for the C-region and unrelated with disorder (see Appendix 5.5) are not taken into account. The simulations reproduce well the absolute energy position and the broadening of the absorption edge as a function of the mean In content of the QWs. Let

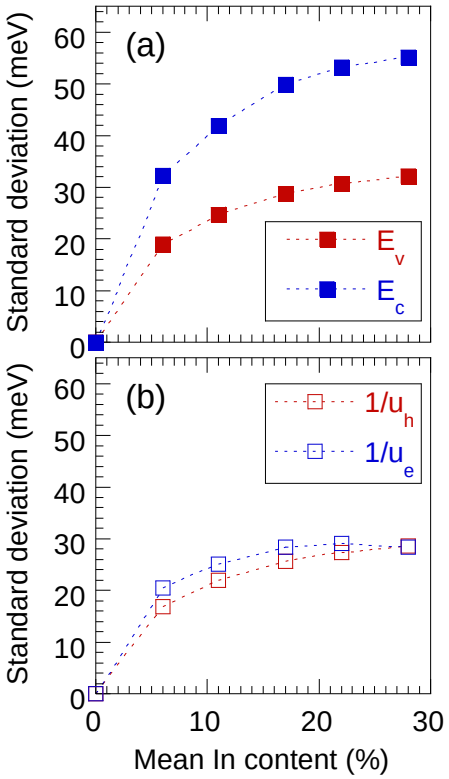

Figure 79: Standard deviations characterizing the amplitude of the fluctuations in InGaN QWs of different In composition for (a) the conduction and valence band potentials, and (b) the corresponding electron and hole effective landscapes.

us remark that the absorption model incorporating compositional alloy disorder, well width fluctuations and electric field effects gives a lower bound on the Urbach energies, explaining why the simulated tails slightly underestimate the experimental measurements. There may be other broadening processes (e.g. defect-induced smearing of band edges) which could decrease the slope of the below-gap absorption tail (thus increase E_0) but these do not seem to play an important role as the agreement with the experiments appears to be already good.

Let us now detail why the observed E_0 values are surprising and the agreement between the theory and the experiments remarkable. In the considered range of In concentrations, compositional disorder is expected to produce large potential fluctuations in the InGaN/GaN QWs. This is clearly observed in the simulations of the conduction band potential E_c for [In]=11% and [In]=28% shown in Figure 78a-c, where the 2D maps correspond to the mid-plane of the QW and the oscillating curves correspond to 1D cuts of these maps. The amplitude of the E_c fluctuations, characterized by the standard

deviation σ_V, ranges between 42 meV ([In]=11%) and 55 meV ([In]=28%). Intuitively, one could think that the typical size of the potential energy fluctuations of the QW defined by σ_V should be closely comparable to the broadening parameter of the below-gap absorption tails, both being directly related to the DOS of the system. However, the E_0 values measured in the InGaN solar cells, being typically around 20 meV, are much smaller than σ_V . Our model based on the localization landscape theory allows explaining this discrepancy. Indeed by computing the energy landscapes $1/u_e$ (Figure 78d-f) corresponding to the conduction band maps (Figure 78a-c) of the InGaN QWs it can be observed that the amplitude of the fluctuations of the "effective" potential, characterized by the standard deviation $\sigma_{1/u}$, is much reduced with respect to σ_V. The values of $\sigma_{1/u}$ are 25 meV ([In]=11%) and 28 meV ([In]=28%), closer to the experimental E_0 values. The quantum effects of confinement and tunneling, which diminish the extreme values of the potential fluctuations, have been taken into account by the wave equation (29) and thus diminish the effective energy fluctuations. This result is extended in Figure 79 showing the dependence of σ_V and $\sigma_{1/u}$ on different In concentrations for both the electron and hole landscapes. These observations suggest that the model based on $1/u$ finely captures the energy landscape effectively seen by the carriers in the disordered InGaN layers, which ultimately allows correctly predicting the broadening of the absorption edge of the InGaN/GaN solar cells.

3.2.4 Conclusions

In this work we investigated, both with experiments and theory, the effect of compositional disorder in the Urbach tails of InGaN layers with different In composition. Experimentally, Urbach tails can be measured by means of biased photocurrent spectroscopy of InGaN/GaN solar cells and LEDs. A detailed analysis of the measured responsivity spectra is required in order to identify different below-gap absorption mechanisms. Below-gap absorption due to type-II well-to-barrier transitions, particularly efficient in near-UV emitting QWs, was observed and modeled. A different mechanism of below-gap absorption corresponding to transitions within the QW was observed to be responsible for the broadening of the absorption edge of InGaN QWs with [In] $\gtrsim$ 6%. A 1D model only considering the effect of QW electric field on absorption due to QCFK allows to reproduce the blue-shift seen in the experiments but does not give origin to the experimental broadening of the absorption edge. A 3D absorption model based on the localization landscape theory is used to predict

absorption spectra of InGaN/GaN QW structures. The model takes into account compositional disorder and electric field effects in the QW and this is sufficient to reproduce the broadening and the bias-dependence of the experimental Urbach tails. The reason of the observed remarkable agreement between experiments and theory lies in the ability of the localization landscape theory to describe the effective energy landscapes seen by the carriers in the disordered InGaN layers.

3.3 Application to carrier transport and recombination in LEDs

Despite the important role played by nitride-based materials in semiconductor markets, a complete fundamental analysis of the intrinsic material properties is still missing to reconcile experiments and theoretical calculations. Atomistic simulations are impractical to calculate a full LED structure with contacts, multiple quantum wells (MQWs), electron blocking layer (EBL) and indium fluctuations, as they do not really allow to compute basic device characteristics, such as current-voltage curves and electro-luminescence spectra, where the determination of many quantum levels and the description of transport among such states is required. Because of the small computation time and of the mature development of the technique, the classical drift-diffusion (DD) equations coupled with the Poisson equation are widely used to describe transport and optical properties although they treat carriers as particles, which behave classically. Many results of quantum theory are however implicitly introduced as energy levels, density of states, quantum Fermi-Dirac statistics, and transport parameters, such as carrier mobilities and diffusion coefficients. In the case of LED simulations also radiative and non-radiative recombination mechanisms are included as described by a Shockley-Read-Hall coefficient A, a radiative coefficient B, and a non-radiative Auger recombination coefficient C. When comparing computational results using typical material parameters for ideal quantum wells or barriers without compositional disorder, the classical transport model leads to experimentally observed turn-on voltages either much too large in LEDs [170,184,185] or too small in electron barriers [186]. It also does not satisfactorily model the droop of the internal quantum efficiency (IQE) [27]. In general, researchers then use a lower density of piezo-electric polarization charge and larger Auger coefficient compared with experimental measurements to fit the experimental quantum efficiency [27] and the turn-on voltage [20,170].

Quantum models such as the non-equilibrium Green's function formalism (NEGF) have been proposed to model quantum transport properties [187,188]. They provide a good description of quantum effects such as tunneling which are absent from DD models. However, to describe indium fluctuations [171] multi-dimensional models are needed and the large burden of computation time (> thousands of CPU hours) makes the NEGF approach impractical.

Previous studies incorporated indium fluctuations into the classical Poisson and drift-diffusion model, by taking into account the fluctuating conduction and valence band

potentials [20,170]. The inclusion of these random potentials led to the enhancement of Auger recombination due to the higher local carrier density. In addition, the many percolation paths through local minima of potential energy for carrier diffusion did reduce the LED turn-on voltage. It was also computed that carrier localization induced by indium fluctuations has a strong influence on the broadening of the light emission spectrum [170]. However the wave nature of electrons leading to localization and delocalization in a disordered potential was not taken into account.

In the following, the localization landscape theory will be implemented into semi-classical Poisson and drift-diffusion equations to model carrier dynamics in LEDs including transport and recombination by using known parameters (mobilities, A, B and C coefficients) from experiments. The quantum effects affecting in-plane and perpendicular transport which arise from indium fluctuations are taken into account by effective electron and hole energies (the landscape energies), electron-hole overlap and disordered densities of states. Thanks to the efficiency of landscape computations, we carry out all calculations self-consistently for the disordered LED system.

3.3.1 Simulation Methods

In this section, the simulation framework is described. Details on the implementation of the localization landscape theory into the Poisson and DD equations were given in Sec. 3.1.2. In the standard classical picture, Poisson and drift-diffusion equations are solved self-consistently to obtain the potential energies $E_{c,v}$ for electrons and holes. The set of equations corresponds to Eqs. (53), and the 2nd and 3rd equations can be rewritten in the case of LEDs as

$$\vec{\nabla}.\vec{J}_{n,p} = q(A_0 + B_0 np + C_0(n^2 p + np^2)) \quad \textbf{(68)}$$

where

$$A_0 = \frac{np - n_i^2}{\tau_n\left(p + n_i e^{\frac{E_i - E_t}{k_B T}}\right) + \tau_p(n + n_i e^{\frac{E_t - E_i}{k_B T}})} \quad \textbf{(69)}$$

This study uses the Shockley-Read-Hall (SRH) model to account for the defect-assisted recombination through a rate A_0 (Eq. (69)), where τ_n and τ_p are the non-radiative carrier lifetimes dependent on the growth condition, which are taken as 1.0x10^{-7} s (300 K), a value typically associated with low-defect density nitride LEDs [189,190]. k_B is the Boltzmann constant and T is taken as room temperature. E_t is the trapping energy

level assumed to be located at the mid-gap, and E_i and n_i are the intrinsic energy level and intrinsic carrier density, respectively. B_0 ($7.0\text{x}10^{-11}$ cm^3/s) [191] is the intrinsic radiative recombination coefficient. Our B_0np represents the usual modified Bnp radiative recombination rate with B including the effect of overlap of the wave functions across the active region [48]. Note that in our model the separations of the electron and hole distributions in the QW both along z due to the quantum-confined Stark effect (QCSE) and in-plane due to indium fluctuations are considered in the np term. C_0 ($2.0\text{x}10^{-31}$ cm^6/s [43]) is the Auger recombination coefficient, where the influence of the electron and hole overlap is included in the n^2p and np^2 terms. B_0 and C_0 are considered temperature-independent in our simulations.

At this point we should emphasize that the choices of B_0 and C_0 are somewhat arbitrary if even not inconsistent: as the computation takes into account disorder-induced localization effects and QW confinement effects, we should take values for the B_0 and C_0 *bulk parameters without disorder*, but any experimental value will incorporate such effects of disorder and QW confinement. Only those values for bulk binary compounds such as GaN would be disorder effect free, but then the band gap change with the QW alloy can be significant. For B_0, Kioupakis *et al*. [192], show that the change from GaN to 25% In containing InGaN changes B_0 by less than 10%. Thus taking the bulk value of $7.0\text{x}10^{-11}$ cm^3/s for B_0 [48] is a good approximation. The C_0 issue is more complex: the Auger recombination term Cn^3 (more precisely $C_{eeh}n^2p + C_{ehh}np^2$) incorporates disorder impact through two effects: increase in local carrier densities through carrier localization; increase in the Auger coefficient through wave function localization [50]. The starting C_0 value for the computation should then be free of both effects, and cannot come from experiment. Theory [43] gives a value of $\approx 10^{-33}$ cm^6 s^{-1} for the direct Auger process in InGaN and $\sim 10^{-31}$ cm^6 s^{-1} for the indirect phonon-assisted Auger process. This latter process would only be marginally modified by alloy disorder induced localization of the wave functions as phonons already remove the k-conservation rule. By taking alloy effects through a supercell model, Kioupakis *et al*. [43] calculate an overall Auger coefficient of $\sim 10^{-33}$ cm^6 s^{-1}. As we have not yet calculated the effect of alloy disorder on the Auger coefficient in the landscape model [193] (cf. Sec. 3.1.2.2), a best starting value for C_0 is the low In content experimental value by David and Grundmann [48] of $\sim 2.0\text{x}10^{-31}$ cm^6/s.

In order to solve the Schrödinger equation to take the disorder-induced quantum effects into account, one should typically plug the disordered potential energy into a

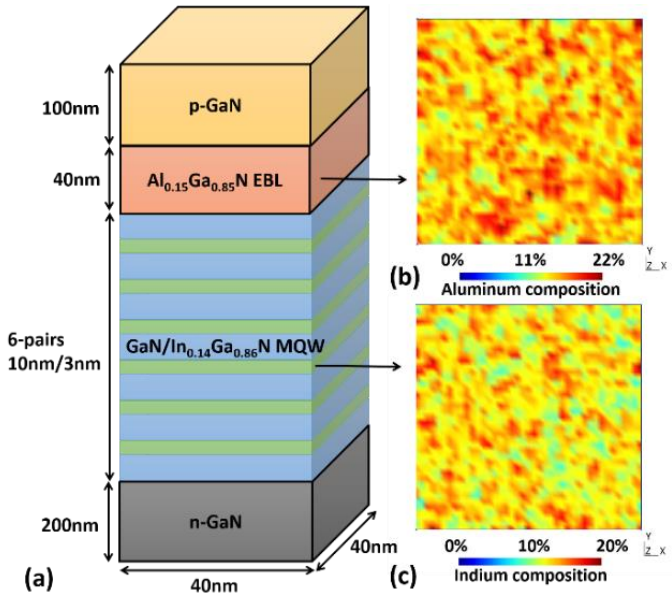

Figure 80 - (a) Schematic full LED structure. (b) In-plane aluminum distribution in the $Al_{0.15}Ga_{0.85}N$ EBL layer. (c) In-plane indium distribution in the third $In_{0.14}Ga_{0.86}N$ QW layer.

Schrödinger solver to calculate the wave functions and eigenenergies iteratively until convergence. Then the carrier density distribution can be obtained by the wave function distribution and relative eigenenergy levels. However, the entire process cannot be formulated solely on the basis of the DD equations. For example, in the case of a confined standing wave in a "flat" QW, i.e. without electric field nor disorder, where carrier density should be stationary according to the Schrödinger equation, the diffusion equation will predict a diffusion current until the carrier density becomes uniform. On the other hand, the self-consistence of a Poisson-Schrödinger solver in 3D is highly time consuming, as will be discussed later.

As a result, we rather apply the localization landscape model presented in Sec. 3.1.2 to obtain the equivalent semi-classical confining potential seen by the carriers. The schematic flowchart of the entire simulation process was shown in Figure 60. After the Poisson and DD equations are solved to obtain E_c and E_v, the landscape equation is solved giving the effective potentials $1/u_e$ and $1/u_h$. Then, the carrier densities of electrons and holes are calculated using $1/u_e$ and $1/u_h$ (Eq. (45), (46)) and fed back to the Poisson-DD equations to be solved in a self-consistent manner. When the potential energy difference between two consecutive iterations is smaller than $1x10^{-5}$ eV, the simulation loop is considered as having converged and the iteration stops.

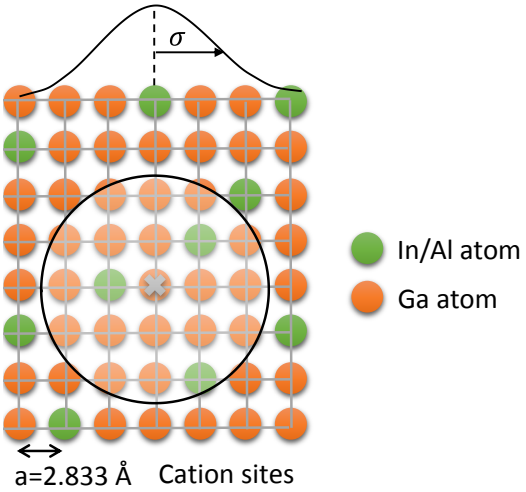

Figure 81 - The In (Al) and Ga atoms are randomly assigned at each cation lattice site by a random number generator in the InGaN (AlGaN) alloy layer. The composition at each site is then determined by a Gaussian averaging method.

In the following sections, realistic GaN-based LED structures with indium fluctuations are modeled to study the impact of disorder as calculated through the localization landscape theory.

3.3.2 The fluctuating potential in InGaN QWs and AlGaN EBL

$In_{0.14}Ga_{0.86}N$ and $Al_{0.15}Ga_{0.85}N$ are adopted as the average alloy composition of the QWs and EBL, respectively, whose dimensions are illustrated in Figure 80a. The indium and aluminum atoms are randomly distributed in the QWs and EBL and the composition maps shown in Figure 80b,c are obtained via the Gaussian averaging method detailed below. Note that the all the in-plane maps shown in this study correspond to a cross of the LED structure, thus representing a domain of 40 nm × 40 nm.

It should be remarked that other alloy systems, for instance $In_xGa_{1-x}As$, are well described by models that do not capture any effect of disorder, such as the virtual crystal approximation (VCA) in which each potentially disordered site is substituted by an artificial atom interpolating between the properties of the actual components. In the VCA the maps of Figure 80b,c would be substituted by homogeneous distributions with the mean composition of the alloy. However, simulations based on the VCA fail in the case of nitrides due to the large band offsets between GaN and InN and the heavy carrier effective masses, both larger than in the arsenide alloy system, thus potential

	GaN	InN	AlN
E_g (eV)	3.437	0.61	6.0
ε (F/cm)	10.4	15.3	10.31
$m_e^{\parallel}$ (m_0)	0.21	0.07	0.32
$m_e^{\perp}$	0.20	0.07	0.30
m_{hh}	1.87	1.61	2.68
m_{lh}	0.14	0.11	0.26
Band gap alloy bowing parameter (eV)		InGaN: 1.4 AlGaN: 0.8	

Table I - Band structure parameters for wurzite III-nitride alloys [215,216]**.**

fluctuations induced by compositional disorder must be taken into account to provide a correct description of physical observables (density of states, carrier distribution, etc.) [194]. Then one has to define the maximum length scale over which the rapidly oscillating distribution of atoms can be averaged to obtain a continuous fluctuating potential while preserving the effects of disorder on the electronic properties of the system. Baranovskii *et al.* [195] showed that the spatial scale of the fluctuations affecting the transport of the electrons and holes is given by the de Broglie wavelength $\lambda = \hbar/\sqrt{m^* E_0}$, where m^* is the carrier effective mass and E_0 is the energy scale of the band edge broadening due to disorder. In Sec. 3.2, a value of E_0~20 meV was obtained by below-gap absorption measurements of $In_xGa_{1-x}N$ QW layers over a large range of In concentrations (x=10%-30%). Taking this value of E_0 and the carrier effective masses of GaN (Table I, note: $m^*_{GaN} > m^*_{InGaN}$) gives a lower bound on the spatial size of fluctuations in InGaN alloys of 4.4 nm for electrons and 1.4 nm for heavy holes. In the computational framework presented here the atomic disorder is smoothened by a Gaussian averaging over a length scale ~0.6 nm, that is smaller than the spatial size of fluctuations seen by the carriers calculated from Ref. [195]. Therefore, the averaged atomic distribution that is used here still incorporates disorder on the relevant scale for

	GaN	InN	AlN
e_{33} (C/m^2)	0.73	0.73	1.55
e_{31} (C/m^2)	-0.49	-0.49	-0.58
e_{15} (C/m^2)	-0.40	-0.40	-0.48

Table II - Piezoelectric coefficients for Wurtzite III-nitrides materials [217]**.**

carrier transport. The details of the algorithm generating the electric potential map from the atomic distribution are described in the following.

At first, a cubic grid is constructed with a spacing corresponding to the average distance between cation atoms in GaN (a=2.833 Å). Then at each cation site either an indium (aluminum) or gallium atom for the InGaN (AlGaN) alloy are randomly assigned, as shown in Figure 81. For each site i the local averaged alloy composition $x(r_i)$ is determined from the Gaussian averaging method as

$$\boldsymbol{x(r_i) = \frac{\sum_j atom(j) \times e^{-(r_j - r_i)/2\sigma^2}}{\sum_j e^{-(r_j - r_i)/2\sigma^2}}} \qquad \textbf{(70)}$$

where the sum goes over all atom sites j of the domain, $atom(j)$ is zero or unity as decided by the random generator, and $\sigma = 2a$ [196] is the half width of the Gaussian broadening parameter.

In our computations, we separate the process of atom grid generation and computation mesh construction to make the random alloy generator independent from the mesh elements. At each mesh node all the material parameters used in the simulation (e.g., band gap, dielectric constant, and effective mass) are assigned according to the local alloy composition map $x(r_i)$. The III-nitrides material parameters we used are shown in Table I. All the parameters of InGaN and AlGaN alloys are obtained by an interpolation method as:

$$\begin{cases} E_g^{In_xGa_{1-x}N} = E_g^{GaN}(1-x) + E_g^{InN}x - 1.4x(1-x) \\ E_g^{Al_xGa_{1-x}N} = E_g^{GaN}(1-x) + E_g^{AlN}x - 0.8x(1-x) \\ \varepsilon^{In_xGa_{1-x}N} = \varepsilon^{GaN}(1-x) + \varepsilon^{InN}x \\ \varepsilon^{Al_xGa_{1-x}N} = \varepsilon^{GaN}(1-x) + \varepsilon^{AlN}x \\ m_*^{In_xGa_{1-x}N} = ((1-x)/m_*^{GaN} + x/m_*^{InN})^{-1} \\ m_*^{Al_xGa_{1-x}N} = ((1-x)/m_*^{GaN} + x/m_*^{AlN})^{-1} \end{cases} \qquad \textbf{(71)}$$

	$In_xGa_{1-x}N$	$Al_xGa_{1-x}N$
a (C/m^2)	-0.042	-0.090
b (C/m^2)	-0.034	-0.034
c (C/m^2)	0.037	0.021

Table III - Parameters of polarization values [218,219]**.**

The band offsets between GaN/InGaN and GaN/AlGaN conduction bands are assumed to be 63% of the bandgap discontinuity.

To model the 3D strain distribution in the disordered system, the 3D continuum strain-stress model is adopted, solved by the finite element method (FEM) to calculate the strain distribution over the entire LED before solving the Poisson and DD equations. The calculated strain is transformed into the piezoelectric polarization field as

$$\boldsymbol{P^{pz}} = [\boldsymbol{e}] \cdot [\boldsymbol{\varepsilon}] = \begin{bmatrix} \boldsymbol{e_{15}\varepsilon_{xz}} \\ \boldsymbol{e_{15}\varepsilon_{yz}} \\ \boldsymbol{e_{31}(\varepsilon_{xx} + \varepsilon_{yy}) + e_{33}\varepsilon_{zz}} \end{bmatrix} \quad \textbf{(72)}$$

where ε_{xx}, ε_{yy}, ε_{zz} are normal strains and ε_{yz}, ε_{zx}, ε_{xy} are shear strains. $\mathbf{P}^{pz}$ is the strain-induced piezoelectric polarization. e_{15}, e_{31}, and e_{33} are the piezoelectric coefficients (Table II), and other terms are zero due to the symmetry of wurtzite crystal structures. On the other hand, the spontaneous polarization values related to the GaN buffer layer is obtained by the following equation

$$\boldsymbol{P^{sp}} = \boldsymbol{ax} + \boldsymbol{b}(\boldsymbol{1} - \boldsymbol{x}) + \boldsymbol{cx}(\boldsymbol{1} - \boldsymbol{x}) \quad \textbf{(73)}$$

where the *a*, *b*, and *c* coefficients can be found in Table III. By taking the divergence of the total polarization $\nabla \cdot \mathbf{P}^{\text{total}}$, which includes the spontaneous and piezoelectric polarization field ($\mathbf{P}^{\text{total}} = \mathbf{P}^{sp} + \mathbf{P}^{pz}$) over the entire domain, $\rho_{pol}(\boldsymbol{r})$ is calculated as

$$\boldsymbol{\nabla}.\mathbf{P}^{\textbf{total}}(\boldsymbol{r}) = \boldsymbol{\rho_{pol}}(\boldsymbol{r}) \quad \textbf{(74)}$$

This induced fixed polarization charge (ρ_{pol}) at different locations is implemented into the Poisson equation as the initial condition, as shown in the flowchart of Figure 60.

	n-GaN	i-InGaN	p-AlGaN	p-GaN
thickness (nm)	200	67	40	100
μ_e (cm^2/Vs)	200	300	100	32
μ_h (cm^2/Vs)	23	10	5	5
Doping (cm^{-3})	$5x10^{18}$	$1x10^{17}$	$3x10^{19}$	$2x10^{19}$
E_a (meV)	25	25	215	170
τ_n (s)	10	$1x10^{-7}$	$1x10^{-7}$	$6x10^{-10}$
τ_p (s)	$7x10^{-10}$	$1x10^{-7}$	10	10
B_0 (cm^3/s)	$3x10^{-11}$	$3x10^{-11}$	$3x10^{-11}$	$3x10^{-11}$
C_0 (cm^6/s)	$2x10^{-31}$	$2x10^{-31}$	$2x10^{-31}$	$2x10^{-31}$

Table IV - Simulation parameters of each epi-layer of the simulated LED structure [137,191,220]**.**

3.3.3 The localization landscape in nitride LEDs

The size of the simulated domain is 40 nm x 40 nm x 418 nm with a full LED structure including six-pairs MQW, an EBL, and p and n transport layers, as shown in Figure 80a. The simulation will model the current injection, transport and carrier screening of polarization fields, by solving the equations self-consistently. The geometric structure was meshed by the Gmsh program [197], where the mesh has 428’655 nodes and 2’438’400 tetrahedral elements. The mesh grid size is 1 nm x 1 nm in the x-y plane and a gradual mesh technique was used for the grid size in the z-direction ranging from 0.15 nm to 20 nm. Differently from the Schrödinger equation which corresponds to an eigenvalue problem, the landscape model solves a much simpler linear equation that significantly diminishes the computation time in each iteration step by a factor of ~1000x as compared to a Schrödinger solver. In addition, the computation time of the landscape equation is approximately the same as that for the DD equation (including

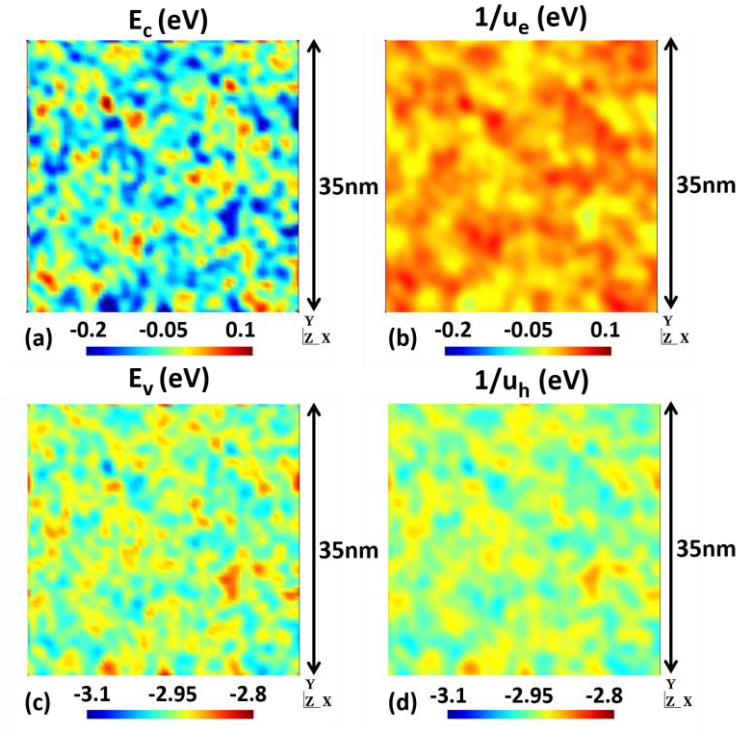

Figure 82 - In-plane potential energy maps computed in the mid-plane of the third QW of the LED structure at 2.8 V bias. (a) and (c) are the conduction and valence band potentials, respectively, solved by the classical Poisson and drift-diffusion model. (b) and (d) are the effective confining potentials solved by the localization landscape theory obtained from the conduction band and valence band potential, respectively.

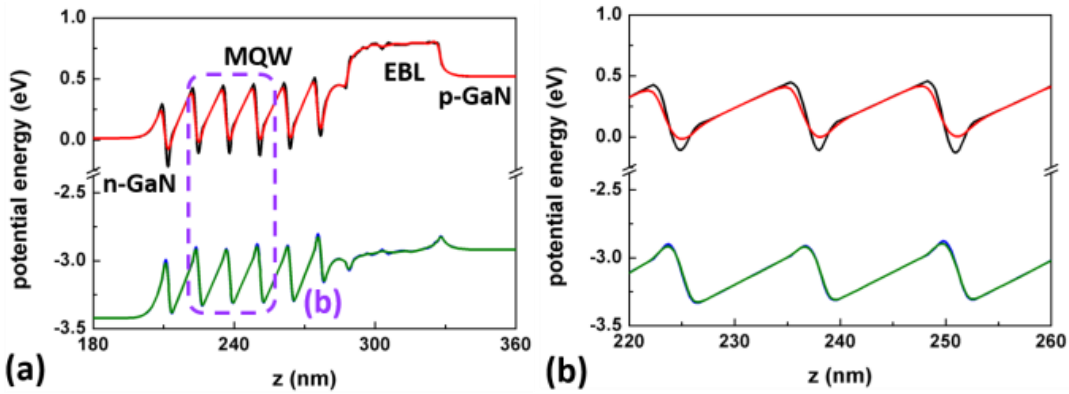

Figure 83 - (a) Band diagrams of the LED structure at 2.8 V bias along the z-direction corresponding to: Ec and Ev (black and blue lines, respectively), $1/u_e$ and $1/u_h$ (red and green lines, respectively) computed self-consistently. (b) The amplified band diagram, where the variations of the effective potentials with respect to the original band edge potentials can be observed.

electrons and holes). The detailed computation time required to solve each equation and a comparison with other models are given in the Appendix 5.6.

At a given applied bias to the LED structure the 3D localization landscape is computed in a self-consistent manner with the original potentials. As an illustration, the 2D energy potential maps corresponding to the mid-plane of a QW and the 1D band diagram of the structure along the z-direction are shown in Figure 82 and Figure 83, both for the original and the effective potentials at a bias of 2.8 V.

Figure 82a and b show the conduction band potential and the corresponding landscape potential $1/u_e$ computed self-consistently in presence of QW disorder. $1/u_e$ appears to be smoother as compared to E_c due to the fact that the landscape theory flattens the rapid fluctuations not "seen" by the quantum states of the disordered system [147]. Moreover, quantum confinement manifests itself by the appearance of closed crest lines of the effective potential 1/u, creating localization regions that did not exist in the original potential. On the other hand, the local peak potentials are lowered and smoothed due to quantum tunneling effects. Besides in-plane quantum effects, the energy reference of $1/u_e$ in Figure 82b is also lifted up with respect to E_c by quantum confinement along z (see Figure 83b). Note that the difference between the E_v and $1/u_h$ maps is smaller, as shown in Figure 82c and d. This is due to the heavy hole effective mass ($1.829m_0$), which is much heavier than the electron effective mass ($0.159m_0$) in the $In_{0.14}Ga_{0.86}N$

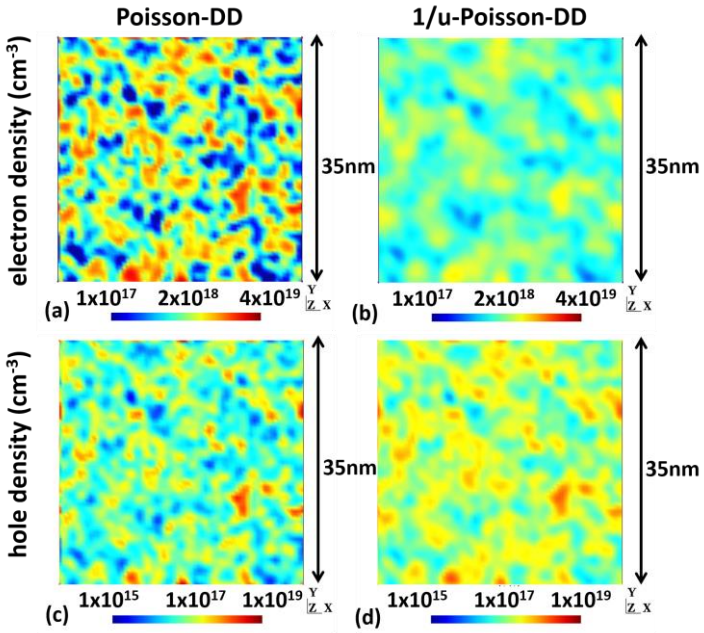

Figure 84 - Electron and hole carrier densities computed in the mid-plane of the third QW with compositional disorder at 20 A/cm^2 current density using: (a),(c) the classical Poisson and drift-diffusion model; (b),(d) the landscape theory implemented in Poisson-DD.

QW. As a result, the quantum confinement and tunneling effects experienced by heavy holes are much reduced.

Similar effects can be clearly observed in the band diagram of the structure shown in Figure 83 obtained when averaging in-plane $1/u_e$ and $1/u_h$: $1/u_h$ remains fairly close to the valence band edge, while in $1/u_e$ the minima of the conduction band edge are raised considerably and the barriers are appreciably lowered. We emphasize that the localization landscape captures the quantum effects in a disordered layer and also plays a role in the description of the effective band diagram of a quantum semiconductor structure (Sec. 3.1.3), therefore influencing both in-plane and perpendicular carrier transport through the LED.

3.3.4 Electrical and optical properties calculated from the localization landscape theory

After understanding how the landscape theory predicts the effective local potentials for electrons and holes used to calculate the carrier concentrations in a self-consistent loop with the Poisson-DD equations, we move to study current-voltage characteristics, carrier densities and the quantum efficiency of the whole GaN-based LED structure.

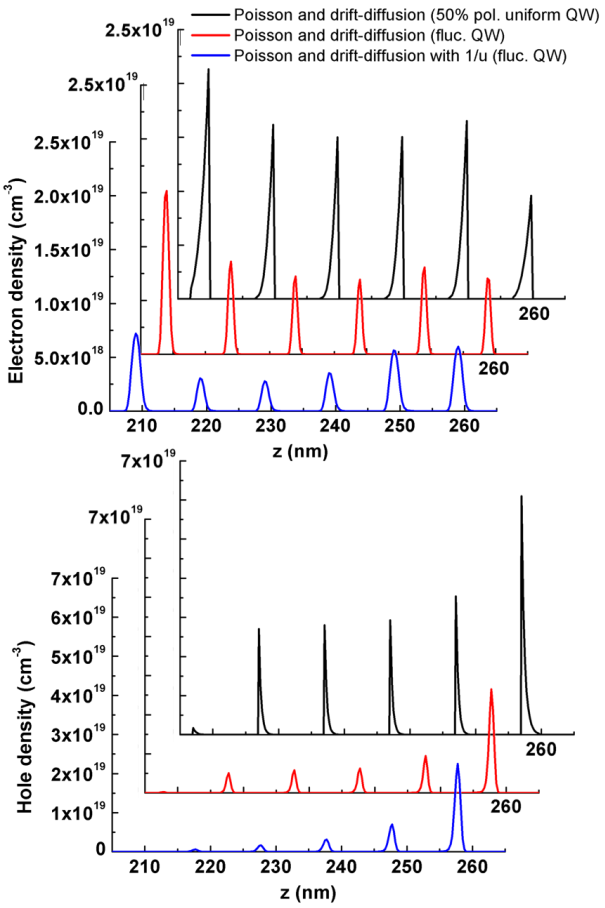

Figure 85 - Carrier distribution in the 6 QWs of the LED for electrical injection at 20 A/cm^2 obtained using a classical Poisson-DD model for uniform layers and the landscape theory implement in Poisson-DD for a structure with random alloy fluctuations. The x- and y-axis are shifted for illustration.

The simulation parameters can be found in Table IV including the doping and recombination coefficients. For the sake of comparison we compute different optoelectronic properties of the LED using the landscape-based Poisson-DD solver with random alloy fluctuations ("1/u-Poisson-DD") and compare it to the classical Poisson-DD method with random alloy fluctuations ("Poisson-DD") or with uniform QWs and EBL ("Poisson-DD (uniform)", developed in Ref. [20]). Note that only the first modeling approach takes into account quantum effects due to disorder because of the implementation of the localization landscape theory.

In Figure 84 the carrier distribution of electrons and holes computed in the mid-plane of the third QW of the LED structure can be compared. The classical Poisson and DD solver treats carriers as particles and, as a consequence, the local carrier density fluctuates strongly reflecting the rapid spatial oscillations of the alloy composition

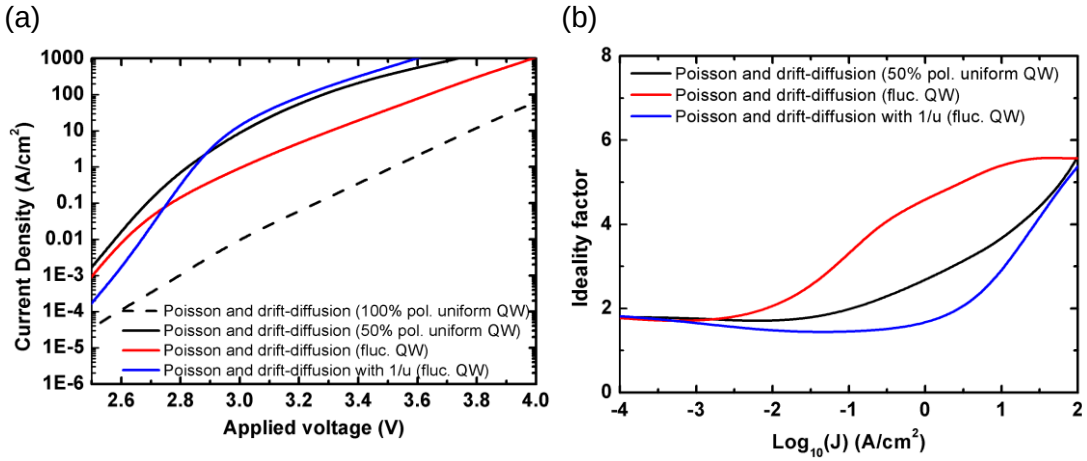

Figure 86 – A comparison of: (a) the I-V characteristics and (b) the corresponding ideality factors, computed from different Poisson-DD models assuming uniform QWs (black lines), In fluctuations described by the real potentials (red lines) or by the localization landscapes (blue curves).

(Figure 84a,c). On the other hand, in the landscape model quantum effects are included and the smoother effective potentials (Figure 82b,d) produce more uniform carrier distributions which are better representative of the standing wave nature of the localized quantum states (Figure 84b,d).

Average carrier densities along each QW of the active region are shown in Figure 85. Usually [170], the classical Poisson-DD model without disorder leads to a very large turn-on voltage when assuming 100% theoretical polarization charge, and in several works [20,27] an internal charge reduced by 50% was used to realize a turn-on voltage and IQE more in line with experiment. In Figure 85, the black curve corresponds to a structure with uniform $In_{0.14}Ga_{0.86}N$ QWs and polarization charge reduced to 50% solved by the classical Poisson and DD model, whereas the blue curves are the QW calculated by the Poisson and drift-diffusion implementing the 1/u landscape. Since at a given LED bias voltage the injected current in the two structures, with and without disorder, can be very different (Figure 86a), it is more significant to compare the carrier densities obtained from the different models at a given current density, therefore in comparable conditions of band filling and carrier-induced electric field screening. We also plot in red in Figure 85 the calculation of the carrier injection when the disorder is taken into account only through the changes in conduction and valence band levels, without the use of the landscape model to account for localization effects. The results lie somewhat in between those of the uniform material model and the landscape model. As

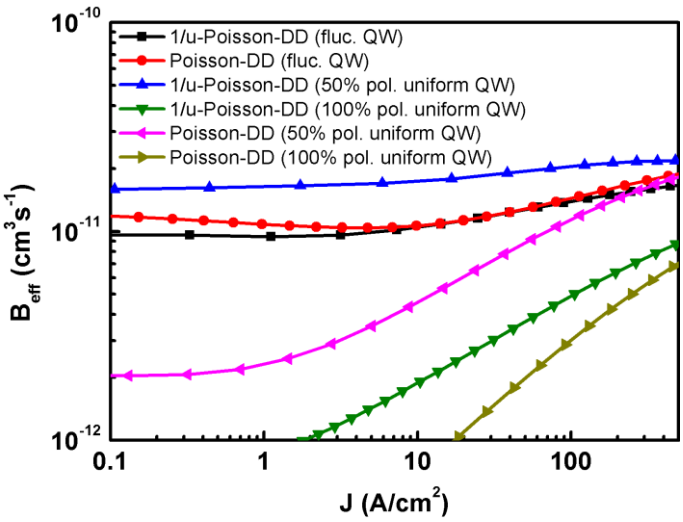

Figure 87 – Variation of the effective radiative coefficient with carrier injection in the last QW (p-side).

we can see, at the same injected current density of 20 A/cm^2, the 1/u-Poisson-DD model predicts a smaller carrier density as a consequence of the larger overlap and higher recombination rates induced by disorder. Moreover, the modeling based on the localization landscape shows that carriers are still quite inhomogeneously injected, leaving room to improvement through better designs of the active region as one wishes homogeneous carrier injection to diminish the highly nonlinear Auger recombination.

Figure 87 shows the simulated effective B coefficient, B_{eff}, for the last QW (p-side) as a function of current density, defined as the recombination rate divided by the product of the QW averaged electron and hole concentrations. As can be seen, B_{eff} increases with current density, mainly due to electric field screening. The increase is particularly important for the simulated uniform QWs, as disorder will smooth out large potential fluctuations. The size of the calculated change in B_{eff} however points that the frequently used ABC model with constant A, B, C parameters is of little use to quantitatively analyze recombination phenomena in LEDs.

Figure 88 shows the z-component of current and the corresponding effective quantum potentials in the mid-plane (x-y plane) of the third QW. As shown in Figure 88d, the current finds percolation paths through lower potential regions, enabling a decrease of the turn-on voltage, where a much smaller voltage is needed to reduce the polarization induced potential barrier. The existence of such percolation paths with high current densities is the basis of the reduced turn-on voltage caused by In fluctuations induced

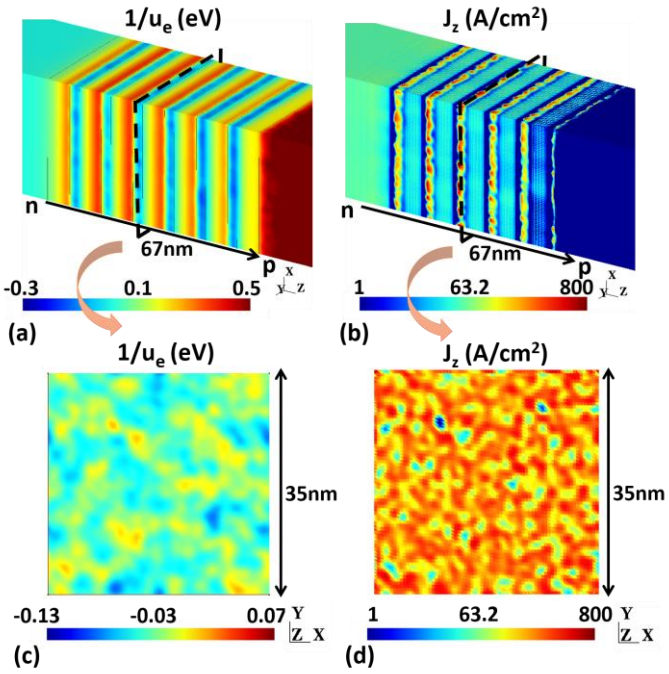

Figure 88 – (a) and (b) are the perspective views along the z-direction of vertical transport of $1/u_e$ and z-component of current (J_z), respectively. (c) and (d) are the $1/u_e$ and J_z value in the mid-plane (x-y plane) of the third QW. All figures are solved by 1/u-Poisson-DD model, where the LED current density is 20 A/cm^2.

by disorder. The similar effects of InGaN alloy fluctuations has been observed and verified in unipolar structures [186,198] .

The I-V characteristics of the LED calculated by different modeling approaches are shown in Figure 86a. Both calculations with disorder, "Poisson-DD" and "1/u-Poisson-DD", use the same input random In distribution and 100% theoretical polarization charge. Due to the higher effective band gap of the 1/u potentials (Figure 83b), the current density of Figure 86a computed using the landscape is slightly lower compared to the classical Poisson-DD solver with adjusted 50% polarization charge before or near turn-on voltage. When the applied voltage increases above the threshold, the current density computed using the landscape becomes larger due to the lower effective barriers of the 1/u potentials (Figure 83b), which effectively reduce the internal resistance for carrier transport. The forward voltage (V_f) computed by 1/u corresponding to 20 A/cm^2 is around 3.0 V at 300 K, which matches quite well commercial blue LED data (2.8-3.1 V). For instance, Nichia Co. reported in Ref. [36] two blue LEDs, a high-efficiency one with V_f = 2.89 V at 10 A/cm² and a high-power one with V_f=3.10 V at 35 A/cm², both

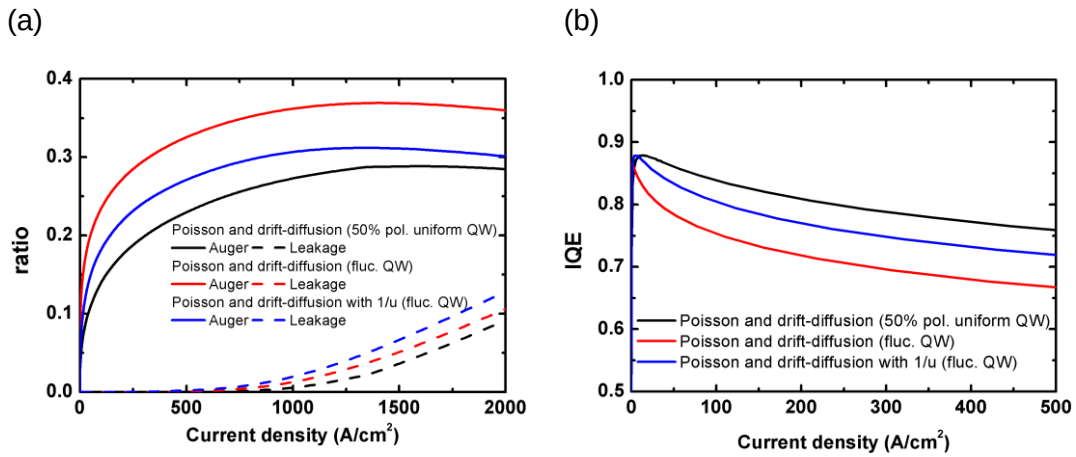

Figure 89 – (a) Ratio of Auger and leakage currents to total injected current and (b) IQE curve for the full structure LED computed from the different models.

values being in good agreement with the I-V characteristic predicted by the 1/u-Poisson-DD model. The remaining difference could be attributed to leakage paths via V-pit structures or dislocation lines [199], to the absence in our modelling of tunneling in perpendicular transport, or to the internal temperature of real LED devices being higher than 300 K, leading to a lower V_f.

3.3.5 Discussion

The above calculation of the I-V characteristic based on 1/u only assuming experimental materials parameters (Tables I-IV) represents well the experimental data. We turn now to more precise results to identify the calculated LED internal features. Figure 86b displays the ideality factor (IF) of the IV characteristics calculated as:

$$\boldsymbol{IF = \frac{q}{k_{BT}} \frac{\partial V}{\partial\, ln(J)}} \qquad \textbf{(75)}$$

The 1/u simulation remarkably reproduces the few experimental data available in high quality LEDs [129,200,201]. At low bias and current, IF is near 2, as in the Sah-Noyce-Shockley theory [130] due to SRH recombination in the depletion region (here mainly in the QWs). Increasing the bias, the IF diminishes close to unity, as modeled in perfect p-n junctions where current is dominated by diffusion in the neutral regions of the junction. This is to be expected: in the bias region where recombination is dominated by a bimolecular radiative recombination process, the current density is approximately $B_0 np$. Expressing n and p as $n = N_c\, e^{-(E_c - E_{Fn})/k_B T}$ and $p = N_v\, e^{-(E_{Fp} - E_v)/k_B T}$ yields

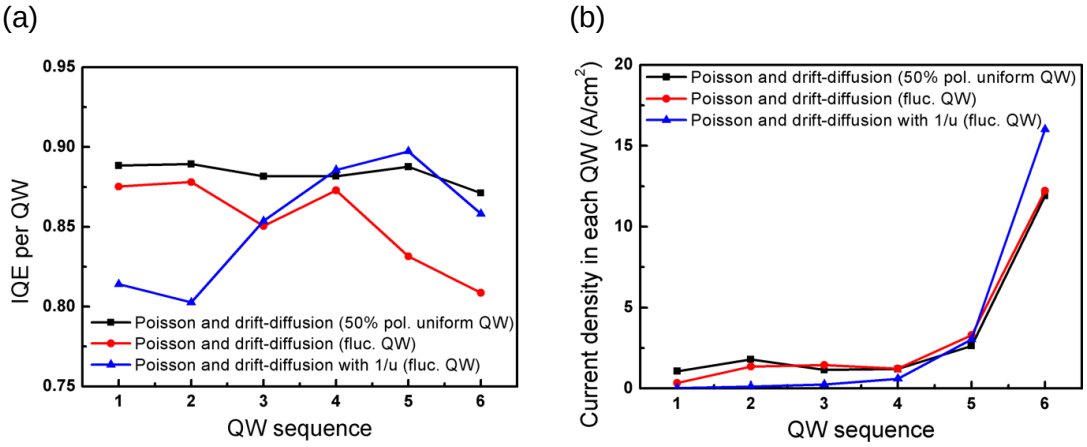

Figure 90 – Distribution among the different QWs of: (a) IQE, (b) Current density. LED current density is 20 A/cm^2.

$J \propto N_c N_v e^{-\frac{E_g}{k_B T}} e^{\frac{eV}{k_B T}} \approx n_i^2 e^{\frac{eV}{k_B T}}$, thus an ideality factor unity. The minimum IF, near unity, is reached at a current density of the order of 0.1 A/cm², in the range of the experimental measurements [129,200,201]. At even larger bias, the IF increases again as the series resistance dominates the device characteristic. The IF calculation shows that the "1/u-Poisson-DD" model including random alloy fluctuations provides an excellent overall description of the transport properties of LEDs.

It must be remarked that an almost ideal IF does not mean at all that carriers are uniformly distributed in the structure (cf. Figure 85) pointing to the inherent shortcomings of electrical measurements to assess that critical phenomenon. We can also calculate the leakage current exiting the active layer region, as shown in Figure 89a. As it can be expected from the low turn-on voltages modeled, quite smaller than the GaN band gap, very little carrier leakage is expected under usual operating conditions. The calculation indeed shows that leakage is negligible until the bias voltage reaches 3.4 V, value corresponding to the GaN band gap, with total currents above 500 A/cm^2. In this calculation, the sheet resistance is not considered since only vertical transport is calculated. If the sheet resistance is considered, it will even need higher voltage to reach the flat band condition since an extra potential drop will occur in the current spreading layer.

Turning to the light emission efficiency curve, shown in Figure 89b, the peak IQE obtained from 1/u is slightly higher than the classical Poisson-DD model because of the more homogeneous in-plane radiative efficiency and carrier injection in each QW: as

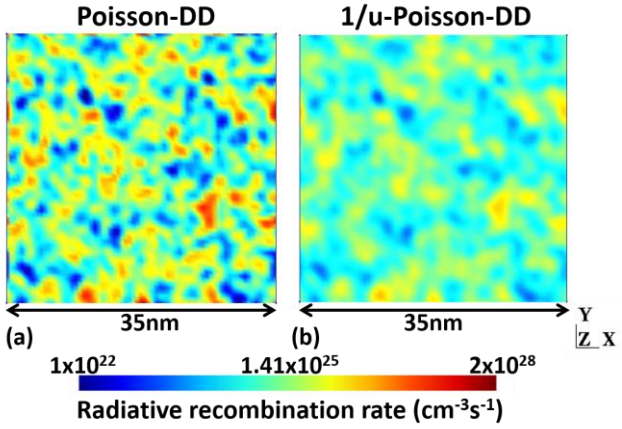

Figure 91 - In-plane local radiative recombination rates in the third QW computed from: (a) the classical Poisson-DD model; (b) 1/u-Poisson-DD model. Current density is fixed at 20 A/cm^2.

Figure 91b shows, the in-plane radiative recombination distribution spreads out in the localization landscape-based model because carriers are localized on larger domains in the QW plane (Figure 84b,d). Let us recall that the influence of wave function overlap in our model is included in the np term instead of the radiative recombination coefficient B_0. Therefore, as shown in Figure 85, the distribution of electrons and holes along the growth direction is more symmetric with respect to the mid-plane of the QWs due to quantum confined wave properties. They have then better overlap compared to the classical DD model, leading to a higher radiative efficiency.

Figure 90b shows the calculation of the integrated recombined current both radiatively and nonradiatively in each well for the uniform QW and disordered QW models at a current density of 20 A/cm^2. The inhomogeneity of carrier injection is well displayed by the total recombination current decreasing from the p-side, on the right, to the n-side. Moreover, the IQE of each QW is also calculated to examine the contribution of each QW as shown in Figure 90a. The IQE of the QW close to the p-layer is smaller in the classical Poisson-DD model due to a smaller overlap as compared to the 1/u-Poisson-DD model. The opposite trend between the classical Poisson-DD model (higher IQE in the QWs close to the n-layer) and 1/u-Poisson-DD model (higher IQE in the QWs close to the p-layer) also reveals a better current injection through MQWs for the 1/u-Poisson-DD model due to reduced effective barriers for electrons. Besides, the Auger recombination will start to dominate in the last QW (p-side well) at higher carrier densities. Due to the increasing local carrier density in the disorder case, the integrated

Auger recombination can be enhanced compared to normal QW (see Figure 89a), which matches well the experimental droop with a C_0 coefficient in line with theory. On the other hand, the different IQE values among QWs can be attributed to the inhomogeneity of carrier injection, which again shows that adopting a constant carrier density (n) in the ABC model is incorrect to represent the IQE behavior in MQW structures. While small, the recombination currents in QWs other than the last one cannot be neglected, as is sometimes done in ABC modeling. In the 50% polarization uniform QWs case, the intentionally reduced polarization field makes electrons and holes overlap better due to the more homogeneous distribution in each well, which does not match experimental observations [202]. It also reduces the influence of Auger recombination due to lower local carrier density (without localization), so that the droop effect is less pronounced. A larger C_0 would then be needed to represent the experimental Auger recombination.

3.3.6 Conclusions

In this study, carrier transport and recombination in a realistic LED structure incorporating random alloy fluctuations were modeled using the localization landscape theory. According to this theory, a function 1/u acts as an effective semi-classical confining potential seen by the carriers. The effective landscape $1/u$ allows analyzing carrier dynamics through the classical drift-diffusion equations while conserving a local formulation (self-consistent and computationally efficient) and, at the same time, taking into account quantum effects such as carrier localization and tunneling.

The in-plane carrier distribution obtained from the landscape model reflects the standing wave nature of the localized eigenstates, while the distribution along the z-direction shows that carriers are still quite inhomogeneously injected leaving room to improvement through better designs of the active region. The I-V curve of the simulated LED predicted by the $1/u$-Poisson-DD model matches well the turn-on voltage of commercial blue LEDs, and the corresponding ideality factor is in agreement with the predictions of the Sah-Noyce-Shockley theory for ideal junctions.

Finally, it should be noted that, in principle, this method is not restricted to the framework of nitride-based devices, but can be expanded in the future to the modeling of other semiconductor materials and devices incorporating disorder effects. With the landscape model, computations are much faster than the conventional Schrödinger

eigensolvers, especially in 3D modeling, typically by a factor 100-1000x, allowing self-consistent calculations.

4 REFERENCES

[1] S. Nakamura, M. Senoh, N. Iwasa, and S. chi Nagahama, Appl. Phys. Lett. **67**, 1868 (1995).

[2] M. A. Caro, Theory of Elasticity and Electric Polarization Effects in the Group-III Nitrides, University College Cork, 2013.

[3] R. Peon, G. Doluweera, I. Platonova, D. Irvine-Halliday, and G. Irvine-Halliday, in *Proc. SPIE* (2005), p. 59410N–15.

[4] E. F. Schubert, *Light-Emitting Diodes*, 2nd Editio (Cambridge University Press, 2006).

[5] C. Weisbuch, M. Piccardo, L. Martinelli, J. Iveland, J. Peretti, and J. S. Speck, Phys. Status Solidi Appl. Mater. Sci. **212**, 899 (2015).

[6] J. T. Leonard, E. C. Young, B. P. Yonkee, D. A. Cohen, T. Margalith, S. P. DenBaars, J. S. Speck, and S. Nakamura, Appl. Phys. Lett. **107**, (2015).

[7] R. S. Pengelly, S. M. Wood, J. W. Milligan, S. T. Sheppard, and W. L. Pribble, IEEE Trans. Microw. Theory Tech. **60**, 1764 (2016).

[8] P. Srivastava, J. Das, D. Visalli, M. Van Hove, P. E. Malinowski, D. Marcon, S. Lenci, K. Geens, K. Cheng, M. Leys, S. Decoutere, R. P. Mertens, and G. Borghs, IEEE Electron Device Lett. **32**, 30 (2011).

[9] S. Keeping, Structural Defects Undermine LED Luminosity, www.digikey.com/en/articles/techzone/2012/apr/structural-defects-undermine-led-luminosity, 2012.

[10] A. Hangleiter, F. Hitzel, C. Netzel, D. Fuhrmann, U. Rossow, G. Ade, and P. Hinze, Phys. Rev. Lett. **95**, (2005).

[11] X. H. Wu, C. R. Elsass, A. Abare, M. Mack, S. Keller, P. M. Petroff, S. P. DenBaars, J. S. Speck, and S. J. Rosner, Appl. Phys. Lett. **72**, (1998).

[12] S. F. Chichibu, A. Uedono, T. Onuma, B. A. Haskell, A. Chakraborty, T. Koyama, P. T. Fini, S. Keller, S. P. DenBaars, J. S. Speck, U. K. Mishra, S. Nakamura, S. Yamaguchi, S. Kamiyama, H. Amano, I. Akasaki, J. Han, and T. Sota, Nat. Mater. **5**, 810 (2006).

[13] H.-Y. Shih, M. Shiojiri, C.-H. Chen, S.-F. Yu, C.-T. Ko, J.-R. Yang, R.-M. Lin, and M.-J. Chen, Sci. Rep. **5**, 13671 (2015).

[14] M. J. Cich, R. I. Aldaz, A. Chakraborty, A. David, M. J. Grundmann, A. Tyagi, M. Zhang, F. M. Steranka, and M. R. Krames, Appl. Phys. Lett. **101**, 223509 (2012).

[15] S. Nakamura, T. Mukai, M. Senoh, and N. Iwasa, Jpn. J. Appl. Phys. **31**, L139 (1992).

[16] H. Amano, M. Kito, K. Hiramatsu, and I. Akasaki, Jpn. J. Appl. Phys. **28**, L2112 (1989).

[17] W. Götz, N. M. Johnson, J. Walker, D. P. Bour, and R. A. Street, Appl. Phys. Lett. **68**, (1996).

[18] U. Mishra and J. Singh, *Semiconductor Device Physics and Design* (Springer Netherlands, 2007).

[19] P. Kozodoy, Magnesium-Doped Gallium Nitride for Electronic and Optoelectronic Device Applications, University of California, Santa Barbara, 1999.

[20] Y.-R. Wu, R. Shivaraman, K.-C. Wang, and J. S. Speck, Appl. Phys. Lett. **101**, 83505 (2012).

[21] R. Shivaraman, Atom Probe Tomography of III-Nitrides, University of California, Santa Barbara, 2013.

[22] R. A. Oliver, S. E. Bennett, T. Zhu, D. J. Beesley, M. J. Kappers, D. W. Saxey, A. Cerezo, and C. J. Humphreys, J. Phys. D. Appl. Phys. **43**, 354003 (2010).

[23] F. Bernardini, V. Fiorentini, and D. Vanderbilt, Phys. Rev. B **56**, 4 (1997).

[24] M. Feneberg and K. Thonke, J. Phys. Condens. Matter **19**, 403201 (2007).

[25] J. S. Speck and S. F. Chichibu, MRS Bull. **34**, 304 (2009).

[26] D. Jena, Polarization Induced Electron Populations in III-V Nitride Semiconductors: Transport, Growth, and Device Applications, University of California, Santa Barbara, 2003.

[27] J. Piprek, Phys. Status Solidi Appl. Mater. Sci. **207**, 2217 (2010).

[28] P.-C. Hung and J. Y. Tsao, Disp. Technol. J. **9**, 405 (2013).

[29] U. S. D. of Energy, Solid-State Lighting Research and Development Multi-Year Program Plan, U.S. Department of Energy, 2014.

[30] T. Fujii, Y. Gao, R. Sharma, E. L. Hu, S. P. DenBaars, and S. Nakamura, Appl. Phys. Lett. **84**, 805 (2004).

[31] K. Tadatomo, in *III-Nitride Based Light Emit. Diodes Appl.*, edited by T.-Y. Seong, J. Han, H. Amano, and H. Morkoc (Springer Netherlands, 2013), pp. 59–81.

[32] M. R. Krames, O. B. Shchekin, R. Mueller-Mach, G. O. Mueller, L. Zhou, G. Harbers, and M. G. Craford, IEEE/OSA J. Disp. Technol. **3**, 160 (2007).

[33] A. David, H. Benisty, and C. Weisbuch, Reports Prog. Phys. **75**, 126501 (2012).

[34] M. Yamada, T. Mitani, Y. Narukawa, S. Shioji, I. Niki, S. Sonobe, K. Deguchi, M. Sano, and T. Mukai, Jpn. J. Appl. Phys. **41**, L1431 (2002).

[35] A. David, C. Meier, R. Sharma, F. S. Diana, S. P. Denbaars, E. Hu, S. Nakamura, C. Weisbuch, and H. Benisty, Appl. Phys. Lett. **87**, 101109 (2005).

[36] Y. Narukawa, M. Ichikawa, D. Sanga, M. Sano, and T. Mukai, J. Phys. D. Appl. Phys. **43**, 354002 (2010).

[37] V. Avrutin, S. D. A. Hafiz, F. Zhang, Ü. Özgür, H. Morkoç, A. Matulionis, U. Özgür, H. Morkoç, and A. Matulionis, J. Vac. Sci. Technol. A Vacuum, Surfaces, Film. **31**, 50809 (2013).

[38] J. Cho, E. F. Schubert, and J. K. Kim, Laser Photon. Rev. **7**, 408 (2013).

[39] I. E. Titkov, D. A. Sannikov, Y. M. Park, and J. K. Son, AIP Adv. **2**, 32117 (2012).

[40] L. Cheng, S. Wu, H. Chen, C. Xia, and Q. Kong, Opt. Quantum Electron. **48**, 1 (2015).

[41] N. I. Bochkareva, Y. T. Rebane, and Y. G. Shreter, Appl. Phys. Lett. **103**, 191101 (2013).

[42] E. Kioupakis, P. Rinke, K. T. Delaney, and C. G. Van de Walle, Appl. Phys. Lett. **98**, 161107 (2011).

[43] E. Kioupakis, P. Rinke, K. T. Delaney, and C. G. Van De Walle, Phys. Rev. B **92**, 35207 (2015).

[44] E. Kioupakis, Q. Yan, and C. G. Van De Walle, Appl. Phys. Lett. **101**, 231107 (2012).

[45] Y. C. Shen, G. O. Mueller, S. Watanabe, N. F. Gardner, A. Munkholm, and M. R. Krames, Appl. Phys. Lett. **91**, 141101 (2007).

[46] A. Laubsch, M. Sabathil, W. Bergbauer, M. Strassburg, H. Lugauer, M. Peter, S. Lutgen, N. Linder, K. Streubel, J. Hader, J. V. Moloney, B. Pasenow, and S. W. Koch, Phys. Status Solidi **6**, S913 (2009).

[47] A. A. David and N. F. Gardner, Appl. Phys. Lett. **97**, 193508 (2010).

[48] A. A. David and M. J. Grundmann, Appl. Phys. Lett. **97**, 33501 (2010).

[49] J. Hader, J. V. Moloney, and S. W. Koch, SPIE Proc. **8625**, 86251M (2013).

[50] R. Vaxenburg, A. Rodina, E. Lifshitz, and A. L. Efros, Appl. Phys. Lett. **103**, 221111 (2013).

[51] M. Deppner, F. Römer, and B. Witzigmann, Phys. Status Solidi - Rapid Res. Lett. **6**, 418 (2012).

[52] M. Binder, a. Nirschl, R. Zeisel, T. Hager, H.-J. Lugauer, M. Sabathil, D. Bougeard, J. Wagner, and B. Galler, Appl. Phys. Lett. **103**, 71108 (2013).

[53] J. Iveland, L. Martinelli, J. Peretti, J. S. J. S. Speck, and C. Weisbuch, Phys. Rev. Lett. **110**, 177406 (2013).

[54] N. F. Gardner, G. O. Müller, Y. C. Shen, G. Chen, S. Watanabe, W. Götz, and M. R. Krames, Appl. Phys. Lett. **91**, 243506 (2007).

[55] M. Mandl, X. Wang, T. Schimpke, C. Kölper, M. Binder, J. Ledig, A. Waag, X. Kong, A. Trampert, F. Bertram, J. Christen, F. Barbagini, E. Calleja, and M. Strassburg, Phys. Status Solidi **7**, 800 (2013).

[56] C. C. Pan, S. Tanaka, F. Wu, Y. Zhao, J. S. Speck, S. Nakamura, S. P. Den Baars,

and D. Feezel, Appl. Phys. Express **5**, 62103 (2012).

[57] A. Inoue, R. Kato, A. Yamada, and T. Yokogawa, IEDM 2012 621 (2012).

[58] J. J. Wierer, J. Y. Tsao, and D. S. Sizov, Phys. Status Solidi Curr. Top. Solid State Phys. **11**, 674 (2014).

[59] S. Krishnamurthy, M. van Schilfgaarde, A. Sher, and A.-B. Chen, Appl. Phys. Lett. **71**, (1997).

[60] Q. Yan, E. Kioupakis, D. Jena, and C. G. de Walle, Phys. Rev. B **90**, 121201 (2014).

[61] Z. C. Huang, R. Goldberg, J. C. Chen, Y. Zheng, D. B. Mott, and P. Shu, Appl. Phys. Lett. **67**, (1995).

[62] B. Aslan and L. F. Eastman, Solid. State. Electron. **64**, 57 (2011).

[63] F. Gütle, V. M. Polyakov, M. Baeumler, F. Benkhelifa, S. Müller, M. Dammann, M. Cäsar, R. Quay, M. Mikulla, J. Wagner, and O. Ambacher, Semicond. Sci. Technol. **27**, 125003 (2012).

[64] E. G. Brazel, M. a. Chin, V. Narayanamurti, D. Kapolnek, E. J. E. Tarsa, S. P. DenBaars, and S. P. Tarsa, Appl. Phys. Lett. **70**, 330 (1997).

[65] N. Nepal, K. B. Nam, J. Li, M. L. Nakarmi, J. Y. Lin, and H. X. Jiang, Appl. Phys. Lett. **88**, 261919 (2006).

[66] M. Semenenko, O. Yilmazoglu, H. L. Hartnagel, and D. Pavlidis, J. Appl. Phys. **109**, 23703 (2011).

[67] C.-K. Sun, Y.-L. Huang, S. Keller, U. Mishra, and S. DenBaars, Phys. Rev. B **59**, 13535 (1999).

[68] S. Wu, P. Geiser, J. Jun, J. Karpinski, D. Wang, and R. Sobolewski, J. Appl. Phys. **101**, 43701 (2007).

[69] A. M. Witowski, K. Pakula, J. M. Baranowski, M. L. Sadowski, and P. Wyder, Appl. Phys. Lett. **75**, 4154 (1999).

[70] M. Drechsler, D. Hofmann, B. Meyer, T. Detchprohm, H. Amano, and I. Akasaki, Jpn. J. Appl. Phys. **34**, 1178 (1995).

[71] B. Santic, Semicond. Sci. Technol. **219**, (2003).

[72] J. C. C. Cao and X. L. L. Lei, Eur. Phys. J. B-Condensed Matter **7**, 79 (1999).

[73] T. Valla, P. Johnson, S. Dhesi, K. Smith, D. Doppalapudi, T. Moustakas, and E. Shirley, Phys. Rev. B **59**, 5003 (1999).

[74] R. Goldhahn, K. Lange, and M. Feneberg, Proc. SPIE **9363**, 93630G (2015).

[75] T. J. Kim, J. S. Byun, Y. D. Kim, Y.-C. Chang, and H. Kim, J. Korean Phys. Soc. **53**, 1575 (2008).

[76] M. Rakel, C. Cobet, N. Esser, F. Fuchs, F. Bechstedt, R. Goldhahn, W. G. Schmidt, and W. Schaff, Phys. Rev. B - Condens. Matter Mater. Phys. **77**, (2008).

[77] D. E. Aspnes, M. Cardona, V. Saile, M. Skibowski, and G. Sprüssel, Solid State Commun. **31**, 99 (1979).

[78] D. E. Aspnes, C. G. Olson, and D. W. Lynch, Phys. Rev. Lett. **37**, 766 (1976).

[79] M. Goano, E. Bellotti, E. Ghillino, G. Ghione, and K. F. Brennan, J. Appl. Phys. **88**, 6467 (2000).

[80] K. T. Delaney, P. Rinke, and C. G. Van de Walle, Appl. Phys. Lett. **94**, 191109 (2009).

[81] R. Wang, P. Ruden, J. Kolnik, I. Oguzman, and K. Brennan, J. Phys. Chem. Solids **58**, 913 (1997).

[82] L. C. de Carvalho, A. Schleife, and F. Bechstedt, Phys. Rev. B **84**, 195105 (2011).

[83] M. Heiblum, E. Calleja, I. M. Anderson, W. P. Dumke, C. M. Knoedler, and L. Osterling, Phys. Rev. Lett. **56**, 2854 (1986).

[84] R. A. Millikan, Phys. Rev. **7**, 355 (1916).

[85] J. J. Scheer and J. van Laar, Solid State Commun. **3**, 189 (1965).

[86] J. Iveland, Electron Emission Spectroscopy of InGaN/GaN Light Emitting Diodes, University of California, Santa Barbara, 2015.

[87] J. Iveland, M. Piccardo, L. Martinelli, J. Peretti, J. W. Choi, N. Young, S. Nakamura, J. S. Speck, and C. Weisbuch, Appl. Phys. Lett. **105**, 52103 (2014).

[88] M. Piccardo, J. Iveland, L. Martinelli, S. Nakamura, J. W. Choi, J. S. Speck, C. Weisbuch, and J. Peretti, J. Appl. Phys. **117**, 112814 (2015).

[89] O. Tereshchenko, G. Shaibler, A. Yaroshevich, S. Shevelev, A. Terekhov, V. Lundin, E. Zavarin, and A. Besyul'kin, Phys. Solid State **46**, 1949 (2004).

[90] G. V Benemanskaya, A. I. Besyul'kin, M. S. Dunaevskii, A. K. Kryzhanovskii,

and N. M. Shmidt, Phys. Solid State **45**, 1026 (n.d.).

[91] M. Eyckeler, J. Vac. Sci. Technol. B Microelectron. Nanom. Struct. **16**, 2224 (1998).

[92] A. V. da Rosa, *Fundamentals of Renewable Energy Processes* (2009).

[93] Z. Yi-Jun, Z. Ji-Jun, W. Xiao-Hui, C. Ben-Kang, Q. Yun-Sheng, Z. Jun-Ju, and G. Pin, Chinese Phys. B **20**, 48501 (2011).

[94] H. Drouhin and M. Eminyan, Rev. Sci. Instrum. **57**, 1052 (1986).

[95] J. Peretti, H.-J. Drouhin, and D. Paget, Phys. Rev. Lett. **64**, 1682 (1990).

[96] J. Peretti, H. Drouhin, and D. Paget, Phys. Rev. B **47**, 3603 (1993).

[97] H.-J. H. Drouhin, C. Hermann, and G. Lampel, Phys. Rev. B **31**, 3859 (1985).

[98] J. Blakemore, J. Appl. Phys. **53**, R123 (1982).

[99] J. Peretti, H.-J. H. Drouhin, D. Paget, A. Mircéa, and A. Mircea, Phys. Rev. B **44**, 7999 (1991).

[100] J. F. Muth, J. H. Lee, I. K. Shmagin, R. M. Kolbas, H. C. Casey, B. P. Keller, U. K. Mishra, and S. P. DenBaars, Appl. Phys. Lett. **71**, 2572 (1997).

[101] W. E. Spicer and A. Herrera-Gómez, Proc. SPIE **2022**, 18 (1993).

[102] A. Pakhnevich, V. Bakin, A. Yaz'kov, G. Shaibler, S. Shevelev, O. Tereshchenko, A. Yaroshevich, and A. Terekhov, J. Exp. Theor. Phys. Lett. **79**, 479 (2004).

[103] A. Pakhnevich, V. Bakin, G. Shaĭbler, and A. Terekhov, Phys. Solid State **49**, 2070 (2007).

[104] B. Monemar, Phys. Rev. B **10**, 4 (1974).

[105] P. A. Shields, R. J. Nicholas, F. M. Peeters, B. Beaumont, and P. Gibart, Phys. Rev. B **64**, 81203 (2001).

[106] S. Syed, Y. J. Wang, M. J. Manfra, R. J. Molnar, H. L. Stormer, J. B. Heroux, Y. J. Wang, M. J. Manfra, R. J. Molnar, and H. L. Stormer, Appl. Phys. Lett. **83**, 6 (2003).

[107] C. J. Stanton and D. W. Bailey, Phys. Rev. B **45**, 8369 (1992).

[108] J. Faure, J. Mauchain, E. Papalazarou, W. Yan, J. Pinon, M. Marsi, and L.

Perfetti, Rev. Sci. Instrum. **83**, (2012).

[109] J. Kanasaki, H. Tanimura, and K. Tanimura, Phys. Rev. Lett. **113**, (2014).

[110] H. Tanimura, J. Kanasaki, and K. Tanimura, Phys. Rev. B **91**, 45201 (2015).

[111] J. E. Yater, J. L. Shaw, K. L. Jensen, D. W. Feldman, N. Moody, and P. G. O'Shea, 2006 IEEE Int. Vac. Electron. Conf. Held Jointly with 2006 IEEE Int. Vac. Electron Sources (IEEE Cat. No.06EX1278) 2 pp. |xxiii+574 (2006).

[112] M. Foussekis, A. A. Baski, and M. A. Reshchikov, J. Vac. Sci. Technol. B **29**, (2011).

[113] E. Yablonovitch, B. J. Skromme, R. Bhat, J. P. Harbison, and T. J. Gmitter, Appl. Phys. Lett. **54**, 555 (1989).

[114] M. Alonso, R. Cimino, and K. Horn, Phys. Rev. Lett. **64**, 1947 (1990).

[115] J. J. Quinn, Phys. Rev. **126**, 1453 (1962).

[116] M. A. Reshchikov and H. Morkoç, J. Appl. Phys. **97**, (2005).

[117] M. Himmerlich, L. Lymperakis, R. Gutt, P. Lorenz, J. Neugebauer, and S. Krischok, Phys. Rev. B **88**, 125304 (2013).

[118] E. Kioupakis, P. Rinke, A. Schleife, F. Bechstedt, and C. G. de Walle, Phys. Rev. B **81**, 241201 (2010).

[119] C. L. Keraly, L. Kuritzky, M. Cochet, C. Weisbuch, C. Lalau Keraly, L. Kuritzky, M. Cochet, and C. Weisbuch, in *III-Nitride Based Light Emit. Diodes Appl.*, edited by T.-Y. Seong, J. Han, H. Amano, and H. Morkoc, 126th ed. (Springer Netherlands, Dordrecht, 2013), pp. 231–269.

[120] S. Bloom, G. Harbeke, E. Meier, and I. B. Ortenburger, Phys. Status Solidi **66**, 161 (1974).

[121] T. L. Gilton, J. P. Cowin, G. D. Kubiak, and A. V Hamza, J. Appl. Phys. **68**, (1990).

[122] H. Fang, H. a Bechtel, E. Plis, M. C. Martin, S. Krishna, E. Yablonovitch, and A. Javey, Proc. Natl. Acad. Sci. U. S. A. **110**, 11688 (2013).

[123] J. Kvietkova, L. Siozade, P. Disseix, A. Vasson, J. Leymarie, B. Damilano, N. Grandjean, and J. Massies, Phys. Status Solidi **190**, 135 (2002).

[124] D. a B. Miller, D. S. Chemla, and S. Schmitt-Rink, Phys. Rev. B **33**, 6976 (1986).

[125] Z. Liu, F. Machuca, P. Pianetta, W. E. Spicer, and R. F. W. Pease, Appl. Phys. Lett. **85**, 1541 (2004).

[126] M. Murakami and Y. Koide, Crit. Rev. Solid State Mater. Sci. **23**, 1 (1998).

[127] K. A. Rickert, A. B. Ellis, J. K. Kim, J.-L. Lee, F. J. Himpsel, F. Dwikusuma, and T. F. Kuech, J. Appl. Phys. **92**, (2002).

[128] J. M. Shah, Y.-L. Li, T. Gessmann, and E. F. Schubert, J. Appl. Phys. **94**, (2003).

[129] D. Zhu, J. Xu, A. N. Noemaun, J. K. Kim, E. F. Schubert, M. H. Crawford, and D. D. Koleske, Appl. Phys. Lett. **94**, (2009).

[130] C. T. Sah, R. N. Noyce, and W. Shockley, Proc. IRE **45**, 1228 (1957).

[131] J. Peretti, C. Weisbuch, J. Iveland, M. Piccardo, L. Martinelli, and J. S. Speck, Proc. SPIE **9003**, 90030Z (2014).

[132] M. Meneghini, N. Trivellin, G. Meneghesso, E. Zanoni, U. Zehnder, and B. Hahn, J. Appl. Phys. **106**, (2009).

[133] M. Shahmohammadi, W. Liu, G. Rossbach, L. Lahourcade, A. Dussaigne, R. Butté, N. Grandjean, B. Deveaud, and G. Jacopin, Private Communication, 2015.

[134] G. E. Cragg and A. L. Efros, Nano Lett. **10**, 313 (2010).

[135] B. Galler, H.-J. H.-J. Lugauer, M. Binder, R. Hollweck, Y. Folwill, A. Nirschl, A. Gomez-Iglesias, B. Hahn, J. Wagner, M. Sabathil, and M. Sabthil, Appl. Phys. Express **6**, 112101 (2013).

[136] C. Lian and H. (Grace) Xing, Appl. Phys. Lett. **88**, (2006).

[137] C. K. Li, M. Rosmeulen, E. Simoen, and Y. R. Wu, IEEE Trans. Electron Devices **61**, 511 (2014).

[138] D. Wee, G. Parish, and B. Nener, J. Appl. Phys. **111**, (2012).

[139] G. Moldovan, P. Kazemian, P. R. Edwards, V. K. S. Ong, O. Kurniawan, and C. J. Humphreys, Ultramicroscopy **107**, 382 (2007).

[140] L. Chernyak, G. Nootz, and A. Osinsky, Electron. Lett. **37**, 922 (2001).

[141] K. Kumakura, T. Makimoto, N. Kobayashi, T. Hashizume, T. Fukui, and H. Hasegawa, J. Cryst. Growth **298**, 787 (2007).

[142] G. Vergara, A. Herrera-Gomez, and W. E. Spicer, Proc. SPIE **2550**, 142 (1995).

[143] P. Polodov, Cathodoluminescence in Semiconductor Structures under Local Tunneling Electron Injection, Ecole Polytechnique, 2015.

[144] J. L. Shaw, R. E. Treece, D. Patel, C. S. Menoni, J. R. Smith, and J. I. Pankove, Appl. Phys. Lett. **81**, 3076 (2002).

[145] K. A. Bulashevich and S. Y. Karpov, in *Phys. Status Solidi Curr. Top. Solid State Phys.* (2008), pp. 2066–2069.

[146] M. Filoche and S. Mayboroda, Proc. Natl. Acad. Sci. **109**, 14761 (2012).

[147] D. N. Arnold, G. David, D. Jerison, S. Mayboroda, and M. Filoche, Phys. Rev. Lett. **116**, 56602 (2016).

[148] C. Weisbuch and B. Vinter, *Quantum Semiconductor Structures* (Academic Press, Boston, 1991).

[149] Z. I. Alferov, Rev. Mod. Phys. **73**, 767 (2001).

[150] H. Kroemer, Rev. Mod. Phys. **73**, 783 (2001).

[151] S. Nakamura, Science (80-.). **281**, 956 (1998).

[152] P. W. Anderson, Phys. Rev. **109**, 1492 (1958).

[153] S. Agmon, *Lectures on Exponential Decay of Solutions of Second-Order Elliptic Equations: Bounds on Eigenfunctions of N-Body Schrödinger Operators* (Mathematical Notes Vol. 28, Princeton University Press, 1982).

[154] S. Agmon, Lect. Notes Math. **1159**, 1 (1985).

[155] J. Singh, *Electronic and Optoelectronic Properties of Semiconductor Structures*, 1st ed. (Cambridge University Press, New York, NY, USA, 2007).

[156] H. Song, K.-S. Jeon, J. Hyoun Joe, S. Kim, M. Lee, E. Ah Lee, H. Choi, J. Sung, M.-G. Kang, Y.-H. Choi, and J. Soo Lee, Appl. Phys. Lett. **103**, (2013).

[157] Y. K. Kuo, M. C. Tsai, S. H. Yen, T. C. Hsu, and Y. J. Shen, IEEE J. Quantum Electron. **46**, 1214 (2010).

[158] F. Urbach, Phys. Rev. **92**, 1324 (1953).

[159] M. V Kurik, Phys. Status Solidi **8**, 9 (1971).

[160] J. D. Dow and D. Redfield, Phys. Rev. B **5**, 594 (1972).

[161] S. John, C. Soukoulis, M. H. Cohen, and E. N. Economou, Phys. Rev. Lett. **57**,

1777 (1986).

[162] C. J. Hwang, Phys. Rev. B **2**, 4117 (1970).

[163] B. Bansal, V. K. Dixit, V. Venkataraman, and H. L. Bhat, Appl. Phys. Lett. **90**, (2007).

[164] G. D. Cody, T. Tiedje, B. Abeles, B. Brooks, and Y. Goldstein, Phys. Rev. Lett. **47**, 1480 (1981).

[165] B. Han, B. W. Wessels, and M. P. Ulmer, J. Appl. Phys. **99**, (2006).

[166] S. C. Bayliss, P. Demeester, I. Fletcher, R. W. Martin, P. G. Middleton, I. Moerman, K. P. O'Donnell, A. Sapelkin, C. Trager-Cowan, W. Van Der Stricht, and C. Young, Mater. Sci. Eng. B **59**, 292 (1999).

[167] K. O'Donnell, R. Martin, and P. Middleton, Phys. Rev. Lett. **82**, 237 (1999).

[168] S. Chichibu, T. Mizutani, T. Shioda, H. Nakanishi, T. Deguchi, T. Azuhata, T. Sota, and S. Nakamura, Appl. Phys. Lett. **70**, 3440 (1997).

[169] M. A. Jacobson, O. V Konstantinov, D. K. Nelson, S. O. Romanovskii, and Z. Hatzopoulos, J. Cryst. Growth **230**, 459 (2001).

[170] T.-J. Yang, R. Shivaraman, J. S. Speck, and Y.-R. Wu, J. Appl. Phys. **116**, 113104 (2014).

[171] C.-K. Wu, C.-K. Li, and Y.-R. Wu, J. Comput. Electron. **14**, 416 (2015).

[172] C.-K. Li, M. Piccardo, L.-S. Lu, S. Mayboroda, L. Martinelli, J. S. Speck, C. Weisbuch, M. Filoche, and Y.-R. Wu, (Submitted to Phys. Rev. B) (2016).

[173] S. Schulz, M. A. Caro, C. Coughlan, and E. P. O'Reilly, Phys. Rev. B **91**, 35439 (2015).

[174] Y. H. Cho, G. H. Gainer, A. J. Fischer, J. J. Song, S. Keller, U. K. Mishra, and S. P. DenBaars, Appl. Phys. Lett. **73**, 1370 (1998).

[175] H. Schömig, S. Halm, A. Forchel, G. Bacher, J. Off, and F. Scholz, Phys. Rev. Lett. **92**, 106802 (2004).

[176] H. Helmers, C. Karcher, and A. W. Bett, Appl. Phys. Lett. **103**, (2013).

[177] R. Collins, K. Klitzing, and K. Ploog, Phys. Rev. B **33**, 4378 (1986).

[178] C. Kim, J. Kim, K. Yee, H. Kwon, H. Lee, and J. Park, J. Korean Phys. Soc. **57**, 793 (2010).

[179] C. Vierheilig, U. T. Schwarz, N. Gmeinwieser, A. Laubsch, and B. Hahn, Phys. Status Solidi **6**, S755 (2009).

[180] J. R. Lang, N. G. Young, R. M. Farrell, Y. R. Wu, and J. S. Speck, Appl. Phys. Lett. **101**, 181105 (2012).

[181] V. Sa-Yakant and H. R. Glyde, Comments Cond. Mat. Phys. **13**, 35 (1987).

[182] Y.-R. Wu, One Dimensional Poisson, Drift-Diffusion, and Schrodinger Solver (1D-DDCC), National Taiwan University, 2015.

[183] C. de Falco, E. Gatti, A. L. Lacaita, and R. Sacco, J. Comput. Phys. **204**, 533 (2005).

[184] S. Y. Karpov, Proc. SPIE **7939**, 79391C (2011).

[185] J. R. Chen, S. C. Ling, H. M. Huang, P. Y. Su, T. S. Ko, T. C. Lu, H. C. Kuo, Y. K. Kuo, and S. C. Wang, Appl. Phys. B Lasers Opt. **95**, 145 (2009).

[186] D. A. Browne, B. Mazumder, Y.-R. Wu, and J. S. Speck, J. Appl. Phys. **117**, 185703 (2015).

[187] A. Shedbalkar, Z. Andreev, and B. Witzigmann, Phys. Status Solidi **253**, 158 (2016).

[188] S. Datta, *Electronic Transport in Mesoscopic Systems* (1995).

[189] C. De Santi, M. Meneghini, M. La Grassa, B. Galler, R. Zeisel, M. Goano, S. Dominici, M. Mandurrino, F. Bertazzi, D. Robidas, G. Meneghesso, and E. Zanoni, J. Appl. Phys. **119**, (2016).

[190] M. Zhang, P. Bhattacharya, J. Singh, and J. Hinckley, Appl. Phys. Lett. **95**, 1 (2009).

[191] A. David and M. J. Grundmann, Appl. Phys. Lett. **96**, (2010).

[192] E. Kioupakis, Q. Yan, D. Steiauf, and C. G. Van De Walle, New J. Phys. **15**, (2013).

[193] J.-M. Lentali, M. Piccardo, C.-K. Li, Y.-R. Wu, C. Weisbuch, and M. Filoche, *To Be Published* (n.d.).

[194] D. P. Nguyen, N. Regnault, R. Ferreira, and G. Bastard, Solid State Commun. **130**, 751 (2004).

[195] S. D. Baranovskii and A. L. Efros, Sov. Phys. Semicond. **12**, 1328 (1978).

[196] D. Watson-Parris, M. J. Godfrey, P. Dawson, R. A. Oliver, M. J. Galtrey, M. J. Kappers, and C. J. Humphreys, Phys. Rev. B - Condens. Matter Mater. Phys. **83**, (2011).

[197] C. Geuzaine and J. F. Remacle, Int. J. Numer. Methods Eng. **79**, 1309 (2009).

[198] M. N. Fireman, D. A. Browne, U. K. Mishra, and J. S. Speck, J. Appl. Phys. **119**, (2016).

[199] C.-K. Li, C.-K. Wu, C.-C. Hsu, L.-S. Lu, H. Li, T.-C. Lu, and Y.-R. Wu, AIP Adv. **6**, (2016).

[200] M. Auf Der Maur, A. Pecchia, G. Penazzi, W. Rodrigues, and A. Di Carlo, Phys. Rev. Lett. **116**, (2016).

[201] M. Binder, B. Galler, M. Furitsch, J. Off, J. Wagner, R. Zeisel, and S. Katz, Appl. Phys. Lett. **103**, (2013).

[202] A. David, M. J. Grundmann, J. F. Kaeding, N. F. Gardner, T. G. Mihopoulos, and M. R. Krames, Appl. Phys. Lett. **92**, 53502 (2008).

[203] C.-K. K. Li and Y.-R. R. Wu, IEEE Trans. Electron Devices **59**, 400 (2012).

[204] H.-Y. Ryu, H.-S. Kim, and J.-I. Shim, Appl. Phys. Lett. **95**, 81114 (2009).

[205] Q. Dai, Q. Shan, J. Wang, S. Chhajed, J. Cho, E. F. Schubert, M. H. Crawford, D. D. Koleske, M.-H. Kim, and Y. Park, Appl. Phys. Lett. **97**, 133507 (2010).

[206] D. A. Zakheim, A. S. Pavluchenko, D. A. Bauman, K. A. Bulashevich, O. V. Khokhlev, and S. Y. Karpov, Phys. Status Solidi **209**, 456 (2012).

[207] G. B. Lin, D. Meyaard, J. Cho, E. Fred Schubert, H. Shim, and C. Sone, Appl. Phys. Lett. **100**, 161106 (2012).

[208] W. B. Joyce and S. H. Wemple, J. Appl. Phys. **41**, (1970).

[209] G. Neuhold, T. Chassé, J. J. Paggel, and K. Horn, Phys. Rev. B **54**, 8623 (1996).

[210] M. Piccardo, L. Martinelli, J. Iveland, N. Young, S. P. DenBaars, S. Nakamura, J. S. Speck, C. Weisbuch, and J. Peretti, Phys. Rev. B **89**, 235124 (2014).

[211] M. E. Levinshtein, S. L. Rumyantsev, and M. Shur, *Properties of Advanced Semiconductor Materials : GaN, AlN, InN, BN, SiC, SiGe* (2001).

[212] R. B. Lehoucq, D. C. Sorensen, and C. Yang, Communication **6**, 147 (1998).

[213] O. Schenk, K. Gärtner, W. Fichtner, and A. Stricker, Futur. Gener. Comput. Syst.

18, 69 (2001).

[214] D. Watson-Parris, Carrier Localization in InGaN/GaN Quantum Wells, University of Manchester, 2011.

[215] I. Vurgaftman, J. R. Meyer, and L. R. Ram-Mohan, J. Appl. Phys. **89**, 5815 (2001).

[216] J. Piprek, *Nitride Semiconductor Devices: Principles and Simulation* (John Wiley & Sons, 2007).

[217] A. E. Romanov, T. J. Baker, S. Nakamura, and J. S. Speck, J. Appl. Phys. **100**, (2006).

[218] V. Fiorentini, F. Bernardini, and O. Ambacher, Appl. Phys. Lett. **80**, 1204 (2002).

[219] O. Ambacher, J. Majewski, C. Miskys, A. Link, M. Hermann, M. Eickhoff, M. Stutzmann, F. Bernardini, V. Fiorentini, V. Tilak, B. Schaff, and L. F. Eastman, Jour. of Physics-Condensed Matter **14**, 3399 (2002).

[220] K. Kumakura, T. Makimoto, N. Kobayashi, T. Hashizume, T. Fukui, and H. Hasegawa, Appl. Phys. Lett. **86**, 1 (2005).

5 APPENDICES

5.1 Shortcomings of the ABC model as a predictive tool

Beyond the characterization of electrical properties brought by the I-V characteristics, the easiest optoelectronic measurement in LEDs is the curve displaying the IQE versus the injected current density J. It is not an easily accessed quantity: the IQE, ratio of the EQE to the light extraction efficiency, is deduced from the measured EQE curve assuming a constant extraction efficiency with current injection. This is true only for LEDs without current crowding as increased emission near the metal contacts increases absorption of the LED light [203], thus leading to an apparent increased droop. Obtaining absolute values of IQE is difficult as the EQE is often not measured in integrating spheres and as the extraction efficiency is not known, unless special LED designs are used where the extraction efficiency can be calculated. Such LEDs can be designed, but they are then not really representative of commercial LEDs. For instance, their electrode area needs to be minimized, to avoid light absorption, but the current crowding might be increased compared to commercial LEDs, leading to more inhomogeneous carrier distribution and increasing the observed droop.

There are two ways to include injection efficiency effects if they are believed to change with current: if the IQE is only related to the EQE by the light extraction, one has to multiply the sum of the recombination terms by a factor representing the injection efficiency. Another way to treat it is to add an injection current loss representing the injection efficiency to the recombination terms.

In spite of these unknowns, the EQE curve alone, considered to represent the IQE, is commonly used to test the contribution of the Auger process to the droop by fitting the

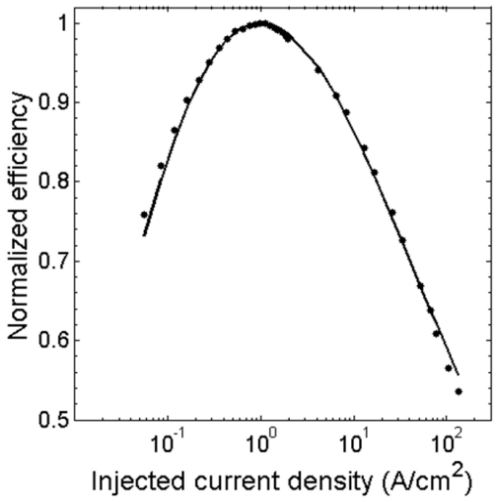

Figure 92 - Example of ABC fit (continuous line) of the experimental EQE vs. J measurement (points) for the sample of Ref. [53]. The experimental EQE has been normalized to unity in order to avoid any assumption on the specific values of light extraction efficiency and carrier injection efficiency.

experimental data with a polynomial through the ABC model or its derivatives. In the following discussion, we will consider both fitting the EQE or IQE curves as equivalent, neglecting the changes in extraction efficiency or current injection.

In the ABC model of the Auger-mediated droop, the injected current density in the LED J and the IQE are given by:

$$\boldsymbol{J = \frac{(An + Bn^2 + Cn^3)ed}{\eta_{inj}}} \qquad \textbf{(76)}$$

$$\mathbf{IQE = \frac{Bn^2}{An + Bn^2 + Cn^3}} \qquad \textbf{(77)}$$

where e is the electron charge, d is the active layer thickness, η_{inj} is the injection efficiency, n is the carrier density, A is the Shockley-Read-Hall (SRH) non-radiative recombination coefficient, B is the bimolecular radiative recombination coefficient, and the Cn^3 term is due to e-e-h (Figure 11c) or e-h-h Auger recombination. In this widely used "ABC model" of IQE along Eq. (77), the carrier density in the active region is an implicit internal variable which varies with carrier injection along Eq. (76). From the derivative of Eq. (77) at the peak efficiency ($dIQE/dn = 0$), Ryu *et al.* [204] remarked that A, B and C are related together through the values of the peak IQE, η_{max}, and of the peak current density, J_{max}, as:

$$\mathbf{B} = \frac{\mathbf{4\eta_{max} \cdot ed}}{\mathbf{\eta_{inj} \cdot J_{max}(1-\eta_{max})^2}}\mathbf{A^2} \quad \mathbf{(78)}$$

$$\mathbf{C} = \frac{\mathbf{4(ed)^2}}{\mathbf{\eta_{inj}^2 \cdot J_{max}^2(1-\eta_{max})^2}}\mathbf{A^3} \quad (79)$$

Then, by knowing the values of η_{max} and J_{max}, only one of the ABC parameters is not known. Dai *et al.* [205] further remarked that a single parameter P ($P = B/\sqrt{AC}$) allows to fit the experimental EQE vs. J curve, independently from the ABC values. From this determination of P by the fit of the EQE curve, one can then obtain

$$\mathbf{\eta_{max} = P/(P+2)} \quad \mathbf{(80)}$$

without having to extract it from the absolute measurement of the EQE and knowledge of the extraction efficiency. Figure 92 shows the ABC fit to the LED studied in Ref. [53] with $P = 6.3$, which leads to $\eta_{max} = 76\%$.

To obtain the values of ABC coefficients, one needs extra information. As A is connected to the SRH mechanism, fully dependent on materials properties, and C is the nonlinear droop mechanism to be determined, one would infer that the parameter to be

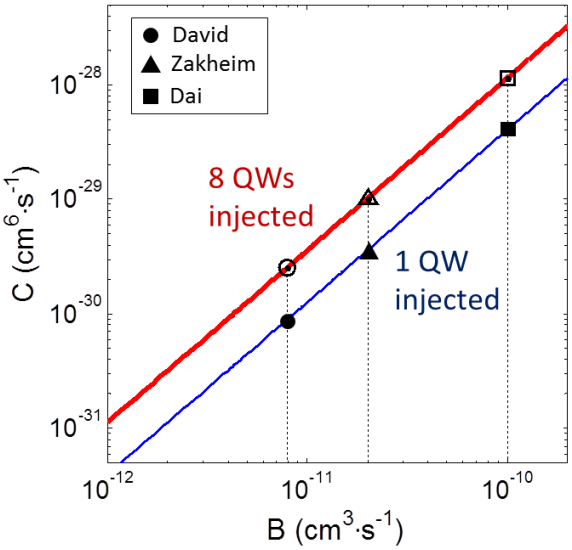

Figure 93 - Calculated *C* coefficient as a function of the *B* coefficient from Eq. (81) assuming homogeneous carrier density in one or all populated QWs and using the *P* parameter fitted to the EQE curve of Figure 92. Data points correspond to different values of the *B* coefficient used in the literature (circles from David and Grundmann [48], triangles from Zakheim *et al.* [206] and squares from Dai *et al.* [205]).

injected is *B* as it relies on an intrinsic phenomenon, the radiative recombination probability. However, values used for *B* cover a wide range, leading to even more widely varying values of *C* as given by:

$$\mathbf{C = B^{3/2} \cdot \sqrt{\frac{ed}{\eta_{inj} \cdot J_{max}} \cdot \frac{P+2}{P^3}}} \qquad \mathbf{(81)}$$

Clearly this approach is not sufficient to determine a precise value of *C* as it varies as $B^{3/2}$ (Figure 93). This problem is well apparent in Ryu's paper [204]: using their Eq. 4 on the relation between *C* and *A* for their measured sample, they find that for a usual range of *A* between 10^7 and 10^8 s^{-1} the values of *C* range from 10^{-28} to 10^{-25} cm^6s^{-1}, both a very wide range and very large values which they attribute to mechanisms other than Auger recombination, as do Hader *et al.* [49].

It should be remarked that this analysis, although quite satisfactory due to its simplicity, is extremely dependent on many assumptions that are unverified in real world devices. Some neglected complications will significantly alter the shape of the EQE curve and of the parameter determination as these will not be uniform over the device area, both in the plane of the device and perpendicular to it. They arise from:

i. *A*, *B* and *C* are not really constants. In c-plane grown nitrides, the internal spontaneous and piezoelectric fields are progressively screened with increasing injected carrier density, changing accordingly *A*, *B* and *C*;
ii. Carrier localization effects, such as due to In compositional fluctuations;
iii. Inhomogeneous carrier injection in MQW LEDs (in particular holes), inducing an uncertainty on the number of injected QWs, at least an inhomogeneous distribution of carriers, hence of recombination rates;
iv. Density-dependent current crowding at contacts which are responsible for inhomogeneous carrier distribution.

These effects can add terms in Eq. (76) and (77) and some also increase the local carrier density, both in-plane and perpendicular, leading to larger effective Auger coefficients. Such deviations from homogeneity are amplified in the numerical analysis leading to Eq. (78) and (79): for instance, a decrease of only a factor 3x in the effective active volume either due to in-plane fluctuations and/or a non-uniform In composition across the QW [170], and an underestimated measurement of J_{max} by another factor 3x due to current crowding effects, can together lead to a change by 81 in *C* along Eq. (79).

Despite these huge unavoidable uncertainties related to the determination of the *C* parameter in the ABC model fitting, insufficiently defined experimental conditions (number of injected QWs, current crowding) and dealing with structures quite different from commercial ones, many authors still claim from their ABC analysis that Auger recombination is to be rejected as the main mechanism responsible for droop. To adapt the ABC model to other mechanisms of droop, some authors have replaced the Cn^3 Auger term appearing in the recombination rate by a more complex term $C \cdot f(n)$, allowing a different functional dependence on carrier concentration (model for carrier escape, [207]).

Others use the temperature dependence of the fits of EQE vs. J curves for supporting other mechanisms than Auger (e.g. Ref. [49]). It should however be kept in mind that the approximations made above of constant *A*, *B* and *C* and of homogeneous carrier densities, both in-plane and across the LED structure, even break down more with lowering temperature (there is more current crowding, the QW population is more uneven, localization effects are stronger). Therefore, the observed strong temperature dependences of droop, used to exclude Auger recombination which is assumed to have weak temperature dependence, could mainly be due to the changes in ABC coefficients and increased carrier inhomogeneity.

Some authors have introduced other terms in the expression of the total current density *J* beyond the ABC term, such as $k(n-n_0)^m$, k and m being mathematical coefficients, in order to represent carrier-induced non-radiative recombination (which occurs above a carrier density threshold n_0) [49] or adding terms such as kJ^m to represent other nonlinear mechanisms such as overflow currents from the active region [27]. It appears then that, due to the new parameters injected, one can better fit the EQE curves while the better fit does not prove the physical existence of the invoked mechanisms. A number of these authors however recognize that one can equally well fit the measured EQE curves with Auger terms or other nonlinear terms, when adjusting accordingly the *A* and *B* coefficients [27,49], which somewhat disproves the whole analysis.

5.2 Current crowding in p-GaN apertures of a holey p-contact

The scope of this Appendix is to investigate current crowding effects in the exposed p-GaN apertures of the holey p-electrodes used in EE experiments (Figure 15). As discussed in Sec. 2.5.1, current crowding may be a cause of potential inhomogeneity in the electron emitting surface which needs to be evaluated as it could cause artifacts in the spectroscopy of the emitted electron energy. The following study is the development of a model first introduced by Joyce and Wemple [208].

The case to be treated constitutes a nonlinear problem since part of the current spreading in the p-layer will leave the film at a rate dependent on the local voltage. In Figure 94 the geometry of the problem is represented: we consider a disk aperture of exposed p-GaN surrounded by a metallic contact. The diode is modeled as a p-n junction, where the internal resistivity of the n-layer is negligible: the n-layer will be considered as grounded and the potential $V(\vec{R})$ in the thin resistive p-layer as dependent on the position $\vec{R}$ (the radial coordinate in circular geometry). Neglecting the presence of the InGaN/GaN MQW active region in this problem is a reasonable approximation as long as the junction-current density (current/area) can be described, as in the case of an ideal LED, by the Shockley equation:

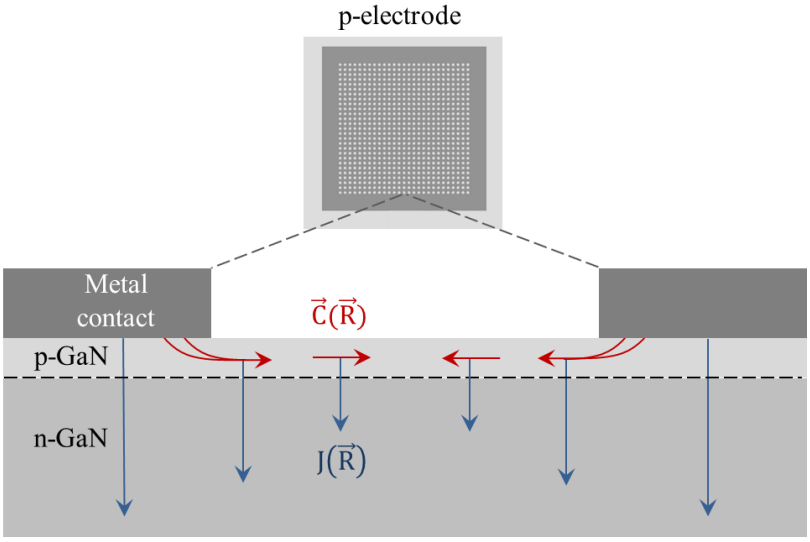

Figure 94 - Lateral section of the geometry considered for the study of current spreading in p-GaN apertures of the p-electrode used in electro-emission experiments. While surface current density $\vec{C}(\vec{R})$ flows in the p-GaN layer, a portion of it $J(\vec{R})$ leaves the film passing through the junction.

$$\mathbf{J}(\vec{\mathrm{R}}) = \mathrm{J_s} \cdot (\mathrm{e}^{\beta \mathrm{V}(\vec{\mathrm{R}})} - \mathbf{1}) \quad (82)$$

where J_s is the reverse-bias saturation current density and $\beta = \frac{e}{nk_BT}$ with n being the ideality factor of the diode. In nitride LEDs under typical forward-bias operations the exponential term in Equation (82) dominates, thus the high-voltage approximation will be used in the following

$$\mathbf{J}(\vec{\mathrm{R}}) = \mathrm{J_s} \cdot \mathrm{e}^{\beta \mathrm{V}(\vec{\mathrm{R}})} \quad (83)$$

The surface current injected from the metallic p-contact and flowing parallel to the junction experiences a sheet resistivity, defined as the ratio of p-GaN bulk resistivity and film thickness, that causes a voltage drop in the aperture, usually well described by Ohm's law in 2D

$$\vec{\nabla}\mathbf{V}(\vec{\mathrm{R}}) = -\boldsymbol{\rho}\vec{\mathrm{C}}(\vec{\mathrm{R}}) \quad (84)$$

where $\vec{C}(\vec{R})$ is the surface current density (current/length), i.e. the film current flowing through a unit width perpendicular to the flow. In Equation (84) the p-layer is considered as homogeneous and isotropic in the two dimensions parallel to the junction plane and any voltage drop perpendicular to the junction is neglected.

As the only way to the leave the p-layer for the current flowing in the aperture region is to pass through the junction, a continuity equation can be established

$$-\vec{\nabla} \cdot \vec{\mathrm{C}}(\vec{\mathrm{R}}) = \mathbf{J}(\vec{\mathrm{R}}) \quad (85)$$

Then, combining Equation (83) and (85) with the divergence of Equation (84) it is obtained

$$-\vec{\nabla} \cdot \vec{\mathrm{C}}(\vec{\mathrm{R}}) = \frac{\nabla^2 \mathrm{V}(\vec{\mathrm{R}})}{\rho} = \mathrm{J_s} \cdot \mathrm{e}^{\beta \mathrm{V}(\vec{\mathrm{R}})} = \mathbf{J}(\vec{\mathrm{R}}) \quad (86)$$

where the central equality constitutes the master equation of the system. For simplicity of notation, Equation (86) is transformed in dimensionless form

$$-\vec{\nabla} \cdot \vec{\mathrm{c}} = \nabla^2 \mathbf{v} = \mathrm{e}^{\mathrm{v}} = \mathbf{j} \quad (87)$$

using the following dimensionless variables: voltage $v = \beta V$, radial coordinate $r = \sqrt{J_s \beta \rho} \cdot R$, surface current density $c = \sqrt{\beta \rho / J_s} \cdot C$ and junction current density $j = J/J_s$. In the case of disk (aperture) geometry the solutions of the master equation are

$$\mathbf{j} = e^{v} = \mathbf{8}b^2/(1 - b^2 r^2)^2 \qquad (88)$$

$$\frac{\mathbf{1}}{\mathbf{2}}\mathbf{r^2 j} - \left(\frac{\mathbf{i}}{\mathbf{4\pi}} - \mathbf{1}\right)^{\mathbf{2}} = \mathbf{-1} \qquad \mathbf{(89)}$$

where in Equation (88**)** b is an integration constant given by

$$\mathbf{b} = \frac{1}{\sqrt{1 - \frac{8\pi}{i_2} \cdot r_2}} \qquad (90)$$

which depends on the total surface current injected inside the aperture (i_2) and on the radius of the disk (r_2). (Since Equation (87**)** is a second-order differential equation two integration constants are needed for its solution. b is obtained using the boundary conditions appearing in Equation (90**)**, while the other constant is fixed by the disk geometry [208].)

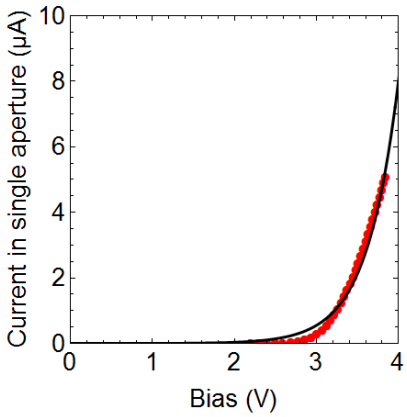

Figure 95 – Fit (black curve) based on Equation (89) of the experimental I-V characteristic (red dots) of the InGaN/GaN LED studied in Ref. [53]. For the purpose of the fit, the measured current injected in the p-electrode is scaled to the current expected to flow inside a single aperture of the electrode (see text for details).

In order to obtain the profile of the junction-current density in the aperture from Equation (88**)**, the integration constant b must first be calculated: this implies relating i_2, associated with a single aperture, to measurable quantities of the macroscopic p-electrode. First of all the following conservation relation between the current injected inside the aperture and the total current injected in the LED i_{tot} is established:

$$|\mathrm{j}_2|\mathrm{a}_\mathrm{M} + |\mathrm{i}_2|\mathbf{N} = \mathrm{i}_\mathrm{tot} \qquad (91\mathbf{)}$$

where j_2 is the junction-current density at the edge of the aperture (assumed to be the constant value held in the regions covered by the metal contact), a_M is the (dimensionless) metal surface and N is the number of apertures in the contact. (Note that $i_2 < 0$ by definition, because of the inward radial flow, thus $|i_2| = -i_2$.) Finally, plugging $j_2(i_2)$ from Equation (91**)** into Equation (89) a well-defined relation $i_2(r_2)$ is obtained, and therefore b can be calculated from Equation (90**)**.

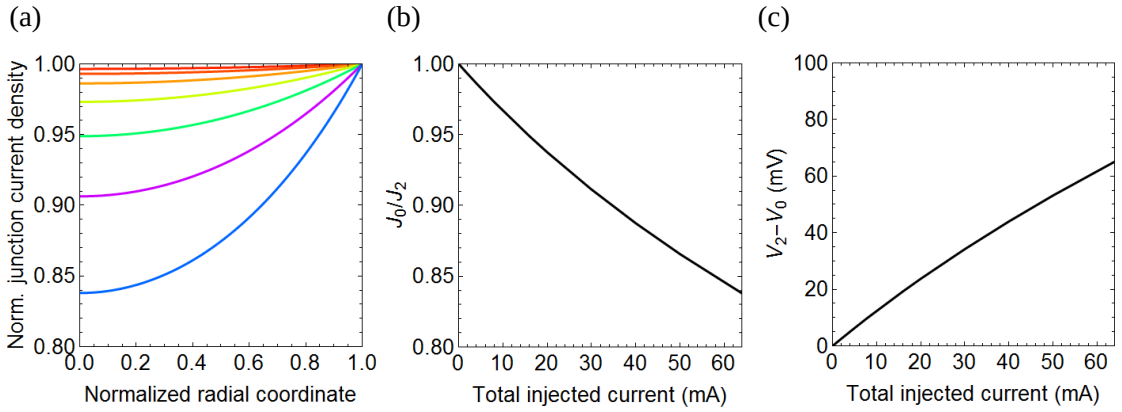

Figure 96 – Prediction of the current crowding model for the p-contact apertures of the device studied in Ref. [53]. (a) Profile of the junction current density across the radial coordinate of a single aperture in the p-contact as a function of the total current injected in the device, corresponding (curves from top to bottom) to 1 mA, 2 mA, 4 mA, 8 mA, 16 mA, 32 mA and 64 mA. The current density is normalized to its value at the edge of the aperture and the radial coordinate is normalized to the aperture radius. (b) Ratio of the junction current density at the center (J_0) and at the edge (J_2) of the aperture as a function of the current injected in the device. (c) Potential difference between the edge (V_2) and the center (V_0) of the aperture due to current crowding in p-GaN as a function of the current injected in the device.

Now the derived model is applied to the sample studied by Iveland *et al*. by electro-emission in Ref. [53]. We recall that the p-contact consists of a square electrode (side 500 μm) with an array of 27×27 circular apertures (5 μm radius) and the thickness of p-GaN is 200 nm. The bulk resistivity may be estimated to be 1 Ω ·cm from Equation (2), using $p = 7.5 \cdot 10^{17}$ cm^{-3} and $\mu_h = 8$ cm^{2}V^{-1}s^{-1} [19].

The ideality factor n of the diode can be obtained by fitting the experimental I-V curve of the device with Equation (89), where the value at the edge of the aperture is taken for the different terms ($r \to r_2$, $j \to e^{v_2(n)}$, $i \to i_2$). Since the model requires to know the current injected into a single aperture (i_2), for the fit of the experimental I-V curve it is assumed that the measured current is equally distributed in the injection area of the p-electrode and therefore, by knowing the size of a single aperture, the experimental i_2 can be estimated. (This is a rough approximation as it neglects current crowding, but is reasonable for the evaluation of n. Moreover, the conclusion of this study is self-consistent with this approximation, as it is found that current crowding effects are negligible for this device in the considered range of currents.) An ideality factor of 14 is obtained from the fit (Figure 95). GaN-based MQW structures often exhibit abnormally large ideality diode factors (though typically in the range between 5 and 7), due to the large resistivity of p-GaN and the polarization-induced triangular band profiles of the quantum barriers [128,129].

The calculated junction-current density distribution inside a single aperture of the p-electrode is shown in Figure 96a as a function of the total current injected in the device (1 mA-64 mA). Due to the p-GaN sheet resistivity, increasing the current injection causes the current profile to become inhomogeneous across the aperture. However, the ratio of the junction current density between the center and the edge of the aperture remains rather close to unity for the typical operation currents of the LED (Figure 96b). Most importantly from the perspective of EE experiments, the potential difference due to current crowding between the edge and the center of the aperture is small: at 64 mA this is only ~65 mV (note that this value decreases for a smaller ideality factor, as in the case of an ideal p-n junction with n=2), which would cause a spectral shift in EE comparable to the energy resolution of the electron analyzer (typically 50 or 80 meV). Moreover, the potential difference due to crowding is predicted to change almost linearly with the injected current, while the shift of the electron peaks observed in the EE experiments Figure 16b was observed to vary ~logarithmically with current (see discussion in Sec. 2.5.1). For all these reasons it is concluded that current crowding is

not the dominant contribution to the potential inhomogeneity of the electron emitting surface. Finally, note that even though the present study has been focused to the LED manufactured by Walsin Lihwa Co. and investigated in Ref. [53], quantitatively similar results and the same conclusions are obtained for LEDs manufactured by Seoul VioSys with slightly different characteristics (contact geometry, p-GaN thickness and doping, ideality factor) studied throughout this thesis.

5.3 Above bandgap photoemission studies of pristine p-GaN surfaces

One may think that the super-energetic PE process observed in cesiated p-GaN surfaces (Sec. 2.4.1) is due to surface states induced by Cs adatoms. For instance a UV angle-resolved photoemission spectroscopy (ARPES) study by Neuhold *et al.* [209] showed that, as a function of the Cs coverage on a GaP surface, two surface states appear, which are tentatively assigned to 1D "chains" and 2D "islands" of Cs atoms. One of these two peaks has a binding energy well above E_F and, increasing the Cs coverage (above ~0.5 monolayer), the two contributions merge as one dominates the other. In the following it will be shown that a super-energetic PE process, reminiscent of that observed on p-GaN/Cs surfaces, also occurs on pristine p-GaN surfaces. This result will reasonably allow to exclude that Cs-induced surface states are at the origin of this process.

The experiments presented here are carried out on the same main structure studied in Sec. 2.4.1 (see Figure 32), though on a different sample to avoid any Cs contamination. The PE sample is annealed as usual but not activated to NEA. The PE excitation source is a Ti:sapphire laser operated in pulsed mode (~100 fs pulses, 80 MHz repetition rate) for frequency tripling through nonlinear crystals giving a tunable light output with photon energy above the band gap of GaN.

The first thing to verify is whether a PE signal can be detected from a pristine p-GaN

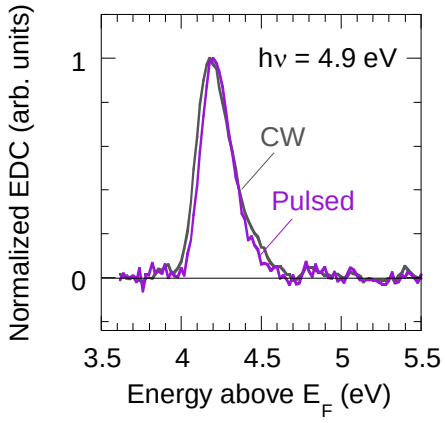

Figure 97 – EDCs measured upon photoexcitation at low power density of a pristine p-GaN surface at $h\nu$ = 4.9 eV using a filtered CW broadband light source (~2 mW/cm^2) and the third harmonic of a Ti:sapphire pulsed laser (~20 mW/cm^2). Spectra are normalized to unity.

surface exciting at a photon energy relatively close to the band gap (i.e. not tens of eV as usually done in UV ARPES), and whether the pulsed or CW operation of the excitation light source produces a difference in the spectra. The PE spectra measured at $h\nu$ = 4.9 eV using a filtered CW broadband light source and the pulsed Ti:sapphire laser at relatively low power densities (~2 mW/cm^2 and ~20 mW/cm^2, respectively) are shown in Figure 97. At such low power density, the spectra exhibit the same lineshape. However, as it will be shown, increasing the incident power of the pulsed laser causes a considerable modification of the spectrum. Two main remarks can be done on the spectra of Figure 97: first, considering the low-energy onset of the spectra as defined by the position of the vacuum level, it is deduced that the work function of the clean p-GaN sample is ϕ_{p-GaN} = 4.0 eV, quite close to the value of 3.60$\pm$0.15 eV given in Ref. [91]; second, the HET of the spectra agrees with the dispersion of ballistic electron energies ε_C as a function of $h\nu$ determined in Ref. [210] by near-band gap PES of cesiated p-GaN (Figure 30a), confirming that the Cs activation layer does not modify the final state energy of the most energetic photoelectrons.

Next, a series of measurements is carried out at a given excitation photon energy, $h\nu$ = 4.70 eV, as a function of the mean power of the pulsed laser (spot diameter ~500 μm). (The power is changed varying the time delay between the pulses of the fundamental and second harmonic wave. The same results described in the following are obtained when the power is varied instead by changing the beam size of the fundamental wave using an iris diaphragm, while keeping a fixed maximum time overlap between the pulses.) The series of spectra is shown in Figure 98a-d. The power dependence of the spectra is reminiscent of the results obtained in below-gap excitation of p-GaN/Cs: at low power a single contribution is observed, while increasing the power a super-energetic contribution appears (highlighted in the shadowed region of Figure 98d).

Note that the super-energetic peak was only observed with the Ti:sapphire operated in femtosecond mode (~100 fs pulses) and not in picosecond mode (~1 ps pulses) at a similar mean power (3× smaller than that corresponding to Figure 98d) but at a much reduced peak power (~30× smaller).

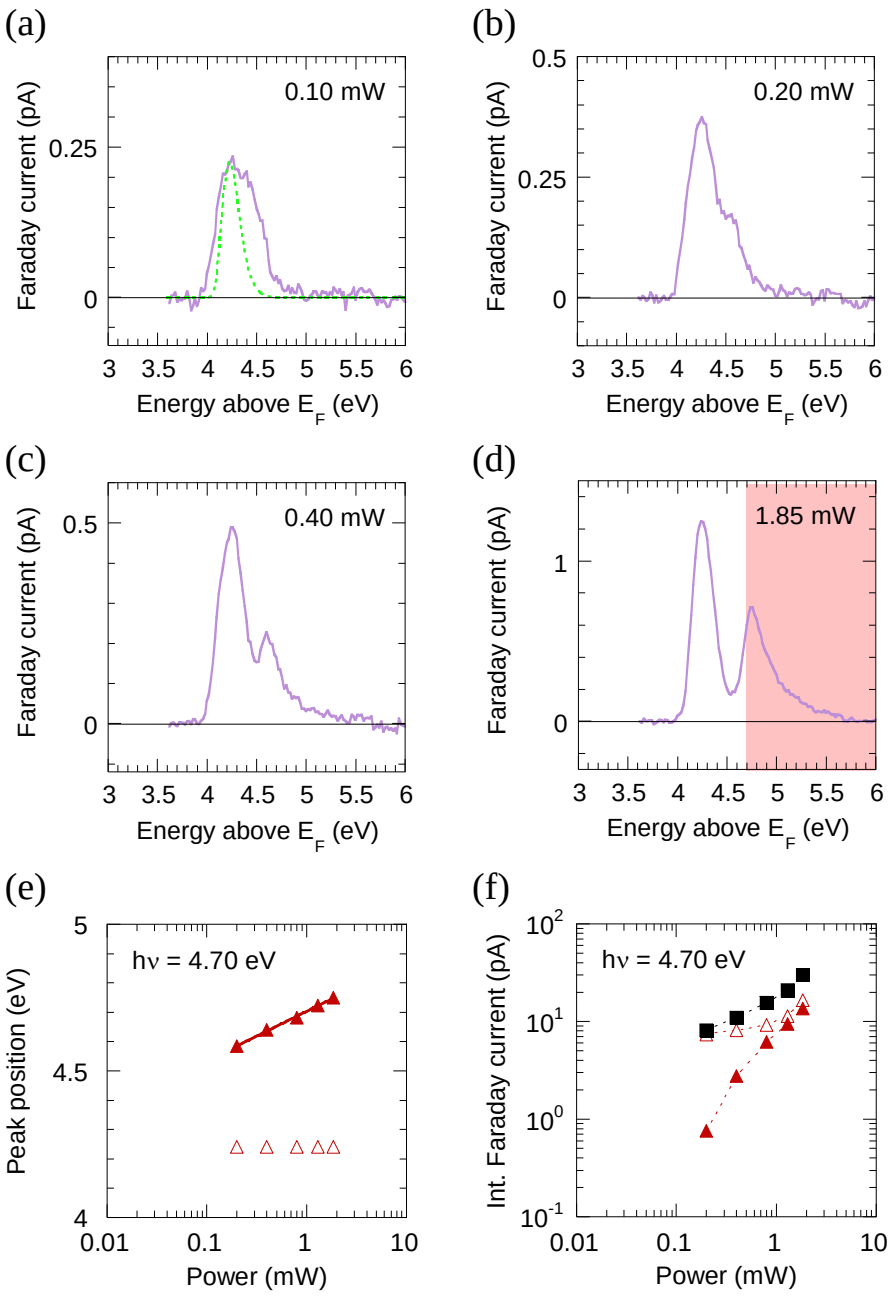

Figure 98 – (a)-(d) PE spectra measured at different excitation powers on pristine p-GaN at $h\nu$ = 4.70 eV by pulsed laser excitation. (e) Energy shift of the maxima of the low- (empty triangles) and high- (filled triangles) energy peak as a function of power. (f) Power dependence of the integrated Faraday current of the low- (empty triangles) and high- (filled triangles) energy peak, and entire spectrum (squares). To separate the two contributions, the lineshape fitted from the low-energy peak observed in (d) and shown as a green curve in (a) is used for the low-energy peak.

This would suggest that the multi-photon population and extraction into vacuum of the initial states giving origin to the super-energetic peak requires a large peak power upon pulsed excitation.

However, it should be reminded that super-energetic electron emission was observed in below-gap PE of p-GaN/Cs upon CW excitation, suggesting that the corresponding initial states, if due to multi-photon PE, are long-lived. Future studies based on pump-probe PES may help to clarify the dynamics of super-energetic PE upon pulsed excitation.

The super-energetic peak shifts logarithmically with power (Figure 98e), similarly to the behavior observed in below-gap PE of p-GaN/Cs. However, in the case of above-gap PE of p-GaN the low-energy peak holds a constant position as a function of power. This cannot be explained within the framework of the model illustrated in Figure 35c,d, according to which a SPV should simultaneously increase the position of the electron quasi-Fermi level (shifting the high-energy peak) and of the vacuum level (shifting the low-energy peak) and the origin of this different behaviour remains to be understood.

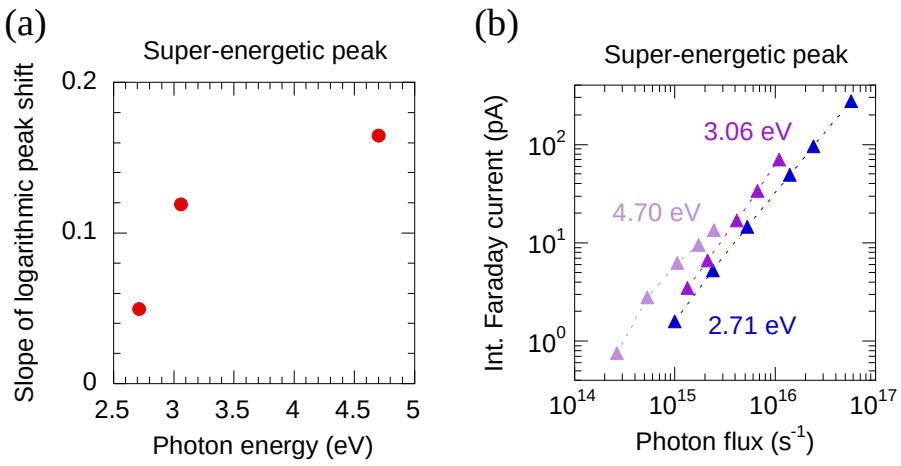

Figure 99 – Quantities related to the super-energetic peak excited in below- and above-gap PE of, respectively, p-GaN/Cs and pristine p-GaN: (a) fitted slope of the semi-log plots describing the peak shift as a function of power; (b) integrated Faraday current of the peak.

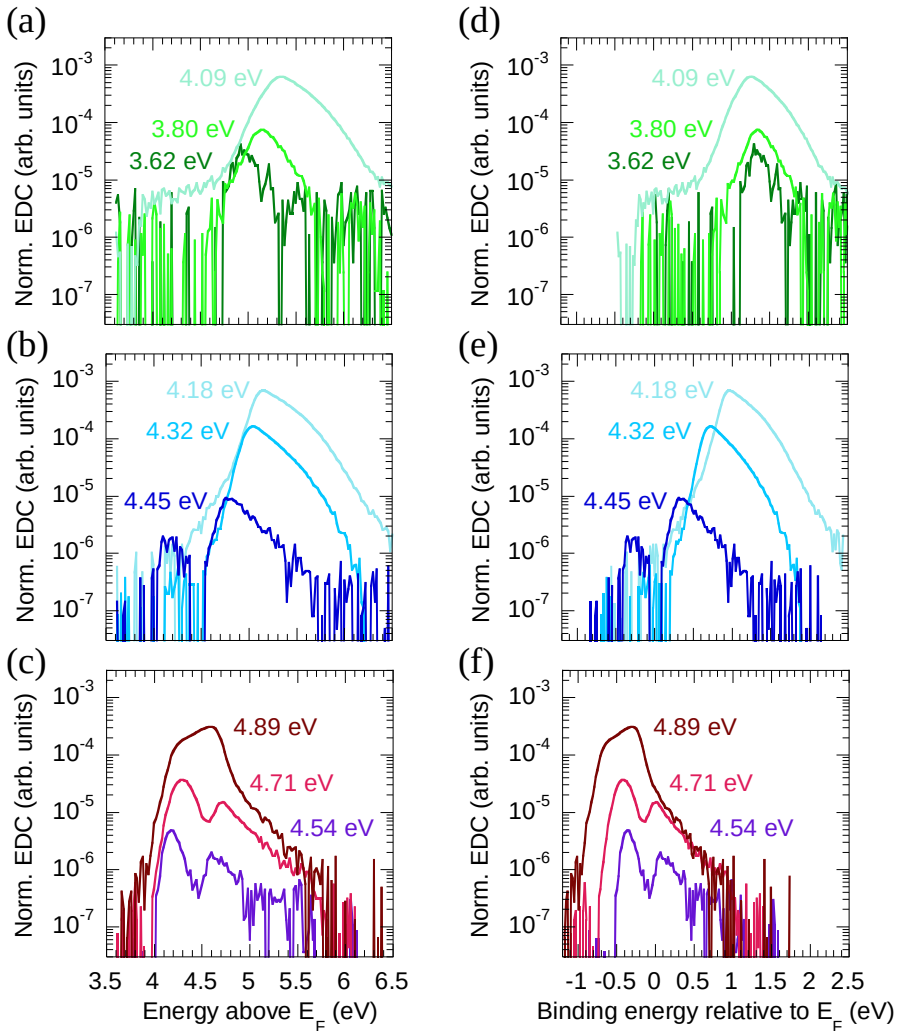

Figure 100 – PE spectra measured in above-gap pulsed excitation on pristine p-GaN at different photon energies. Spectra are normalized to the incident photon flux and plotted as a function of: (a)-(c) measured emission energy; (d)-(f) deduced binding energy.

All the observations related to the power series of above-gap PE of pristine p-GaN that have just been discussed were reproducible on an ARPES setup [108] of the group led by Luca Perfetti at the synchrotron SOLEIL. The excitation photon energy was $h\nu = 4.65$ eV obtained from frequency tripling of a Ti:sapphire laser operated in femtosecond mode and the same sample was used. The setup differed from the one used at Ecole Polytechnique in the electron energy analyzer, which is hemispherical for angular resolution and operated in constant acceleration mode (i.e. the analyzer potentials are varied to scan the electron energy distribution, rather than the sample-analyzer bias), and in the illumination condition, which allows to shine the laser beam directly on the sample (without having to be transmitted through a hole in the analyzer

as in Figure 24). The reproducibility of the results strengthens the reliability of super-energetic PE as an intrinsic process occurring in the crystal and not due to an analyzer artifact.

A quantitative comparison of different properties related to the super-energetic peak measured at above- and below-gap PE of, respectively, p-GaN and p-GaN/Cs is shown in Figure 99. (The low-energy peak is not compared as this corresponds to the "well-behaved" PE, object of the study of Sec. 2.3 and highly sensitive to the electron affinity of the surface.) The slope of the semi-log plots reporting the shift of the super-energetic peak as a function of power (Figure 33e, Figure 34e, Figure 98e) is observed to increase as a function of $h\nu$ (Figure 99a). The integrated current of the super-energetic peak exhibits a similar dependence as a function of the incident photon flux (note: due to the larger spot size the photon irradiance at $h\nu$ = 4.70 eV is ~6× smaller than in the below-gap excitations, however comparable), and it increases with $h\nu$. Both observations are compatible with a SPV effect, which increases with photon energy due to the larger optical absorption in the surface BBR and, in the case of above-gap excitation, also in the bulk. This is however not sufficient to definitively assign a common origin to the super-energetic PE peak observed with above-bandgap pulsed (in femtosecond mode) excitation with the super-energetic PE peak observed with below-bandgap CW excitation. Indeed, the simultaneous shift of the vacuum level and of the super-energetic peak with light power in below-bandgap CW PE allows a coherent explanation in terms of surface gap states shifted by a SPV effect while this explanation is not coherent with the fixed low energy cut-off observed in above-bandgap pulsed PE, as already mentioned.

To study the dependence on $h\nu$ of the super-energetic PE process for above-gap pulsed photoexcitation, a spectroscopy study is carried out. Some representative EDCs are shown in Figure 100 as a function of the measured emission energy and deduced binding energy. The spectra are normalized to the incident photon flux for the corresponding mean excitation power (Figure 101a). (To maximize the super-energetic PE signal, the used power is the maximum achievable laser power shone on the sample after transmission through the optics. Due to the varying efficiency of the nonlinear crystals for THG, the range of powers is distributed within an order of magnitude.) The spectra can be analyzed in three groups, depending on the QY (Figure 101) and exciting photon energy:

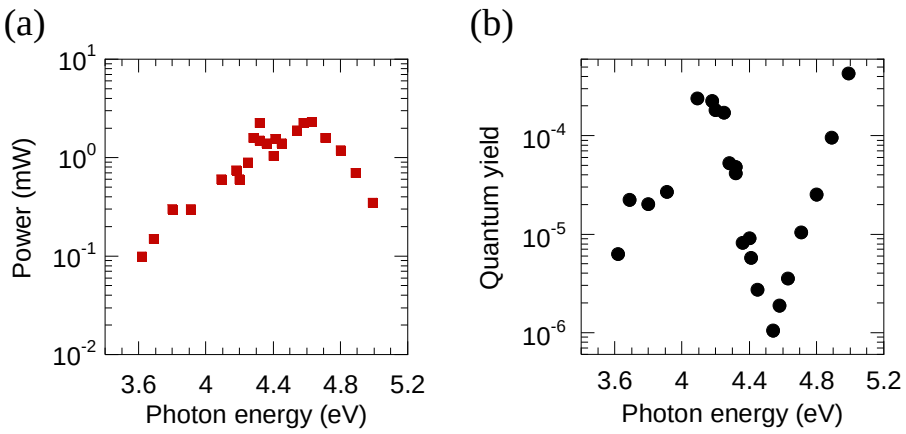

Figure 101 – (a) Mean excitation power used in pulsed above-gap PE of p-GaN at different photon energies. The corresponding measured spectra are shown in Figure 100 and Figure 102a. (b) Quantum yield measured as a function of $h\nu$ at the corresponding powers in (a).

- From 3.6 eV to 4.1 eV: strongly super-energetic electrons are observed (binding energy ~2 eV above E_F) with a QY that increases with $h\nu$. In these conditions no low-energy peak is observed, as expected from the ballistic electron dispersion of Figure 30a since $\varepsilon_C(h\nu) < \phi_{p-GaN}$. In other words, no "well-behaved" PE signal is measured as the final state energy of these photoelectrons lies below the vacuum level. Moreover this electron trapping should enhance the surface accumulation charge responsible for SPV;
- From 4.1 eV to 4.5 eV: increasing $h\nu$ the super-energetic peak decreases in intensity and a low-energy peak starts to appear, in agreement with the fact that $\varepsilon_C(h\nu) > \phi_{p-GaN}$. It is surprising to observe that the QY decreases exponentially at increasing $h\nu$, which is a very unusual phenomenon in standard photoemission. This effect may be related with the progressive decrease of surface accumulation charge, and therefore decrease in super-energetic PE intensity, when a larger fraction of photoelectrons is excited above the vacuum level at increasing $h\nu$;
- From 4.5 eV to 5 eV: increasing $h\nu$ the intensity of the "well-behaved" PE peak (i.e. with binding energy below E_F) increases, as well as the overall QY. The low-energy peak dominates the super-energetic contribution at large photon energy.

One may think that the observed change in the EDCs as a function of $h\nu$ is not due to an intrinsic effect related to various electronic energy transitions occurring in the crystal, but is rather caused by the slightly changing excitation conditions at different $h\nu$, for instance differing in peak power or pulse duration. The following experiments can prove that this is not the case: instead of varying the excitation energy, the sample is excited at a given $h\nu$ = 4.70 eV while its temperature T is progressively varied across a considerable range, from 135K to 700K, by annealing. The temperature series of EDCs is shown in Figure 102b (one spectrum every 2K increment). At fixed optical excitation conditions, the electron distribution undergoes major changes solely because of the temperature variations: at low T mainly a super-energetic electron peak is observed, while increasing T a low-energy peak appears (at ~210K), which progressively dominates the spectrum leading to an integrated current at 700K much larger (20×) than that at 135K. The modifications of the spectra at increasing temperature are closely reminiscent of those observed increasing photon energy at 300K (Figure 102a).

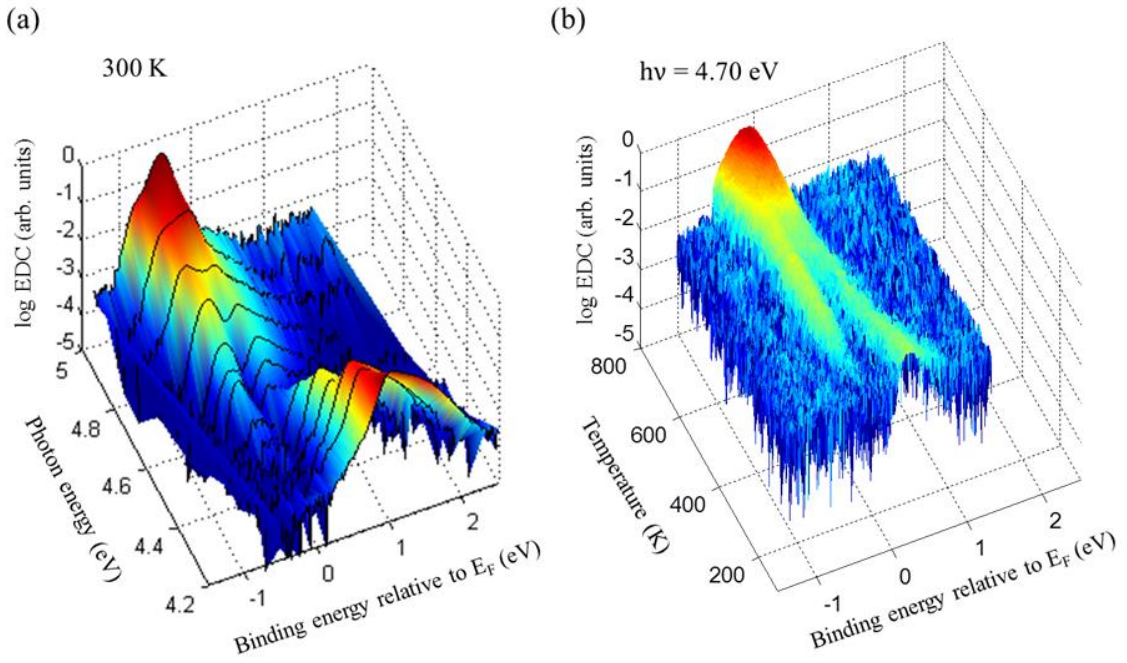

Figure 102 – (a) Series of PE spectra (black lines) measured at 300K in above-gap pulsed excitation on pristine p-GaN at different photon energies. The surface is obtained by linear interpolation between the EDCs. (b) Series of PE spectra measured at $h\nu$ = 4.70 eV on the same sample as a function of temperature (spectra every 2 K).

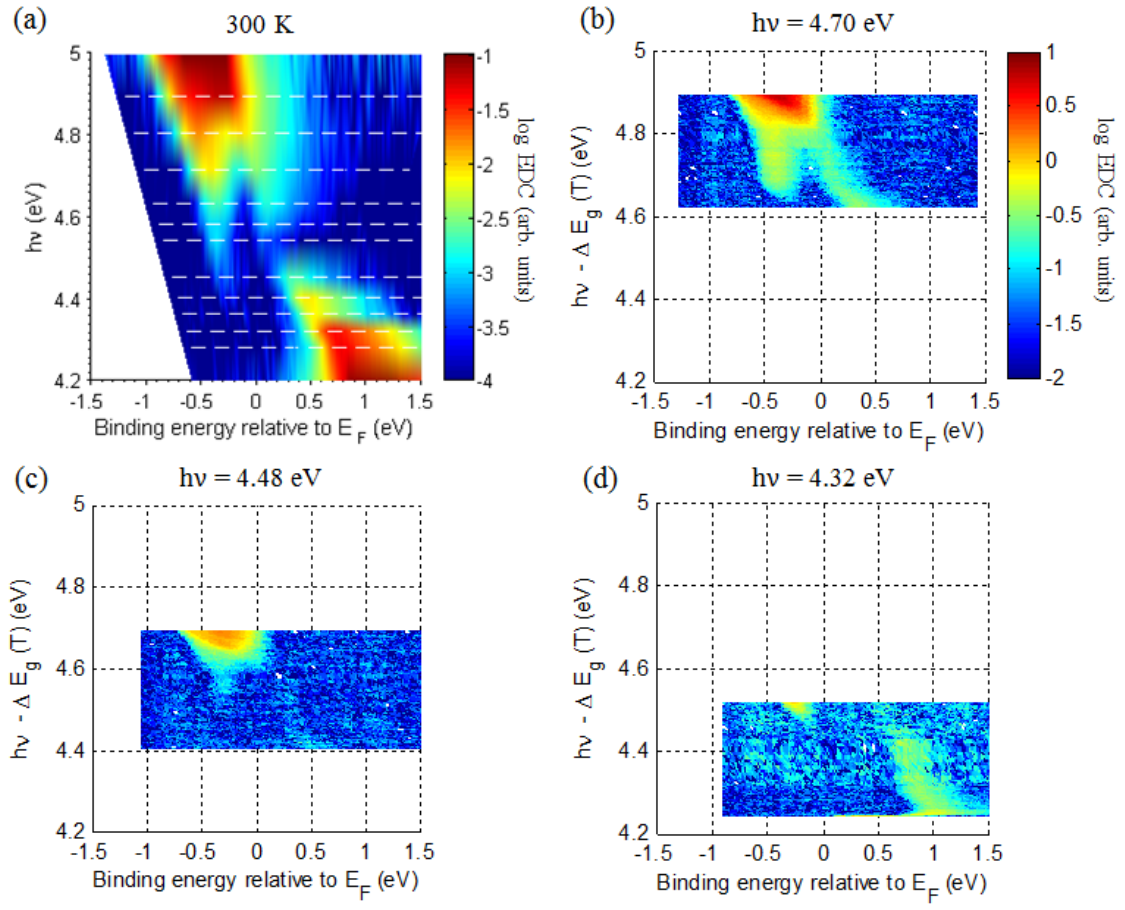

Figure 103 – (a)-(b) Contour plots corresponding to the surfaces shown in Figure 102. (c)-(d) Contour plots obtained as in (b) but at different excitation energy (same colorbar). The y-axis in (b)-(d) corresponds to an "effective" photon energy for interband transitions calculated taking into account the change in band gap energy of GaN as a function of temperature.

For a quantitative comparison between the measurements obtained from the two different type of experiments, the contour plots corresponding to the surfaces of Figure 102a,b are shown in Figure 103a,b. On the assumption that the dominant thermal effect in the temperature series of EDCs is the change in gap energy of GaN, which effectively modifies the energy separation between the initial and final state of a given interband transition, the curves in Figure 103b are plotted as a function of an "effective" photon energy, $h\nu - \Delta E_g(T)$, where $h\nu$ is the actual excitation photon energy and $\Delta E_g(T)$ is the change in gap energy of GaN as a function of temperature (IOFFE GaN database, Bougrov et al. [211]) with respect to its value at 300K. (Note that the term "interband" is here intended in a general meaning of transitions between different electronic bands, therefore not only from the valence to the conduction band, but also from bands in the

gap to the conduction band.) The striking similarity between the different features observed in the spectroscopy measurements as a function of $h\nu$ (Figure 103a) and the temperature series at exciting photon energies of 4.70 eV, 4.48 eV and 4.32 eV (Figure 103b-d) confirm that the PE spectra, including the super-energetic contributions, originate from intrinsic PE processes occurring in p-GaN and sensitive to its band gap.

5.4 Photoemission excited by electro-luminescence light

5.4.1 Contribution of the electro-luminescence-excited photoemission to the LED electro-emission

A PE+EE control experiment was carried out in Ref. [87] to verify whether shining on an LED sample an external light source at the same emission wavelength of the LED would allow generating the high-energy peaks, called ① (or L) and ② (or Γ), typically observed in LED EE, in addition to the low-energy peak ③. The outcome of the control experiment was considered as negative, in particular it was stated:

> *We disprove the possibility that the L and Γ-valley peaks could be generated by photon absorption of LED light. […] Both the measurements performed under zero and forward bias generated only a low energy peak ③. In the high energy region around peak ①, the measured electron PE current was not discernible from noise. The high energy electrons observed in peak ① must therefore be due to an internal process generating hot electrons inside the LED, i.e., the Auger process.*

The relevant spectra of Ref. [87] are reproduced in Figure 104 with a different scale on the y-axis, corresponding to the measured Faraday current (not corrected for the different duty cycles). The LED EE spectrum (gray curve) was measured at 128 mA with a duty cycle of 6% and a pulse width of 6 μs. PE experiments were carried out at $h\nu$ = 2.71 eV using a Kr/Ar laser modulated with a chopper wheel at 50% duty cycle and a frequency of 41 Hz. Synchronous lock-in detection was used to extract the photoemission signal. The (unchopped) laser power was 18.1 mW and the beam had a spot diameter of ~140 μm. PE spectra were measured: without any bias applied to the LED (blue curve); with simultaneous electrical injection at 128 mA and an electrical duty cycle of 12.5% (red curve). As mentioned in Ref. [87], only a noise signal was detected in the control experiments in the high-energy region corresponding to the extension of peak ① (dashed rectangle). However, a shoulder was present on the high-energy side of the main peak in PE without bias (marked by an arrowhead), and partly smeared out in PE+EE (probably due to an effect of the electrical duty cycle).

Following experiments presented in Sec. 2.4.2 demonstrated that it is possible to photogenerate a high-energy contribution in the same energy range of the high-energy peak observed in EE alone (Figure 43b). Moreover, it was clearly shown that such high-energy contribution shifts towards high energies at increasing I_{LED}. The difference

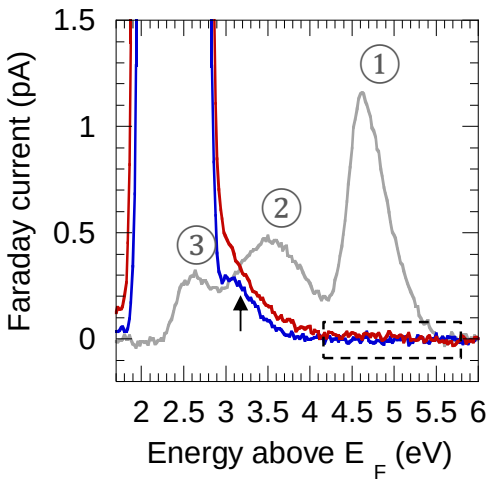

Figure 104 – PE and EE experiments carried out on the LED sample of Ref. [87]. LED EE is measured at 128 mA and at a duty cycle of 6% (gray curve). Peaks are labeled as in the original study. PE excitation is at hν = 2.71 eV. PE spectra are measured by synchronous lock-in detection at zero- (blue curve) and forward-bias (red curve, 128 mA injected) on the LED, and exhibit a hot electron tail (arrowhead). Spectra are not corrected for the different duty cycles.

between the observations of the two PE+EE experiments is ascribed to the electrical operation of the LED, which was continuous in Sec. 2.4.2 and pulsed in Ref. [87]. Due to the electrical duty cycle, in average, during 87.5% of the illumination time I_{LED} was zero generating the high-energy peak in proximity of the low-energy peak. It was only during the remaining 12.5% of the time that the current was injected in the LED and the shift towards high energy due to I_{LED} should be expected to occur, setting the expected intensity of this peak close to the noise level.

In summary, as showed by later experiments it is actually possible to photogenerate the high-energy peak observed in LED electro-emission. The conclusions drawn in Ref. [87] did not take into account a shift mechanism affecting the position of the high-energy peak as a function of the current injected in the LED, which is ultimately due to the rectifying character of the p-contact of the device (see Figure 47).

5.4.2 Contribution of the electro-luminescence-excited photoemission to the electro-emission of a GaN p-n junction

Another control experiment that was presented in Ref. [87] consisted in measuring a simple p-n junction by electro-emission. Since the high-energy peak observed in LED EE was interpreted as due to Auger recombination in the QWs, then the goal of the

control experiment was to verify that no Auger electron peak can be generated in a structure without sufficient carrier confinement.

The sample was a simple p-n junction structure grown at UCSB by MOCVD and consisted of: p+ GaN cap/p-GaN (200 nm, [Mg] = $2 \cdot 10^{19}$ cm^{-3})/UID GaN (120 nm, $1 \cdot 10^{16}$ cm^{-3} [donors])/n-GaN (200 nm, [Si] = $5 \cdot 10^{17}$ cm^{-3})/n-GaN (2 µm, [Si] = $5 \cdot 10^{18}$ cm^{-3})/ GaN buffer.

The EDCs corresponding to p-n EE for injected currents in the device (I_{p-n}) ranging between 2 mA and 16 mA are shown in Figure 105a. At 2 mA a single peak with a HET

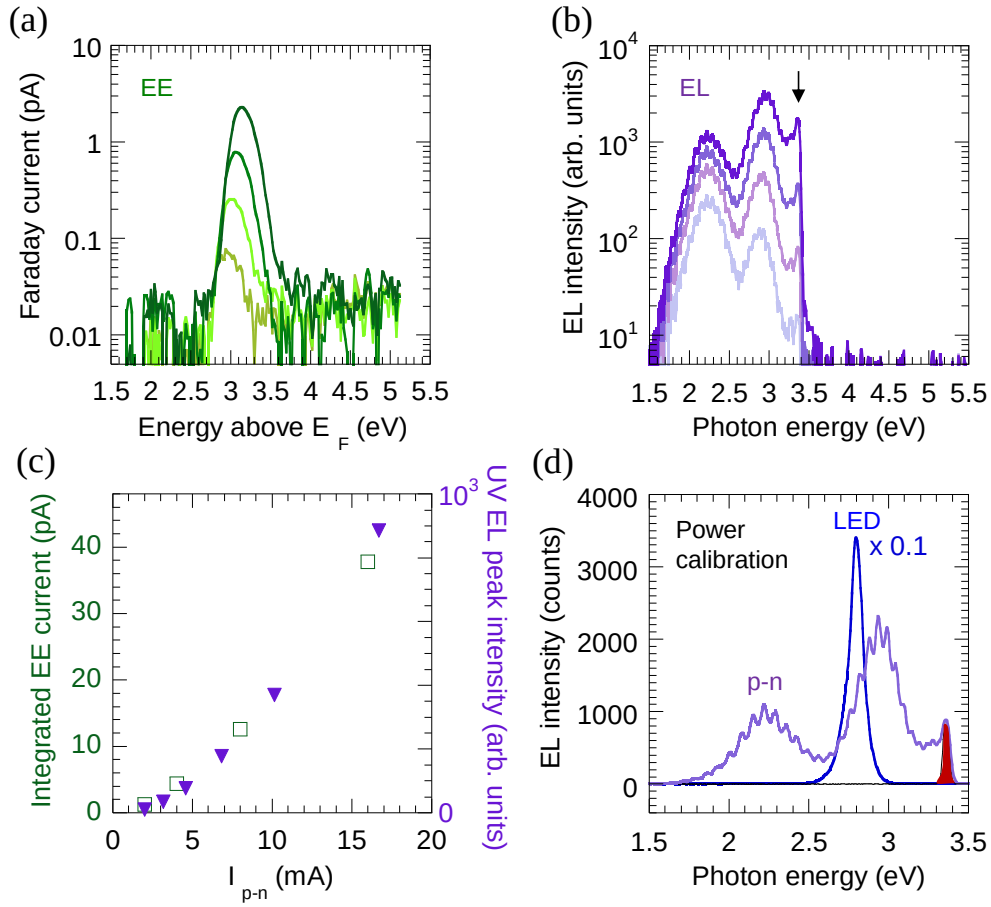

Figure 105 – (a) p-n junction EE spectra from Ref. [87] measured at (from bottom to top): 2 mA, 4 mA, 8 mA, 16 mA. (b) EL spectra of the p-n junction measured at (from bottom to top): 2.0 mA, 4.6 mA, 10.2 mA, 25.4 mA. A UV EL peak is observed (arrowhead). (c) Integrated Faraday current measured in EE (squares) and intensity of the UV EL peak (triangles) as a function of the injected current in the p-n junction. (d) EL spectra of a blue LED (blue curve) and the p-n junction (violet curve) to calibrate the internal power of the p-n junction.

lying at the energy of the CBM in the bulk is observed. Increasing I_{p-n} the peak undergoes a non-ohmic shift towards higher energy, similarly to what observed in LED EE. This peak was interpreted in Ref. [87] as directly originating from electrons that leaked past the junction region into p-GaN. The control outcome was negative and the absence of a high-energy peak, like the one observed in LED EE, was attributed to the insufficient carrier confinement to generate the locally high electron and hole densities necessary for a high Auger recombination rate. The studies that will be presented in the following led to different conclusions, namely that: 1) the main peak observed in p-n EE could be photogenerated by the internal p-n junction electro-luminescence; 2) a hot electron peak may be observed in p-n EE; 3) a hot electron peak can be photoexcited in a p-n junction in PE+EE experiments similar to those carried out on a LED (cf. Sec. 2.4.2).

The EL spectra obtained at different I_{p-n} for the sample measured in Ref. [87] are shown in Figure 105b. In addition to yellow and blue impurity bands, a luminescence peak in the UV range is observed at hν = 3.36 eV, corresponding to the energy separation between the minimum of the Γ valley and E_F, as determined in Sec. 2.3.4. In principle, the main electron peak observed in p-n EE could be photoexcited by this UV EL peak, rather than being directly populated by a leakage process. Indeed, both the EE and UV EL peak increase super-linearly with I_{p-n} (Figure 105c), indicating a correlation between the two processes.

One could think that the EL intensity of a simple p-n junction is too weak to photoexcite a detectable electron emission signal. However it should be considered that near-band gap excitation of cesiated p-GaN gives a much larger PE QY than below-gap excitation (for instance at hν = 3.36 eV the QY is of few %, over an order of magnitude larger than at hν = 2.8 eV [102]). Therefore, the weak UV EL intensity may be somewhat compensated by the relatively high electron escape probability into vacuum. Ultimately, the best way to verify whether the p-n EE peak is photogenerated is to mimic the UV EL peak by external photoexcitation and then compare the EE and PE spectra.

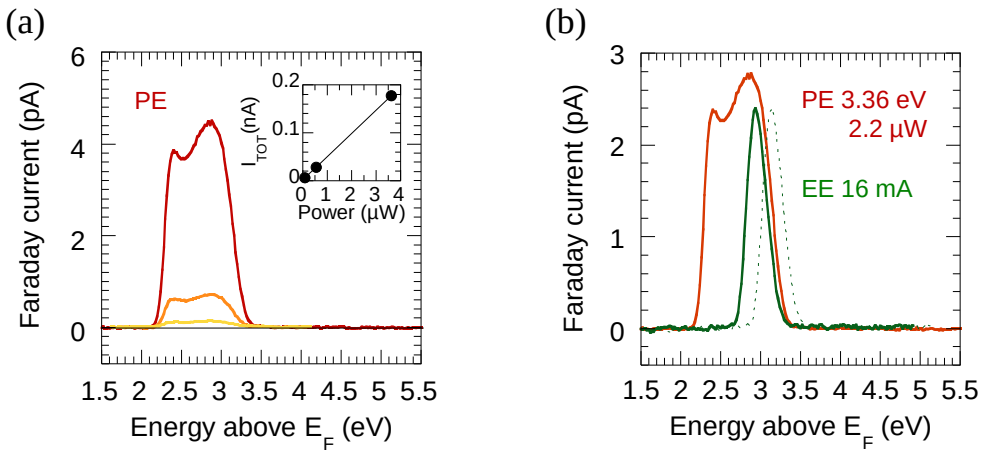

Figure 106 - (a) PE spectra measured on a p-n junction processed for PE with an excitation spectrum corresponding to the red region in Figure 105d and at a photon energy of (from top to bottom): 0.09 μW, 0.56 μW, 3.63 μW. The inset shows the linearity of the integrated current with excitation power. (b) p-n junction PE spectrum of the p-n junction rescaled from (a) to correspond to an excitation power of 2.2 μW (red curve). EE spectrum of the p-n junction from Figure 105a at 16 mA (dashed green curve) and after correction for the non-ohmic shift with current (solid green line).

For this purpose, the internal optical power of the p-n junction has to be evaluated and this is done as follows. First, the EL of an LED, used as a calibration sample and processed with the same contact geometry of the p-n junction, is measured at I_{LED} = 0.3 mA (blue curve in Figure 105d). The internal optical power of the LED can be estimated as 574 μW from $I_{LED} \cdot h\nu/e \cdot IQE$, where an IQE of 68% has been taken (from the relative QE curve and the peak IQE fitted from the ABC model using Eq. (80)). Then the EL of the p-n junction is measured at I_{p-n} = 16 mA (violet curve in Figure 105d). The alignment of the setup used for the EL measurement is unchanged (notably the light collection efficiency is unvaried). Therefore, assuming the same light extraction efficiency for the two samples, the measured EL spectral intensities can be directly compared. From this it is deduced that the total internal optical power of the p-n junction at 16 mA is 213 μW.

The PE experiment is carried out on a p-n junction sample (same [Mg] doping of the EE sample, p-GaN layer thickness of 1 μm) processed for PE, especially to avoid any metal PE from the p-contact. The excitation spectrum used in PE mimics the UV EL peak of the p-n junction and is obtained using the same broadband light source and

monochromator described in Sec. 2.3.1, with an output spectrum corresponding to the red region of Figure 105d. The integrated internal power of the p-n junction EL at 16 mA in this red region is $P_{pn,UV}$=5.4 µW. The equivalent $\mathbf{P_{ext,PE}}$ to be used to mimic the UV EL peak is 2.2 µW, as obtained from:

$$\mathbf{P_{ext,PE} = \frac{P_{pn,UV} \cdot f_{ap}}{T_{rot} \cdot (1 - R)}} \qquad \mathbf{(92)}$$

which takes into account for the difference in the illumination condition of the EE and "PE on PE sample" experiment (cf. Figure 41).

The PE EDCs measured at different excitation powers in the range 0.1-4 µW are presented in Figure 106a and are observed to scale linearly with power (inset). Therefore, the PE EDC measured at the highest power can be re-normalized to correspond to the required excitation power of 2.2 µW and finally be compared with the p-n EE EDC measured at 16 mA (corrected for the non-ohmic energy shift), as shown in Figure 106b. The PE spectrum exhibits a higher NEA, likely due to the higher annealing temperature used in the sample preparation, which reveals an additional low-energy contribution, already observed in previous near-band gap PES studies ("S" peak, described in Sec. 2.3.3) and attributed to thermalization in the BBR. Taking into account the difference in vacuum level position, the quantitative agreement in the intensity and position of the main peak in PE and EE is excellent. This result suggests that the p-n junction EE spectrum is substantially generated by the internal UV EL, which rises an important question: why no leakage electrons are measured? Two

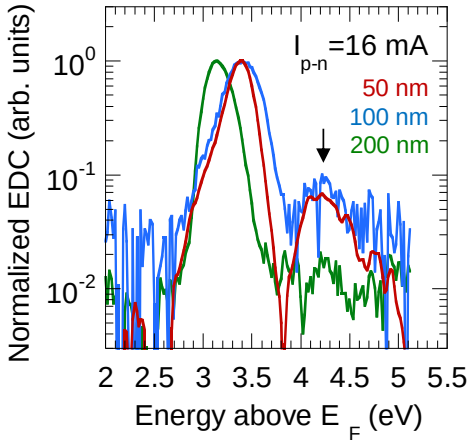

Figure 107 – Normalized EE spectra measured at an injected current of 16 mA in p-n junction devices of different p-GaN layer thickness (50 nm, 100 nm, 200 nm). A high-energy peak is observed (arrowhead).

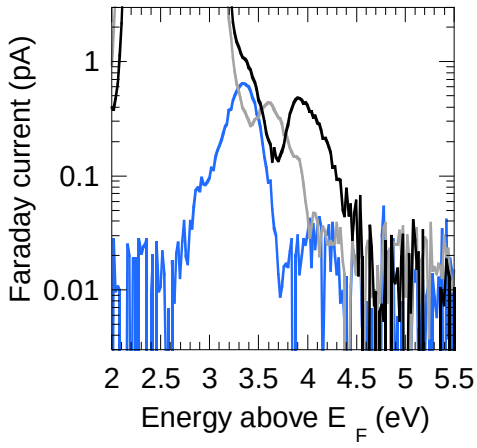

Figure 108 – PE and EE experiments showing the photocreation of a high-energy peak in a p-n junction. The EE spectrum is measured at 8 mA (blue curve). PE excitation is at hν = 3.06 eV. PE spectra are measured at zero- (gray curve) and forward-bias (black curve, 8 mA injected) on the p-n junction.

hypotheses could be proposed to explain this: i) the minority carrier diffusion length in p-GaN is much shorter than the 200 nm thickness of the considered p-GaN layer of the structure; ii) some potential inhomogeneity across the injection area prevents the leakage electrons from reaching the apertures and be emitted into vacuum. These problems are discussed in Sec. 2.6.1.2 and 2.6.1.3.

The next point that shall be discussed is the possible presence of a high-energy peak in p-n EE. As already mentioned, the conclusion reported in Ref. [87] was that no high-energy peak is observed in p-n EE due to the insufficient carrier confinement to generate a significant Auger rate. However, repeating the EE measurement on similar p-n junction structures differing only in the thickness of the p-GaN layer, a high-energy peak was clearly detected in a p-n junction with a 50 nm thick p-GaN layer, as shown in Figure 107 (marked by an arrowhead). Actually a comparison of the EDCs measured at I_{p-n} = 16 mA in the different devices suggests that such high-energy peak should be emitted from all samples (including the sample studied in Ref. [87] corresponding to the green curve in Figure 107) but with an intensity that is 10-50× smaller than the main peak, which may make it almost unnoticeable depending on the signal-to-noise ratio. The energy separation between the HET of the main and high-energy peak is ~1.25 eV, a little larger than the one measured between the two high-energy peaks in LED EE, but the lineshape of the high-energy peak observed in LED and p-n EE is the same.

The observation of a high-energy peak in p-n junction EE is surprising and, for the aforementioned reason, a generation from an Auger process should be excluded. Drawing inspiration from the LED EE and PE results presented in Sec. 2.4.2, it may be supposed that the internal electro-luminescence of the device, due to a photoelectric process that is still not completely identified, could photoexcite in the p-GaN layer not only the main EE peak but also the high-energy peak.

To test this mechanism, PE+EE experiments similar to those carried out in the LED structure and presented in Figure 43a,b are repeated on the p-n junction EE sample with a 100 nm thick p-GaN layer. The excitation source for PE is a laser diode in continuous wave (CW) operation emitting at $h\nu = 3.06$ eV, below the band gap of GaN, with an external excitation power of 38 mW.

The results are shown in Figure 108. The EE spectrum measured at $I_{p-n} = 8$ mA (blue curve) shows a main peak with a weak high-energy peak. The PE spectrum measured exciting the p-n junction at zero forward bias (gray curve) shows an intense peak due to PE from the p-contact and a hot electron peak. In simultaneous PE+EE this hot peak shifts towards high energies, as in the similar LED experiments, and holds the same energy position of the high-energy peak observed in EE alone. From these measurements it can be concluded that: first, the high-energy peak which may be observed in p-n junction EE can be photogenerated; second, the PE+EE experiments carried out in LEDs (cf. Sec. 2.4.2) give similar results in a p-n junction structure, which leads to the conclusion that the photoelectric process involved must occur in GaN.

5.5 Type-II well-to-barrier transitions in InGaN/GaN QWs

The mechanism giving origin to the C-region observed in the BPCS measurements at below-gap photon energies (Sec. 3.2) is modeled in the following as a type-II well-to-barrier transition, similarly to the process suggested in Ref. [178]. The final state of the transition corresponds to a hole occupying the ground state of the QW and an electron excited in the barrier (Figure 109a), which should correspond to the electronic process giving the dominant contribution to the photocurrent signal for type-II absorption because of the light mass of the unbound carrier. Due to the presence of the barrier and QW electric fields both wave functions are Airy functions.

Already at this point we can remark that the present model may explain why the C-region is well observed in UV diodes but progressively disappears going in the visible range. Indeed, increasing the In content of the QW increases the well-barrier conduction band offset ΔE_C and decreases the threshold photon energy for below-gap transitions. This in turn spatially shifts the final state electron Airy function further from the bound hole wave function, decreasing the electron-hole overlap and thus the probability amplitude of type-II transitions, as schematized in Figure 109b. For this reason, other mechanisms of below-gap absorption, namely compositional disorder and QCFK in the QW, are observed to dominate in the spectra of the measured solar cells with high In composition and large well-barrier conduction band offset.

The final electron state ψ_e is calculated in the bulk approximation as an Airy function with parameters defined by the barrier material [124]:

$$\boldsymbol{\psi_e}\,(\boldsymbol{E_e}, \boldsymbol{z}) = \boldsymbol{Ai}[\left(\frac{\boldsymbol{2m_e \cdot e \cdot |\vec{E}_b|}}{\boldsymbol{\hbar^2}}\right)^{\boldsymbol{\frac{1}{3}}} \cdot \left(-\frac{\boldsymbol{E_e}}{\boldsymbol{|\vec{E}_b|}} + \boldsymbol{z}\right)] \qquad \textbf{(93)}$$

where $\vec{E}_b$ is the electric field in the barrier of the structure, m_e and E_e are the electron effective mass and energy, respectively, and z is the growth direction. The hole ground state $\psi_{h,0}$ is calculated analytically from the Schrödinger equation in the approximation of an infinitely deep potential well of width L_{QW} in presence of an electric field $\vec{E}_{QW}$:

$$\boldsymbol{\psi_{h,0}(E_{h,0}, z) = Ai[Z_{h,0}(E_{h,0}, z)] + c_{h,0} \cdot Bi[Z_{h,0}(E_{h,0}, z)]} \qquad \textbf{(94)}$$

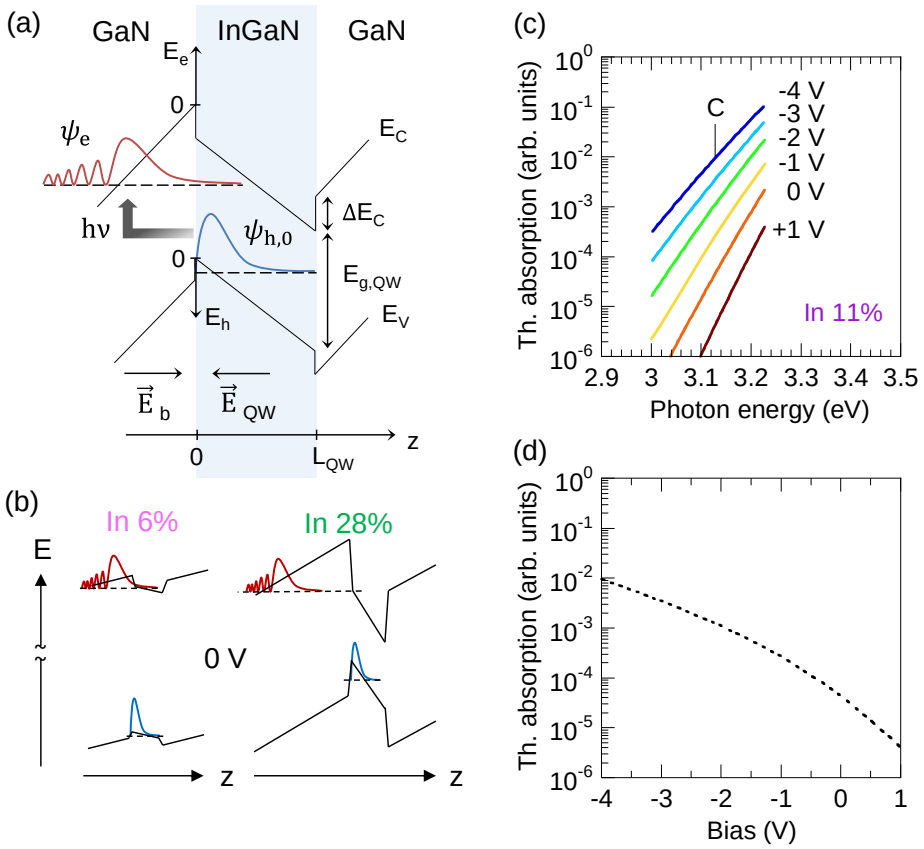

Figure 109: (a) Schematic of type-II well-to-barrier transitions in an InGaN/GaN QW. In presence of barrier and QW electric fields the electron and hole final states, ψ_e and $\psi_{h,0}$, are Airy functions with tails extending in the gap and allowing below-gap absorption at photon energies $h\nu < E_{g,QW}$. (b) Schematic explaining why type-II transitions have a higher probability in InGaN/GaN structures with low In content. Band diagrams are calculated with a 1D Poisson-drift-diffusion solver and show realistic QW electric fields. (c) Simulated type-II absorption curves for an $In_{0.11}Ga_{0.89}N$/GaN QW as a function of applied bias. (d) Change in the simulated type-II absorption as a function of bias at a photon energy marked as "C" in (c).

where Ai and Bi are Airy functions; $Z_{h,0}(E_{h,0}, z)$ is defined as $(2m_h \cdot e \cdot |\vec{E}_{QW}|/\hbar^2)^{1/3} \cdot (\frac{E_{h,0}}{|\vec{E}_{QW}|} + z)$; m_h is the hole effective mass; the coefficient $c_{h,0}$ and the hole energy $E_{h,0}$ are obtained from the boundary conditions $\psi_{h,0}(E_{h,0}, 0) = \psi_{h,0}(E_{h,0}, L_{QW}) = 0$. Then the optical absorption will be proportional to the overlap integral $I(E_e, E_{h,0})$ as:

$$\alpha(h\nu) \propto \int I(E_e, E_{h,0})\,\delta(E_e + E_{h,0} + E_{g,QW} + \Delta E_C - h\nu)\,dE_e \qquad \textbf{(95)}$$

where $I(E_e, E_{h,0}) = \left|\int_0^{L_{QW}} \psi^*{}_e(E_e, z)\, \psi_{h,0}(E_{h,0}, z)\, dz\right|^2$ with the integral boundaries fixed by the boundary conditions of $\psi_{h,0}$; $E_{g,QW}$ is the energy gap of the QW; ΔE_C is assumed to be 80% of the band offset of the heterojunction.

From the electron and hole wave functions type-II absorption is calculated as a function of applied bias for a single QW structure representative of the measured solar cell with In=11%. It is assumed $E_{g,QW} = 3.23$ eV as the experimental value measured at 5 K, and the bias-dependence of $\vec{E}_{QW}$ and $\vec{E}_b$ is obtained from 1D Poisson-drift-diffusion simulations of the device [182].

The results of the model are shown in Figure 109c. A qualitative agreement is observed between the simulated absorption curves and the experimental features of the C-region shown in Figure 72a: increasing the reverse bias from +1 V to -4 V the absorption rapidly increases while the slope of the tail decreases. The change in absorption as a function of bias at a fixed photon energy (marked "C" in Figure 109c) is plotted in Figure 109d. Qualitatively, the nearly exponential increase in absorption resembles the experimental increase in responsivity measured at 5 K shown in Figure 72d. The larger signal observed in the experiments at 300 K in the $\sim[-1, +1]$ V range is attributed to additional mechanisms of below-gap absorption exciting carriers in the QW, namely disorder and FK. Indeed, while type-II transitions directly create carriers in the barrier ready to contribute to the photocurrent signal (if we neglect subsequent recapture by other QWs), other mechanisms involving absorption in the QW will require thermal energy in order to allow thermionic emission from the QW and contribute to photocurrent. (These different processes are schematized in Figure 72e.)

The proposed model gives considerable qualitative insights into the mechanism responsible for the observation of the C-region. Finally, it should be remarked that while the model only considers type-II well-to-barrier transitions, in the experimental C-region it may be present, even at 5 K, a residual contribution to the responsivity signal due to other mechanisms of absorption. This may be the source of quantitative disagreement on the rate of the increase of the modeled absorption vs. the experimental responsivity as a function of bias, in addition to the approximations used (ψ_e in the bulk limit, $\psi_{h,0}$ in the infinitely deep well limit) and the sensitivity of the model on different parameters, such as ΔE_C, $\vec{E}_{QW}$, $\vec{E}_b$, which have been assumed here.

5.6 Computation time of the landscape theory applied to LEDs compared to other models

Table V shows the approximate computation time required for each iteration step when solving different equations, including the Poisson equation, drift-diffusion equation, localization landscape equation, and Schrödinger equation. The ARPACK solver [212] for the generalized eigenvalue problem was used. For the solution of the inverse problem, the PARDISO solver [213] was used. Typically, the environment of clusters to which the computation is submitted is 2 Intel Xeon 5650V2 8 cores 2.6 GHz CPUs with 396GB memory.

Let us draw a comparison with the computation time deduced from the simulations of InGaN/GaN QWs incorporating random indium fluctuations as reported by other groups using different computational methods. D. Watson-Parris *et al*. used the finite difference method with a number of nodes of ~1’500’000 to solve the 3-D effective mass Schrödinger equation [196,214],. Their computation time is ~60’000 s, which is extremely time consuming. Current injection and carrier screening are not considered, and the Poisson-Schrödinger solver is not self-consistent. Concerning atomistic simulations, S. Schulz *et al*. adopted the empirical tight binding method (TBM) and valence force field model to account for the strain-induced polarization field and band structure of the QW, while the perpendicular carrier transport was overlooked [173]. The simulation domain is limited near the single QW region with a size of 10 nm × 9 nm × 10 nm, containing ~82’000 atoms. The typical node size should be around 82’000×4, with an estimated computation time of 7’500 s. M. Auf der Maur *et al*. also applied the empirical TBM to model indium fluctuations in InGaN QWs [200]. Although the classical Poisson and drift-diffusion model was used to solve the electrostatic potential, the atomistic calculation was not performed self-consistently with the classical model. The dimension of the atomistic simulation is still limited near the QW region (10 nm × 10 nm × 11 nm containing~100’000 atoms), which cannot be used to model full MQW LED structure by considering the computation time of 24’000.

It can be concluded that the landscape model coupled to the Poisson-DD equations is much more computationally efficient with respect to state-of-the-art quantum solvers, while still incorporating quantum effects such as tunneling and quantum confinement.

	Number of nodes	**Computation time (s)**
Poisson	428’655	25
Drift-diffusion	428’655	50
Localization landscape	428’655	50
Schrödinger	428’655	63’650
Watson-Parris *et al.* [196,214]	1’500’000	60’000
Schulz *et al.* [173]	328’000	7’500
Auf der Maur *et al.* [200]	100’000	24’000

Table V - Computation time required for each iteration step when solving the Poisson, drift-diffusion, localization landscape, and Schrödinger equations for a given number of nodes, as tested by the home-built software of our collaborators (Yuh-Renn Wu’s group, National Taiwan University) and compared with other referenced models.

université PARIS-SACLAY
ÉCOLE DOCTORALE
INTERFACES
Approches Interdisciplinaires : Fondements, Applications et Innovation

Titre : Spectroscopie des processus photoélectriques dans les structures et dispositifs III-N

Mots clés : diodes émettrices de lumière, nitrures, spectroscopie électronique, localisation

Résumé : Malgré les rapides progrès technologiques dans les nitrures, les propriétés intrinsèques des alliages de nitrures et les processus physiques qui gouvernent la physique de ces dispositifs sont encore mal connus. Au cours de mon travail de thèse, de nouvelles approches expérimentales et théoriques ont été développées pour aborder l'étude des mécanismes microscopiques qui gouvernent les propriétés électroniques des dispositifs à base de nitrures semi-conducteurs.
Une nouvelle technique expérimentale permettant de mesurer directement la distribution en énergie des électrons de conduction d'une LED en fonctionnement est explorée. Cette approche permet l'observation directe de populations d'électrons chauds excités dans le dispositif optoélectronique sous injection électrique et émis dans l'ultravide.
Une théorie récente de la localisation dans les systèmes désordonnés est appliquée aux matériaux et dispositifs optoélectroniques à base de nitrures. Cette méthode permet pour la première fois la détermination du paysage de localisation induit par le désordre d'alliage sans résoudre l'équation de Schrödinger. Expérimentalement, une signature claire du désordre d'alliage est observée par des mesures de spectroscopie de photocourant dans des puits quantiques d'InGaN sous forme d'une queue d'Urbach pour des excitations d'énergie inférieure à la largeur de la bande interdite. Ceci permet de définir une énergie caractéristique du désordre qui est en excellent accord avec les prédictions fournies par la nouvelle théorie de la localisation.

Title : Spectroscopy of photoelectric processes in III-N structures and devices

Keywords : light-emitting diodes, nitrides, electron emission spectroscopy, localization

Abstract : In spite of the rapid technological progress in nitrides, the intrinsic properties of nitride alloys and the physics of III-N devices are still not well understood. In the course of my thesis work, novel experimental and theoretical approaches to tackle the study of the microscopic mechanisms governing the electronic properties of nitride semiconductors have been developed.
A new experimental technique allowing to directly measure the energy distribution of conduction electrons of an operating LED is explored. This approach allows the direct observation of hot electron populations excited in the optoelectronic device under electrical operation and emitted in ultra-high vacuum.
A recent theory of localization in disordered systems is applied to nitride materials and optoelectronic devices. This method allows for the first time the determination of the localization landscape induced by alloy disorder without resorting to the Schrödinger equation. Experimentally, a clear signature of alloy disorder is observed by biased photocurrent spectroscopy of InGaN quantum wells in the form of an Urbach tail for below-gap excitation and is found to be in excellent agreement with the predictions given by the novel localization theory.

Université Paris-Saclay
Espace Technologique / Immeuble Discovery
Route de l'Orme aux Merisiers RD 128 / 91190 Saint-Aubin, France